Titre: Title:	Microwave Heating-Assisted Chemical Looping Dry Reforming of Methane
Auteur: Author:	Mohammad Khodabandehloo
Date:	2024
Type:	Mémoire ou thèse / Dissertation or Thesis
Référence: Citation:	Khodabandehloo, M. (2024). Microwave Heating-Assisted Chemical Looping Dry Reforming of Methane [Thèse de doctorat, Polytechnique Montréal]. PolyPublie. https://publications.polymtl.ca/59646/

URL de PolyPublie: PolyPublie URL:	https://publications.polymtl.ca/59646/
Directeurs de recherche: Advisors:	Jamal Chaouki, Jean-Philippe Harvey, & Jaber Shabanian
Programme: Program:	Génie chimique

POLYTECHNIQUE MONTRÉAL

affiliée à l'Université de Montréal

Microwave heating-assisted chemical looping dry reforming of methane

MOHAMMAD KHODABANDEHLOO

Département de génie chimique

Thèse présentée en vue de l'obtention du diplôme de *Philosophiæ Doctor*

Génie chimique

Octobre 2024

POLYTECHNIQUE MONTRÉAL

affiliée à l'Université de Montréal

Cette thèse intitulée :

Microwave heating-assisted chemical looping dry reforming of methane

présentée par **Mohammad KHODABANDEHLOO**

en vue de l'obtention du diplôme de *Philosophiæ Doctor*

a été dûment acceptée par le jury d'examen constitué de :

Charles DUBOIS, président
Jamal CHAOUKI, membre et directeur de recherche
Jaber SHABANIAN, membre et codirecteur de recherche
Jean-Philippe HARVEY, membre et codirecteur de recherche
Oumarou SAVADOGO, membre
Ange NZIHOU, membre externe

DEDICATION

To my GOD, my parents, and my sister, who are my best friends to infinity and beyond that.

To every child around the world deprived of their fundamental right to education: whatever I achieve, I dedicate to you.

ACKNOWLEDGEMENTS

I would like to express my heartfelt gratitude to everyone who contributed to the completion of this project.

To my father and my mother: All that I have accomplished and all that I will achieve in the future is thanks to you. Every good deed I perform is a reflection of your invaluable teachings and guidance.

To my sister: You are my best friend for eternity and beyond. You are the first person I turn to with any news. Words cannot adequately express how deeply your support warms my heart.

I would like to extend my heartfelt gratitude to my supervisors, Prof. Jamal Chaouki, and my co-supervisors Dr. Jaber Shabanian and Dr. Jean Philippe Harvey, for their invaluable mentorship, assistance, motivation, and patience during my Ph.D. journey. Collaborating with them has been a privilege and an immense educational opportunity.

I would like to thank Prof. Charles Dubois, Prof. Oumarou Savadogo, and Prof. Ange Nzihou for accepting to serve as members of the thesis committee.

I would like to thank Sharif University of Technology for helping me find friends who have become absolute treasures to me.

I would like to extend my heartfelt gratitude to all the members of our research group (PEARL), especially Mr. Siavash Beigiparast, Mr. Javad Vahabzadeh Pasikhani, Dr. Iman Soleimani, Dr. Mojtaba Mokhtari, Mr. Kazem Adavai, Dr. Mohammad Latifi, Dr. Adrián Carrillo Garcia, Dr. Fadoua Laasri, and Dr, Mohamed Khalil for the amazing discussions that we had.

I would like to extend my heartfelt gratitude to all the members of CRCT, specially Dr. Kentaro Oishi, Ms. Camille Rincent, Dr. Paul Lafaye, and Ms. Dyhia Ait.

Last but not least, I am deeply thankful to the technicians of the Chemical Engineering department, particularly Mr. Santini Pace and Mr. Mario Grenier, whose technical expertise and support was crucial to accomplish this project.

RÉSUMÉ

Le syngaz ou gaz de synthèse, est un mélange gazeux de monoxyde de carbone (CO) et d'hydrogène (H_2). Le gaz de synthèse est une matière première essentielle pour la production de plusieurs produits chimiques, tels que l'éthanol et le méthanol. En outre, plus de la moitié de la production mondiale de H_2 est obtenue par la séparation entre H_2 et le gaz de synthèse. L'objectif principal de cette recherche est d'étudier la production durable de gaz de synthèse en utilisant le méthane (CH_4) et le dioxyde de carbone (CO_2), qui représentent ensemble plus de 90% des gaz à effet de serre (GHG). Par conséquent, cette recherche a proposé et étudié un concept innovant de production de gaz de synthèse en intégrant la boucle chimique (CL) au chauffage par micro-ondes (MWH), tout en utilisant du CH_4 et du CO_2. Ce concept, appelé reformage à sec du méthane par CL assisté par MWH (MWHCL-DRM), vise à améliorer l'efficacité du processus d'utilisation du CO_2 et du CH_4 pour la production de gaz de synthèse. La première étape de cette recherche visait à développer et à évaluer un montage à l'échelle du laboratoire pour le MWHCL-DRM. Cette étape a permis d'évaluer l'influence de la méthode de chauffage, chauffage conventionnel (CH) et MWH, sur la productivité du procédé. La productivité du procédé a été attribuée à sa capacité à empêcher le dépôt de carbone ainsi qu'à augmenter le taux de réduction de Fe_3O_4 par CH_4, conduisant à la production de gaz de synthèse et l'oxydation de Fe par CO_2, conduisant à la production de CO. Une évaluation initiale a été menée pour chauffer la magnétite (Fe_3O_4), transporteur d'oxygène choisi dans cette étude, sous MW pour montrer la supériorité du MWH par rapport au carbure de silicium (SiC). La productivité du procédé du MWHCL-DRM à l'échelle du laboratoire a ensuite été comparée au CL-DRM assisté par CH à l'échelle du laboratoire (CHCL-DRM). Dans le CHCL-DRM, le dépôt de carbone sur les particules a été détecté, alors qu'aucun signe de dépôt de carbone n'a été observé dans le MWHCL-DRM. De plus, par rapport au CHCL-DRM, le MWHCL-DRM a amélioré le taux de réduction de Fe_3O_4 (l'augmentant de 2.5 fois). En outre, par rapport au CHCL-DRM, une augmentation (environ 50%) du taux d'oxydation de Fe en Fe_3O_4 a été mesurée dans le MWHCL-DRM.

La deuxième phase de cette recherche visait à entreprendre une vaste étude sur la vitesse de réaction intrinsèque – contrôlée par les réactions chimiques gaz-solide – du MWHCL-DRM lorsque Fe_3O_4 était utilisé comme transporteur d'oxygène. Cette phase de cette recherche était essentielle pour appliquer avec succès la technologie proposée à plus grande échelle. Le développement de la vitesse de réaction intrinsèque peut être entravé par la présence de résistances au transfert de masse

internes (à l'intérieur de la particule) et externes (l'interface fluide-particule). Le choix d'une vitesse superficielle du gaz suffisamment élevée U_g (9 cm/s) a permis de minimiser la résistance au transfert de masse de l'interface fluide-particule. De plus, les vitesses de réaction formulées n'étaient pas affectées par le transfert de masse interne, car la taille des particules de 10 μm a été sélectionnée. L'obtention des vitesses de réaction intrinsèques était ainsi assurée. Pour explorer l'effet de MW sur les vitesses de réaction, deux températures différentes (température du solide T_s et température de masse T_b) ont été utilisées pour calculer E_r et E_o pour le MWHCL-DRM. E_r est l'énergie d'activation calculée pour la réduction de Fe_3O_4 à l'aide de CH_4, et E_o représente l'énergie d'activation calculée pour l'oxydation de Fe à l'aide de CO_2. En formulant les taux de réaction du MWHCL-DRM sur la base de Ts et en utilisant Fe_3O_4 comme transporteur d'oxygène, $E_r = 8.5\times10^4$ J/mol et $E_o = 2.2\times10^4$ J/mol ont été calculés. Pour le même transporteur d'oxygène, la formulation des taux de réaction du MWHCL-DRM à l'aide de T_b a donné $E_r = 6.8\times10^4$ J/mol et $E_o = 1.8\times10^4$ J/mol. La comparaison de Er calculé (8.5×10^4 et 6.8×10^4 J/mol) pour le MWHCL-DRM avec E_r de 9.0×10^4 J/mol pour le CHCL-DRM a révélé qu'il est essentiel d'adopter T_s pour établir un taux de réaction intrinsèque fiable pour les réactions gaz-solide sous le MWH. Il a également été démontré qu'au lieu d'influencer E_r, qui met en lumière l'influence non thermique du MW sur les taux de réaction, les constantes de vitesse de réaction ont été améliorées grâce à l'effet thermique par rayonnement du MW. Par conséquent, pour une réaction gaz-solide alimentée par le MWH, l'utilisation de T_s est essentielle pour formuler un taux de réaction intrinsèque fiable. Une contrainte technique majeure dans la mise à l'échelle du MWHCL-DRM est la limitation de la puissance maximale de sortie des sources/générateurs MW. Cette restriction nécessite l'installation simultanée de plusieurs réacteurs. Par conséquent, le troisième objectif de cette étude visait à introduire et à mener la conception, la modélisation et l'optimisation d'un nouveau réacteur – le réacteur à lit mobile simulé cyclique assisté par MWH (MWH-CSMBR) – pour surmonter cette limitation technique. Cet objectif a été atteint en utilisant des données expérimentales et des taux de réaction obtenus dans les première et deuxième parties de cette recherche. Un modèle multiphysique a été créé pour simuler le MWH-CSMBR. Le logiciel COMSOL Multiphysics a été utilisé pour effectuer les simulations. Afin de valider le modèle multiphysique avec les données expérimentales, la configuration à l'échelle du laboratoire alimentée par le MWH, développée dans le premier objectif, a été appliquée. Sur la base des résultats obtenus à partir de la simulation multiphysique, le MWH-CSMBR a pu: (i) réduire avec succès le nombre total de réacteurs à seulement quatre, au lieu de nécessiter le déploiement simultané de plus de 100 réacteurs, (ii) transférer plus de 97% de l'énergie MW au lit chargé, (iii) atteindre les performances d'un lit mobile, et (iv) diminuer le coût total de production en réduisant le nombre de réacteurs. Le quatrième objectif de cette étude visait à mener une évaluation approfondie des préoccupations et aspects environnementaux, techniques et économiques de la production de H_2 à l'échelle industrielle en adaptant le MWHCL-DRM. Les conversions de CO_2 et de CH_4 obtenues à partir de la simulation multiphysique du troisième objectif ont été saisies dans le logiciel Aspen Plus pour effectuer les bilans énergétiques et massiques de l'usine développée. L'usine a été optimisée encore davantage grâce à un réseau d'échangeurs de chaleur pour récupérer le contenu énergétique des flux chauds. Avec 50 tonnes/jour de CH_4 introduites dans l'usine, le coût total estimé de production de H_2 était de 3.6 $ par kg de H_2. L'étude technico-économique a conclu que la réduction des prix de l'électricité et de la production/capture/séparation du CO_2 réduirait le coût total de production de H_2 à environ 2 $ par kg de H_2, ce qui fait du MWHCL-DRM une alternative viable et rentable au reformage du méthane (SRM) pour la production de H_2. Pour la production de 1 kg H_2 en Amérique du Nord, l'étude du cycle de vie a été réalisée en utilisant le logiciel openLCA 2.1. Sur la base de la base de données Ecoinvent, il a été prédit que le processus développé de production de H_2 pourrait émettre 2.11 kg d'équivalent CO_2 (eq) à effet de serre. Après une évaluation technico-économique et du cycle de vie approfondie et en tenant compte du potentiel de réchauffement climatique important du SRM (>9 kg CO_2 eq) et de l'électrolyse (>30 kg CO_2 eq lorsque l'électricité est produite à partir de combustibles fossiles), le quatrième objectif a donc proposé le MWHCL-DRM pour la production de H_2 à grande échelle.

ABSTRACT

Syngas, or synthesis gas, is a gaseous mixture of hydrogen (H_2) and carbon monoxide (CO). Syngas is a key feedstock to produce several chemicals, such as ethanol and methanol. In addition, over half of the global H_2 production is achieved by separating H_2 from syngas. This research's main objective is to develop a sustainable syngas production method by utilizing methane (CH_4) and carbon dioxide (CO_2), which are the vast majority (over 90%) of the greenhouse gas (GHG) emissions. To simultaneously utilize CO_2 and CH_4 as well as produce syngas, one can integrate chemical looping (CL) with dry reforming of methane (DRM). However, the CL-DRM heated conventionally encounters serious constraints, which are mainly the need to operate the fuel (reducer) reactor at elevated temperatures (usually over 900°C) and the deposition of coke in the fuel reactor due to the thermal decomposition of CH_4 in the gas phase. Electrifying a process through microwave heating (MWH) can mitigate or minimize GHG emissions caused by generating heat from fossil fuels. In addition, the MWH can radically accelerate process productivity.

Hence, this research mainly focuses on incorporating the MWH with the CL-DRM to propose and investigate an innovative concept for syngas production by utilizing CH_4 and CO_2. The novel concept of MWH-assisted CL-DRM (MWHCL-DRM) is a sustainable GHG utilization technology capable of accelerating process efficiency.

The first stage of this research was founded on the laboratory-scale investigation of the MWHCL-DRM. This stage assessed the influence of the heating method, conventional heating (CH) and MWH, on the productivity of the process. The productivity of the process was attributed to its ability to (i) prevent the deposition of coke, (ii) accelerate the rate of Fe_3O_4 reduction using CH_4, yielding to syngas production, and (iii) accelerate the rate of Fe oxidation using CO_2, yielding to CO production. An initial assessment was conducted to heat magnetite (F_3O_4), an oxygen carrier that was chosen in this study, under MW to exhibit its superior MWH capacity compared to silicon carbide (SiC). The productivity of the laboratory-scale MWHCL-DRM was then compared with the laboratory-scale CH-assisted CL-DRM (CHCL-DRM). In the CHCL-DRM, the deposition of coke was detected, while no sign of coke generation was observed in the MWHCL-DRM. Additionally, compared to the CHCL-DRM, the MWHCL-DRM accelerated the Fe_3O_4 reduction

rate (enhancing it by 2.5 times). Moreover, compared to the CHCL-DRM, an increase (around 50%) in the oxidation rate of Fe to Fe_3O_4 was measured in the MWHCL-DRM.

The second phase of this research intended to undertake a broad investigation of the intrinsic reaction rate – one that is controlled by gas-solid chemical reactions – of the MWHCL-DRM when Fe_3O_4 was used as the oxygen carrier. This phase of the research was essential for successfully applying the proposed technology on a larger scale. Developing the intrinsic reaction rates can be affected by the presence of internal (within the particle) and external (the fluid-particle interface) mass transfer resistances. Choosing a sufficiently high superficial gas velocity U_g (9 cm/s) guaranteed minimizing the fluid-particle interface mass transfer resistance. Additionally, the formulated reaction rates were not affected by internal mass transfer, as the particle size of 10 µm was selected. Achieving the intrinsic reaction rates was thus ensured. To investigate the MW's impact on the reaction rates, two different temperatures (temperature of solid T_s and bulk T_b) were used to calculate E_r and E_o for the MWHCL-DRM. E_r is the activation energy calculated for Fe_3O_4 reduction using CH_4, and E_o represents the activation energy calculated for Fe oxidation using CO_2. By formulating the reaction rates of the MWHCL-DRM based on T_s and using Fe_3O_4 as the oxygen carrier, $E_r = 8.5\times10^4$ J/mol and $E_o = 2.2\times10^4$ J/mol were calculated. For the identical oxygen carrier, formulating the reaction rates of the MWHCL-DRM using T_b resulted in $E_r = 6.8\times10^4$ J/mol and $E_o = 1.8\times10^4$ J/mol. Comparing the calculated E_r (8.5×10^4 and 6.8×10^4 J/mol) for the MWHCL-DRM with E_r of 9.0×10^4 J/mol for the CHCL-DRM revealed that it is essential to adopt T_s for establishing a reliable intrinsic reaction rate for gas-solid reactions under the MWH. It also revealed that in lieu of influencing E_r, which illuminates the none-thermal influence of the MW on reaction rates, the reaction rate constants were enhanced, indicating the thermal effect of the radiated MW. Hence, for a gas-solid reaction powered by the MWH, using T_s is essential for formulating a reliable intrinsic reaction rate.

A major technical constraint in scaling up the MWHCL-DRM is the limitation on the maximum power output of the MW sources/generators. This restriction necessitates the simultaneous installation of multiple reactors. Therefore, the third objective of this study aimed at introducing and conducting the design, modeling, and optimization of a new reactor – the MWH-assisted cyclic simulated moving bed reactor (MWH-CSMBR) – to tackle this technical limitation. This objective was reached using experimental data and reaction rates that were obtained in the first and second parts of this research. A model was created to simulate the MWH-CSMBR. COMSOL Multiphysics software was applied for performing the simulations. To validate the established model with the experimental data, the laboratory-scale setup powered by the MWH, developed in the first objective, was applied. Based on the results obtained from the Multiphysics simulation, the MWH-CSMBR was able to: (i) successfully decrease the total number of reactors to just four, instead of requiring the simultaneous deployment of over a hundred reactors, (ii) transfer over 97% of the MW energy to the loaded bed, (iii) secure the performance of a moving bed, and (iv) decrease the total production cost by lowering the number of reactors.

This study's fourth objective was to conduct an in-depth evaluation of the environmental, technical, and economic concerns and aspects of producing H_2 at an industrial scale by adapting the MWHCL-DRM. The CO_2 and CH_4 conversions obtained from the simulation studies in the third objective were input into the Aspen Plus software to perform the developed plant's energy and mass balances. The plant was further optimized through a network of heat exchangers to utilize the energy content of the hot streams. With 50 tons/day of CH_4 fed into the plant, \$3.6 per kg of H_2 was the estimated total cost of producing H_2. The techno-economic study concluded that lowering the electricity and CO_2 production/capturing/separation prices would decrease the total cost of producing H_2 to around \$1.2 per kg of H_2, which makes the MWHCL-DRM a viable and cost-effective alternative to steam reforming of methane (SRM) for H_2 production. For 1 kg H_2 production in North America, the life cycle study was carried out by implementing the openLCA 2.1 software. Based on the Ecoinvent database, there was a prediction that the developed process of producing H_2 could emit 2.11 kg of CO_2 equivalent (eq) to the greenhouse effect. Following thorough techno-economic and life cycle assessments and taking into account the SRM’s significant global warming potential (>9 kg CO_2 eq) and electrolysis (>30 kg CO_2 eq when electricity is generated using fossil fuels), the fourth objective thus proposed the MWHCL-DRM for large-scale H_2 production.

TABLE OF CONTENTS

LIST OF TABLES

LIST OF FIGURES

LIST OF APPENDICES

CHAPTER 1 INTRODUCTION

Carbon dioxide (CO_2) and methane (CH_4) make up the vast majority (almost 92%) of GHG emissions. A gaseous mixture made of hydrogen (H_2) and carbon monoxide (CO), known as syngas or synthesis gas, is a vital chemical substance for the catalytic synthesis of numerous chemicals, like liquid hydrocarbons. H_2 separation from the synthesis gas is also the foremost global pathway (more than 50%) of H_2 generation. H_2 combustion with air produces water (H_2O) instead of CO_2. In addition to combustion, H_2 is a critical chemical substance for diverse sectors, like synthesis of ammonia. Similar to the synthesis gas and H_2, CO can be valorized to produce chemicals, such as benzaldehyde and acetic acid [1-9]. Accordingly, synthesis gas and H_2-generating units through CH_4 and CO_2 utilization is a sustainable or an eco-friendly chemical process.

More than 50% of the global H_2-generating units is sourced via the catalytic reaction of steam reforming of CH_4 (C-SRM; where the synthesis gas is produced by H_2O reacting with CH_4) merged with a H_2 separation technology. The main constraints of the syngas manufacturing units applying the C-SRM are:

- Substantial carbon footprint (emitting over 9 kg of CO_2, while manufacturing 1 kg of H_2).
- The moderately high molar concentration of H_2 in the manufactured syngas (H_2-CO mixture with 75 mol.% H_2), which is a nonideal ratio to be used for different downstream processes, including the Fischer-Tropsch (FT) process.

To tackle these two constraints, many studies focused on the C-DRM, where C and DRM respectively stand for catalytic and dry reforming of CH_4. In the C-DRM, the synthesis gas is manufactured by CO_2 reacting with CH_4 to: (i) utilize CH_4 and CO_2, and (ii) manufacture synthesis gas containing equimolar H_2-CO ratio, i.e., 50 mol.% H_2, to be further used for the FT process [1-9]. Unlike the high amount of CO_2 utilization via the C-DRM – consuming over 11 kg-CO_2 to manufacture 1 kg of H_2 – and the suitable ratio of H_2 and CO of the manufactured synthesis gas, the key constraints delaying the scale-up of the C-DRM are [1-13]:

- Thermodynamic favorability of deposition of coke (even up to 1000°C), caused by simultaneous feeding of CO_2 and CH_4 into a single reactor.
- Thermodynamic favorability of deposition of coke (even for temperatures down to 650°C), caused by the decomposition of fuel (CH_4 here) in the gas.

- High demand of energy (maintaining the reaction temperature normally over 850°C) to increase the rate of CH_4 conversion.

Contrasting the C-DRM, DRM via chemical looping (CL) uses an oxygen carrier to partially oxidize the fuel (CH_4 in this study) in the fuel (reducer) reactor, i.e., partially or fully reducing the particles (oxygen carrier). This can lead to synthesis gas generation. In a different oxidizer reactor, the gaseous oxidizing agent (CO_2 in this study) re-oxidizes the oxygen carrier. Thus, the CL-DRM can cease thermodynamic favorability of deposition of coke caused by simultaneous feeding of CO_2 and CH_4 into a single reactor [6, 14-23].

One can utilize conventional heating (CH) to power the CL-DRM. The CH can lead to a local-temperature balance, i.e., similar solid and gas temperatures. Additionally, the endothermic nature of reducing oxygen carrier using the fuel (CH_4 in this study) necessitates a high temperature, usually above 900°C. Thus, the main constraints of the CH-assisted CL-DRM, abbreviated as CHCL-DRM, where the gas and solid particles have the same temperature, are [6, 14-23]:

- The thermodynamic favorability of deposition of coke, owing to the thermal decomposition of fuel (CH_4 in this study) in the gas.
- The high demand of energy of the fuel reactor necessitates a high temperature, usually over 800°C.

Gas phase is in general MW transparent. Therefore, by MW irradiation of a gas-solid medium comprised of the particles that are MW receptor (absorber) and the gas phase that is transparent to MW, one can secure the aimed solid-gas temperature gradient, i.e., greater particle temperature [8-13, 24]. Therefore, pertaining to the abovementioned discussion, by leveraging the concept of CL-DRM and selectively heating the particles (oxygen carriers) through MW irradiation, the following objectives could be attained:

- Preventing the thermodynamic favorability of deposition of coke owing to the simultaneous injection of CO_2 and CH_4 into the reactor.
- Preventing the thermodynamic favorability of deposition of coke owing to the decomposition of fuel (CH_4 in this study) in the gas.
- Accelerating CH_4 conversion.

Hence, this study intends to innovate and investigate the concept of microwave heating-assisted chemical looping dry reforming of methane as a sustainable syngas manufacturing and GHG utilization method.

Nomenclature

Acronym

C-DRM	Catalytic dry reforming of methane
CH	Conventional heating
CHCL-DRM	Conventional heating-assisted chemical looping dry reforming of methane
CL	Chemical looping
CL-DRM	Chemical looping dry reforming of methane
C-SRM	Catalytic Steam reforming of methane
DRM	Dry reforming of methane
FT	Fischer-Tropsch
GHG	Catalytic dry reforming of methane
GHG	Greenhouse gas
MW	Microwave
MWHCL-DRM	Microwave heating-assisted chemical looping dry reforming of methane
MWH	Microwave heating
SRM	Steam reforming of methane

CHAPTER 2 LITERATURE REVIEW

A gas stream made of hydrogen (H_2) and carbon monoxide (CO), typically H_2 to CO ratio varying from 1:1 to 3:1, is known as synthesis gas or syngas. On a worldwide scale, H_2 is predominantly supplied by manufacturing synthesis gas and the subsequent separation of H_2 from the synthesis gas. Despite the natural gas combustion, which emits carbon dioxide (CO_2), the byproduct of H_2 combustion is water (H_2O). Therefore, H_2 is a clean energy carrier. Additionally, various sectors, like the production of ammonia, use H_2 as their feedstock. Moreover, as summarized in Figure 2.1, several chemicals, including liquid hydrocarbon, are manufactured utilizing the synthesis gas as the feedstock.

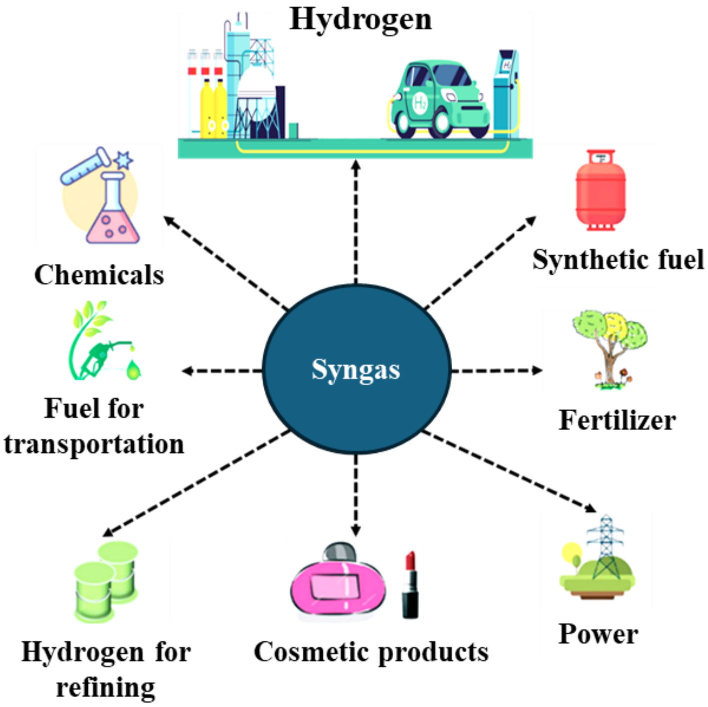

Figure 2.1. Main applications of synthesis gas (syngas).

Significant (annually, more than fifty-one trillion kilograms) greenhouse gas (GHG) emissions is a vital environmental issue on a global scale. GHG is comprised of CO_2, methane (CH_4), H_2O, chlorofluorocarbons (CFCs), ozone (O_3), and nitrous oxide (N_2O). However, CH_4 and CO_2, making 17% and 76% respectively, are its major components [1-6]. The advancement of CO_2 and/or CH_4 utilization technologies to manufacture syngas and H_2, thus, is a pressing global task at hand.

2.1 Catalytic reforming of methane

C-SRM, where C and SRM respectively stand for catalytic and steam (H_2O in vapor phase) reforming of CH_4, resources more than half of the global syngas demand. This process, seen in (R-2.1), involves the reaction of H_2O (an oxidizing agent) with CH_4 (reducing agent) to manufacture synthesis gas. A 1:3 molar ratio of CO to H_2 makes up the synthesis gas that is manufactured through the C-SRM. Even though this ratio introduces the C-SRM an appealing H_2-manufacturing pathway, the main constraints of the C-SRM are listed below [1-13]:

- The H_2 to CO ratio of 3:1 cannot be directly fed to the FT process.
- The C-SRM has a high CO_2 footprint: for 1 kg of H_2, over 9 kg of CO_2 is emitted.

Therefore, although the C-SRM is a reliable, century-old technology, the global concern over the high GHG emissions necessitates innovating alternative GHG utilization methods for manufacturing synthesis gas and/or H_2 [1-13].

$$\mathrm{CH_{4\,(g)} + H_2O_{(g)} \leftrightarrow CO_{(g)} + 3H_{2\,(g)}} \qquad \Delta H^{\circ}_{298.15} = 206 \text{ kJ/mol} \qquad \text{(R-2.1)}$$

As presented in (R-2.2), one can use oxygen (O_2), rather than steam, to partially oxidize CH_4. This exothermic catalytic reaction, known as catalytic partial oxidation of CH_4 (C-POM), can generate synthesis gas comprised of H_2/CO of 2:1. The synthesized syngas is thus suitable for downstream applications, like FT process. Additionally, compared to the other catalytic CH_4 reforming processes, the C-POM is moderately fast. The exothermic nature of the C-POM also helps reduce the total energy consumption of syngas manufacturing [1-13]. However, the major constraints that delay scaling up this syngas manufacturing method are:

- The necessity of supplying pure O_2.
- The possibility of deposition of coke.
- Safety risks associated with pure O_2 injection.

$$\mathrm{2CH_{4\,(g)} + O_{2\,(g)} \leftrightarrow 2CO_{(g)} + 4H_{2\,(g)}} \qquad \Delta H^{\circ}_{298.15} = -22.6 \text{ kJ/mol} \qquad \text{(R-2.2)}$$

Dry reforming of methane (DRM; presented in (R-2.3)) employs CO_2, in lieu of H_2O or O_2, for partially oxidizing fuel (CH_4 in this study). Two aspects that differentiate the catalytic DRM (C-DRM) from the C-SRM and C-POM are [1-13]:

- Simultaneous utilization of major components of GHG.
- Equimolar ratio of CO and H_2 (CO/H_2 of 1), which facilitates utilization of the manufactured syngas for the FT process.

In addition to (R-2.3), by simultaneously injecting CH_4 and CO_2 to the reactor, several reactions may occur, which are sorted in Table 2.1.

Table 2.1. Reaction pathways that could occur for the C-DRM [8].

$CH_4 + CO_2 \leftrightarrow 2CO + 2H_2$	(R-2.3)
$CO_2 + H_2 \leftrightarrow CO + H_2O$	(R-2.4)
$2CH_4 + CO_2 \leftrightarrow CO + C_2H_6 + H_2O$	(R-2.5)
$CH_4 + CO_2 \leftrightarrow 0.5C_2H_4 + H_2O + CO$	(R-2.6)
$C_2H_6 \leftrightarrow C_2H_4 + H_2$	((R-2.7)
$CO + 2H_2 \leftrightarrow CH_3OH$	(R-2.8)
$CO_2 + 3H_2 \leftrightarrow H_2O + CH_3OH$	(R-2.9)
$CH_4 \leftrightarrow C + 2H_2$	(R-2.10)
$2CO \leftrightarrow C + CO_2$	(R-2.11)
$CO_2 + 2H_2 \leftrightarrow C + 2H_2O$	(R-2.12)
$CO + H_2 \leftrightarrow C + H_2O$	(R-2.13)
$CO_2 + CH_3OCH_3 \leftrightarrow 3CO + 3H_2$	(R-2.14)
$3H_2O + CH_3OCH_3 \leftrightarrow 6H_2 + 2CO_2$	(R-2.15)
$CH_3OCH_3 + H_2O \leftrightarrow 4H_2 + 2CO$	(R-2.16)
$2CH_3OH \leftrightarrow CH_3OCH_3 + H_2O$	(R-2.17)
$CO_2 + 4H_2 \leftrightarrow 2H_2O + CH_4$	(R-2.18)
$3H_2 + CO \leftrightarrow CH_4 + H_2O$	(R-2.19)

According to Table 2.1 and based on the detailed thermodynamic calculations performed by the FactSage software (referring to Figure 2.2a), deposition of coke in the C-DRM is thermodynamically favorable even up to 1000°C. Additionally, thermal decomposition of CH_4 is thermodynamically favorable at gas temperatures above 650°C. The deposition of coke in the C-DRM is thus a major scale-up hinderance, as reported in literature [1-13]. Another scale-up obstacle of the C-DRM is its high enthalpy of reaction ($\Delta H^{\circ}_{298.15}$ = 247 kJ/mol), which necessitates the C-DRM to be executed at a high temperature, normally above 850°C.

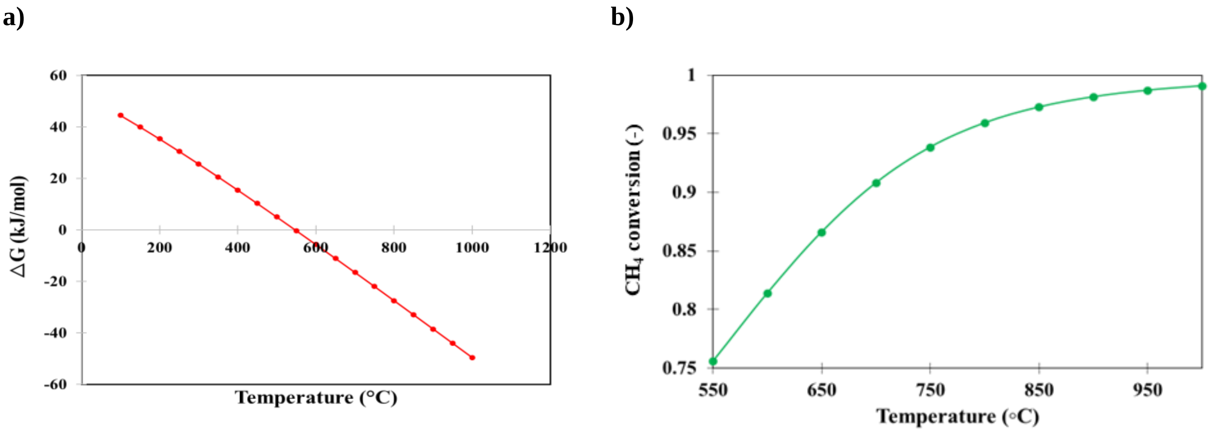

Figure 2.2. Reaction temperature's impact on a) Gibbs free energy of formation of carbon in the gas phase (R-2.10) and b) CH_4 decomposition in the C-DRM, based on the thermodynamic calculations conducted by the FactSage software.

In most cases under atmospheric pressure, the gas phase does not interfere with the microwave (MW). Thus, in a solid-fluid(gas in this research) bed exposed to MW, adopting/synthesizing solid catalysts that are MW receptor (absorber) allows for selectively heating the catalysts, which secures the solid-gas temperature gradient, i.e., higher catalyst temperature. For instance, it is reported in the literature that exposing a bed made of MW receptor catalysts to MW can yield a solid-gas temperature gradient of up to 300°C. Additionally, as appeared in Figure 2.2: (i) reducing the gas temperature reduces the thermodynamic favorability of deposition of coke, and (ii) enhancing the catalyst temperature accelerates CH_4 conversion. Accordingly, the mentioned solid-gas temperature gradient can boost the rate of CH_4 conversion and cease/decrease the deposition of coke caused by the thermal decomposition of CH_4 in the gas [1-23].

The MW's selective heating thus led various researchers to focus on the integration of MW with the C-DRM. Before reviewing these studies, we need to introduce the foundational background of the MW heating (MWH) and its benefits over conventional heating (CH). Accordingly, the MWH is reviewed in detail in Sections 2.2 and 2.3.

2.2 Conventional and microwave heating

Since gas phase mostly does not interfere with the MW, exposing a bed made of MW receptors with MW allows for selectively transferring the energy to the MW receptor particles, which secures the aimed solid-gas temperature gradient, i.e., higher temperature of MW receptors. Contrasted with the MWH, by applying the CH, one can aim at a uniform temperature, i.e., $T_s \approx T_g \approx T_b$ [3, 14-23]. T_s, T_g, and T_b are temperatures of solid/particle, gas, and bulk. In Figure 2.3, the potential effects of the MWH and CH on the temperature gradient is shown.

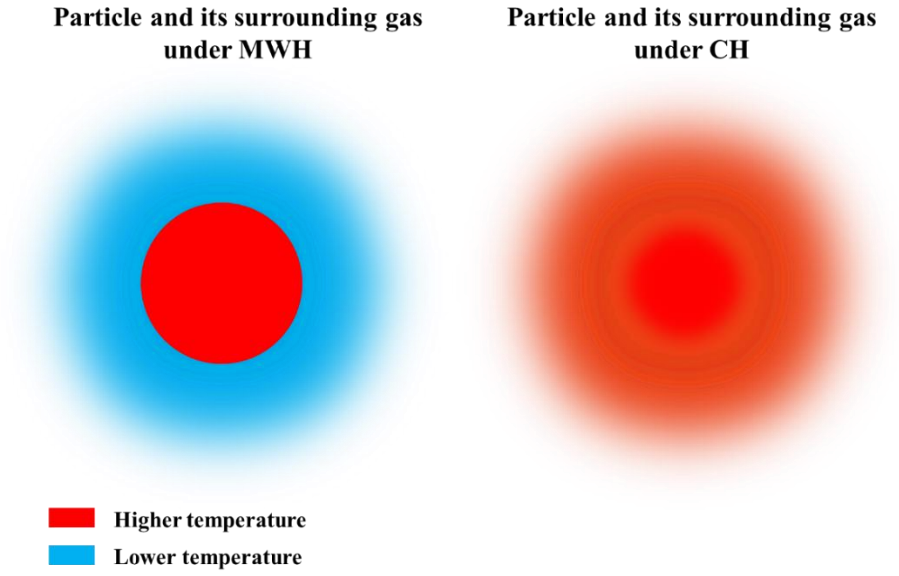

Figure 2.3. Temperature distribution of a MW receptor particle and its surrounding gas under MWH and CH.

2.3 Microwave heating

In 1967, MW (electromagnetic waves (EMWs) with frequencies in the range of 0.3-300 GHz) was utilized to heat the chemical unit operations, such as reactors and dryers. Following the international standards for preventing interference with the communication devices, the MWH in the chemical industry is normally applied at a frequency of 915 MHz or 2.45 GHz. As shown in

Figure 2.4, an EMW is made of a magnetic (M)-field perpendicular to an electric (E)-field. To efficiently heat a solid-gas bed made of MW receptors, one must analyze the simultaneous interaction of the particles with E- and M-fields [3, 14-23].

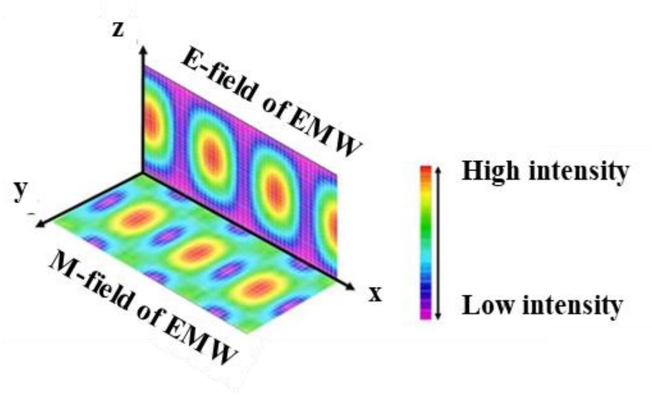

Figure 2.4. Schematic representation of electric and magnetic fields of EMWs [14].

Relative dielectric constant ε', which signifies the real part of relative permittivity ε_r (Eq. (2.1)), quantifies the capacitance of a material, i.e., its ability in absorbing/storing electrical energy of an E-field. Relative dielectric loss factor ε'', i.e., imaginary part of ε_r, quantifies the material's ability to dissipate the absorbed electrical energy. Likewise, relative magnetic constant μ', i.e., the real part of relative permeability μ_r (Eq. (2.3)), and relative magnetic loss factor μ'', i.e., imaginary part of μ_r, respectively quantify ability of the material in absorbing and dissipating magnetic energy when it is exposed to a M-field. Accordingly, as shown in Eqs. (2.2) and (2.4), dielectric loss tangent $\tan(\delta)$, often reported as loss tangent, as well as magnetic loss tangent $\tan(\delta_\mu)$ illustrate material's effectiveness in dissipating the E- and M-fields of emitted MWs to heat, respectively. Hence, heat generation inside non-magnetic particles, i.e., $\mu'' = 0$ and $\tan(\delta_\mu) = 0$, like silicon carbide (SiC), is resulting from their interactions with the electric field of emitted MWs [3, 14-18].

$$\varepsilon_r = \varepsilon' - j\varepsilon'' \tag{2.1}$$

$$\tan(\delta) = \frac{\varepsilon''}{\varepsilon'} \tag{2.2}$$

$$\mu_r = \mu' - j\mu'' \tag{2.3}$$

$$\tan(\delta_\mu) = \frac{\mu''}{\mu'} \tag{2.4}$$

EM penetration depth, also known as penetration depth D_p, is the distance from material's surface where the intensity of EMWs drops to around 1/e (37%) of the intensity of electromagnetic waves on the surface of the material. Therefore, in addition to $\tan(\delta)$ and $\tan(\delta_\mu)$, d_p and D_p are crucial properties of a particle that determine its potential to be heated under MW irradiations in gas-solid MW heated units. If $\frac{d_p}{D_p}$ of a particle is considerably smaller than 1, e.g., quartz, it could behave as a MW transparent material. If d_p of the particle is considerably larger than D_p, e.g., bulk of metals, it could either experience a surface reflection or surface heating [3, 14, 15]. Thus, an optimal $\frac{d_p}{D_p}$ is required to help a solid particle properly be heated by MWs, while its $\tan(\delta)$ and $\tan(\delta_\mu)$ are adequate. The potential interaction of different catalyst supports and active metals that were frequently employed in the gas-solid catalytic reformers, e.g., the C-DRM, is summarized in Table 2.2. The table reveals that a MW receptor catalyst can be synthesized or adopted for heating the catalyst in a selective manner, resulting a temperature gradient among the catalyst particles and gas. For delivering a complete overview on the MWH and the challenges to scale up MWH-assisted processes, a comprehensive review was undertaken and presented in APPENDIX A.

Table 2.2. MW-absorbing potential of various compounds at 25 °C, which are commonly tested in different catalytic conversion processes [14, 15, 17]. Water as a reference is brought.

Compound	D_p ***(μm)***	ε'	$tan(\delta)$	***Interaction***
Water	3×10^4	77	0.157	MW absorber
SiC	1.93×10^4	30	0.37	MW absorber
MgO	12.99×10^6	9	0.005	MW Transparent
TiO_2	5.5×10^5	50	0.005	MW Transparent
Al_2O_3	12.6×10^6	9	0.007	MW Transparent
ZrO_2	4.4×10^4	20	0.1	MW absorber
Fe	1.3	-	-	MW reflective
Al	1.7	-	-	MW reflective
Ni	2.5	-	-	MW reflective
Zn	3.2	-	-	MW reflective
Cu	2.7	-	-	MW reflective

2.4 Microwave heating-assisted catalytic dry reforming of methane

A summary of different studies on the MWH-assisted C-DRM is brought in Table 2.3.

Table 2.3. Some of the research studies accomplished for the MWH-assisted C-DRM.

Catalyst	***MW-absorber(s)***	***Main remarks***
Ni/Al_2O_3 Ni/SiC	SiC [9]	• The employment of Al_2O_3, $MgAl_2O_4$, and CeO_2 as the catalyst supports and local hot spots on the MW receptor decreased the rate of coke generation. However, the deposition of coke was not fulley avoided. • The MWH increased the rate of CH_4 conversion.
Ni/Al_2O_3	C-SiO_2 [10]	
Activated carbon	Activated carbon [24]	
NiFe/$MgAl_2O_4$	NiFe/$MgAl_2O_4$ [25]	
Ni/CeO_2-SiC	SiC [26]	

As Table 2.3 demonstrates, by exposing the bed with MW, deposition of coke due to the thermal decomposition of fuel (CH_4) was lowered. However, the deposition of coke was not fully avoided. Consequently, the deposition of coke is still a scale-up hinderance for the MWH-assisted C-DRM. To tackle this concern from a process perspective, a novel concept, i.e., CL-DRM (chemical looping DRM), was presented to partially oxidize CH_4 and reduce CO_2 by operating two separate reactors [9, 10, 24, 26].

2.5 Chemical looping dry reforming of methane

The key idea of the CL-DRM is depicted in Figure 2.5. Contrasting the C-DRM, the CL-DRM utilizes the concept of cyclic reduction and oxidation (redox) of $M_xO_{y\ (s)}$ for syngas and CO manufacturing, while utilizing CO_2 and CH_4 [6, 12, 27-32].

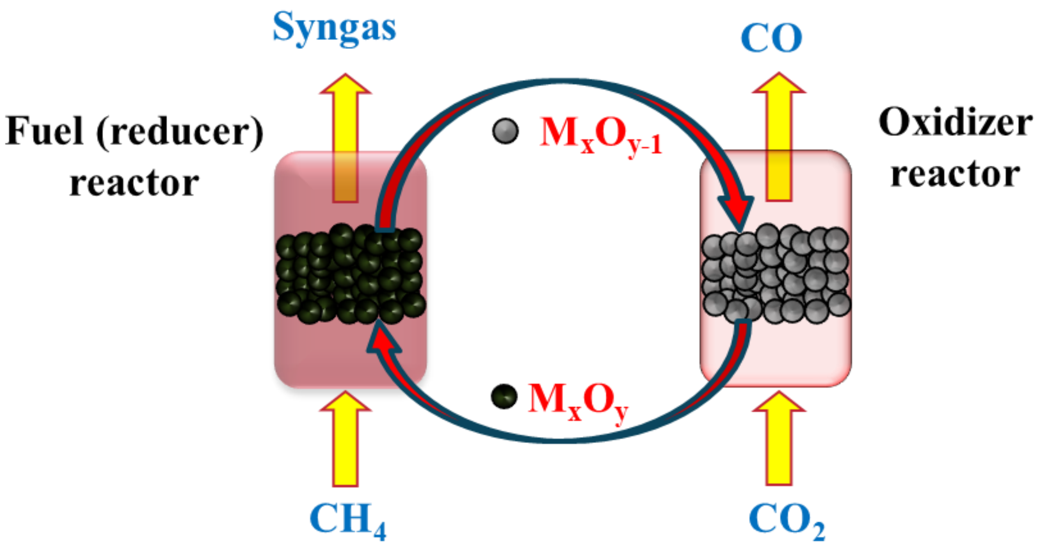

Figure 2.5. Principle of the CL-DRM.

The benefits of the CL-DRM over the C-DRM are [6, 12, 27-32]:

- Generating synthesis gas that contains $H_2/CO = 2/1$.
- CO_2 utilization, referring to Figure 2.5.
- Inherent hinderance of deposition of coke due to the distinct occurrence of the redox reactions.
- Separate occurrence of the redox reactions, which avoids the H_2 selectivity loss.

Considering the benefits of the CL-DRM over the C-DRM, many studies examined this synthesis gas manufacturing method [6, 12, 27-32]. The endothermic reaction in the fuel (reducer) reactor ($M_xO_{y(s)}$ reduction by CH_4) necessitates retaining the fuel reactor's bed at a high temperature (normally above 950°C). This, as described in Section 2.1, yields thermal decomposition of CH_4 inside the gas and the subsequent deposition of coke inside the fuel reactor. This agrees with the information presented in literature [6, 12, 27-32]. A major obstacle to scaling up the CHCL-DRM is thus the unwanted thermal decomposition of CH_4 inside the gas.

2.6 Microwave heating-assisted chemical looping dry reforming of methane

Based on the information presented in “scholar.google.com”, as of July 2024, the number of publications in which the words “microwave” and “looping” appeared in their titles is 17. These publications focused on ammonia synthesis as well as gasification of microalgae, heavy metals, aquatic plant water hyacinth, and chlorella vulgaris and reported the influence of the MW’s selective heating on enhancing the productivity of the chemical looping. Considering these outcomes resulted from merging the MWH with the chemical looping concept and the advantages of the CL-DRM over the C-DRM, this research aimed at developing the innovative concept of the MWHCL-DRM. This research will create the foundation of a novel and dependable syngas and H_2 generation method. The MWCL-DRM is schematically shown in Figure 2.6.

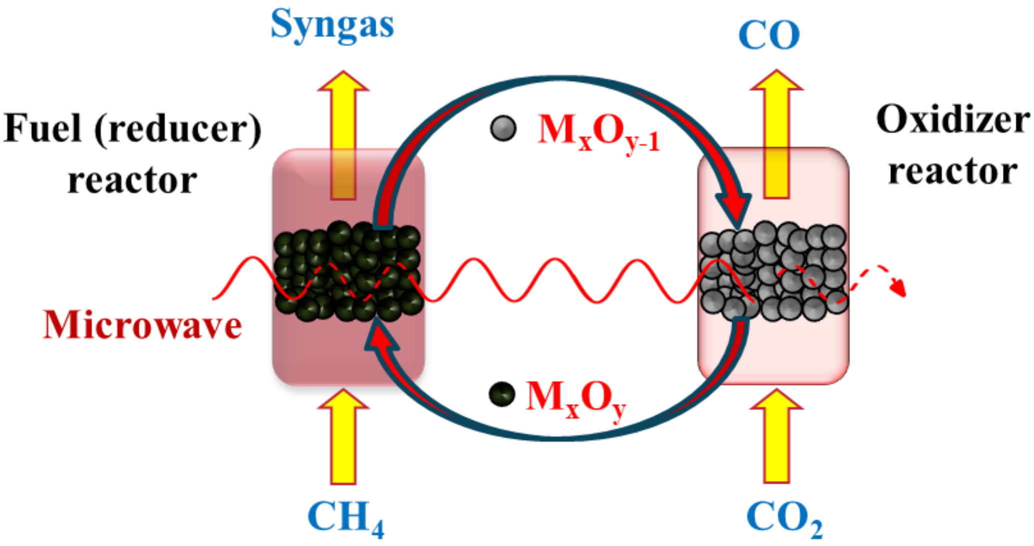

Figure 2.6. The concept of MWHCL-DRM.

Nomenclature

Acronym

C-DRM	Catalytic dry reforming of methane
CH	Conventional heating
CHCL-DRM	Conventional heating-assisted chemical looping dry reforming of methane
CL	Chemical looping
CL-DRM	Chemical looping dry reforming of methane

C-POM	Catalytic partial oxidation of methane
C-SRM	Catalytic steam reforming of methane
FT	Fischer-Tropsch
GHG	Catalytic dry reforming of methane
GHG	Greenhouse gas
MW	Microwave
MWH	Microwave heating
MWHCL-DRM	Microwave heating-assisted chemical looping dry reforming of methane

CHAPTER 3 COHERENCE OF THE CHAPTERS

The critical importance of developing innovative technologies of GHG utilization and syngas manufacturing is presented in CHAPTER 1. An overview of the C-SRM (the core method of syngas production) and the C-DRM (a GHG utilization method for producing syngas) were then covered in CHAPTER 1. The advantages and downsides of the C-SRM and C-DRM were then compared. The capacity of the CHCL-DRM in tackling the corresponding issues of the C-DRM was subsequently introduced. The potential outcomes of merging MWH with the CL-DRM was lastly mentioned in CHAPTER 1.

In CHAPTER 2, C-SRM, C-POM, and C-DRM, as the core syngas manufacturing methods were first reviewed. The major advantages of the C-DRM over the C-SRM and the C-POM can be summarized as:

- Achieving an equimolar CO-H_2 mixture (H_2/CO of 1) in the generated syngas, which facilitates its direct utilization for the FT process.
- Utilization of major components of GHG, i.e., CO_2 and CH_4.

The listed advantages that encouraged many researchers focusing on the C-DRM, particularly on the catalyst fabrication to accelerate the rate of CH_4 conversion and cease the deposition of coke, were reviewed in CHAPTER 2. However, it was concluded that the deposition of coke is the central challenge delaying the scale-up of the C-DRM. To tackle this issue, the MWH and its selective heating characteristics were reviewed. Based on a detailed review over the MWH-assisted C-DRM, it was concluded in CHAPTER 2 that, although the MWH method lowered the deposition of coke, this crucial issue was not fully resolved due to its thermodynamic favorability when applying the concept of DRM. By introducing the concept of CL-DRM heated conventionally, the thermodynamic favorability of deposition of coke due to the simultaneous injection of CO_2 and CH_4 to the reactor was resolved. However, to fully avoid the deposition of coke resulted from thermal decomposition of CH_4 in the gas, while increasing the productivity/efficiency of the process, the innovative concept of MWHCL-DRM was proposed in CHAPTER 2.

In the first objective of this research, presented in CHAPTER 4, by using Fe_3O_4, we designed and tested the laboratory-scale MWHCL-DRM. Process efficiency – principally the rates of favorable (redox) reactions as well as the deposition of coke – was compared with the CHCL-DRM. It was discussed in CHAPTER 4 that the MWHCL-DRM boosted the process efficiency, i.e., accelerating the favorable redox reaction rates and inhibiting the deposition of coke.

Using the developed laboratory-scale setup of the first objective, the second objective of this research, presented in CHAPTER 5, aimed at developing the intrinsic kinetics of (i) partial oxidation of CH_4 using Fe_3O_4 and (ii) reduction of CO_2 to CO using Fe. In this objective, T_b and T_s were applied to formulate two sets of intrinsic kinetics. Additionally, the influence of MW's thermal impact on the intrinsic kinetics of the current study was demonstrated and presented in CHAPTER 5.

Considering the constraints of scaling up the MWHCL-DRM, the novel concept of MWH-CSMBR was proposed in CHAPTER 6. Using the experimentally measured data from the first stage of this research (presented in CHAPTER 4) and the reaction kinetics (presented in CHAPTER 5), modeling and simulation of industrial-scale MWH-CSMBR was conducted. The simulation results demonstrated that the MWH-CSMBR could overcome the technical limitation of simultaneous operation of numerous (over a hundred) MWH-assisted reactors.

Since H_2 separation from the synthesis gas is the main approach of producing H_2, the potential application of the MWHCL-DRM for large-scale H_2 production was discussed in CHAPTER 7, as the last objective of this research. To accomplish this objective, the simulation's findings of the third objective (presented in CHAPTER 6) were utilized to proceed the process simulation of the MWHCL-DRM plant for H_2 production. The intention of the plant's process simulation – performed applying Aspen Plus software – was to achieve energy and mass balances. Following the process simulation of an industrial-scale plant (inlet daily flow of 50 tons of CH_4 to the plant), the technical and economic aspects, as well as environmental footprints of the plant were analyzed via TEA and LCA. The TEA's results indicated that by decreasing costs associated with supplying CO_2 and electricity, the MWHCL-DRM can compete with the C-SRM – the main commercialized H_2 generation method. Lastly, the accomplished cradle to gate LCA in CHAPTER 7 suggested the development of the MWHCL-DRM for producing H_2 in North America.

In CHAPTER 8, the general discussion of the thesis is presented. The primary achievements of this research and the future's recommendations are also presented in CHAPTER 9.

CHAPTER 4 ARTICLE 1 : MICROWAVE HEATING-ASSISTED CHEMICAL LOOPING DRY REFORMING OF METHANE

Mohammad Khodabandehloo[1,2], Jaber Shabanian[1], Jean-Phillipe Harvey[2], Jamal Chaouki[1,†]

[1] *Process Engineering Advanced Research Lab (PEARL), Chemical Engineering Department, Polytechnique Montreal, P.O. Box 6079, Station Centre-Ville, Montreal, (Quebec) Canada, H3C 3A7*

[2] *Centre for Research in Computational Thermochemistry (CRCT), Chemical Engineering Department, Polytechnique Montreal, P.O. Box 6079, Station Centre-Ville, Montreal, (Quebec) Canada, H3C 3A7*

[†] Corresponding author: Tel.: +1-514-340-4711 X 4034; Fax: +1-514-340-4159.

E-mail addresses: mohammad.khodabandehloo@polymtl.ca (M. Khodabandehloo), jaber.shabanian@polymtl.ca (J. Shabanian), jean-philippe.harvey@polymtl.ca (JP. Harvey), jamal.chaouki@polymtl.ca (J. Chaouki)

(Published in International Journal of Hydrogen Energy on May 27, 2024, DOI: https://doi.org/10.1016/j.ijhydene.2024.05.295)

Abstract

Chemical looping dry reforming of methane (CLDRM) offers a sustainable pathway to convert methane (CH_4) and carbon dioxide (CO_2) to syngas, i.e., a mixture of hydrogen (H_2) and carbon monoxide (CO). However, carbon deposition caused by high gas temperature remains a crucial challenge for the CLDRM. We proposed microwave (MW) heating-assisted CLDRM to leverage the selective heating feature of MW heating to create a thermal gradient between solid and gas phases. This thermal gradient, i.e., a higher solid temperature than the gas temperature, can promote desired reduction and oxidation (redox) reactions, while suppressing undesired gas phase reactions, particularly CH_4 decomposition. At bulk temperature of 800°C, the MW heating-assisted CLDRM achieved a maximum CH_4 conversion of 97% and H_2/CO ratio of around 2. Compared to the conventionally heated CLDRM, the MW heating increased the redox extents of magnetite (the oxygen carrier) by 2.5 and 1.5 times, respectively, and suppressed carbon deposition.

Keywords: Chemical looping dry reforming of methane; Process electrification; Microwave heating; Syngas; Hydrogen; Greenhouse gas utilization.

4.1 Introduction

Syngas, i.e., a mixture of hydrogen (H_2) and carbon monoxide (CO), is the building block of many catalytic conversion processes, such as methanol and dimethyl ether production, and is employed in processes like Fischer-Tropsch [1, 2]. In addition to versatile applications of syngas, it is the principal source for H_2 production. H_2 is employed in several sectors, such as ammonia production, steel manufacturing, and fuel cell electric vehicles. H_2 is also considered as a promising clean energy carrier [1, 2]. CO could be employed to synthesize various chemicals, such as acetic anhydride, polycarbonates, acetic acid, polyketones, metal carbonyls, and benzaldehyde [3]. Therefore, developing a sustainable process to produce syngas, H_2, and/or CO, while consuming carbon dioxide (CO_2) and/or methane (CH_4), i.e., key compounds of greenhouse gas (GHG) emissions, could offer a potential solution for meeting the increasing demands of syngas, H_2, and CO production, while minimizing GHG emissions [1, 2].

Catalytic steam reforming of methane (SRM), where steam (H_2O) and CH_4 are converted to syngas, is the dominant industrial process for syngas and H_2 production [4-7]. While an H_2/CO production ratio of around 3 makes the catalytic SRM a suitable technology for H_2 production, this ratio may not be interesting for various catalytic conversion technologies, like Fischer-Tropsch process. In addition, substantial CO_2 emissions (around 9.3 kg of CO_2 emission per 1 kg of H_2 production [5-7]) arising from fuel combustion for generating superheated steam at temperatures above 800°C represents a critical challenge for the catalytic SRM. Therefore, there is a need to develop alternative sustainable technologies for syngas production. To overcome the technical challenges of conventional catalytic reforming of methane, such as steam, dry, and autothermal reforming of methane, while reducing the total cost of the process, researchers investigated the novel concept of chemical looping reforming (CLR) of CH_4 [8-20]. Compared to the conventional catalytic reforming of methane, in the CLR of CH_4, a solid oxygen carrier, instead of a gaseous oxidant, is employed to accomplish the reduction and oxidation (redox) reactions via two separate reactors. In the reducer reactor, the reaction between the lattice oxygen of the oxygen carrier with CH_4 produces syngas with an H_2/CO production ratio of 2, as shown in (R-4.1), while it avoids carbon (C) deposition on the oxygen carrier. In the oxidizer reactor of the CLR of CH_4, the reduced oxygen carrier is re-oxidized to its initial state by employing CO_2, H_2O, and/or air [14-16, 20].

$$\mathrm{CH_{4\,(g)} + M_xO_{y\,(s)} \leftrightarrow M_xO_{y-1\,(s)} + 2H_{2\,(g)} + CO_{(g)}} \tag{R-4.1}$$

where $\mathrm{M_xO_{y\,(s)}}$ and $\mathrm{M_xO_{y-1\,(s)}}$ in (R-4.1) respectively represents the initial and reduced states of the oxygen carrier. M, g, and s represent metal, gas, and solid, respectively.

Several researchers investigated conventionally heated chemical looping steam reforming of methane (CLSRM) to produce syngas with an H_2/CO of around 2 in the reducer reactor and H_2 in the oxidizer reactor [8-13]. In the study by Quan et al. [13], the authors synthesized $NiFeAlO_4$, as a nickel (Ni)-based oxygen carrier, and employed it in a conventionally heated CLSRM. They obtained a CH_4 conversion of 94.32% with an H_2/CO production ratio of around 2 due to the uniform distribution of the metals on the oxygen carrier. In the study by Hu et al. [10], the authors aimed at H_2 production via the CLR of CH_4. The authors reported complexity of producing synthetic oxygen carrier, high price, and low mechanical stability as critical issues of synthesizing the oxygen carrier for the CLR of CH_4. Accordingly, to solve these issues, the authors proposed Ni-iron (Fe) modified natural ores, as oxygen carriers, for the conventionally heated CLSRM. Calcite, maifanite, hematite, dolomite, and volcanics were the natural ores employed in the mentioned study and the authors achieved a high purity (>98%) of H_2 stream with a nearly complete conversion of CH_4 (>98%) by adjusting the oxygen carrier to CH_4 ratio. Therefore, the concept of CLSRM was successfully investigated by several researchers [8-13] to produce syngas with an H_2/CO of around 2 in the reducer reactor and H_2 in the oxidizer reactor.

Compared to the CLSRM, by developing chemical looping dry reforming of methane (CLDRM), to re-oxidize the oxygen carrier, CO_2, instead of H_2O, is employed as the oxidizer in the oxidizer reactor, while CH_4 acts as the reducer in the reducer reactor. Therefore, by developing the CLDRM, one can produce syngas with an H_2/CO production ratio of around 2 in the reducer and CO in the oxidizer reactor, while simultaneously consuming CH_4 and CO_2. CO_2 and CH_4 contribute to around 76 and 16% of the global GHG emissions, respectively [1, 2, 14-23]. Therefore, the CLDRM is a promising technology for syngas production, aiming at achieving the desirable H_2/CO production ratio of 2, while simultaneously decreasing process expenses, alleviating safety concerns, tackling technical challenges, and mitigating GHG emissions, specifically CO_2 emissions. A schematic representation of the CLDRM is illustrated in Figure 4.1. In this figure, $Q_{net,r}$ and $Q_{net,o}$ respectively represent the required net energy to operate the reducer reactor and the net energy that is released from the oxidizer reactor [14-23].

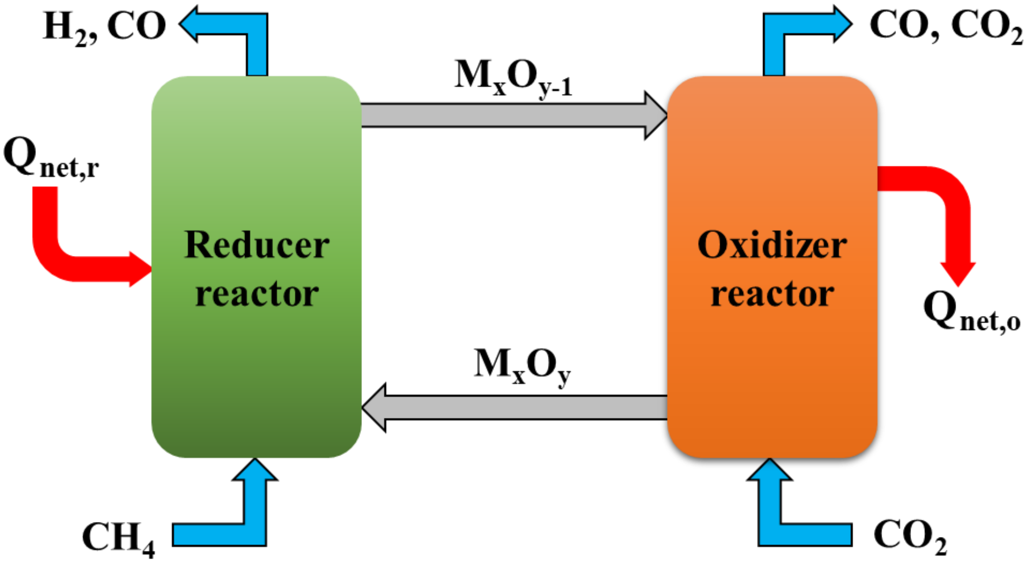

Figure 4.1. A schematic representation of the CLDRM.

Despite the mentioned advantages of the conventionally heated CLDRM, high endothermicity of the reduction of the oxygen carrier by CH_4, which often occurs at temperatures above 650°C, and undesired gas phase reactions, like CH_4 decomposition, are still crucial scale-up challenges of the reducer reactor of the CLDRM [14-19]. One could employ the conventional heating method, known as the surface heating method, to provide the required heat for the reducer reactor. When employing the conventional heating method, the gas phase is first heated. The particles' surface is subsequently heated by convection, conduction, and/or radiative heat transfer mechanisms. Lastly, the heat is transferred toward the inner body of the particles. Hence, the local thermal equilibrium between gas and solid phases can be achieved in a conventionally heated reactor [24-27].

When employing the microwave (MW) heating method to (partially/fully) supply the required heat in a gas-solid reactor, irradiated MWs interact with the MW absorber particles, such as magnetite (Fe_3O_4) and silicon carbide (SiC), leading to an increase of the internal kinetic energy of the particles. This increase of the internal kinetic energy of particles leads to a temperature gradient that promotes heat transfer toward the outer layers of the particles and the gas phase. Accordingly, in contrast to the conventional heating method, the difference between the dielectric properties of particles and the gas phase in a gas-solid system is responsible for the selective MW heating of MW absorber particles, where the solid phase is at a higher temperature than the gas phase [24-27]. The relatively low gas phase temperature can avoid secondary undesired gas phase reactions, like C deposition on a solid's surface due to gas phase CH_4 decomposition [24-27]. In addition, the desired gas-solid reactions, like Fe_3O_4 reduction by CH_4, are promoted due to the relatively high temperature of the solid phase. Moreover, the MW heating method, which could be coupled with renewable sources of electricity, such as wind turbines, solar panels, and hydroelectricity, is identified as a promising process electrification technology to mitigate GHG emissions and increase the process productivity [24-27]. To overcome the challenges of conventionally heated CLR technologies, there is thus a need for the development of MW heating-assisted CLR of gaseous fuels. This will effectively help meet the global H_2 and syngas demand, mitigate CO_2 emissions and/or utilize CO_2, and increase productivity and decrease energy consumption of syngas production processes. Hence, in this study, we focused on development of the MW heating-assisted CLDRM as a GHG utilization technology.

We first investigated the screening and selection of the oxygen carrier based on the reactivity and MW absorption capability of materials. Following the experimental setup and procedure explanation, the MW heating capability of Fe_3O_4 (the selected oxygen carrier) was studied. Thermodynamic calculations were also conducted to select the optimum operating conditions for the redox reactions. In addition to the cyclic performance of the Fe_3O_4 oxygen carrier in the MW heating-assisted CLDRM, the reduction extent of Fe_3O_4 by CH_4, CH_4 conversion, the evolution of the syngas compounds, and C deposition resulting from Fe_3O_4 reduction by CH_4 in the MW and conventional heating-assisted reactors were investigated.

4.2 Materials and methods

4.2.1 Oxygen carrier selection

Oxygen-carrying capacity, i.e., reactivity of the oxygen carrier with oxidizing and reducing materials (gases here), thermal stability, toxicity, attrition resistance, MW absorption capability, and price are principal items for selecting and/or synthesizing an oxygen carrier for the MW heating-assisted CLR processes. Ni-, copper (Cu)-, Fe-, manganese (Mn)-, and cobalt (Co)-based oxygen carriers, as well as mixed oxides, are studied and employed for chemical looping combustion (CLC) and CLR processes [21-23, 28-32].

Ni-based oxygen carriers combined with oxides, mostly zirconium dioxide (ZrO_2), titanium oxide (TiO_2), silicon oxide (SiO_2), aluminum oxide (Al_2O_3), magnesium oxide (MgO), lanthanum oxide (La_2O_3), and cerium oxide (CeO_2), as supporting materials, have been employed in chemical looping dry and steam reforming of gaseous fuels. The primary advantage of employing Ni-based oxygen carriers is their high thermal stability, which can withstand high temperatures (up to 1100°C) when suitable supports, like Al_2O_3 are employed, and their remarkable reactivity with methane (CH_4). However, high price, toxicity, and rapid deactivation, i.e., decreasing the reactivity after successive cyclic operations, are the main drawbacks of employing Ni-based oxygen carriers in CLR processes. In addition, the low MW absorption capability of Ni-based oxygen carriers, such as Ni-Al_2O_3, Ni-La_2O_3, and Ni-CeO_2, are crucial barriers to employ them for the MW heating-assisted CLR processes. Cu-based oxygen carriers have demonstrated a great capability in the selective oxidation of CH_4. However, their low MW absorption capability, high possibility of agglomeration at elevated temperatures (above 750°C), low mechanical strength, and low stability after successive redox cycles are their main drawbacks [28-31, 33].

Mn-based oxygen carriers are considered non-toxic and cost-effective oxygen carriers. However, compared to Cu- and Ni-based oxygen carriers, Mn-based oxygen carriers have shown lower reactivity toward the selective oxidation of CH_4. In addition, Mn-based oxygen carriers supported by inert oxides, such as SiO_2, TiO_2, Al_2O_3, and ZrO_2, are prone to form irreversible and undesired phases that decrease their reactivity for the selective oxidation of CH_4. Due to the capability of having different oxidation states, Co-based oxygen carriers have displayed a high tendency for selective oxidation of CH_4. However, the decline in the oxygen-carrying capacity at high temperatures (above 800°C) after successive redox cycles is their main drawback [28-31, 33].

To improve thermal and mechanical stability, as well as the reactivity of the oxygen carrier, mixed metal oxides can be employed as oxygen carriers. However, the possibility of the formation and/or precipitation of undesired phases during the successive redox cycles, which decreases the reactivity of the oxygen carriers, is the principal drawback of employing mixed metal oxides as oxygen carriers in the MW heating-assisted CLR processes.

Considering the abundancy, relatively low price, high oxygen storage and transport capacity, high C deposition resistivity, low toxicity, and high thermal stability of hematite (Fe_2O_3) and Fe_3O_4 as Fe-based oxygen carriers, various studies employed Fe_2O_3 and Fe_3O_4 to perform the redox cycles in CLR and CLC processes [28-31, 33, 34]. Thermodynamic analysis has illustrated the high capability of Fe_2O_3 and Fe_3O_4 in syngas production for the CLR processes fed by gaseous fuels. In addition, synthesizing methods for Fe-based oxygen carriers are relatively simple [26, 28-31, 33]. Due to a higher oxygen-carrying capacity of Fe_2O_3 in comparison with Fe_3O_4, Fe_2O_3 reduction by CH_4 is more favorable for CLC of CH_4, yielding CO_2 and H_2O, rather than syngas. In addition, compared to Fe_3O_4, it is reported that micron-sized Fe_2O_3 and ferrous oxide (FeO) have low MW absorption capabilities [26, 28-31, 33]. Hence, Fe_3O_4 was selected as the MW absorber oxygen carrier in this study.

4.2.2 Materials

Micron-sized Fe_3O_4 with average particle size d_p of 10 µm (ThermoFisher Scientific, 97% (metals basis)) was employed as the MW absorber oxygen carrier. In addition, to compare the MW heating performance of the Fe_3O_4 oxygen carrier with SiC, we employed SiC particles with average d_p of 356 µm (ThermoFischer Scientific, coarse). Nitrogen (N_2; 99.99% purity, Canadian Air Liquid), CH_4 (99.92% purity, Canadian Air Liquid) and CO_2 (99.92% purity, Canadian Air Liquid) were the gas cylinders employed to supply the gaseous streams for the MW and conventional heating assisted setups.

4.2.3 Experimental setup

4.2.3.1 Microwave heating-assisted reactor

Due to the simple design and operation of fixed bed reactors in lab-scale, these reactors were principally opted to operate CLR and CLC of CH_4 in lab-scale studies [14-20]. In addition, as explained later in Sections 4.3.1 and 4.3.2, by injecting the gaseous feed at a superficial gas velocity U_g of 9 cm/s (total volumetric flowrate of the inlet gaseous stream Q_i of 2700 cm^3/min), the developed MW heating-assisted reactor in this study was capable of avoiding hot and/or cold spots formation within the solids inventory under a fixed bed regime. Therefore, in this work, a lab-scale

MW heating-assisted reactor capable of working under the fixed bed regime was designed and constructed to accomplish the redox cycles. As shown in Figure 4.2a, the quartz reactor was placed inside a modified lab-scale MW oven with a metallic box (stainless steel 306), as the MW cavity. The MW cavity was connected to a magnetron (MW source) by a rectangular waveguide (WR-340 on the side of the cavity; dimensions of 43.18 mm × 86.36 mm). The employed magnetron could generate MWs with operating frequency of 2.45 GHz and MW powers ranging from 110 to 1100 W.

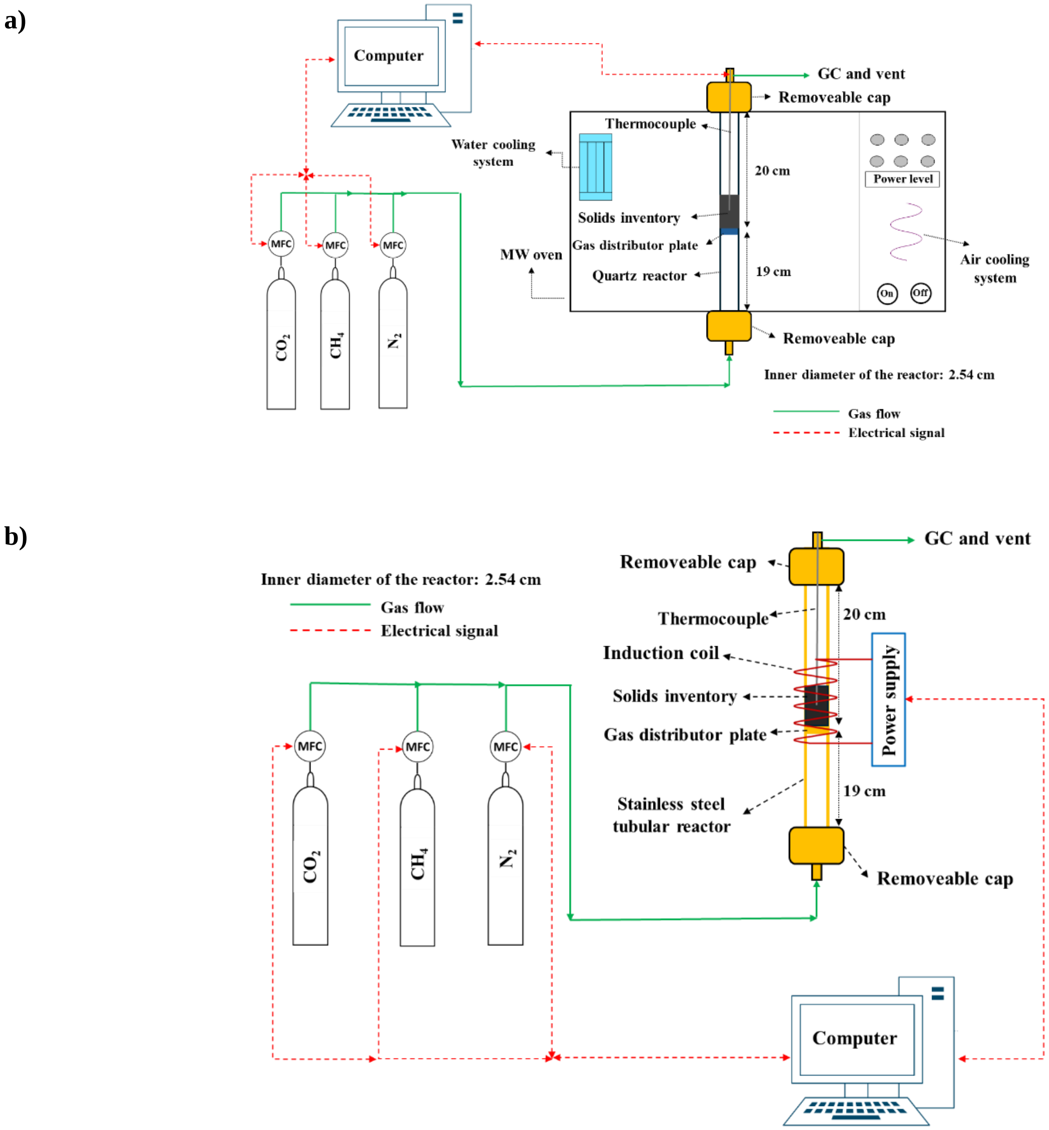

Figure 4.2. A schematic representation of a) the developed MW heating-assisted reactor and b) the adopted conventional heating-assisted reactor.

4.2.3.2 Conventional heating-assisted reactor

To compare the performance of the MW and conventional heating methods in Fe_3O_4 reduction by CH_4, we also employed a lab-scale reactor that was heated conventionally. A schematic diagram of the adopted conventional heating-assisted setup is presented in Figure 4.2b. Induction heating is a method employed to electrically heat conductive materials, predominantly metals, leveraging Faraday's law of electromagnetic induction. According to this principle, when an electrically conductive material is exposed to a time-varying magnetic field created by the passage of an alternating current through a coil of wire, eddy currents are induced within the electrically conductive material. These eddy currents then circulate within the material in a closed loop. Consequently, the resistance encountered by these circulating electrical currents within the material leads to the generation of heat, a phenomenon known as Joule heating [35, 36]. The induction heating-assisted reactor employed in this study is schematically presented in Figure 4.2b. As shown in this figure, due to the Faraday's law of electromagnetic induction, heat is first generated within the reactor’s wall. The generated heat is subsequently transferred from the reactor’s wall to the gas phase. The heat is then transferred from the gas phase to particle’s surface and its inner layers. Accordingly, the employed induction heating-assisted setup in this study provides the surface heating method, i.e., the conventional heating method. Therefore, we employed the induction heating-assisted reactor (Figure 4.2b) to accomplish the redox reactions by the conventional heating method.

4.2.4 Experimental procedure and operating conditions

4.2.4.1 Microwave and conventional heating of oxygen carrier

Before carrying out Fe_3O_4 reduction by CH_4 in the conventional heating assisted setup, the Fe_3O_4 oxygen carrier should be heated to the target bulk temperature T_b in a non-reactive environment. Accordingly, in each test, a total of 10 gm of solid sample with H_{bed} of around 1.5 cm was loaded into the customized stainless steel 316 reactor from the top aperture. H_{bed} represents the initial height of the fixed bed medium. To ensure a complete removal of air from the reactor, N_2 was injected into the reactor for 5 min before heating the bed. We investigated the gas leakage prior to heating the setup and T_b was constantly monitored during the tests. In addition, to monitor O_2 and CH_4 levels in the lab during the reactivity tests, we employed networkable gas detectors

(Honeywell Analytics, E3SA). To control inlet gaseous volumetric flowrate to the reactor, while monitoring T_b, a LabView application was employed. For all tests, following the cutoff of heating, N_2 injection to the reactor was maintained until the T_b fell below 30°C. The customized stainless steel 316 reactor was also washed and dried at 100°C for 30 min prior to each test.

In addition to the reactivity of the selected and/or synthesized oxygen carrier, its MW absorption capability is a critical parameter, which influences the heating performance of the MW heating-assisted CLR processes. We hence studied the MW heating performance of a solids inventory comprised of the Fe_3O_4 oxygen carrier. The MW heating performance of the Fe_3O_4 oxygen carrier was also compared with that of a solids inventory comprised of SiC particles. T_b was chosen in several studies to represent the MW absorption capability of the particles [37-40]. Therefore, in addition to measuring the dielectric properties of the Fe_3O_4 oxygen carrier, to investigate its MW absorption capability, T_b of the solids inventory was measured. To heat up the solids inventory via the MW heating-assisted setup, in each test, a total of 10 gm of solid sample with H_{bed} of around 1.5 cm was loaded into the quartz reactor from the top aperture. To ensure a complete removal of air from the reactor, N_2 was injected into the reactor for 5 min before MW irradiation. We investigated the gas leakage prior to MW irradiation and MW leakage from the setup was monitored during the tests. In addition, to monitor O_2 and CH_4 levels in the lab during the reactivity tests, we employed networkable gas detectors (Honeywell Analytics, E3SA). To control inlet gaseous volumetric flowrate to the reactor, while monitoring T_b, a LabView application was employed. For all tests, following the cutoff of MW irradiation, N_2 injection to the reactor was maintained until the T_b fell below 30°C. The quartz reactor was also washed and dried at 100°C for 30 min prior to each test. In addition, all the tests presented in Section 4.3 were accomplished at U_g = 9 cm/s (Q_i = 2700 cm^3/min). For all the tests presented in Section 4.3, no indications of fluidization were detected for the solids inventory comprised of Fe_3O_4 and/or Fe-Fe_3O_4 mixture. However, for the solids inventory comprised of SiC particles, we observed fluidization at U_g = 9 cm/s (Q_i = 2700 cm^3/min) starting from the room temperature.

4.2.4.2. Redox cycles for the microwave heating-assisted chemical looping dry reforming of methane

To determine the optimum operating conditions for Fe_3O_4 reduction by CH_4, we first calculated the Fe_3O_4-CH_4 phase diagram at atmospheric pressure by FactSage 8.1 [41] (Figure 4.3a). As presented in this diagram, by adjusting the temperature and $Fe_3O_4/(CH_4+Fe_3O_4)$ ratio within region 3, one can achieve a complete reduction of Fe_3O_4 to Fe without C deposition. Accordingly, by selecting 10 gm as the bed inventory and for $T_b \geq 650°C$, considering $Q_i = 2700\ cm^3/min$ and the reaction time of 10 min, a gaseous inlet comprised of N_2-CH_4 mixture with 10 vol.% CH_4 was injected to the reactor during the reduction reaction to adjust the $Fe_3O_4/(Fe_3O_4+CH_4)$ ratio for staying in region 3 of Figure 4.3a.

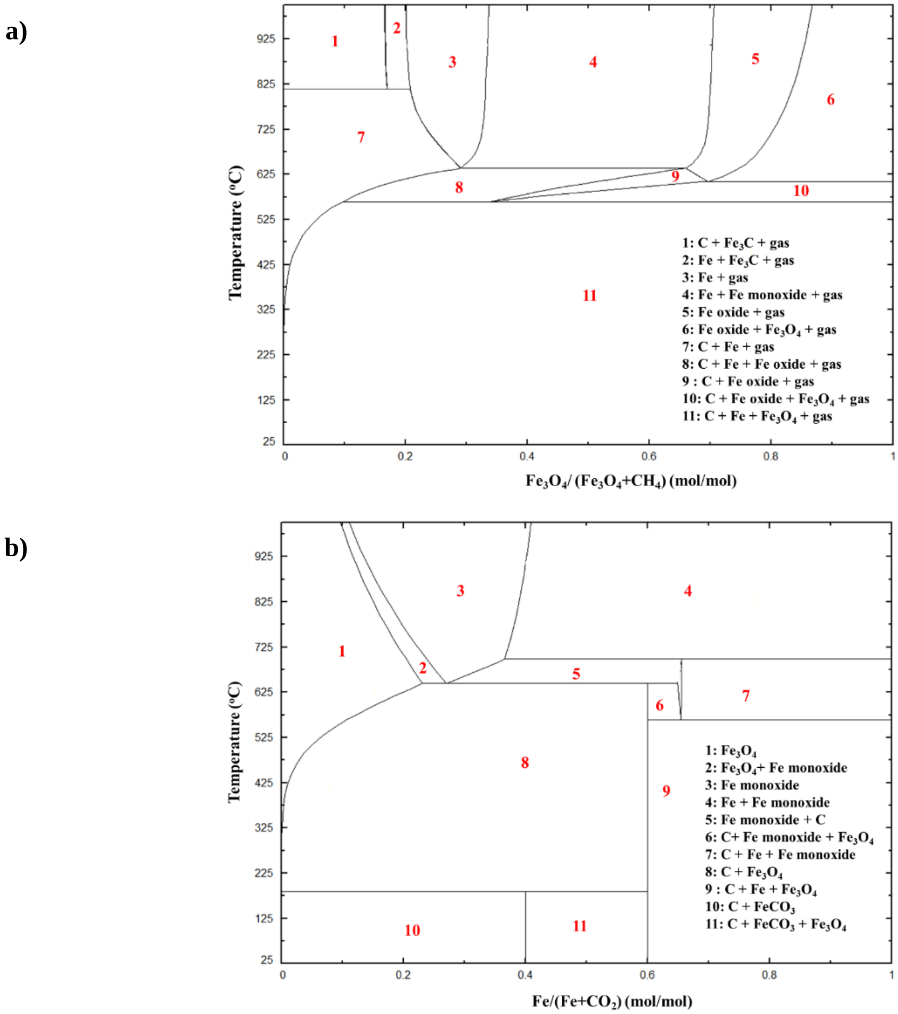

Figure 4.3. a) Fe_3O_4-CH_4 and b) Fe-CO_2 phase diagrams at 1 atm, which were calculated by "Phase Diagram" module of FactSage 8.1 with FTOxid, FSstel, and FactPS databases.

The developed MW heating-assisted reactor was employed to investigate the effect of cyclic redox reactions on CH_4 conversion. To initiate the cyclic redox experiments, 10 gm of fresh Fe_3O_4 was loaded into the MW heating-assisted reactor. While only N_2 was injected to the reactor, the solids inventory was heated by irradiated MWs. After reaching the stable T_b, where Fe_3O_4 reduction by CH_4 was measured, the gaseous stream was switched to the N_2-CH_4 mixture with 10 vol.% CH_4 to accomplish the reduction reaction for 10 min. Subsequently, prior to injecting CO_2 into the reactor, the MW heating was stopped and the inlet gaseous stream was switched to only N_2 until reaching to T_b < 30°C. This choice was made to avoid re-oxidation of the solids inventory by air. After reaching to T_b < 30°C, while maintaining N_2 injection to the reactor, the reactor was irradiated with MWs to reach the stable T_b = 600°C. After reaching the stable T_b = 600°C, the inlet gaseous stream was switched to 30 vol.% CO_2 and 70 vol.% N_2. As discussed in Section 4.2.4.4, with this choice, we were able to avoid the formation of undesired C and Fe monoxide phases. The oxidation reaction by CO_2 was performed for 25 min. The MW heating was then stopped and the inlet gaseous stream was switched to only N_2. Prior to initiating the next redox cycle, to avoid air leakage to the reactor, the inlet gaseous stream comprised of only N_2 was injected to the reactor until reaching to T_b < 30°C. The next redox cycle was subsequently accomplished.

4.2.4.3 Reactivity tests with CH_4 in the microwave and conventional heating-assisted reactors

Reactivity tests in Section 4.3.3.2, i.e., reduction of stable Fe_3O_4 (referring to Fe_3O_4 oxygen carrier collected after four redox cycles) by CH_4, in the MW and conventional heating-assisted reactors were performed to prove the ability of the MW heating-assisted CLDRM in: (i) achieving a higher rate of oxygen carrier reduction compared to the conventionally heated CLDRM (Section 4.3.3.2), (ii) achieving a higher H_2 selectivity compared to the MW heating-assisted catalytic dry reforming of methane (DRM) (Section 4.3.3.2), and (iii) preventing C deposition on the solid phase (Section 4.3.3.3).

We followed similar procedures for the reactivity tests with CH_4 in the MW and conventional heating-assisted reactors. To ensure complete removal of air from the reactors, N_2 was first injected into the reactors for 5 min before heating the reactor via MW irradiation or conventional heating. Sole N_2 injection to the reactor was maintained before reaching T_b, where Fe_3O_4 reduction by CH_4

was measured. After reaching the stable T_b, the gaseous inlet was switched to a N_2-CH_4 mixture with 10 or 1.5 vol.% CH_4. After performing the reduction reaction for 10 min, heating (MW or conventional heating) was stopped and the gaseous inlet was switched to only N_2. To avoid air leakage to the reactor, which could re-oxidize the reduced solids inventory, N_2 injection to the reactor was maintained until reaching a $T_b < 30°C$. Moreover, to measure CH_4 conversion and H_2/CO production ratio, the outlet gaseous stream passed through GC and ultimately vented. In addition to comparing the reduction extent of Fe_3O_4 by CH_4 in the MW and conventional heating-assisted reactors, we carried out a parametric study to investigate the effects of $Q_{CH_{4,i}}/m_{i,t}$ and T_b on CH_4 conversion and H_2/CO production ratio in the MW heating-assisted reactor. $Q_{CH_{4,i}}$ and $m_{i,t}$ represents, respectively, the volumetric flowrate of CH_4 in the inlet gaseous stream of the reactor and initial mass of a solids inventory comprised of Fe_3O_4.

According to literature [42, 43], regardless of the ultimate solid phases that are produced, determining the reduction extent of Fe_3O_4 by CH_4 involves comparing the mass loss of a solids inventory containing Fe_3O_4 with the mass loss observed upon complete reduction of Fe_3O_4, i.e., $Fe_3O_4 \rightarrow Fe$. For a solids inventory comprised of Fe_3O_4 with $m_{i,t}$, and assuming a complete reduction of Fe_3O_4 to Fe, one can achieve $0.72m_{i,t}$ as the final mass of the solids inventory. Consequently, we employed Eq. (4.1) to calculate the reduction extent of Fe_3O_4 by CH_4. In addition, we employed Eq. (4.2) to calculate CH_4 conversion.

$$\text{Reduction extent of } Fe_3O_4 \text{ by } CH_4 = \frac{\text{Total weight loss of the solids inventory}}{m_{i,t}} \times \frac{1}{0.28} \times 100\% \tag{4.1}$$

$$CH_4 \text{ conversion } (\%) = \frac{C_{CH_{4,i}} - C_{CH_{4,o}}}{C_{CH_{4,i}}} \times 100\% \tag{4.2}$$

where $C_{CH_{4,i}}$ and $C_{CH_{4,o}}$ refer to CH_4 concentration in the inlet and outlet gaseous streams of the reactor, respectively.

4.2.4.4 Re-oxidation of Fe_3O_4 oxygen carrier

To prepare the solid samples for the re-oxidation tests (Section 4.3.4), the stable Fe_3O_4 oxygen carrier was reduced at $T_b = 800^{\circ}C$ via the MW heating-assisted reactor and employing N_2-CH_4 mixture with 10 vol.% CH_4. The reduced solid samples were mainly comprised of Fe_3O_4 and Fe

(Section 4.3.3.3) with minor peaks of wustite ($Fe_{0.91}O$). Consequently, referring to Sections 4.3.3.2 and 4.3.3.3, for the re-oxidation of Fe by CO_2, we assumed that the reduced solid samples loaded into the MW and the conventional heating-assisted reactors contained 49 wt.% Fe and 51 wt.% Fe_3O_4.

To determine the optimum operating condition for the re-oxidation of Fe by CO_2, we first employed the "Phase Diagram" module of FactSage 8.1 to generate an isoplethal section of the Fe-CO_2 phase diagram, Figure 4.3b. As shown in this diagram, to re-oxidize Fe to Fe_3O_4 by CO_2, while preventing C deposition and Fe monoxide formation, it is imperative to stay in region 1 of Figure 4.3b. In addition, as explained in Section 4.3.4, the solids inventory that was employed to be re-oxidized by CO_2 contained 5 gm of Fe. Consequently, to stay in region 1 of Figure 4.3b, for 5 gm of Fe and with the oxidation time of 25 minutes, the CO_2 concentration of 30 vol.%, i.e., 820 cm^3/min of CO_2 flowrate in the inlet gaseous stream, ensured staying in region 1 of Figure 4.3b for $T_b \geq 600°C$.

For the re-oxidation tests by CO_2 in the MW and the conventional heating-assisted reactors (Section 4.3.4), T_b was increased to 600°C by irradiating MWs or employing the conventional heating method, while injecting only N_2. After reaching a stable T_b = 600°C, inlet gas was switched to a N_2-CO_2 mixture with 30 vol.% CO_2 to carry out the re-oxidation reaction. The re-oxidation tests were accomplished for 5 and 25 min. Upon completion of the isothermal step, heating (MW or conventional heating) was stopped and the inlet gas was switched to only N_2 until reaching T_b below 30°C. Similar to the redox experiments explained in Section 4.3.3.1, this choice was made to avoid re-oxidation of the solids inventory by air.

To calculate the oxidation extent of Fe to Fe_3O_4, we followed a similar approach that was adapted for developing Eq. (4.1). For a solids inventory comprised of Fe and Fe_3O_4 with the corresponding initial masses of $m_{i,Fe}$ and $m_{i,\,Fe_3O_4}$, respectively, and assuming a complete oxidation of Fe to Fe_3O_4, one can achieve ($1.38m_{i,Fe} + m_{i,\,Fe_3O_4}$) as the final mass of the solids inventory after oxidation by CO_2. Consequently, as illustrated in Section 4.3.4, since Fe was principally converted to Fe_3O_4 and no peaks of Fe_2O_3 and FeO were detected, we employed Eq. (4.3) to calculate the oxidation extent of Fe by CO_2.

$$\text{Oxidation extent of Fe by } CO_2 = \frac{\text{Total weight gain of the solids inventory}}{m_{i,Fe}} \times \frac{1}{0.38} \times 100\% \qquad (4.3)$$

4.2.5 Characterization methods

A Phillips X'PERT XRD analyzer equipped with Cu-Kα radiation was employed to identify the phase compositions of the original, reduced, and re-oxidized solid samples. The diffraction angle scanning was set in the range of 10° to 80°/90° with a scan rate of 0.175°/s. Before the XRD analysis, the solid samples were grinded with a mortar and pestle to have a homogenous sample. A LECO CS 744 analyzer was deployed to estimate the C content of the reduced oxygen carrier. Surface morphology of the solid samples was investigated by a scanning electron microscopy (SEM; HITACHI TM-3030 PLUS). We also employed a vector network analyzer (750 GHz KEYSIGH) to measure the dielectric properties of the Fe_3O_4 oxygen carrier.

4.3 Results and discussion

4.3.1 Microwave heating performance of Fe_3O_4 oxygen carrier

To study the MW absorption performance of Fe_3O_4 in the MW heating-assisted reactor, we selected solids inventories comprised of Fe_3O_4 under an inert gaseous environment, i.e., employing N_2 as the inlet gaseous stream. To investigate the possibility of hot and/or cold spots formation, T_b was measured at three different positions during each test: (i) $0.1H_{bed}$, (ii) $0.5H_{bed}$, and (iii) $0.9H_{bed}$ above the gas distributor plate. Bulk temperatures for inserting the tip of the thermocouple probe at $0.1H_{bed}$, $0.5H_{bed}$, and $0.9H_{bed}$ above the gas distributor plate are represented as $T_{b,l}$, $T_{b,m}$, and $T_{b,u}$, respectively. During each test, we observed a minor difference (less than 3%) between these temperature readings (as shown in Figure 4.4b). This observation effectively demonstrated the system's ability to mitigate hot and/or cold spots formation for non-reactive environments. In addition, we employed a thermal imaging camera (FLIR T621) to investigate the possibility of hot and/or cold spots formation within the solids inventory. By monitoring the surface temperature of the bed, no sign of hot and/or cold spots formation was detected within the solids inventory, which was another observation to demonstrate the system's ability to mitigate hot and/or cold spots formation. Therefore, for a non-reactive environment, the location of the tip of the thermocouple within the solids inventory did not affect the accuracy of T_b measurement in the system studied here. Accordingly, to measure T_b for non-reactive environments, we inserted the tip of the thermocouple at $0.5H_{bed}$ above the gas distributor plate.

At 2.45 GHz, by employing the vector network analyzer, we measured 1.85 and 0.30 as relative dielectric constant ε' and relative dielectric loss factor ε'' of the Fe_3O_4 oxygen carrier, respectively. Based on the resulted dielectric loss tangent $\tan(\delta)$ of 0.16 and the magnetic loss tangent $\tan(\delta_\mu)$ of Fe_3O_4 that highlights its magnetic properties, one can predict a high MW absorption capability for the Fe_3O_4 oxygen carrier. As shown in Figure 4.4a, the solids inventory comprised of Fe_3O_4 illustrated a higher MW absorption capability, compared to SiC, for the same input MW power. Considering the high MW absorption capability of SiC particles (ε' and $\tan(\delta)$ of around 10 and 0.25 [44], respectively, at an operating frequency of 2.45 GHz), different scientists reported a promising MW heating of SiC particles in non-reactive and reactive gas-solid systems [37, 39, 44]. While magnetic materials, like Fe_3O_4, interact with the electric and magnetic fields of the MWs, non-magnetic materials, like SiC, mainly interact with the electric field of irradiated MWs. Therefore, despite the lower $\tan(\delta)$ of Fe_3O_4, due to its interaction with both electric and magnetic fields of irradiated MWs, one expects a good MW absorption capability of the solids inventory comprised of Fe_3O_4. This is in agreement with the results reported in literature [26, 45] and obtained in this study, Figure 4.4a. In addition, for an identical U_g, solids inventory, inlet gaseous stream, and heating time, one anticipates a higher T_b with increased input MW powers, which is observed in Figure 4.4a.

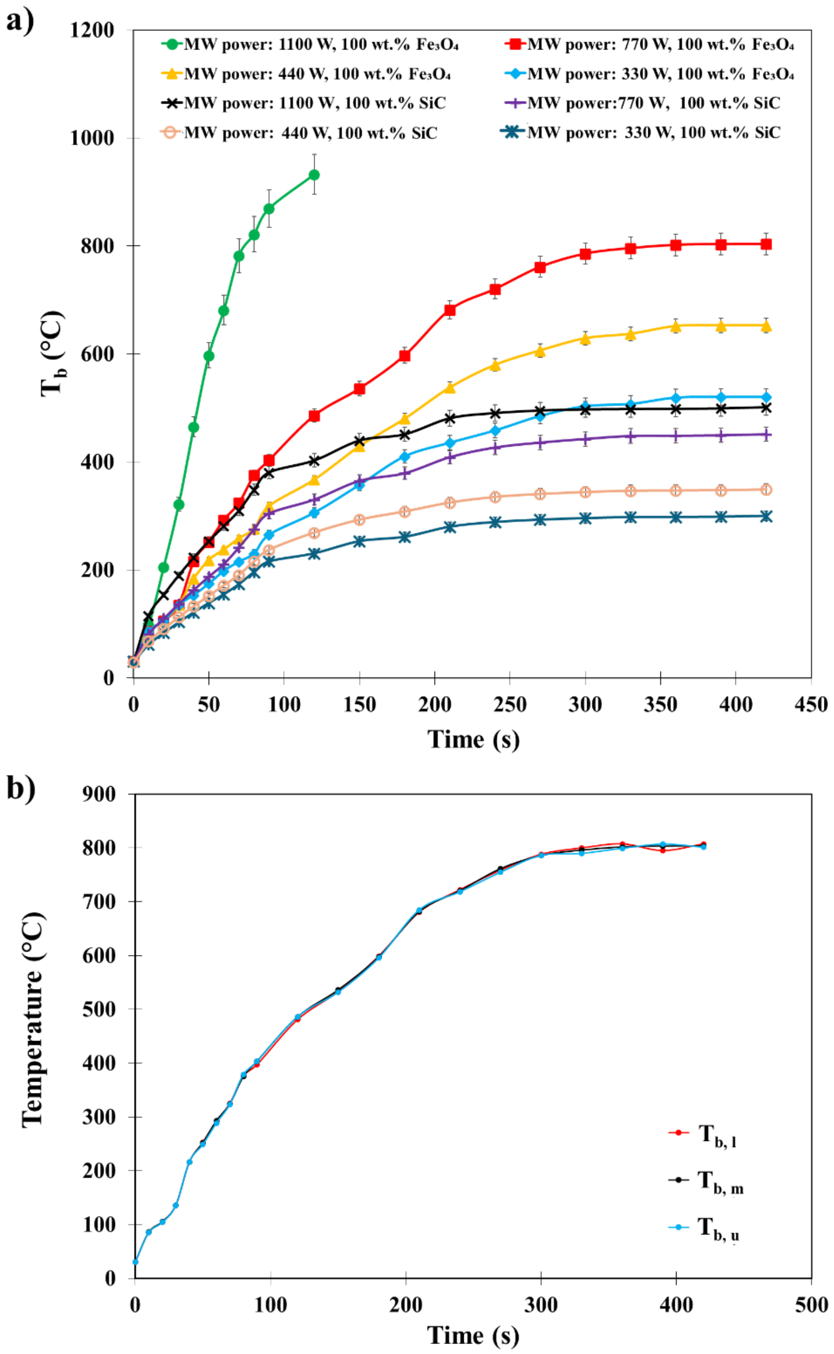

Figure 4.4. a) MW heating of solids inventories comprised of Fe$_3$O$_4$ and SiC, and b) $T_{b,l}$, $T_{b,m}$, and $T_{b,u}$ for input MW power of 770 W and the solids inventory comprised of Fe$_3$O$_4$. Bed inventory: 10 gm, Q_i : 2700 cm^3/min, gaseous feed: N$_2$. The error bars indicate that the tests were conducted three times.

4.3.2 Microwave heating and temperature measurement for the reactive system

Compared to the non-reactive environment, by feeding a N_2-CH_4 mixture from the bottom of the reactor, a multi-stage reduction pathway can occur in a fixed bed. Therefore, as the lower portion of the solids inventory contacts the gaseous fuel first, a greater extent of Fe_3O_4 reduction can happen for the lower portion of the solids inventory compared to its upper section, in particular, for a non-shallow bed. D_p represents the penetration depth of electromagnetic waves in a material. It is well-documented in literature that due to a low D_p of pure metals, like Fe with D_p = 1.3 µm at room temperature, micron-sized Fe (Fe with d_p in the order of a few hundred microns) can exhibit a low MW absorption capability at room temperature [26, 33]. However, by increasing T_b up to 800°C, the electrical resistivity of Fe can drastically increase (more than 14 times [46]), which leads to a high MW absorption capability of elemental Fe. This can help maintain the MW absorption capability of the solids inventory at elevated T_b ($\geq$ 650°C) even after Fe_3O_4 reduction. Consequently, we investigated the effect of reduction of Fe_3O_4 by CH_4 on T_b measurement and uniform MW heating within the solids inventory.

Similar to the non-reactive environment, we positioned the tip of the thermocouple at a height of $0.5H_{bed}$ above the gas distributor plate to compare T_b for non-reactive (employing only N_2 as the inlet gaseous stream) and reactive (employing a N_2-CH_4 mixture as the inlet gaseous stream) environments. By employing identical U_g, the solids inventory, MW power, and MW irradiation time, a minor T_b fluctuation (less than 3%) during reduction of Fe_3O_4 was observed, as shown in Figure 4.5a and b. This observation demonstrated the system's capability to maintain its MW absorption capability even after Fe_3O_4 reduction.

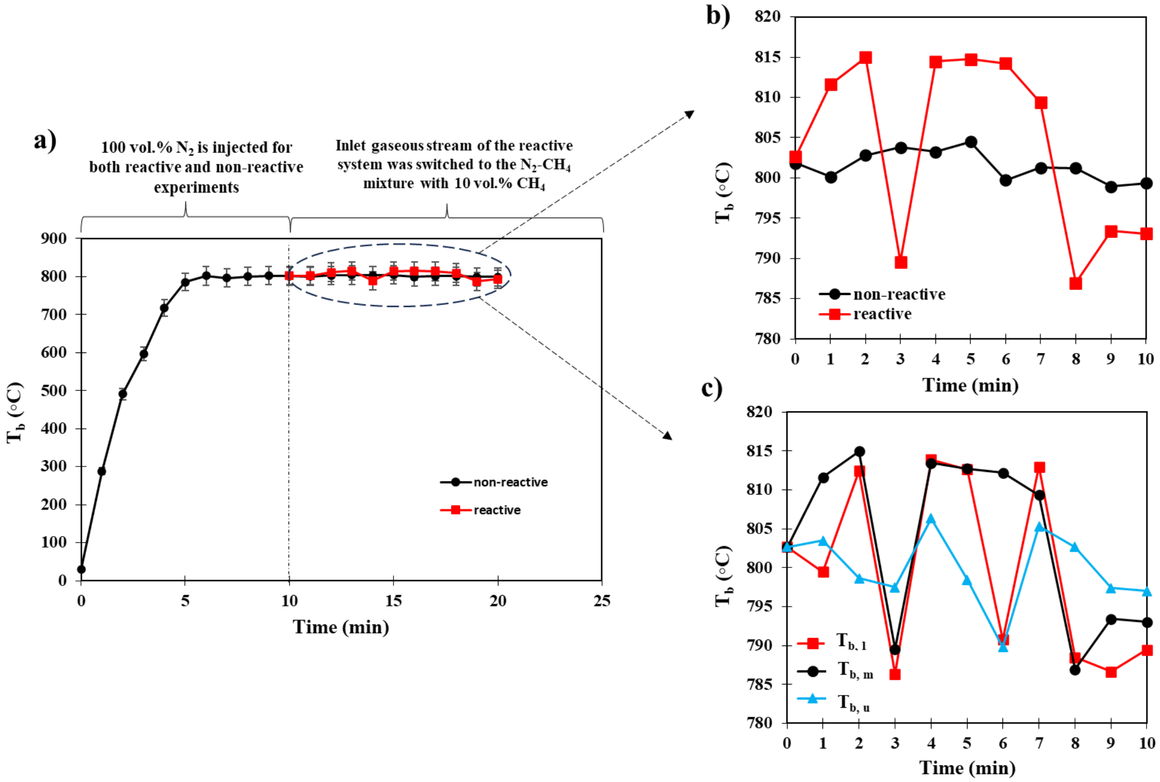

Figure 4.5. a and b) T_b of non-reactive and reactive systems when keeping the tip of thermocouple at $0.5H_{bed}$ above the gas distributor plate and c) $T_{b,l}$, $T_{b,m}$, and $T_{b,u}$ of the reactive system (loaded Fe_3O_4, MW power, and Q_i were fixed at 10 gm, 770 W, and 2700 cm^3/min, respectively). The error bars indicate that the tests were conducted three times.

For the reactive environment with the maximum reduction extent of Fe_3O_4 at 49%, as shown in Figure 4.5c, we observed a minor difference (less than 3%) between $T_{b,l}$, $T_{b,m}$, and $T_{b,u}$, which effectively demonstrated a uniform MW heating within the solids inventory during the reactivity tests. The uniform MW heating for the reactive environment can be attributed to: (i) uniform Fe_3O_4 reduction by CH_4 due to the low H_{bed} (around 1.5 cm), (ii) production of intermediate Fe monoxide phases (Section 4.3.3.3), specifically $Fe_{0.91}O$ as a better MW absorber than Fe_3O_4 [45], and (iii) increase of electrical resistivity of Fe at $T_b \geq 650°C$ [46]. Accordingly, similar to the non-reactive environment, to measure T_b during the reactivity tests (Sections 4.3.3 and 4.3.4), the thermocouple tip was placed at a height of $0.5H_{bed}$ above the gas distributor plate.

4.3.3 Reduction of Fe_3O_4 oxygen carrier

4.3.3.1 Cyclic performance of Fe_3O_4 oxygen carrier

CH_4 conversion and the evolution of the syngas compounds from Fe_3O_4 reduction by CH_4 at T_b = 800°C during twenty successive redox cycles are presented in Figure 4.6. According to these results, a stable reactivity of Fe_3O_4 with CH_4 was achieved in the fourth redox cycle. Results presented in Figure 4.6b show that a relatively constant H_2/CO production ratio around 2 was observed for different redox cycles.

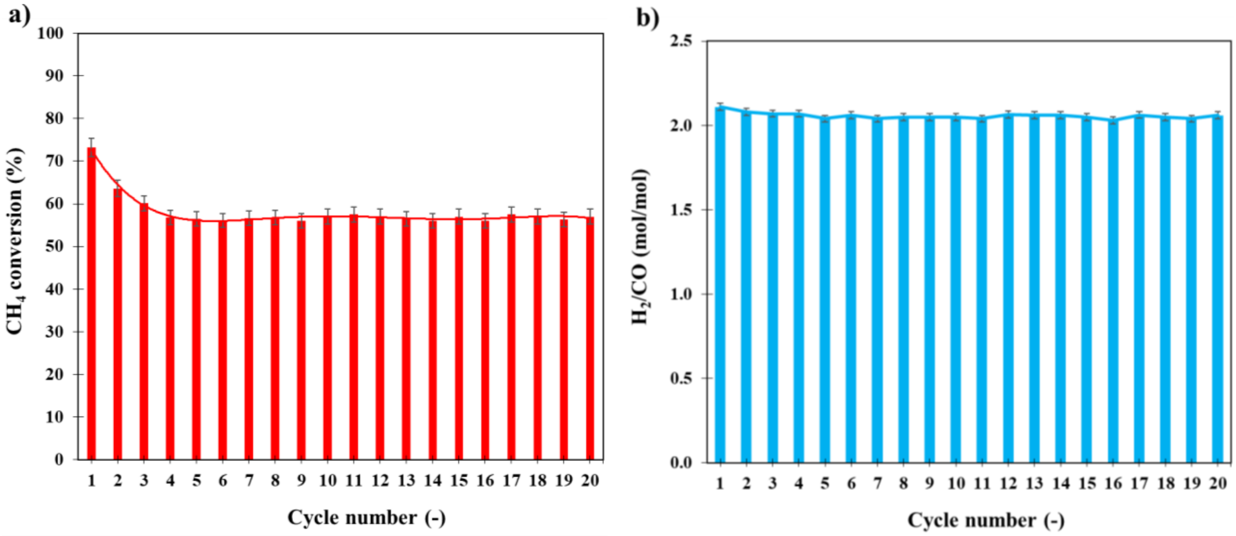

Figure 4.6. Effect of redox cycles on a) CH_4 conversion and b) the evolution of the syngas compounds in the reduction stage of the MW heating-assisted CLDRM. MW power, reduction reaction time, oxidation reaction time, T_b, Q_i, $m_{i,t}$, and gaseous feed were fixed at 770 W, 10 min, 25 min, 800°C, 2700 cm^3/min, 10 gm, and N_2-CH_4 mixture with 10 vol.% CH_4, respectively. Solids inventory was comprised of Fe_3O_4. The error bars indicate that the reduction tests were conducted three times.

Several researchers reported that the reduction of Fe_3O_4 and Fe_2O_3 by gaseous reductants (primarily CH_4, H_2, and CO) is controlled by phase-boundary, gas diffusion, Avrami-Erofeyev equations as nucleation-based models, and/or the combination of phase-boundary and gas diffusion mechanisms [34, 47, 48]. Following the reduction of Fe_3O_4 to Fe, formation of the elemental Fe on the surface of Fe_3O_4 oxygen carrier decreases its sintering temperature and ultimately results in particle agglomeration. This can subsequently decrease the contact surface area between the oxygen carrier and the gaseous fuel. Therefore, a relatively constant H_2/CO production ratio, the decline in CH_4 from the first to third redox cycles, and the constant CH_4 conversion after the fourth redox cycle can be attributed to the deleterious impact of sintering and agglomeration of Fe on decreasing/eliminating the effect of phase-boundary reaction mechanism on the reduction of Fe_3O_4 by CH_4. In addition, compared to fresh Fe_3O_4, the reduction extent of the stable Fe_3O_4 oxygen carrier by CH_4 was notably decreased, as shown in Figure 4.7. This observation was another reason to illustrate the effect of sintering and agglomeration of Fe on decreasing/eliminating the effect of the phase-boundary reaction mechanism on the reduction of Fe_3O_4 by CH_4. Consequently, to increase the sintering temperature of Fe_3O_4, one can employ refractory materials, such as zirconium dioxide (ZrO_2), titanium oxide (TiO_2), silicon oxide (SiO_2), and aluminum oxide (Al_2O_3) to synthesize composite oxygen carriers of Fe_3O_4 with these compounds. In addition, considering the presence of Ti, Si, and Al elements (with weight fraction of up to 10 wt.%) in the naturally occurring magnetite ore, the magnetite ore has shown a high oxygen carrying capacity for the CLR of CH_4 [34], while it performed a high resistivity towards sintering for T_b up to 1025°C. Therefore, employing naturally occurring magnetite ore for the successive redox cycles of the MW heating-assisted CLDRM can decrease the costs associated with buying and/or synthesizing oxygen carriers, while it minimizes the issues related to the sintering of the oxygen carrier. Moreover, by increasing d_p, sintering temperatures of Fe and Fe_3O_4 increase. For example, it was illustrated in the study by Zhong et al. [49] that by increasing d_p of Fe powders from 50 to around 180 µm, the sintering temperature was increased from 585 to around 725°C.

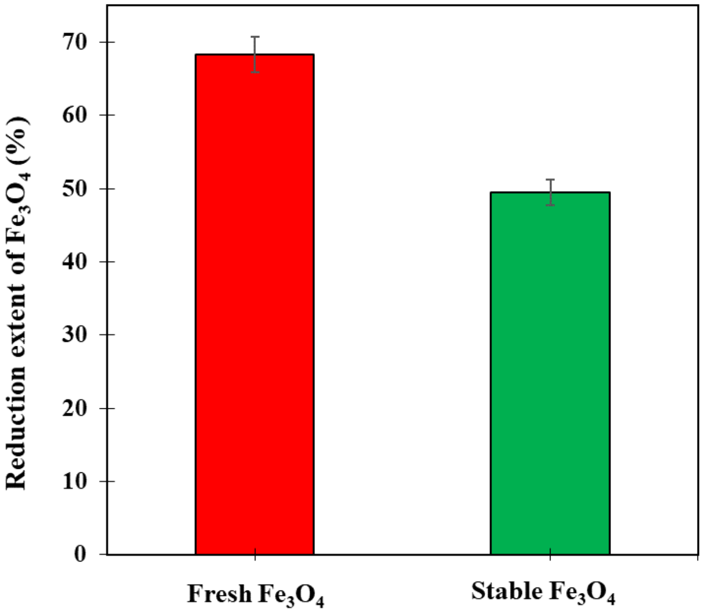

Figure 4.7. Fe_3O_4 reduction by CH_4 in the MW heating-assisted reactor. MW power, reduction reaction time, T_b, Q_i, $m_{i,t}$, and gaseous feed were fixed at 770 W, 10 min, 800°C, 2700 cm^3/min, 10 gm, and N_2-CH_4 mixture with 10 vol.% CH_4, respectively. Solids inventory was comprised of Fe_3O_4. The error bars indicate that the reduction tests were conducted three times.

4.3.3.2 Fe_3O_4 reduction by CH_4 in the microwave and conventional heating-assisted reactors

The reduction behavior of the stable Fe_3O_4 oxygen carrier by CH_4 in the MW and conventional heating-assisted reactors is illustrated in Figure 4.8. Due to the selective heating feature of the MW heating method, for the same reactor geometry, reactor's volume, U_g, T_b, solids inventory, and reaction time, a higher rate of Fe_3O_4 reduction by CH_4 was obtained in the MW heating-assisted reactor.

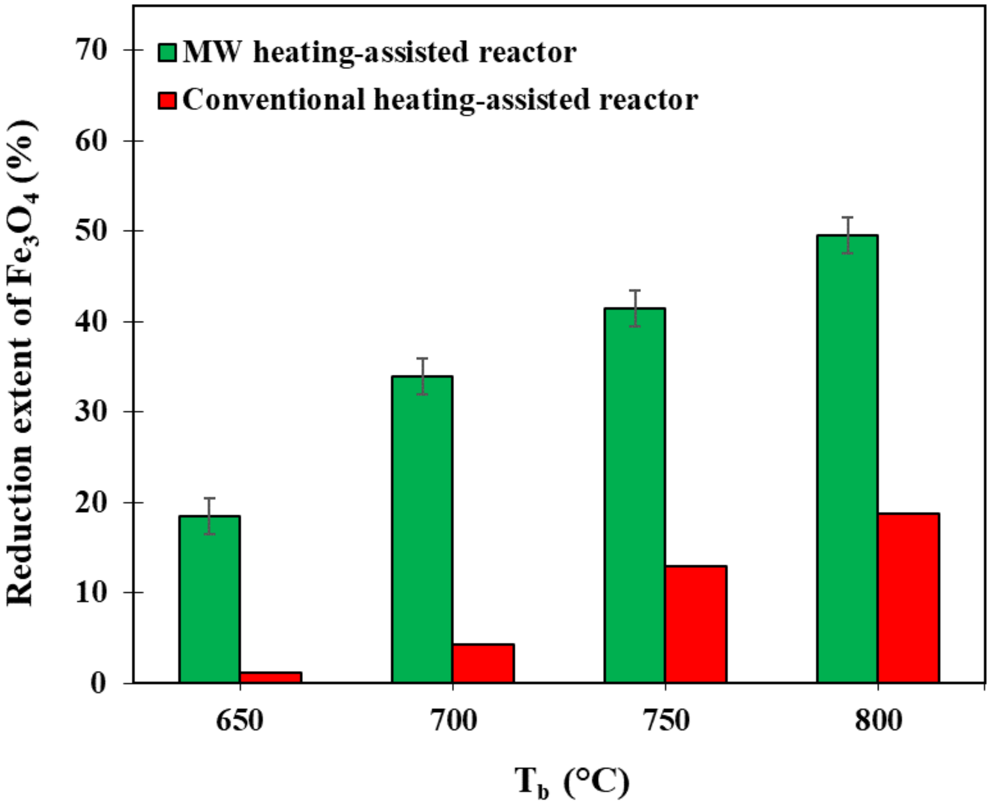

Figure 4.8. Reduction of the stable Fe_3O_4 oxygen carrier by CH_4 in the MW and conventional heating-assisted reactors. MW power, reduction reaction time, Q_i, $m_{i,t}$, and gaseous feed were fixed at 770 W, 10 min, 2700 cm^3/min, 10 gm, and N_2-CH_4 mixture with 10 vol.% CH_4, respectively. The loaded solids inventory was comprised of Fe_3O_4. The error bars indicate that the tests were conducted three times.

Effects of $Q_{CH_{4,i}}/m_{i,t}$ and T_b on CH_4 conversion and the evolution of the syngas compounds from Fe_3O_4 reduction by CH_4 in the MW heating-assisted reactor are illustrated in Figure 4.9. As expected, considering the endothermic behavior of Fe_3O_4 reduction by CH_4, by increasing T_b, CH_4 conversion was enhanced. In addition, as shown in Figure 4.9a, at T_b = 800°C, by decreasing $Q_{CH_{4,i}}/m_{i,t}$ from 27 to 2 $cm^3_{CH_4}/(g_{Fe_3O_4}.min)$, the CH_4 conversion was increased from 56 to 97%. For a fixed U_g, by decreasing $Q_{CH_{4,i}}$ and increasing $m_{i,t}$, contact time between Fe_3O_4 oxygen carrier and CH_4 increases. This predicts a higher rate of CH_4 conversion. The effects of T_b and $Q_{CH_{4,i}}/m_{i,t}$ on the evolution of the syngas compounds resulting from Fe_3O_4 reduction by CH_4 are also shown in Figure 4.9b. As discussed earlier in Section 4.1, the reduction of Fe_3O_4 by CH_4 yields an H_2/CO production ratio of 2. We measured a similar H_2/CO production ratio (ranging from 2.04 to 2.11) from the reduction of Fe_3O_4 by CH_4 in the MW heating-assisted reactor. It should be considered that in addition to partial oxidation of CH_4 by lattice oxygen of Fe_3O_4 (R-4.1), complete oxidation of CH_4, i.e., CH_4 combustion with surface and lattice oxygens of the oxygen carrier can occur. CH_4 combustion results in CO_2 and H_2O production, rather than syngas production. Consequently, the produced H_2O and CO_2 can react with CH_4 by SRM and DRM reactions. Accordingly, a slight deviation of H_2/CO production ratio from 2 can be attributed to the simultaneous occurrence of catalytic SRM and DRM. Moreover, less than 2 mol.% of H_2O and CO_2 were detected during the Fe_3O_4 reduction by CH_4 at T_b = 800°C, which was another demonstration for occurrence of SRM and DRM. The presence of minor (less than 2 mol.%) CO_2 in the output stream of the reactor also illustrated the capability of the MW heating-assisted reactor to mitigate CO_2 emission, while reducing Fe_3O_4 by CH_4. Hence, the benefits of irradiating the reactor with MWs to avoid undesired gas phase reactions, including CH_4 decomposition to other hydrocarbons, was also depicted.

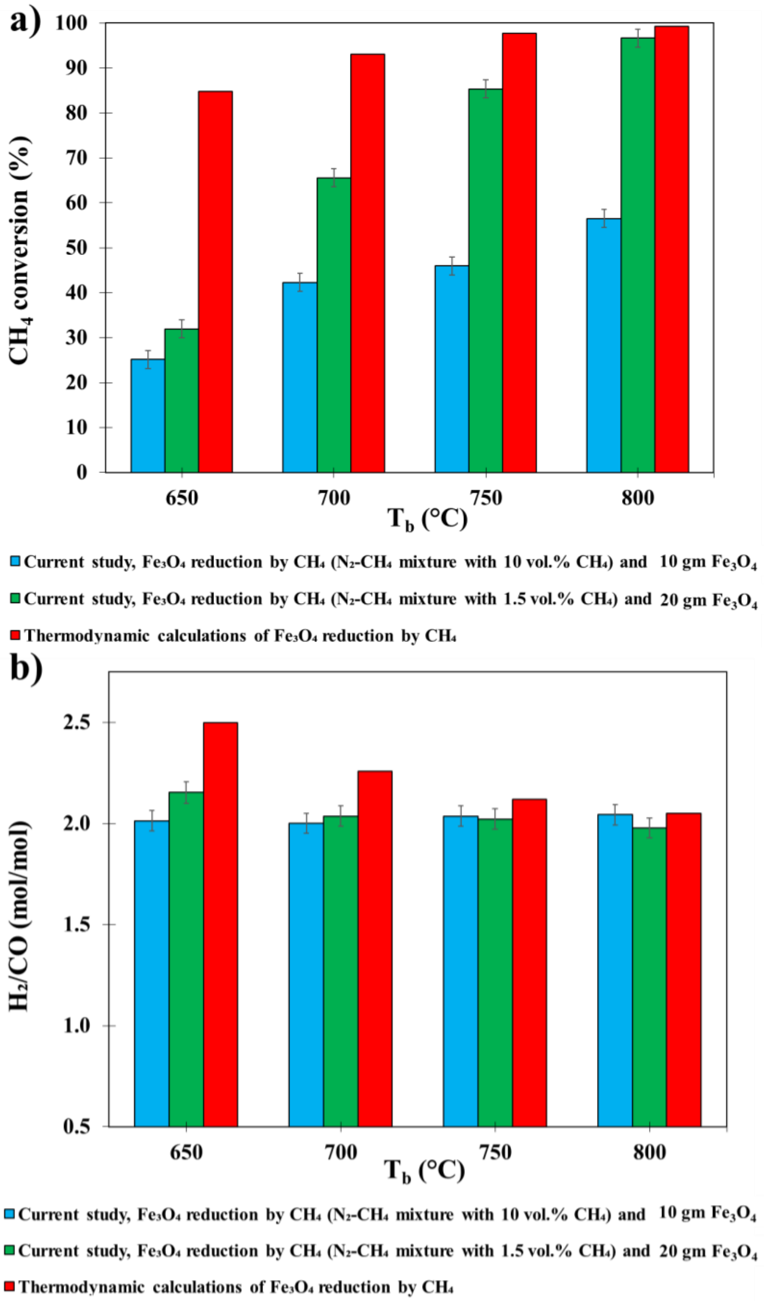

Figure 4.9. Effects of T_b and $Q_{CH_{4,i}}/m_{i,t}$ on a) CH_4 conversion and b) the evolution of the syngas compounds from reduction of the stable Fe_3O_4 oxygen carrier by CH_4 in the MW heating-assisted reactor. Solids inventory was comprised of Fe_3O_4. MW power of 770 and 880 W were employed for bed inventories of 10 and 20 gm, respectively. The error bars indicate that the tests were conducted three times.

4.3.3.3 Characteristics of the reduced Fe_3O_4 oxygen carrier

XRD pattern of fresh Fe_3O_4 (Figure 4.10) shows diffracted XR peaks associated with Fe_3O_4 crystalline structure with a very minor peak of Fe crystalline structure, which corresponds to the impurity of the fresh oxygen carrier. XRD patterns of the reduced solids inventories in the MW and conventionally heated reactors at T_b = 800°C are also shown in Figure 4.10. When reducing Fe_3O_4 in the MW heating-assisted reactor, minor $Fe_{0.91}O$ crystalline structures were detected. Compared to the conventionally heated reactor, the higher rate of complete reduction Fe_3O_4 to Fe, instead of formation of intermediate Fe monoxide phases, such as FeO and $Fe_{0.91}O$, in the MW heating-assisted reactor can be attributed to the selective heating feature of the MW heating method. In addition, the XRD pattern revealed no sign of C deposition on the solid phase (see Figure 4.10) in the case of employing the MW heating-assisted reactor. To further confirm the prevention of C deposition on Fe_3O_4, we employed a LECO analyzer to check the C content of the reduced Fe_3O_4 oxygen carrier that was achieved in the MW heating-assisted reactor. Results collected from the LECO analyzer showed no sign of C deposition (<0.01 wt.%). Hence, in addition to Fe_3O_4 reduction for syngas production, the MW heating-assisted CLDRM can mitigate C deposition, which is a crucial challenge in the commercialization of MW and conventionally heated catalytic DRM. Like the MW heating method, due to a high T_b (800°C), minor peaks of Fe_2O_3 and $Fe_{0.91}O$ crystalline structures were detected when the conventional heating method was employed. However, as detected in XRD analysis shown in Figure 4.10, accomplishing Fe_3O_4 reduction by CH_4 at T_b = 800°C in the conventionally heated reactor caused C deposition. This could be attributed to the gas phase decomposition of CH_4 at gas phase temperature of 800°C.

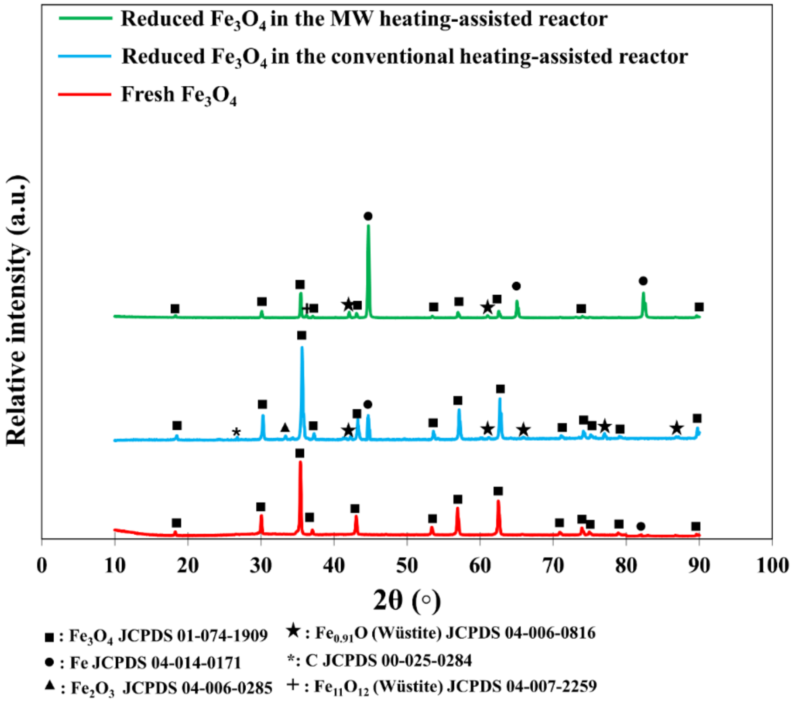

Figure 4.10. XRD patterns of fresh and reduced Fe_3O_4 oxygen carriers by N_2-CH_4 mixture (10 vol.% CH_4) in the MW and conventional heating-assisted reactors at T_b = 800°C.

The morphology analysis of fresh and reduced Fe_3O_4 oxygen carriers by SEM images are shown in Figure 4.11. As noted in Figure 4.11c, following the Fe_3O_4 reduction by CH_4, solid-solid bridges between the reduced Fe_3O_4 oxygen carriers were observed. In addition, as depicted in Figure 4.11b, upon heating the solids inventory comprised of only Fe_3O_4 to T_b = 800°C and under a N_2 environment, i.e., a non-reactive environment, relatively fewer solid-solid bridges between the oxygen carriers were observed. Consequently, the higher solid-solid bridges can be attributed to the sintering of the particles due to the formation of elemental Fe.

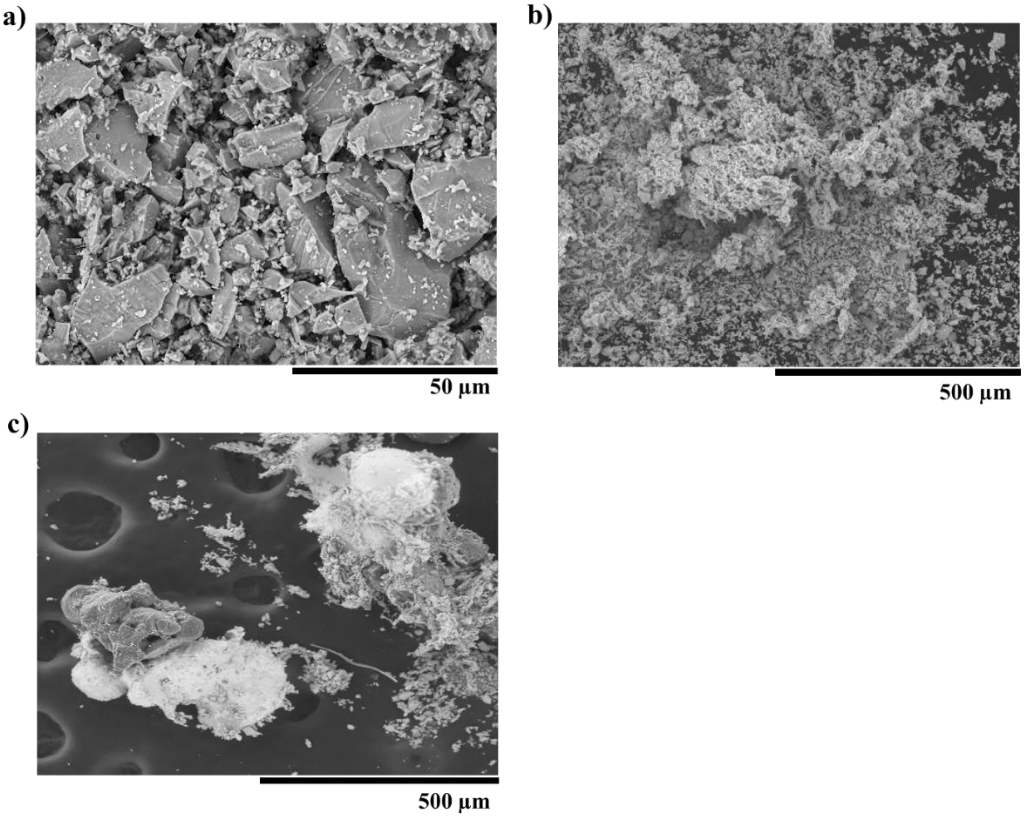

Figure 4.11. SEM images of: a) fresh Fe_3O_4 oxygen carrier, b) Fe_3O_4 oxygen carrier that was heated to T_b = 800°C under N_2 environment, and c) reduced Fe_3O_4 oxygen carrier by CH_4 (N_2-CH_4 mixture with 10 vol.% CH_4) in the MW heating-assisted reactor at T_b = 800°C.

4.3.4 Oxidation of the reduced Fe_3O_4 oxygen carrier

To prepare the solid samples for the re-oxidation tests in this section, the stable Fe_3O_4 oxygen carrier was first reduced at $T_b = 800^{\circ}C$, $Q_i = 2700\ cm^3/min$, reduction reaction time of 10 min, and employing a N_2-CH_4 mixture with 10 vol.% CH_4 in the MW heating-assisted reactor. Consequently, based on 49% as the reduction extent of Fe_3O_4 by CH_4, for 10 gm as the total solids inventory loaded into the MW and conventional heating-assisted reactors for the re-oxidation of the solid samples by CO_2, we estimated $m_{i,Fe}$ = 5 gm. For the same reactor geometry, reactor's volume, U_g, T_b, and solids inventory, we obtained 18% and 12% as the oxidation extent of Fe to Fe_3O_4 by CO_2 in the MW and conventional heating-assisted reactors, respectively, for the oxidation time of 5 min. The higher rate of oxidation reaction in the MW heating-assisted reactor can be attributed to the selective heating feature of the MW heating method. XRD pattern of the re-oxidized oxygen carrier in the MW heating-assisted reactor is elucidated in Figure 4.12. As shown in this figure, we did not detect any sign of Fe_2O_3 or FeO production and C deposition.

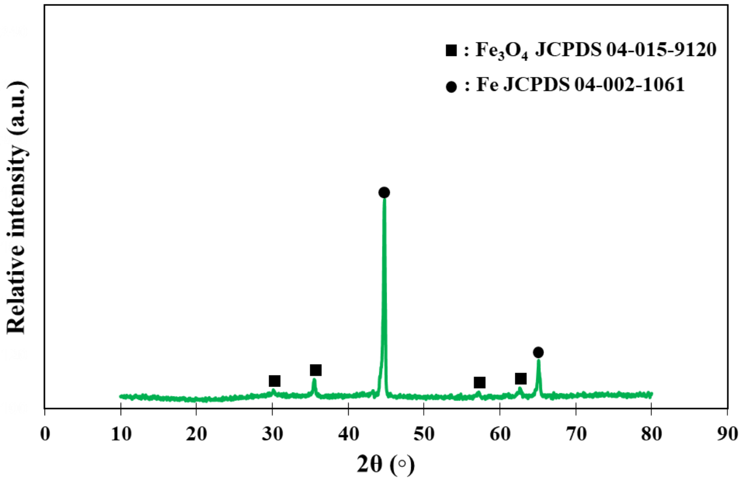

Figure 4.12. XRD pattern of the collected solids inventory after re-oxidation by CO_2 in the MW heating-assisted reactor at T_b = 600°C and for oxidation reaction time of 5 min.

After 25 min of re-oxidation by CO_2 in the MW heating-assisted reactor, the concentration of CO in the outlet gaseous stream of the reactor fell below 2 mol.%. In addition, based on the thermodynamic calculations presented in Section 4.2.4.4, accomplishing the oxidation reaction by CO_2 at T_b = 600°C avoids formation of FeO and Fe_2O_3 phases (staying in region 1 of Figure 4.3b). Moreover, based on the results of the LECO analyzer, we did not detect C on the oxygen carrier. Furthermore, we achieved nearly complete re-oxidation of the solids inventory (oxidation extent of 94%). Consequently, we assumed a complete oxidation of the oxygen carrier after 25 min.

4.4 Conclusion

In this study, we proposed the MW heating-assisted CLDRM as a novel syngas production technology to leverage the selective heating feature of the MW heating method to create a thermal gradient between solid and gas phases, yielding a higher solid temperature than the gas temperature.

This thermal gradient can promote the desired redox reactions, while suppressing undesired gas phase reactions, in particular C deposition due to CH_4 decomposition.

We first illustrated the high MW absorption capability of Fe_3O_4, as the selected oxygen carrier. A stable CH_4 conversion resulting from Fe_3O_4 reduction by CH_4 was achieved in the fourth redox cycle of the MW heating-assisted CLDRM. For the stable Fe_3O_4 oxygen carrier and $Q_{CH_{4,i}}/m_{i,t}$ of $2\ cm^3_{CH_4}/(g_{Fe_3O_4}.min)$, a maximum CH_4 conversion of 97% with an H_2/CO production ratio of around 2 were achieved at T_b = 800°C. We also compared the reduction extents of Fe_3O_4 by CH_4 in the MW and conventional heating-assisted reactors. For $Q_{CH_{4,i}}/m_{i,t}$ of $27\ cm^3_{CH_4}/(g_{Fe_3O_4}.min)$, 19% and 49% were measured as the maximum reduction extent of Fe_3O_4 via the conventional and MW heating-assisted reactors, respectively, at T_b = 800°C. In addition, no sign of C deposition on the solid phase was detected when reducing Fe_3O_4 by CH_4 at T_b = 800°C in the MW heating-assisted reactor. Moreover, other minor gaseous species, such as CO_2 and H_2O, accounted for less than 2 mol.% of the outlet gaseous stream of the MW heating-assisted reactor during the Fe_3O_4 reduction by CH_4. Furthermore, compared to the conventional heating-assisted reactor, the re-oxidation of Fe_3O_4 oxygen carrier by CO_2 via the MW heating-assisted reactor increased (up to 1.5 times) the oxidation extent of Fe, with no sign of undesired gas phase reactions.

The proposed MW heating-assisted CLDRM (i) was capable of achieving a nearly complete CH_4 conversion (97%) with an H_2/CO production ratio of around 2, (ii) prevented C deposition on Fe_3O_4, and (iii) had a higher reduction extent of Fe_3O_4 compared to the conventionally heated CLDRM. We also illustrated that the developed MW heating-assisted reactor with a bed inventory of 10 gm and at U_g = 9 cm/s (Q_i of 2700 cm^3/min) could avoid hot and/or cold spots formation within the solids inventory for reactive and non-reactive environments.

Understanding the kinetics of the redox reactions in the MW heating-assisted CLDRM is essential to design and/or simulate pilot- and industrial-scale reactors for the proposed syngas production technology and help with the technology deployment. In addition, to effectively address technical and economic challenges of scaling up this syngas production technology, a detailed techno-economic evaluation, while focusing on the effect of energy efficiency of MW heating method, i.e., electricity to MW conversion of the MW generators and MW dissipation within the solids inventory, is required. Moreover, one needs to accomplish a life cycle assessment for the proposed technology to achieve a holistic approach regarding all its environmental impacts.

CRediT authorship contribution statement

Mohammad Khodabandehloo: Conceptualization, Methodology, Validation, Investigation, Data curation, Writing - Original draft, Visualization.

Jaber Shabanian: Conceptualization, Methodology, Writing - review & editing, Co-supervision, Project administration.

Jean-Phillipe Harvey: Methodology, Writing – review & editing, Co-supervision.

Jamal Chaouki: Conceptualization, Resources, Writing - review & editing, Supervision, Funding acquisition.

Nomenclature

Acronym

CLC	Chemical looping combustion
CLDRM	Chemical looping dry reforming of methane
CLSRM	Chemical looping steam reforming of methane
CLR	Chemical looping reforming
DRM	Dry reforming of methane
SRM	Steam reforming of methane
GC	Gas chromatography
GHG	Greenhouse gas
MFC	Mass flow controller
MW	Microwave
Redox	Reduction and oxidation
SRM	Steam reforming of methane

Symbols

$C_{CH_{4,i}}$	CH_4 concentration in the inlet gaseous stream of the reactor (mol/m^3)
$C_{CH_{4,o}}$	CH_4 concentration in the outlet gaseous stream of the reactor (mol/m^3)
D_p	Penetration depth of the electromagnetic waves in the particle (m)
$D_{p,s}$	Penetration depth of the electromagnetic waves in the solids inventory (m)
d_p	Particle size (m)
H_{bed}	Initial height of fixed bed medium (m)

$m_{i,t}$	Initial mass of solids inventory comprised of Fe_3O_4 (gm)
$m_{i,Fe}$	Initial mass of Fe in solids inventory (gm)
$m_{i,\,Fe_3O_4}$	Initial mass of Fe_3O_4 in solids inventory (gm)
$Q_{CH_4,i}$	Volumetric flowrate of CH_4 in the inlet gaseous stream of the reactor (cm^3/min)
Q_i	Total volumetric flowrate of the inlet gaseous stream (cm^3/min)
$Q_{net,r}$	Required net energy to operate reducer reactor (W)
$Q_{net,o}$	Net energy released from oxidizer reactor (W)
T_b	Bulk temperature (°C)
$T_{b,l}$	Bulk temperature at height of $0.1H_{bed}$ above the gas distributor plate (°C)
$T_{b,m}$	Bulk temperature at height of $0.5H_{bed}$ above the gas distributor plate (°C)
$T_{b,u}$	Bulk temperature at height of $0.9H_{bed}$ above the gas distributor plate (°C)
$\tan(\delta)$	Dielectric loss tangent (-)
$\tan(\delta_\mu)$	Magnetic loss tangent (-)
U_g	Superficial gas velocity (m/s)
U_{mf}	Minimum fluidization velocity (m/s)
Greek letters	
ε'	Relative dielectric constant (-)
ε''	Relative dielectric loss factor (-)
ε_r	Relative permittivity (-)

Acknowledgments

The authors would like to acknowledge the Natural Sciences and Engineering Research Council of Canada (NSERC), Alliance Missions grants (Grant no. ALLPR 570793-2021), and OCP Group of Morocco for financial support of the research. Mr. Khodabandehloo is grateful to the Fonds de Recherche du Québec Nature et technologies (FRQNT) for the provided scholarship. The authors would also like to acknowledge Dr. Mohammad Latifi for his great help in operating the conventional heating-assisted reactor.

4.5 References

1. Wang, C., Y. Wang, M. Chen, D. Liang, Z. Yang, W. Cheng, Z. Tang, J. Wang and H. Zhang, Recent advances during CH4 dry reforming for syngas production: A mini review.

International Journal of Hydrogen Energy, 2021. 46(7): pp. 5852-5874, https://doi.org/10.1016/j.ijhydene.2020.10.240.

2. Kalamaras, C.M. and A.M. Efstathiou. Hydrogen production technologies: current state and future developments. in Conference papers in science. 2013. Hindawi https://doi.org/10.1155/2013/690627.
3. George, C., Carbon monoxide. Kirk-Othmer Encyclopedia of Chemical Technology, 2000.
4. Ighalo, J.O. and P.B. Amama, Recent advances in the catalysis of steam reforming of methane (SRM). International Journal of Hydrogen Energy, 2024. 51: pp. 688-700, https://doi.org/10.1016/j.ijhydene.2023.10.177.
5. Dincer, I. and C. Acar, Review and evaluation of hydrogen production methods for better sustainability. International Journal of Hydrogen Energy, 2015. 40(34): pp. 11094-11111, https://doi.org/10.1016/j.ijhydene.2014.12.035.
6. Ishaq, H., I. Dincer and C. Crawford, A review on hydrogen production and utilization: Challenges and opportunities. International Journal of Hydrogen Energy, 2022. 47(62): pp. 26238-26264, https://doi.org/10.1016/j.ijhydene.2021.11.149.
7. Dincer, I. and C. Acar, Innovation in hydrogen production. International Journal of Hydrogen Energy, 2017. 42(22): pp. 14843-14864, https://doi.org/10.1016/j.ijhydene.2017.04.107.
8. Das, S., A. Biswas, J. Bhattacharya, C.S. Tiwary and M. Paliwal, Utilization of laterite ore as an oxygen carrier in chemical looping reforming of methane for syngas production. International Journal of Hydrogen Energy, 2023. 48(51): pp. 19411-19421, https://doi.org/10.1016/j.ijhydene.2023.02.054.
9. Wang, X., S. Abanades, S. Chuayboon, J. Zhang and J. Wei, Solar-driven chemical looping reforming of methane over SrFeO3-δ-Ca0.5Mn0.5O nanocomposite foam. International Journal of Hydrogen Energy, 2022. 47(79): pp. 33664-33676, https://doi.org/10.1016/j.ijhydene.2022.07.241.
10. Hu, Z., Z. Miao, J. Wu and E. Jiang, Nickel-iron modified natural ore oxygen carriers for chemical looping steam methane reforming to produce hydrogen. International Journal of Hydrogen Energy, 2021. 46(80): pp. 39700-39718, https://doi.org/10.1016/j.ijhydene.2021.09.242.
11. Nazari, M., M. Soltanieh, A. Heydarinasab and B. Maddah, Synthesis of a new self-supported Mgy(CuxNi0.6-xMn0.4)1-yFe2O4 oxygen carrier for chemical looping steam methane reforming process. International Journal of Hydrogen Energy, 2021. 46(37): pp. 19397-19420, https://doi.org/10.1016/j.ijhydene.2021.03.081.
12. Bhosale, R., F. AlMomani and G. Takalkar, Thermodynamic analysis of solar-driven chemical looping steam methane reforming over Cr2O3/Cr redox pair. International Journal of Hydrogen Energy, 2020. 45(17): pp. 10370-10380, https://doi.org/10.1016/j.ijhydene.2019.08.205.
13. Quan, J., Y. Chen, H. Mai, Q. Zeng, J. Lv, E. Jiang and Z. Hu, Uniformly dispersed NiFeAlO4 as oxygen carrier for chemical looping steam methane reforming to produce

syngas. International Journal of Hydrogen Energy, 2024. 61: pp. 901-913, https://doi.org/10.1016/j.ijhydene.2024.02.355.

14. Bayham, S.C., A. Tong, M. Kathe and L.S. Fan, Chemical looping technology for energy and chemical production. Wiley Interdisciplinary Reviews: Energy and Environment, 2016. 5(2): pp. 216-241, https://doi.org/10.1002/wene.173.
15. Li, D., R. Xu, Z. Gu, X. Zhu, S. Qing and K. Li, Chemical-looping conversion of methane: a review. Energy Technology, 2020. 8(8): pp. 1900925, https://doi.org/10.1002/ente.201900925.
16. Ramezani, R., L. Di Felice and F. Gallucci, A review of chemical looping reforming technologies for hydrogen production: recent advances and future challenges. Journal of Physics: Energy, 2023 https://doi.org/10.1088/2515-7655/acc4e8.
17. Chein, R.-Y. and W.-H. Hsu, Thermodynamic analysis of syngas production via chemical looping dry reforming of methane. Energy, 2019. 180: pp. 535-547, https://doi.org/10.1016/j.energy.2019.05.083.
18. Mantripragada, H.C. and G. Veser, Hydrogen production via chemical looping dry reforming of methane: Process modeling and systems analysis. AIChE Journal, 2022. 68(5): pp. e17612, https://doi.org/10.1002/aic.17612.
19. García-García, F. and I.S. Metcalfe, Chemical looping dry reforming of methane using mixed oxides of iron and cerium: Operation window. Catalysis Communications, 2021. 160: pp. 106356, https://doi.org/10.1016/j.catcom.2021.106356.
20. Chen, L., Z. Qi, S. Zhang, J. Su and G.A.J.C. Somorjai, Catalytic hydrogen production from methane: A review on recent progress and prospect. 2020. 10(8): pp. 858, http://dx.doi.org/10.3390/catal10080858.
21. Zhang, X., A.C.K. Yip and S. Pang, Advances in the application of active metal-based sorbents and oxygen carriers in chemical looping biomass steam gasification for H2 production. International Journal of Hydrogen Energy, 2023. 48(28): pp. 10394-10422, https://doi.org/10.1016/j.ijhydene.2022.11.317.
22. Siriwardane, R., H. Tian and J. Fisher, Production of pure hydrogen and synthesis gas with Cu–Fe oxygen carriers using combined processes of chemical looping combustion and methane decomposition/reforming. International Journal of Hydrogen Energy, 2015. 40(4): pp. 1698-1708, https://doi.org/10.1016/j.ijhydene.2014.11.090.
23. Das, S., A. Biswas, C.S. Tiwary and M. Paliwal, Hydrogen production using chemical looping technology: A review with emphasis on H2 yield of various oxygen carriers. International Journal of Hydrogen Energy, 2022. 47(66): pp. 28322-28352, https://doi.org/10.1016/j.ijhydene.2022.06.170.
24. Siddique, I.J., A.A. Salema, E. Antunes and R. Vinu, Technical challenges in scaling up the microwave technology for biomass processing. Renewable and sustainable energy reviews, 2022. 153: pp. 111767, https://doi.org/10.1016/j.rser.2021.111767.
25. Goyal, H., T.-Y. Chen, W. Chen and D.G. Vlachos, A review of microwave-assisted process intensified multiphase reactors. Chemical Engineering Journal, 2022. 430: pp. 133183, https://doi.org/10.1016/j.cej.2021.133183.

26. Amini, A., M. Latifi and J. Chaouki, Electrification of materials processing via microwave irradiation: A review of mechanism and applications. Applied Thermal Engineering, 2021: pp. 117003, https://doi.org/10.1016/j.applthermaleng.2021.117003.
27. Chaouki, J., S. Farag, M. Attia and J. Doucet, The development of industrial (thermal) processes in the context of sustainability: The case for microwave heating. The Canadian Journal of Chemical Engineering, 2020. 98(4): pp. 832-847, https://doi.org/10.1002/cjce.23710.
28. Li, K., H. Wang and Y. Wei, Syngas generation from methane using a chemical-looping concept: a review of oxygen carriers. Journal of Chemistry, 2013. 2013 https://doi.org/10.1155/2013/294817.
29. Tian, M., C. Wang, Y. Han and X. Wang, Recent advances of oxygen carriers for chemical looping reforming of methane. ChemCatChem, 2021. 13(7): pp. 1615-1637, https://doi.org/10.1002/cctc.202001481.
30. Cheng, Z., L. Qin, J.A. Fan and L.-S. Fan, New insight into the development of oxygen carrier materials for chemical looping systems. Engineering, 2018. 4(3): pp. 343-351, https://doi.org/10.1016/j.eng.2018.05.002.
31. Luo, S., L. Zeng and L.-S. Fan, Chemical looping technology: oxygen carrier characteristics. Annual review of chemical and biomolecular engineering, 2015. 6: pp. 53-75, https://doi.org/10.1146/annurev-chembioeng-060713-040334.
32. Zhu, X., Y. Wei, H. Wang and K. Li, Ce–Fe oxygen carriers for chemical-looping steam methane reforming. International Journal of Hydrogen Energy, 2013. 38(11): pp. 4492-4501, https://doi.org/10.1016/j.ijhydene.2013.01.115.
33. Sun, J., W. Wang and Q. Yue, Review on microwave-matter interaction fundamentals and efficient microwave-associated heating strategies. Materials transactions, 2016. 9(4): pp. 231, https://doi.org/10.3390/ma9040231.
34. Lu, C., K. Li, H. Wang, X. Zhu, Y. Wei, M. Zheng and C. Zeng, Chemical looping reforming of methane using magnetite as oxygen carrier: Structure evolution and reduction kinetics. Applied Energy, 2018. 211: pp. 1-14, https://doi.org/10.1016/j.apenergy.2017.11.049.
35. Kim, Y.T., J.-J. Lee and J. Lee, Electricity-driven reactors that promote thermochemical catalytic reactions via joule and induction heating: A review. Chemical Engineering Journal, 2023: pp. 144333, https://doi.org/10.1016/j.cej.2023.144333.
36. Wang, W., G. Tuci, C. Duong-Viet, Y. Liu, A. Rossin, L. Luconi, J.-M. Nhut, L. Nguyen-Dinh, C. Pham-Huu and G. Giambastiani, Induction heating: An enabling technology for the heat management in catalytic processes. ACS Catalysis, 2019. 9(9): pp. 7921-7935, https://doi.org/10.1021/acscatal.9b02471.
37. Ke, C., T. Liu, Y. Zhang and Q. Xiong, Energy absorption performances of silicon carbide particles during microwave heating process. Chemical Engineering and Processing-Process Intensification, 2022. 172: pp. 108796, https://doi.org/10.1016/j.cep.2022.108796.

38. Hamzehlouia, S., S.A. Jaffer and J. Chaouki, Microwave heating-assisted catalytic dry reforming of methane to syngas. Scientific reports, 2018. 8(1): pp. 1-7, https://doi.org/10.1038/s41598-018-27381-6.

39. de Dios García, I., A. Stankiewicz and H. Nigar, Syngas production via microwave-assisted dry reforming of methane. Catalysis Today, 2021. 362: pp. 72-80, https://doi.org/10.1016/j.cattod.2020.04.045.

40. Zhang, M., Y. Gao, Y. Mao, W. Wang, J. Sun, Z. Song, J. Sun and X. Zhao, Enhanced dry reforming of methane by microwave-mediated confined catalysis over Ni-La/AC catalyst. Chemical Engineering Journal, 2023. 451: pp. 138616, https://doi.org/10.1016/j.cej.2022.138616.

41. Harvey, J.-P., F. Lebreux-Desilets, J. Marchand, K. Oishi, A.-F. Bouarab, C. Robelin, A.E. Gheribi and A.D. Pelton, On the application of the Factsage thermochemical software and databases in materials science and pyrometallurgy. Processes, 2020. 8(9): pp. 1156, https://doi.org/10.3390/pr8091156.

42. Nasr, S. and K.P. Plucknett, Kinetics of iron ore reduction by methane for chemical looping combustion. Energy & fuels, 2014. 28(2): pp. 1387-1395, https://doi.org/10.1021/ef402142q.

43. Su, M., J. Ma, X. Tian and H. Zhao, Reduction kinetics of hematite as oxygen carrier in chemical looping combustion. Fuel Processing Technology, 2017. 155: pp. 160-167.

44. Adavi, K., J. Shabanian and J. Chaouki, Temperature Distribution Assessment in Gas–Solid Reactive and Nonreactive Systems Heated by Microwaves. Industrial & Engineering Chemistry Research, 2023 https://doi.org/10.1021/acs.iecr.3c00575.

45. Amini, A., K.-i. Ohno, T. Maeda and K. Kunitomo, Effect of the ratio of magnetite particle size to microwave penetration depth on reduction reaction behaviour by H2. Scientific reports, 2018. 8(1): pp. 15023, https://doi.org/10.1038/s41598-018-33460-5.

46. Lide, D.R. and H. Frederikse, CRC Handbook of Chemistry and Physics 76th Eddition. New York, 1994: pp. 1195-1996.

47. Fedunik-Hofman, L., A. Bayon and S.W. Donne, Kinetics of solid-gas reactions and their application to carbonate looping systems. Energies, 2019. 12(15): pp. 2981, https://doi.org/10.3390/en12152981.

48. Go, K.S., S.R. Son and S.D. Kim, Reaction kinetics of reduction and oxidation of metal oxides for hydrogen production. International Journal of Hydrogen Energy, 2008. 33(21): pp. 5986-5995, https://doi.org/10.1016/j.ijhydene.2008.05.039.

49. Zhong, Y., Z. Wang, Z. Guo and Q. Tang, Defluidization behavior of iron powders at elevated temperature: Influence of fluidizing gas and particle adhesion. Powder technology, 2012. 230: pp. 225-231, https://doi.org/10.1016/j.powtec.2012.07.036.

CHAPTER 5 ARTICLE 2 : KINETIC STUDY OF MICROWAVE HEATING-ASSISTED CHEMICAL LOOPING DRY REFORMING OF METHANE OVER MAGNETITE

Mohammad Khodabandehloo[1, 2], Jaber Shabanian[1], Jean-Phillipe Harvey[2], Jamal Chaouki[1, †]

[1] *Process Engineering Advanced Research Lab (PEARL), Chemical Engineering Department, Polytechnique Montreal, P.O. Box 6079, Station Centre-Ville, Montreal, Quebec, H3C 3A7, Canada*

[2] *Centre for Research in Computational Thermochemistry (CRCT), Chemical Engineering Department, Polytechnique Montreal, P.O. Box 6079, Station Centre-Ville, Montreal, Quebec, H3C 3A7, Canada*

[†] Corresponding author: Tel.: +1-514-340-4711 X 4034; Fax: +1-514-340-4159.

E-mail addresses: mohammad.khodabandehloo@polymtl.ca (M. Khodabandehloo), jaber.shabanian@polymtl.ca (J. Shabanian), jean-philippe.harvey@polymtl.ca (J.-P. Harvey), jamal.chaouki@polymtl.ca (J. Chaouki)

(Submitted to International Journal of Hydrogen Energy on July 25, 2024)

Abstract

Dry reforming of methane carried out via the chemical looping concept and employing microwave heating is a sustainable syngas (a mixture comprising hydrogen and carbon monoxide) production technology. Understanding the intrinsic reaction kinetics of reduction and oxidation is essential for successful scale-up of this technology. By employing magnetite as a microwave absorber oxygen carrier, we investigated the reaction kinetics at bulk temperatures in the range of 650 to 800°C for reduction and 500 to 650°C for oxidation. Results indicated both reactions followed a phase-boundary controlled (contracting sphere) reaction mechanism. Upon developing the reaction kinetics based on solid temperature relevant to microwave-heated particles, we estimated the activation energy to be 85 kJ/mol for the reduction reaction and 22 kJ/mol for the oxidation reaction. By developing the reaction kinetic of the reduction under microwave heating and based on bulk temperature, we estimated 68 kJ/mol as the activation energy of the reduction reaction. Comparing these values with the activation energy of magnetite reduction by methane under

conventional heating (around 90 kJ/mol) indicated that microwave irradiation apparently decreased the activation energy. Consequently, by developing the reaction kinetics based on an appropriate temperature, i.e., solid temperature, we demonstrated that microwaves primarily had a thermal effect in our study, increasing the reaction rate constant, rather than a non-thermal effect, like altering the activation energy.

Keywords: Chemical reaction kinetics; Dry reforming of methane through microwave-heated chemical looping; Hydrogen; Syngas; Greenhouse gases utilization.

5.1 Introduction

Hydrogen (H_2) separation from syngas, which is comprised of carbon monoxide (CO) and H_2, is the primary H_2 production method. Syngas also serves as a key chemical intermediate in synthesizing many compounds, including methanol and ethanol. Hence, the development of a syngas production technology that consumes greenhouse gases (GHGs), particularly methane (CH_4) and carbon dioxide (CO_2), presents a sustainable pathway to produce syngas, while mitigating/decreasing GHGs emissions [1-3]. Many researchers studied catalytic DRM (R-5.1) [4, 5], a GHGs utilization technology, for syngas generation. DRM stands for dry reforming of CH_4. However, a high reaction temperature (typically ranging from 800 to 950°C), the possibility of formation and deposition of carbon, and the H_2 selectivity loss due to the reverse water-gas shift reaction, presented in (R-5.2), are crucial scale-up challenges of the catalytic DRM [2, 4-8].

$$\mathrm{CH_4 + CO_2 \leftrightarrow 2H_2 + 2CO} \qquad \Delta \mathrm{H}_{298} = 247\ \frac{\mathrm{kJ}}{\mathrm{mol}} \qquad \text{(R-5.1)}$$

$$\mathrm{H_2 + CO_2 \leftrightarrow H_2O + CO} \qquad \Delta \mathrm{H}_{298} = 41\ \frac{\mathrm{kJ}}{\mathrm{mol}} \qquad \text{(R-5.2)}$$

As shown in Figure 5.1, unlike the catalytic DRM that adopts CO_2 (gaseous oxidant), the chemical looping DRM (CL-DRM) adapts an oxygen carrier (M_xO_y) as a solid particle to separately carry out the reduction and oxidation (redox) reactions. By employing CH_4, the compound M_xO_y is reduced (R-5.3) within the reducer (fuel) reactor of the CL-DRM, resulting in the production of syngas and preventing the formation of carbon. Subsequently, as presented in (R-5.4), in a separate oxidizer reactor, by consuming CO_2, M_xO_{y-1} is re-oxidized to M_xO_y [9-17]. M_xO_{y-1} represents the oxygen carrier that is reduced by CH_4.

$$CH_4 + M_xO_y \leftrightarrow M_xO_{y-1} + 2H_2 + CO \qquad \text{(R-5.3)}$$

$$CO_2 + M_xO_{y-1} \leftrightarrow M_xO_y + CO \qquad \text{(R-5.4)}$$

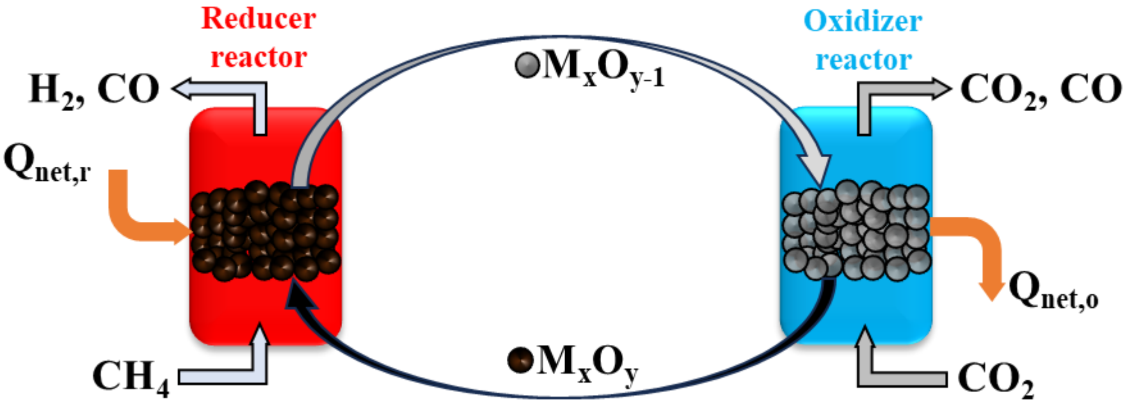

Figure 5.1. A schematic diagram illustrating CL-DRM.

Although the CL-DRM offers several benefits in comparison with the catalytic DRM, CH_4 decomposition due to a high gas phase temperature (typically above 800°C), which leads to undesired carbon deposition on solid particles, is still a critical scale-up challenge of this syngas production technology. One can employ a conventional heating method (CHM) to achieve a thermal balance within the bed inventory of a gas-solid medium, i.e., gas and solid temperatures are in equilibrium with the bulk temperature T_b. Compared to the CHM, the selective-heating of the irradiated microwave (MW) can establish a thermal gradient within the bed inventory of a gas-solid medium, i.e., solid temperature T_s is higher than the gas temperature T_g [7, 18-21]. In a recent study by the group [22], by employing magnetite (Fe_3O_4), which is a MW absorber oxygen carrier, we developed a MW heating-assisted CL-DRM (MWCL-DRM) and illustrated that the established temperature difference between the particles and the gas phase caused by the microwave heating (MWH) method is capable of increasing process productivity. In comparison with the CL-DRM heated conventionally, for the same reactor's geometry, and by applying the same operating condition, i.e., same T_b = 800°C, duration of heating, and inlet flow of gas, the MWCL-DRM increased the reduction conversion by a factor of 2.5 and oxidation conversion by a factor of 1.5. In addition, unlike the CL-DRM heated conventionally, the MWCL-DRM suppressed carbon formation and deposition.

The successful scale-up of the MWCL-DRM technology requires a proper design, performance evaluation, and operation of its reactor(s). To achieve this and accurately simulate pilot- and industrial-scale MWCL-DRM reactor(s), we need to first investigate and develop the kinetics of redox reactions for Fe_3O_4 (oxygen carrier in this study). We comprehensively studied oxygen carrying capacity and MWH performance of Fe_3O_4 in a laboratory-scale MWH-assisted setup [22]. The objective of this research is to investigate its redox reaction kinetics under the MWH method. We discussed the adopted strategy for the development of reaction kinetics in Section 5.2. We described the experimental methodology, including material preparation, and experimental setup and procedure in Section 5.3. Upon discussing the effects of internal and external mass transfers on redox performance in Section 5.4.1 to identify conditions with their minimal effects and obtaining intrinsic reaction kinetics, we determined intrinsic redox reaction kinetics of the MW heated Fe_3O_4 oxygen carrier in Section 5.4.2. We evaluated the performance of the developed redox reaction kinetics in Section 5.4.3.

5.2 Kinetic model

The conversion of a solid sample α could be calculated to study the reaction progress between the gas phase and the solid particles [23-32]. For the gas-solid reactions (non-catalytic in this study), one can define α as:

$$\alpha = \frac{m_i - m_f}{m_i - m_\infty} \tag{5.1}$$

where m_i and m_f represent the masses of the initial and final solid samples, respectively. m_∞ is the ultimate solid sample mass upon a complete reduction ($Fe_3O_4 \rightarrow$ iron (Fe)) or a complete oxidation ($Fe \rightarrow Fe_3O_4$ in this study), respectively. By assuming a complete reduction of Fe_3O_4 by CH_4, $m_\infty = 0.72m_i$ must be achieved. In addition, for a complete oxidation of Fe to Fe_3O_4, $m_\infty = 1.38m_i$ must be achieved. Accordingly, we applied Eqs. (5.2) and (5.3) to calculate reduction conversion α_r and oxidation conversion α_o, respectively.

$$\alpha_r = \frac{m_i - m_f}{0.28m_i} \tag{5.2}$$

$$\alpha_o = \frac{m_f - m_i}{0.38m_i} \tag{5.3}$$

By employing XRD and GC analysis for solid and gas phases, we demonstrated the capability of MW due to its selective-heating in enhancing the Fe_3O_4 reduction to Fe by CH_4 (R-5.5) and Fe oxidation to Fe_3O_4 by CO_2 (R-5.6) [22]. We provided supplementary calculations, referring to Section S-1 (Section 5.7.1) in the provided Supplementary Material, to confirm that the fractional conversions presented in Eqs. (2) and (3) are equivalent to the corresponding molar conversions.

$$4CH_{4\,(g)} + Fe_3O_{4\,(s)} \rightarrow 3Fe_{\,(s)} + 8H_{2\,(g)} + 4CO_{(g)} \tag{R-5.5}$$

$$4CO_{2\,(g)} + 3Fe_{\,(s)} \rightarrow 4CO_{(g)} + Fe_3O_{4\,(s)} \tag{R-5.6}$$

To determine the kinetics of redox reactions, one can employ a general kinetic model (Eq. (5.4)) [23-32].

$$\frac{d\alpha}{dt} = k.f(\alpha) \tag{5.4}$$

where k in Eq. (5.4) stands for the reaction rate constant, which depends on the reaction temperature T_{rx} and activation energy E_a, as described in Eq. (5.5). We adapted $f(\alpha)$ to represent the differential form of the kinetic model, describing mechanism of reaction. By employing the Arrhenius equation (Eq. (5.5)), Eq. (5.4) is modified to Eq. (5.6).

$$k = A \exp\left(-\frac{E_a}{RT_{rx}}\right) \tag{5.5}$$

$$\frac{d\alpha}{dt} = A \exp\left(-\frac{E_a}{RT_{rx}}\right).f(\alpha) \tag{5.6}$$

where R stands for the universal gas constant. In addition, we employed A to represent the pre-exponential factor. Regarding the MW's selective-heating that yields a higher T_s than T_g, we adopted T_s as the T_{rx} in reaction kinetic expressions (Eqs. (5.4) to (5.18)). By employing the model fitting method, one can analyze the reaction kinetic (Eq. (5.6)) with respect to different reaction mechanisms (Table 5.1), represented in different forms for $f(\alpha)$. In addition, by substituting $f(\alpha)$ with $g(\alpha)$, Eqs. (5.4) and (5.6) can be rearranged to analyze the integration form of the reaction kinetics, resulting in Eqs. (5.7) and (5.8).

$$g(\alpha) = \int_0^{\alpha} \frac{d\alpha}{f(\alpha)} = A \int_0^{t} \exp\left(-\frac{E_a}{RT_{rx}}\right) dt \tag{5.7}$$

$$g(\alpha) = k.t_f \tag{5.8}$$

where t_f represent the final reaction time. We reported principal reaction mechanisms with corresponding forms of $f(\alpha)$ or $g(\alpha)$ employed in the literature to develop reaction kinetics for non-catalytic gas-solid reactions in Table 5.1. We applied the graphical method presented in Eq. (5.9) , which was established by Hancock and Sharp [33], to choose the best fitted reaction mechanism based on the model fitting method.

$$\ln\big(-\ln(1-\alpha)\big) = \ln(\beta) + n\ln(t) \tag{5.9}$$

In this equation, n, i.e., the slope of the plot, and β, i.e., the intersection of the plot with the vertical axis, are constants of Eq. (5.9). By employing Eq. (5.9), we can identify the mechanism of the reaction upon generating $\ln\big(-\ln(1-\alpha)\big)$ versus $\ln(t)$ by the available experimental data and determining n. For n < 1, the diffusion mechanism is dominant. For 1 < n < 2, the phase-boundary sphere/cylinder controlled reaction mechanism can be employed. The growth of nuclei mechanism is the principal reaction mechanism when n > 2.

Table 5.1. Principal reaction mechanisms employed for non-catalytic gas-solid reactions [23-32].

Reaction mechanism	$\boldsymbol{f(\alpha)}$	$\boldsymbol{g(\alpha)}$	*Eq.*
Geometrical mechanism			
Phase-boundary sphere controlled	$3(1\text{-}\alpha)^{\frac{2}{3}}$	$1 - (1\text{-}\alpha)^{\frac{1}{3}}$	(5.10)
Phase-boundary cylinder controlled	$2\sqrt{1\text{-}\alpha}$	$1 - \sqrt{1\text{-}\alpha}$	(5.11)
Diffusion mechanism			
One-dimensional	$\frac{1}{2}\alpha$	α^2	(5.12)
Two-dimensional	$-\frac{1}{\ln(1\text{-}\alpha)}$	$(1\text{-}\alpha)\ln(1\text{-}\alpha)+\alpha$	(5.13)
Three-dimensional	$-\frac{3(1\text{-}\alpha)^{2/3}}{2[1\text{-}(1\text{-}\alpha)^{1/3}]}$	$\left[1\text{-}(1\text{-}\alpha)^{1/3}\right]^2$	(5.14)
Power law mechanism	$2\sqrt{\alpha}$	$\sqrt{\alpha}$	(5.15)
Avrami-Erofeev (nucleation) mechanism			
2D growth of nuclei	$2(1\text{-}\alpha)\sqrt{\text{-}\ln(1\text{-}\alpha)}$	$\sqrt{\text{-}\ln(1\text{-}\alpha)}$	(5.16)
3D growth of nuclei	$3(1\text{-}\alpha)\sqrt[3]{(-\ln(1-\alpha))^2}$	$\sqrt[3]{(-\ln(1-\alpha))^2}$	(5.17)

In addition to selecting an appropriate reaction mechanism based on the Hancock and Sharp method, we generated parity plots, e.g., Figure S.3 of the Supplementary Material, to ensure that the chosen reaction mechanism accurately aligns with the experimentally measured data. We also employed the model free method (Eq. (5.18)) to estimate E_a. In this method, one needs to generate dα/dt versus 1/T from the experimental data. Subsequently, we compared the estimated E_a from the model fitting (Eq. (5.8)) method with the one obtained from the model free (Eq. (5.18)) method to cross-check the accuracy of the developed reaction kinetic.

$$\ln\left(\frac{d\alpha}{dt}\right) = \ln\big(k.f(\alpha)\big) - \frac{E_a}{RT_{rx}} \tag{5.18}$$

5.3 Experimental

5.3.1 Material preparation and characterization

We adopted Fe_3O_4 powder with d_p of 10 µm and less than 3 wt.% impurity, supplied from Thermo Fisher Scientific. d_p is average particle size. We comprehensively tested the MW absorption capability and oxygen-carrying capacity, phase compositions, and morphology of the Fe_3O_4 oxygen carrier in a previous study by the group [22]. We adopted CH_4 and CO_2 cylinders with purity of 99.92% and supplied from Canadian Air Liquid to conduct redox reactions in this study. We also employed a nitrogen (N_2) cylinder with purity of 99.99%, supplied from Canadian Air Liquid, to provide N_2-CH_4 and N_2-CO_2 mixtures.

5.3.2 Experimental setup

We performed experiments of this study in a laboratory-scale fixed bed reactor heated by MW irradiation, depicted in Figure 5.2. In addition to providing a uniform heating (MW dissipation) [22], the fixed bed medium minimized the effect of external mass transfer limitations (Section 5.4.1).

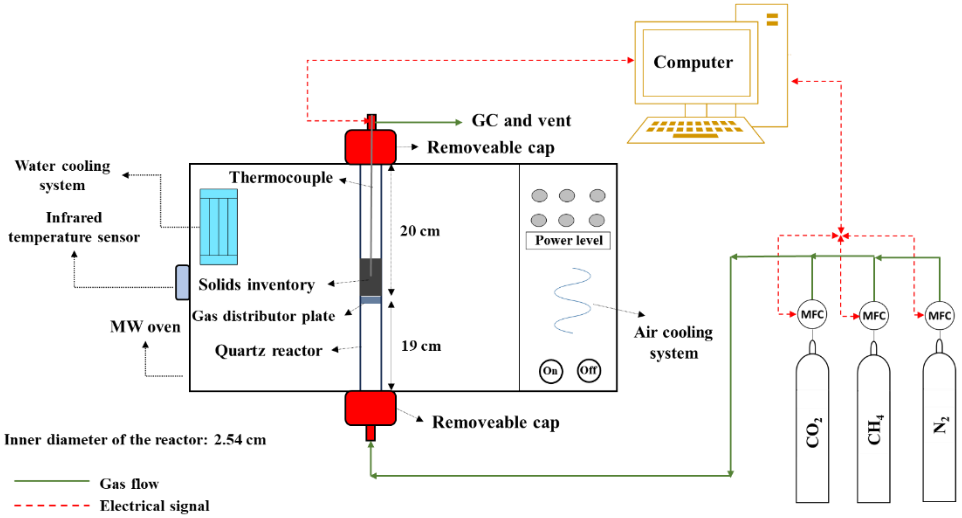

Figure 5.2. The implemented MWCL-DRM in a lab-scale.

As shown in Figure 5.2, the main components of the setup are: (i) a laboratory-scale MW oven (MW frequency of 2.45 GHz and the MW power in the range of 100 to 1100 W), (ii) a quartz reactor with the geometry highlighted in Figure 5.2, (iii) a Lab-View application to monitor T_b, while adjusting the inlet gaseous flowrate and its composition, (iv) a grounded type K thermocouple with the probe diameter of 1/8 inch and made of stainless steel 316 to measure T_b, (v) an infrared temperature sensor (model: CTM- 3SF75H2-C3, temperature Range: 200-1200°C) to measure T_s, (vi) mass flow controllers (MFCs) for CH_4, CO_2, and N_2 gases with the inlet gaseous flowrates in the range of, respectively, 0 - 0.8 l/min, 0 - 0.8 l/min, and 0 - 3 l/min, and (vii) N_2,

CO_2, and CH_4 cylinders with the specifications highlighted in Section 5.3.1. As shown in Figure 5.2, we also employed water- and air-cooling systems to avoid MW accumulation inside the MW oven and overheating of the MW generator, respectively.

5.3.3 Experimental procedure

We conducted redox reactions for a bed inventory m_i of 5 gm of the Fe_3O_4 oxygen carrier. To measure T_b, we installed the thermocouple's tip at $0.5H_{bed,i}$. $H_{bed,i}$ represents the bed inventory's initial height. We detailed the MWH performance and T_b measurement of non-reactive and reactive environments in our previous study [22]. To conduct the redox reactions, we initially reduced Fe_3O_4 particles under the MWH for 120 s by a N_2-CH_4 mixtures and at T_b= 800°C. We accomplished the oxidation reactions after reaching α_r of 0.28. Therefore, we assumed that the initial solids inventory employed to accomplish the oxidation reaction was comprised of a Fe-Fe_3O_4 mixture with 28 wt.% Fe. Prior to accomplishing the redox reactions, we solely injected N_2 with an inlet N_2 flowrate Q_{i,N_2} of 2.7 l/min for 5 min. Following the gas leakage tests, we irradiated the reactor with MWs. Upon reaching the target T_b, at which we measured α_r, we switched the inlet gaseous stream to N_2-CH_4 mixture for reduction reaction. After accomplishing the reduction reaction, we stopped the MW irradiations and switched the inlet gaseous stream to 100 vol.% N_2 with an inlet N_2 flowrate Q_{i,N_2} of 2.7 l/min for 5 min. Subsequently, under sole N_2 injection, we irradiated the reactor with MWs to reach to the target T_b at which α_o was measured. Upon reaching the target T_b, at which we measured α_o, we switched the inlet gaseous stream to N_2-CO_2 mixture for the oxidation reaction. During the redox reactions, we maintained the total inlet gaseous flowrate Q_i at 2.7 l/min. Upon halting MW irradiations, we switched the inlet gaseous stream to only N_2, while maintaining a Q_i of 2.7 l/min.

5.4 Results and discussion

5.4.1 Mass transfer limitations

Gas-solid reactions, including non-catalytic redox reactions, can involve several steps, which are [28, 29, 34-36]: (i) external mass transfer, which involves the species transfer from the gas bulk to the particle's external surface, (ii) internal mass transfer/diffusion of gaseous species within the solid particles, (iii) chemical reactions between the gaseous species and solid reactants, (iv) the gaseous products outward diffusion from the internal pores of the particle towards its external surface, and (v) the gaseous products transfer from the particle's external surface to the gas bulk. To determine intrinsic rates of redox reactions, i.e., the chemical reactions determine the mechanism of redox reactions, the effects of external and internal mass transfers must be minimized.

External mass transfer can control the rate of reaction when external mass transfer resistance dominates the chemical reaction resistance. Based on various experimental investigations [23, 24, 26, 28, 29, 34, 37-42], a relatively high gas flowrate (typically, a gas flowrate to solid ratio above 50 ml/(g.min)) minimized the impact of external mass transfer during the redox reactions of the CLR of CH_4. Referring to Section S-2 (Section 5.7.2) in the provided Supplementary Material, by selecting $\mathrm{Q_{i,CH_4}/m_i}$ and $\mathrm{Q_{i,CO_2}/m_i}$ = 137 ml/(min.gm), i.e., superficial gas velocity $\mathrm{U_g}$ of 2.25 cm/s for the reactor geometry and tested conditions of the current study, we minimized the effect of external mass transfer on developing intrinsic redox reactions kinetics. $\mathrm{Q_{i,CH_4}}$ and $\mathrm{Q_{i,CO_2,}}$ represent the inlet gaseous flowrates of CH_4 and CO_2, respectively.

For a selected and/or synthesized oxygen carrier, different studies have identified $\mathrm{d_p}$ as the principal factor in minimizing the internal mass transfer limitation [26, 38-40, 42]. Referring to Section S-2 (Section 5.7.2) in the provided Supplementary Material, the selected Fe_3O_4 oxygen carrier with a $\mathrm{d_p}$ of 10 µm was capable of effectively minimizing the impact of the internal mass transfer. Accordingly, by adjusting the operating conditions and $\mathrm{d_p}$, we could ascertain that chemical reactions controlled the kinetic studies accomplished in this work.

5.4.2 Reduction and oxidation kinetic models

We investigated the effects of $\mathrm{T_b}$ as well as reduction reaction time $\mathrm{t_r}$ and oxidation reaction time $\mathrm{t_o}$ on $\mathrm{\alpha_r}$ (Figure 5.3a) and $\mathrm{\alpha_o}$ (Figure 5.4a). To predict the best fitted kinetic models based on $\mathrm{T_s}$, i.e., $\mathrm{T_{rx} = T_s}$, for the reduction and oxidation reactions, respectively, at $\mathrm{T_b}$ in the range of 650 - 800°C and 500 - 650°C, we plotted $\mathrm{ln\big(-ln(1-\alpha)\big)}$ versus $\mathrm{ln(t)}$ in Figure 5.3b and Figure 5.4b. $\mathrm{\Delta T_{sb} = T_s - T_b}$ represents the difference between solid and bulk temperatures.

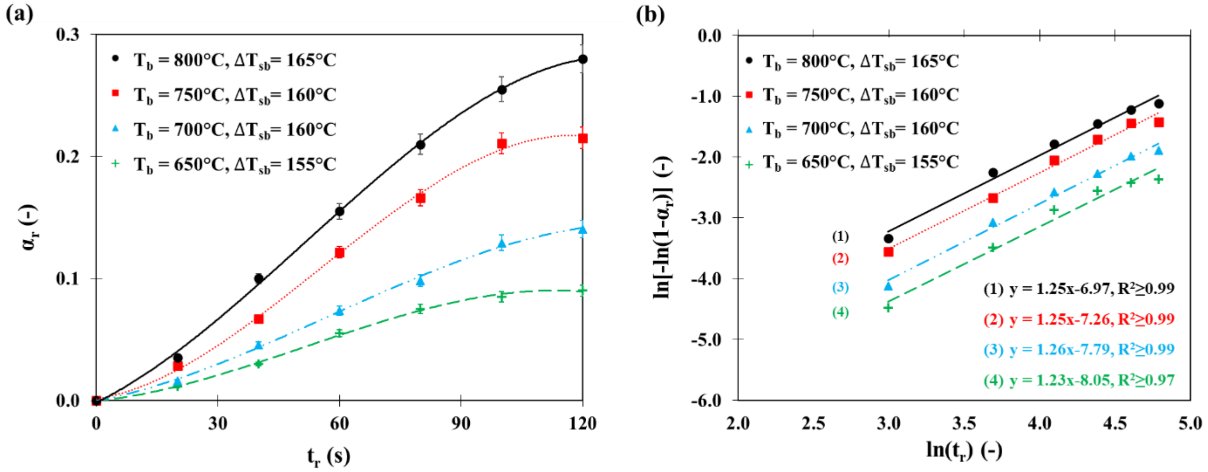

Figure 5.3. a) Effects of t_r and T_b on α_r and b) Hancock and Sharp plots at different T_b. U_g, m_i, and inlet gas stream were respectively applied at 9 cm/s, 5 gm, and 25 vol.% CH_4 for the mixture of N_2-CH_4. The solids inventories initially contained 100 wt.% Fe_3O_4.

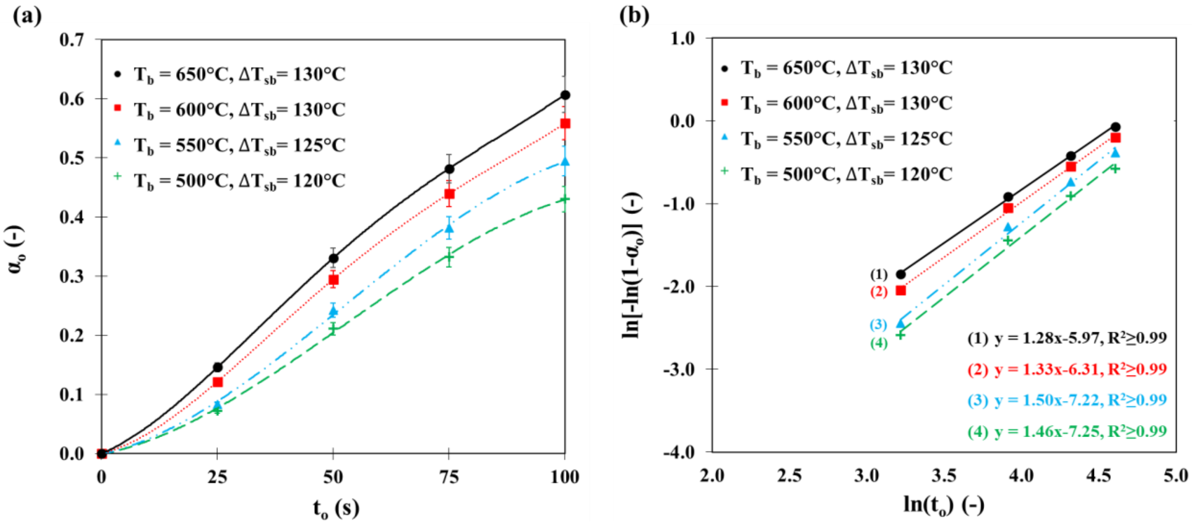

Figure 5.4. a) Effects of t_o and T_b on α_o and b) Hancock and Sharp plots at different T_b. U_g, m_i, and inlet gas stream were respectively applied at 9 cm/s, 5 gm, and 25 vol.% CO_2 for the mixture of N_2-CO_2. The solids inventories initially contained a Fe-Fe_3O_4 mixture with 28 wt.% Fe.

As shown in Figure 5.3b, we achieved an average value of 1.25 (ranging from 1.23 to 1.26) for n for the reduction reaction. We reached an average value of 1.39 (ranging from 1.28 to 1.50) for n for the oxidation reaction (Figure 5.4b). Hence, the redox reactions were controlled by the phase-boundary sphere controlled reaction mechanisms, Eq. (5.10). Applying the integration form of the kinetic analysis, Eq. (5.8), we generated Arrhenius plots of redox reactions and presented them in Figure 5.5.

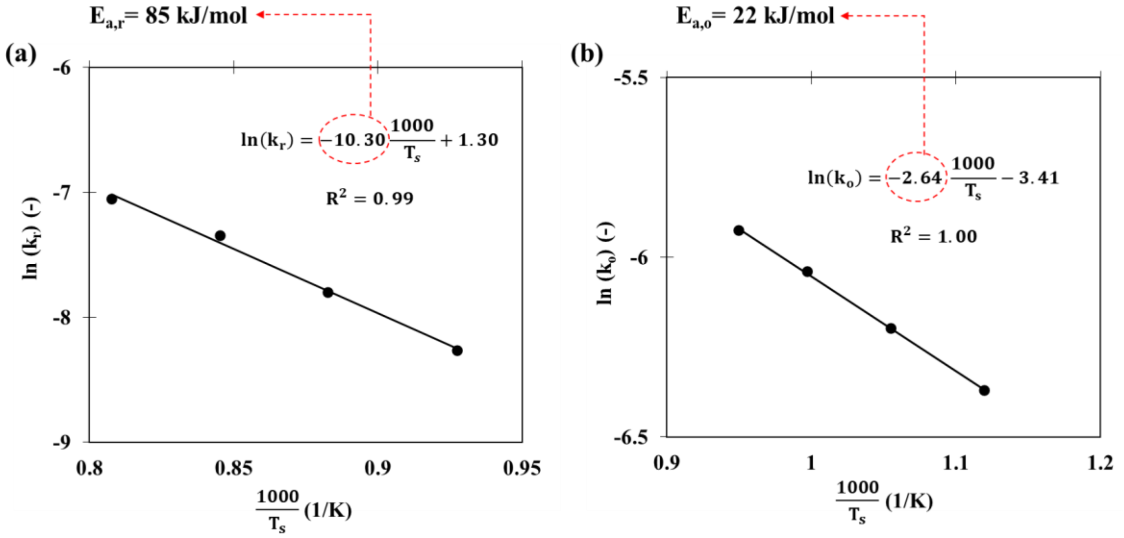

Figure 5.5. Arrhenius plots of a) the Fe_3O_4 oxygen carrier reduction reaction based on the phase-boundary sphere controlled reaction mechanism (N_2-CH_4 mixture with 25 vol.% CH_4 was employed) and b) Fe oxidation reaction based on the phase-boundary sphere controlled reaction mechanism (N_2-CO_2 mixture with 25 vol.% CO_2 was employed). U_g and m_i were fixed at 9 cm/s and 5 gm, respectively.

As shown in Figure 5.5, the phase-boundary sphere controlled kinetic model was well fitted ($R^2 \geq 0.99$) to the experimental data, which agrees with the obtained n values by Hancock and Sharp method. $E_{a,r}$ and $E_{a,o}$ in Figure 5.5 respectively represent the activation energies of the redox reactions, respectively. According to the data presented in Figure 5.5, $E_{a,r}$ and $E_{a,o}$ were estimated as 85 and 22 kJ/mol, respectively. We compared the estimated $E_{a,r}$ under MWH conditions with other experimental investigations accomplished under the CHM, Figure 5.6a. As shown in this figure, by developing the reaction kinetics based on $T_{rx} = T_s$, we obtained $E_{a,r}$ under the MWH that closely align with the reported $E_{a,r}$ values in the literature [43] for the reduction reactions heated conventionally. In addition, to investigate the impact of the MW's selective-heating on reactions, we developed two sets of reduction reaction kinetics for T_{rx} equals T_b and T_s. We presented the corresponding $E_{a,r}$ values in Figure 5.6b. As shown in this figure, the reduction reaction kinetic based on $T_{rx} = T_b$ and $T_{rx} = T_s$ resulted in $E_{a,r}$ of 68 and 85 kJ/mol, respectively. Comparing these values with $E_{a,r}$ under CHM (around 90 kJ/mol) indicated that the MWH method can enhance k, i.e., an apparent decrease in E_a. Consequently, our study illustrated that by establishing reaction kinetics at the appropriate temperature ($T_{rx} = T_s$), MWs predominantly exerted a thermal influence, increasing k, rather than a non-thermal influence, like changing E_a. Adavi et al. [44] detailed further information related to the non-thermal and thermal impacts of MWs on chemical reactions.

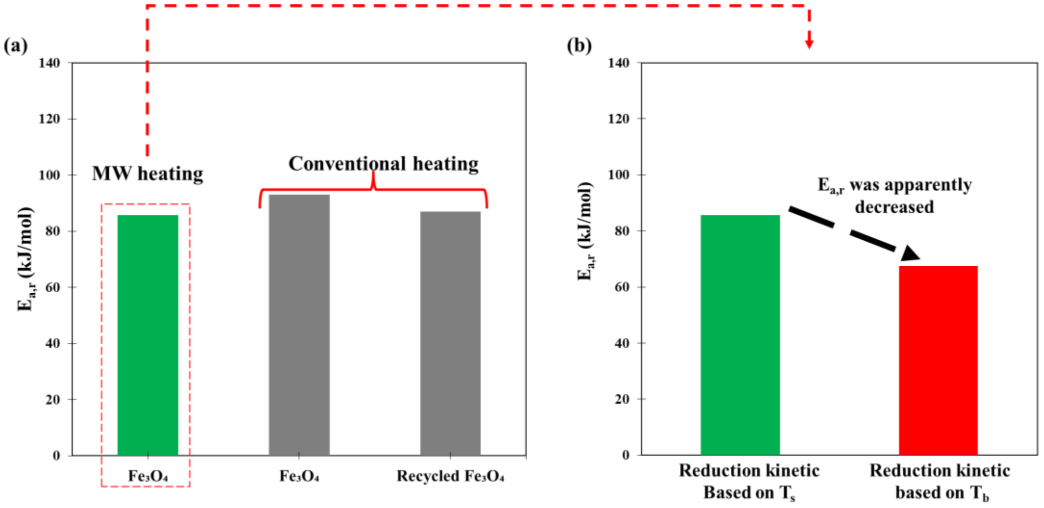

Figure 5.6. a) Impact of MWH and CH [43] methods on $E_{a,r}$ (we determined $E_{a,r}$ for the current study under MW irradiation based on T_s, i.e., we developed the reduction reaction kinetic under MW irradiation assuming $T_{rx} = T_s$), and b) determination of $E_{a,r}$ under MW irradiation based on T_s and T_b, i.e., we determined $E_{a,r}$ under MW irradiation based on $T_{rx} = T_s$ and $T_{rx} = T_b$.

The developed intrinsic redox reaction kinetics for the MWCL-DRM over Fe_3O_4 according to the appropriate reaction temperature, i.e., $T_{rx} = T_s$, are summarized in Table 5.2.

Table 5.2. Intrinsic redox kinetics of MWCL-DRM over Fe_3O_4 based on T_s.

Reaction	***Kinetic expression***	***$E_{a,r}$ and $E_{a,o}$ (kJ/mol)***	***A (1/s)***	***$f(\alpha)$***
Reduction of Fe_3O_4 by CH_4 under the MWH method	$\frac{d\alpha_r}{dt} = A\exp\left(-\frac{E_{a,r}}{RT_s}\right).f(\alpha_r)$	85	3.67	$3(1\text{-}\alpha_r)^{2/3}$
Oxidation of Fe by CO_2 under the MWH method	$\frac{d\alpha_o}{dt} = A\exp\left(-\frac{E_{a,o}}{RT_s}\right).f(\alpha_o)$	22	0.03	$3(1\text{-}\alpha_o)^{2/3}$

5.4.3 Model performance

To assess the accuracy of the developed reaction kinetics obtained through the model fitting method for the MWCL-DRM, we adopted the model free method. We, hence, generated Figure 5.7 based on the experimental data (originally presented in Figure 5.3a Figure 5.4a). We observed minor differences between the estimated E_a from the phase-boundary sphere controlled reaction mechanisms ($E_{a,r}$ = 85 kJ/mol and $E_{a,o}$ = 22 kJ/mol in Figure 5.5) and those from the model free method ($E_{a,r}$ = 90 kJ/mol and $E_{a,o}$ = 18 kJ/mol in Figure 5.7). This confirmed the accuracy of the phase-boundary sphere controlled reaction mechanism to predict the redox reaction kinetics for the MWCL-DRM over the chosen oxygen carrier (Fe_3O_4) based on the appropriate temperature, i.e., $T_{rx} = T_s$. We also developed parity plots of the reduction reactions kinetics based on geometrical, diffusion, power law, and Avrami-Erofeev reaction mechanisms (referring to Section S-3 (Section 5.7.3) in the provided Supplementary Material). All the developed reduction reaction kinetics highlighted the disparity (up to 57% of relative difference) between the estimated α_r and the experimentally measured data, except for the phase-boundary sphere controlled reaction mechanism. This further demonstrates that the developed redox reaction kinetics based on the phase-boundary sphere controlled mechanism (Figure 5.5) is the best representative for the redox reaction kinetics for the MWCL-DRM over Fe_3O_4.

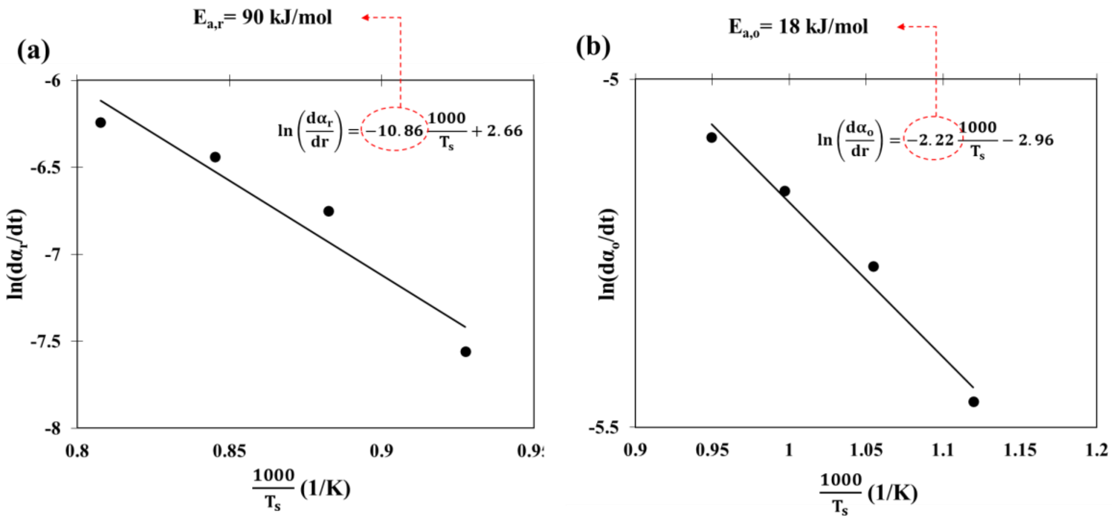

Figure 5.7. Estimation of a) $E_{a,r}$ and b) $E_{a,o}$ under MW irradiation employing the model free method based on $T_{rx} = T_s$.

5.5 Conclusion

This research studied the kinetics of redox reactions for the MWCL-DRM over Fe_3O_4 oxygen carrier. We performed the tests for T_b ranging from 650 to 800°C and 500 to 650°C for redox reactions, respectively. By adjusting operating conditions and d_p, we minimized the internal as well as the external mass transfer resistances and ascertained that the chemical reaction was the rate controlling step. Based on the Hancock and Sharp method, we achieved average values of 1.25 and 1.39 for n for reduction and oxidation reactions, respectively, indicating that these reactions were controlled by the phase-boundary sphere controlled reaction mechanisms. When employing the model fitting method to develop the reaction kinetics, we ensured that the phase-boundary sphere controlled reaction mechanisms performed the best among the analyzed models. We further cross-checked the accuracy of the developed reaction kinetic with that obtained by the model free kinetic estimation method. By developing the reaction kinetics based on T_s as T_{rx}, we estimated $E_{a,r}$ and $E_{a,o}$ of 85 and 22 kJ/mol, respectively.

To investigate the impact of MW's selective-heating on redox reactions, we developed two sets of reduction reaction kinetics for T_{rx} equals T_b and T_s. The reduction reaction kinetic based on $T_{rx} = T_b$ and $T_{rx} = T_s$ resulted in $E_{a,r}$ of 68 and 85 kJ/mol, respectively. Comparing these values with $E_{a,r}$ under CHM (around 90 kJ/mol) indicated that the MWH method can enhance k, i.e., an apparent decrease in E_a. Accordingly, we established the kinetics of redox reactions based on the appropriate temperature ($T_{rx} = T_s$). Our study demonstrated that MWs mainly had a thermal effect, increasing k, rather than a non-thermal effect, like altering E_a.

The obtained intrinsic kinetics of redox reactions in this study are crucial for comprehensive redox reactors modeling, large-scale process design and simulation, and techno-economic and life cycle analysis of the MWCL-DRM. They help address scale-up uncertainties of the MWCL-DRM for large-scale H_2 and syngas production and improve the performance of this technology.

CRediT authorship contribution statement

Mohammad Khodabandehloo: Conceptualization, Investigation, Formal analysis, Methodology, Writing - Original draft, Validation, Software, Data curation, Visualization.

Jaber Shabanian: Co-supervision, Methodology, Project administration, Writing - review & editing.

Jean-Phillipe Harvey: Co-supervision, Methodology, Project administration, Writing – review & editing.

Jamal Chaouki: Supervision, Conceptualization, Resources, Funding acquisition, Writing - review & editing.

Nomenclature

Acronym

CHM	Conventional heating method
CL-DRM	Chemical looping-dry reforming of methane
CLR	Chemical looping reforming
DRM	Dry reforming of methane
GHG	Greenhouse gas
MW	Microwave
MWCL-DRM	Microwave heating-assisted chemical looping dry reforming of methane
MWH	Microwave heating
Redox	Reduction and oxidation

Symbols

A	Pre-exponential factor (1/s)
D_e	Effective diffusivity (m_2/s)
E_a	Activation energy (J/mol)
$E_{a,o}$	Oxidation reaction's activation energy of (J/mol)
$E_{a,r}$	Reduction reaction's activation energy of (J/mol)
$H_{bed,i}$	Initial height of the fixed bed (m)
k	Reaction rate constant (1/s)
k_o	Reaction rate constant of oxidation reaction (1/s)
k_r	Reaction rate constant of reduction reaction (1/s)
m_i	Initial mass of the solid sample (gm)
m_f	Final mass of the solid sample (gm)
m_∞	Ultimate mass of the solid sample (gm)
P_{CH_4}	Partial pressure of CH_4 (bar)

Q_i	Total inlet gaseous flowrate (l/min)
Q_{i,N_2}	Inlet N_2 flowrate (l/min)
Q_{i,CH_4}	Inlet gaseous flowrates of CH_4 (l/min)
q_{i,CH_4}	Volumetric concentration of CH_4 in the inlet gas flow (vol.%)
Q_{i,CO_2}	Inlet gaseous flowrate of CO_2 (l/min)
q_{i,CO_2}	Volumetric concentration of CO_2 in the inlet gas flow (vol.%)
t	Time (s)
T_b	Bulk temperature (°C)
t_f	Final reaction time (s)
t_o	Oxidation reaction time (s)
t_r	Reduction reaction time (s)
T_{rx}	Reaction temperature (°C)
T_s	Solid temperature (°C)
U_g	Superficial gas velocity (m/s)

Greek letters

α	Conversion of solid sample (-)
α_o	Oxidation conversion (-)
α_r	Reduction conversion (-)
$\alpha_{r,max}$	Maximum reduction conversion of the solid sample (-)
ρ_p	Particle density (kg/m^3)

Acknowledgments

The scholarship support from the Fonds de Recherche du Québec - Nature et Technologies (FRQNT) is deeply appreciated by Mr. Khodabandehloo. Financial support for this research was also provided by the OCP Group of Morocco and Natural Sciences and Engineering Research Council of Canada (NSERC), in particular through the Alliance Missions grants (Grant no. ALLPR 570793-2021). The authors would like to extend their gratitude to both organizations. In addition, the authors extend their thanks to Drs. Adrián Carrillo Garcia and Ahmadreza Amini for their assistance in choosing the most suitable model comparison. The authors would like to thank Mr. Santini Pace and Mr. Mario Grenier for their appreciated help in constructing and operating the reactor.

5.6 References

1. Niu, J., F. Guo, J. Ran, W. Qi and Z. Yang, Methane dry (CO2) reforming to syngas (H2/CO) in catalytic process: From experimental study and DFT calculations. International Journal of Hydrogen Energy, 2020. 45(55): pp. 30267-30287, https://doi.org/10.1016/j.ijhydene.2020.08.067.
2. Wang, C., Y. Wang, M. Chen, D. Liang, Z. Yang, W. Cheng, Z. Tang, J. Wang and H. Zhang, Recent advances during CH4 dry reforming for syngas production: A mini review. International Journal of Hydrogen Energy, 2021. 46(7): pp. 5852-5874, https://doi.org/10.1016/j.ijhydene.2020.10.240.
3. Kalamaras, C.M. and A.M. Efstathiou. Hydrogen production technologies: current state and future developments. in Conference papers in science. 2013. Hindawi https://doi.org/10.1155/2013/690627.
4. Sharifianjazi, F., A. Esmaeilkhanian, L. Bazli, S. Eskandarinezhad, S. Khaksar, P. Shafiee, M. Yusuf, B. Abdullah, P. Salahshour and F. Sadeghi, A review on recent advances in dry reforming of methane over Ni- and Co-based nanocatalysts. International Journal of Hydrogen Energy, 2022. 47(100): pp. 42213-42233, https://doi.org/10.1016/j.ijhydene.2021.11.172.
5. Awad, M.M., I. Hussain, U. Mustapha, O. Ahmed Taialla, A. Musa Alhassan, E. Kotob, A. Shafiu Abdullahi, S.A. Ganiyu and K. Alhooshani, A critical review of recent advancements in catalytic dry reforming of methane: Physicochemical properties, current challenges, and informetric insights. International Journal of Hydrogen Energy, 2024. 76: pp. 202-233, https://doi.org/10.1016/j.ijhydene.2024.03.319.
6. Hamzehlouia, S., S.A. Jaffer and J. Chaouki, Microwave heating-assisted catalytic dry reforming of methane to syngas. Scientific reports, 2018. 8(1): pp. 1-7, https://doi.org/10.1038/s41598-018-27381-6.
7. Pham, T., K.S. Ro, L. Chen, D. Mahajan, T.J. Siang, U. Ashik, J.-i. Hayashi, D. Pham Minh and D.-V.N. Vo, Microwave-assisted dry reforming of methane for syngas production: a review. Environmental Chemistry Letters, 2020. 18(6): pp. 1987-2019, https://doi.org/10.1007/s10311-020-01055-0.
8. Mondal, K., S. Sasmal, S. Badgandi, D.R. Chowdhury, V.J.E.S. Nair and P. Research, Dry reforming of methane to syngas: a potential alternative process for value added chemicals—a techno-economic perspective. 2016. 23(22): pp. 22267-22273, https://doi.org/10.1007/s11356-016-6310-4.
9. Li, D., R. Xu, Z. Gu, X. Zhu, S. Qing and K. Li, Chemical-looping conversion of methane: a review. Energy Technology, 2020. 8(8): pp. 1900925, https://doi.org/10.1002/ente.201900925.
10. Ramezani, R., L. Di Felice and F. Gallucci, A review of chemical looping reforming technologies for hydrogen production: recent advances and future challenges. Journal of Physics: Energy, 2023 https://doi.org/10.1088/2515-7655/acc4e8.

11. Zhu, X., Y. Wei, H. Wang and K. Li, Ce–Fe oxygen carriers for chemical-looping steam methane reforming. International Journal of Hydrogen Energy, 2013. 38(11): pp. 4492-4501, https://doi.org/10.1016/j.ijhydene.2013.01.115.

12. Das, S., A. Biswas, J. Bhattacharya, C.S. Tiwary and M. Paliwal, Utilization of laterite ore as an oxygen carrier in chemical looping reforming of methane for syngas production. International Journal of Hydrogen Energy, 2023. 48(51): pp. 19411-19421, https://doi.org/10.1016/j.ijhydene.2023.02.054.

13. Wang, X., S. Abanades, S. Chuayboon, J. Zhang and J. Wei, Solar-driven chemical looping reforming of methane over SrFeO3-δ-Ca0.5Mn0.5O nanocomposite foam. International Journal of Hydrogen Energy, 2022. 47(79): pp. 33664-33676, https://doi.org/10.1016/j.ijhydene.2022.07.241.

14. Hu, Z., Z. Miao, J. Wu and E. Jiang, Nickel-iron modified natural ore oxygen carriers for chemical looping steam methane reforming to produce hydrogen. International Journal of Hydrogen Energy, 2021. 46(80): pp. 39700-39718, https://doi.org/10.1016/j.ijhydene.2021.09.242.

15. Nazari, M., M. Soltanieh, A. Heydarinasab and B. Maddah, Synthesis of a new self-supported Mgy(CuxNi0.6-xMn0.4)1-yFe2O4 oxygen carrier for chemical looping steam methane reforming process. International Journal of Hydrogen Energy, 2021. 46(37): pp. 19397-19420, https://doi.org/10.1016/j.ijhydene.2021.03.081.

16. Bhosale, R., F. AlMomani and G. Takalkar, Thermodynamic analysis of solar-driven chemical looping steam methane reforming over Cr2O3/Cr redox pair. International Journal of Hydrogen Energy, 2020. 45(17): pp. 10370-10380, https://doi.org/10.1016/j.ijhydene.2019.08.205.

17. Quan, J., Y. Chen, H. Mai, Q. Zeng, J. Lv, E. Jiang and Z. Hu, Uniformly dispersed NiFeAlO4 as oxygen carrier for chemical looping steam methane reforming to produce syngas. International Journal of Hydrogen Energy, 2024. 61: pp. 901-913, https://doi.org/10.1016/j.ijhydene.2024.02.355.

18. Amini, A., M. Latifi and J. Chaouki, Electrification of materials processing via microwave irradiation: A review of mechanism and applications. Applied Thermal Engineering, 2021: pp. 117003, https://doi.org/10.1016/j.applthermaleng.2021.117003.

19. Chaouki, J., S. Farag, M. Attia and J. Doucet, The development of industrial (thermal) processes in the context of sustainability: The case for microwave heating. The Canadian Journal of Chemical Engineering, 2020. 98(4): pp. 832-847, https://doi.org/10.1002/cjce.23710.

20. Goyal, H., T.-Y. Chen, W. Chen and D.G. Vlachos, A review of microwave-assisted process intensified multiphase reactors. Chemical Engineering Journal, 2022. 430: pp. 133183, https://doi.org/10.1016/j.cej.2021.133183.

21. Adavi, K., J. Shabanian and J. Chaouki, Temperature Distribution Assessment in Gas–Solid Reactive and Nonreactive Systems Heated by Microwaves. Industrial & Engineering Chemistry Research, 2023 https://doi.org/10.1021/acs.iecr.3c00575.

22. Khodabandehloo, M., J. Shabanian, J.-P. Harvey and J. Chaouki, Microwave heating-assisted chemical looping dry reforming of methane. International Journal of Hydrogen Energy, 2024. 71: pp. 1380-1391, https://doi.org/10.1016/j.ijhydene.2024.05.295.

23. Shirchi, S., B. Khoshandam and F. Hormozi, Reduction kinetics of cobalt oxide powder by methane in a fluidized bed reactor. Journal of the Taiwan Institute of Chemical Engineers, 2015. 51: pp. 171-176.

24. Su, M., J. Ma, X. Tian and H. Zhao, Reduction kinetics of hematite as oxygen carrier in chemical looping combustion. Fuel Processing Technology, 2017. 155: pp. 160-167.

25. Yang, L., Z. Zhao, J. Hao, J. Wei and J. Zhang, Oxygen release and reduction kinetics of La0. 35Sr0. 35Ba0. 3Fe1-xCoxO3 as oxygen carriers for chemical looping dry reforming of methane. Applications in Energy and Combustion Science, 2023. 15: pp. 100173.

26. Nasr, S. and K.P. Plucknett, Kinetics of iron ore reduction by methane for chemical looping combustion. Energy & fuels, 2014. 28(2): pp. 1387-1395, https://doi.org/10.1021/ef402142q.

27. He, K., Z. Zheng and Z. Chen, Multistep reduction kinetics of Fe3O4 to Fe with CO in a micro fluidized bed reaction analyzer. Powder technology, 2020. 360: pp. 1227-1236, https://doi.org/10.1016/j.powtec.2019.10.094.

28. Monazam, E.R., R.W. Breault, R. Siriwardane, G. Richards and S. Carpenter, Kinetics of the reduction of hematite (Fe2O3) by methane (CH4) during chemical looping combustion: A global mechanism. Chemical Engineering Journal, 2013. 232: pp. 478-487, https://doi.org/10.1016/j.cej.2013.07.091.

29. Go, K.S., S.R. Son and S.D. Kim, Reaction kinetics of reduction and oxidation of metal oxides for hydrogen production. International Journal of Hydrogen Energy, 2008. 33(21): pp. 5986-5995, https://doi.org/10.1016/j.ijhydene.2008.05.039.

30. Longbottom, R.J. and L. Kolbeinsen, Iron ore reduction with CO and H2 gas mixtures–Thermodynamic and kinetic modelling. 2008.

31. Domşa, A., L. Szabó, Z. Spîrchez and A. Pálfalvi, The kinetics of direct reduction of iron oxides with methane, in Modern Developments in Powder Metallurgy: Volume 1 Fundamentals and Methods. 1966, Springer. pp., 3-14, https://doi.org/10.1007/978-1-4684-7706-1_1.

32. Fedunik-Hofman, L., A. Bayon and S.W. Donne, Kinetics of solid-gas reactions and their application to carbonate looping systems. Energies, 2019. 12(15): pp. 2981, https://doi.org/10.3390/en12152981.

33. Hancock, J. and J. Sharp, Method of comparing solid-state kinetic data and its application to the decomposition of kaolinite, brucite, and BaCO3. Journal of the American Ceramic Society, 1972. 55(2): pp. 74-77, https://doi.org/10.1111/j.1151-2916.1972.tb11213.x.

34. Dai, X., J. Cheng, Z. Li, M. Liu, Y. Ma and X. Zhang, Reduction kinetics of lanthanum ferrite perovskite for the production of synthesis gas by chemical-looping methane reforming. Chemical Engineering Science, 2016. 153: pp. 236-245, https://doi.org/10.1016/j.ces.2016.07.011.

35. Shabanian, J. and J. Chaouki, Fluidized Beds for Gas–Solid Reactions☆. Essentials of Fluidization Technology, 2020: pp. 363-404.

36. Khawam, A. and D.R. Flanagan, Solid-state kinetic models: basics and mathematical fundamentals. The journal of physical chemistry B, 2006. 110(35): pp. 17315-17328.

37. Cetinkaya, S. and S. Eroglu, A Single-Step Process for Direct Reduction of Iron Oxide to Sponge Iron by Undiluted Methane. JOM, 2017. 69: pp. 993-998, https://doi.org/10.1007/s11837-017-2323-9.

38. Alizadeh, R., E. Jamshidi and H. Ale Ebrahim, Kinetic study of nickel oxide reduction by methane. Chemical Engineering & Technology: Industrial Chemistry-Plant Equipment-Process Engineering-Biotechnology, 2007. 30(8): pp. 1123-1128, https://doi.org/10.1002/ceat.200700067.

39. Tang, Q., Y. Ma and K. Huang, Fe3O4/ZrO2 composite as a robust chemical looping oxygen carrier: a kinetics study on the reduction process. ACS Applied Energy Materials, 2021. 4(7): pp. 7091-7100, https://doi.org/10.1021/acsaem.1c01152.

40. Yang, L., Z. Zhao, J. Hao, J. Wei and J. Zhang, Oxygen release and reduction kinetics of La0.35Sr0.35Ba0.3Fe1-xCoxO3 as oxygen carriers for chemical looping dry reforming of methane. Applications in Energy and Combustion Science, 2023. 15: pp. 100173, https://doi.org/10.1016/j.jaecs.2023.100173.

41. Hosseini, S.Y., M.R. Khosravi-Nikou and A. Shariati, Kinetic Study of the Reduction Step for Chemical Looping Steam Methane Reforming by CeO2-Fe2O3 Oxygen Carriers. Chemical Engineering & Technology, 2020. 43(3): pp. 540-552, https://doi.org/10.1002/ceat.201900290.

42. Liu, W., J.Y. Lim, M.A. Saucedo, A.N. Hayhurst, S.A. Scott and J.S. Dennis, Kinetics of the reduction of wüstite by hydrogen and carbon monoxide for the chemical looping production of hydrogen. Chemical Engineering Science, 2014. 120: pp. 149-166, https://doi.org/10.1016/j.ces.2014.08.010.

43. Lu, C., K. Li, H. Wang, X. Zhu, Y. Wei, M. Zheng and C. Zeng, Chemical looping reforming of methane using magnetite as oxygen carrier: Structure evolution and reduction kinetics. Applied Energy, 2018. 211: pp. 1-14, https://doi.org/10.1016/j.apenergy.2017.11.049.

44. Adavi, K., A. Amini, M. Latifi, J. Shabanian and J. Chaouki, Kinetic study of multiphase reactions under microwave irradiation: a mini-review. Frontiers in Chemical Engineering: pp. 102, https://doi.org/10.3389/fceng.2022.1059160.

5.7 Supplementary Material

Kinetic Study of Microwave Heating-Assisted Chemical Looping Dry Reforming of Methane Over Magnetite

Mohammad Khodabandehloo[1, 2], **Jaber Shabanian**[1], **Jean-Phillipe Harvey**[2], **Jamal Chaouki**[1, †]

[1] *Process Engineering Advanced Research Lab (PEARL), Chemical Engineering Department, Polytechnique Montreal, P.O. Box 6079, Station Centre-Ville, Montreal, Quebec, H3C 3A7, Canada*

[2] *Centre for Research in Computational Thermochemistry (CRCT), Chemical Engineering Department, Polytechnique Montreal, P.O. Box 6079, Station Centre-Ville, Montreal, Quebec, H3C 3A7, Canada*

[†] Corresponding author: Tel.: +1-514-340-4711 X 4034; Fax: +1-514-340-4159.

E-mail addresses: mohammad.khodabandehloo@polymtl.ca (M. Khodabandehloo), jaber.shabanian@polymtl.ca (J. Shabanian), jean-philippe.harvey@polymtl.ca (J.-P. Harvey), jamal.chaouki@polymtl.ca (J. Chaouki)

5.7.1 Derivation of molar reduction and oxidation conversions

Molar conversions of reduction and oxidation reactions can be defined by Eqs. (S.5.1) and (S.5.2), respectively.

$$\alpha_r = \frac{\text{Moles of oxygen resleased from the base solid } (Fe_3O_4)}{\text{Initial moles of the base solid } (Fe_3O_4)} \tag{S.5.1}$$

$$\alpha_o = \frac{\text{Moles of oxygen added to the base solid (Fe)}}{\text{Initial moles of the base solid (Fe)}} \tag{S.5.2}$$

Considering the reduction (R-5.5 in the main manuscript) and oxidation (R-5.6 in the main manuscript) reactions in this study, the crystalline structure of Fe_3O_4 (Figure S.5.1), as well as molecular weights of Fe, oxygen (O), and Fe_3O_4 as M_O = 16.00 g/mol, M_{Fe} = 55.84 g/mol, and $M_{Fe_3O_4}$ = 231.53 g/mol, respectively, by complete reduction of 1 mole Fe_3O_4 to Fe (R-5.5 in the main manuscript) and complete oxidation of 1 mole of Fe to Fe_3O_4 (R-5.6 in the main manuscript), one can define molar conversions of reduction and oxidations reactions by Eqs. (S.5.3) and (S.5.4), respectively.

$$\alpha_r = \frac{\text{Moles of oxygen resleased from the base solid } (Fe_3O_4)}{\text{Initial moles of the base solid } (Fe_3O_4)} = \frac{\frac{(m_i\text{-}m_f)}{4M_O}}{\frac{m_i}{M_{Fe_3O_4}}} = \frac{m_i\text{-}m_f}{0.28m_i} \qquad \text{(S.5.3)}$$

$$\alpha_o = \frac{\text{Moles of oxygen added to the base solid } (Fe)}{\text{Initial moles of the base solid } (Fe)} = \frac{\frac{(m_i\text{-}m_f)}{4M_O}}{\frac{m_i}{3M_{Fe}}} = \frac{m_i\text{-}m_f}{0.38m_i} \qquad \text{(S.5.4)}$$

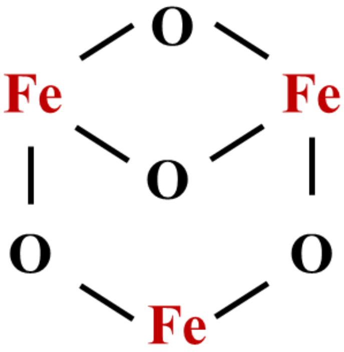

Figure S.5.1. Fe_3O_4 crystalline structure.

These show that Eqs. (S.5.3) and (S.5.4) are equivalent to Eqs. (2) and (3) in the main manuscript.

5.7.2 Mass transfer limitations

We investigated the effect of Q_{i,CH_4} and Q_{i,CO_2} on redox reactions, Figure S.5.2. As shown in this figure, by increasing $Q_{i,CH_4}/m_i$ from 82 ml/(min.gm) to 109 ml/(min.gm), equivalent to an increase of U_g from 1.4 to 1.8 cm/s, α_r at t_f of 120 s was increased from around 20 to 28%. However, by increasing $Q_{i,CH_4}/m_i$ from 109 ml/(min.gm) to 137 ml/(min.gm), i.e., U_g of 2.3 cm/s, we observed a minor difference (≤ 1%) in α_r. Like the reduction reaction, as shown in Figure S.5.2, for $Q_{i,CO_2}/m_i$ ≥ 109 ml/(min.gm), we observed a minor difference (≤ 1%) for the measured α_o. Hence, to minimize the impact of external mass transfer limitations on developing the intrinsic redox reactions kinetics, we conducted the redox reactions employing Q_{CH_4}/m_i and Q_{CO_2}/m_i equal to 137 ml/(min.gm), while adjusting $q_{i,CH_{4,i}}$ at 25 vol.% CH_4 and $q_{CO_{2,i}}$ at 25 vol.% CO_2. $q_{i,CH_{4,i}}$ and $q_{CO_{2,i}}$ represent volumetric concentration of CH_4 and CO_2 in the inlet gaseous stream, respectively.

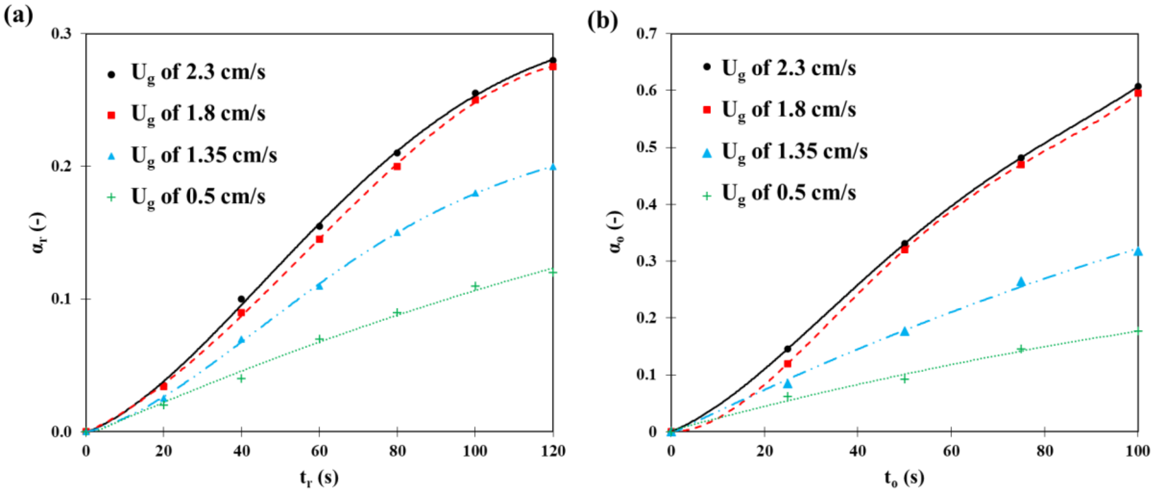

Figure S.5.2. Effects of U_g on a) α_r for the solids inventories comprised of Fe_3O_4 with sole CH_4 injection and b) α_o for the solids inventories comprised of Fe-Fe_3O_4 mixtures with 28 wt.% Fe with sole CO_2 injection. Experiments were accomplished at m_i = 5 gm and T_b = 800°C.

We employed Mears and Weisz–Prater criterion, as reported in Eq (S.5.5) [1-7], to ensure that we minimized the effect of internal mass transfer in this study.

$$\frac{\rho_p.d_p^2.r_{max}.R.T_{rx}}{P_{CH_4}.D_e}<1 \tag{S.5.5}$$

In this equation, ρ_p, r_{max}, D_e, and P_{CH_4} are the particle density, maximum overall reaction rates (reduction and oxidation), effective diffusivity, and partial pressure of CH_4 in the inlet gaseous stream, respectively. Based on Eq (S.5.5), for T_b ranging from 650 to 800°C for the measured α_r and T_b ranging from 500 to 650°C for the measured α_o, the Fe_3O_4 oxygen carrier with d_p< 500 µm is capable of eliminating the effect of internal mass transfer. Therefore, the selected Fe_3O_4 oxygen carrier with an average d_p of 10 µm can effectively minimize the impact of internal mass transfer. Accordingly, the chemical reactions occurring between the gas and solid phases are the rate-controlling step to develop the reaction kinetics.

5.7.3 Model comparison

We generated parity plots for different reduction reaction mechanisms and presented the results in Figure S.5.3. These plots reveal considerable deviations (up to 57% of relative difference) between the predicted values by different reaction mechanisms and the experimental data, except for the phase-boundary controlled (contracting sphere) reaction mechanism. Hence, the developed redox reaction kinetics based on the phase-boundary controlled (contracting sphere) mechanism accurately predicted the redox reaction kinetics for the MW heating assisted CLDRM over Fe_3O_4.

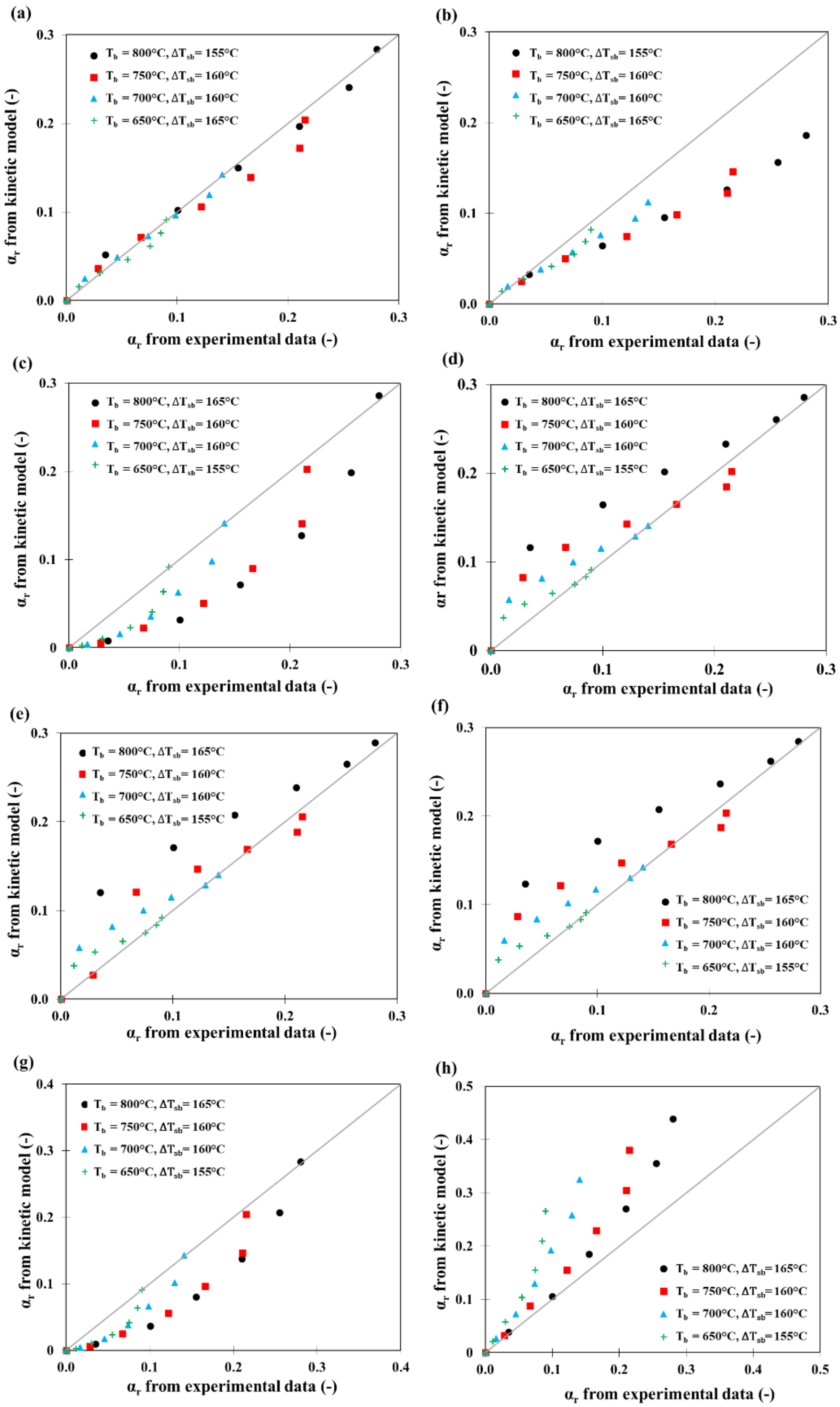

Figure S.5.3. α_r prediction performances of a) phase-boundary controlled (contracting sphere), b) phase-boundary controlled (contracting cylinder), c) power law d) 1-D diffusion, e) 2-D diffusion, f) 3-D diffusion, g) 2-D growth of nuclei, and h) 3-D growth of nuclei reaction kinetic models based on the model fitting method.

5.7.4 References

1. Das, S., M. Shah, R.K. Gupta and A.J.J.o.C.U. Bordoloi, Enhanced dry methane reforming over Ru decorated mesoporous silica and its kinetic study. 2019. 29: pp. 240-253, https://doi.org/10.1016/j.jcou.2018.12.016.

2. Zhou, L., L.R. Enakonda, Y. Saih, S. Loptain, D. Gary, P. Del-Gallo and J.M.J.C. Basset, Catalytic methane decomposition over Fe-Al2O3. 2016. 9(11): pp. 1243-1248, https://doi.org/10.1002/cssc.201600310.

3. Santacesaria, E. and R.J.C.S.I.P.A.d. Tesser, The Chemical Reactor from Laboratory to Industrial Plant. 2018. 10: pp. 978-3, https://doi.org/10.1007/978-3-319-97439-2.

4. Fogler, H.S. and S.H. Fogler, Elements of chemical reaction engineering. 1999: Pearson Educación.

5. Weisz, P. and C. Prater, Interpretation of measurements in experimental catalysis, in Advances in catalysis. 1954, Elsevier. pp., 143-196, https://doi.org/10.1016/S0360-0564(08)60390-9.

6. Tesser, R. and E.J.P. Santacesaria, Revisiting the Role of Mass and Heat Transfer in Gas–Solid Catalytic Reactions. 2020. 8(12): pp. 1599, https://doi.org/10.3390/pr8121599.

7. Pino, L., C. Italiano, M. Laganà, A. Vita, V.J.C.S. Recupero and Technology, Kinetic study of the methane dry (CO 2) reforming reaction over the Ce 0.70 La 0.20 Ni 0.10 O 2− δ catalyst. 2020. 10(8): pp. 2652-2662, https://doi.org/10.1039/C9CY02192B.

CHAPTER 6 ARTICLE 3 : A NOVEL MICROWAVE HEATING-ASSISTED REACTOR FOR INDUSTRIAL-SCALE SYNGAS PRODUCTION

Mohammad Khodabandehloo[1, 2], Jaber Shabanian[1], Jean-Phillipe Harvey[2], Jamal Chaouki[1, †]

[1] *Process Engineering Advanced Research Lab (PEARL), Chemical Engineering Department, Polytechnique Montreal, P.O. Box 6079, Station Centre-Ville, Montreal, (Quebec) Canada, H3C 3A7*

[2] *Centre for Research in Computational Thermochemistry (CRCT), Chemical Engineering Department, Polytechnique Montreal, P.O. Box 6079, Station Centre-Ville, Montreal, (Quebec) Canada, H3C 3A7*

[†] Corresponding author: Tel.: +1-514-340-4711 X 4034; Fax: +1-514-340-4159.

E-mail addresses: mohammad.khodabandehloo@polymtl.ca (M. Khodabandehloo), jaber.shabanian@polymtl.ca (J. Shabanian), jean-philippe.harvey@polymtl.ca (JP. Harvey), jamal.chaouki@polymtl.ca (J. Chaouki)

(Submitted to Applied Energy on September 3, 2024)

Abstract

Syngas, i.e., a mixture made of carbon monoxide and hydrogen, is a valuable feedstock to produce different chemicals, e.g., methanol. In our recent study (Khodabandehloo et al., Int. J. Hydrogen Energy 71 (2024) 1380-1391), we demonstrated the efficacy of syngas production through chemical looping dry reforming of methane heated by microwaves. However, installing a large number (typically over a hundred) of microwave-heated reactors in parallel is a major technical challenge for scaling up this syngas-generating technology. In this work, we introduced a novel microwave heating-assisted cyclic simulated moving bed reactor to mitigate this technical challenge. We developed a model that incorporates bed hydrodynamics, mass transfer, and reaction kinetics. We integrated it with temperature distribution in the bed, to simulate the reactivity of methane and carbon dioxide with the loaded bed, and Maxwell's equation to capture distribution of electromagnetic waves throughout the system. We verified this model with simulation results from literature and validated it by experimental data collected in this study. Upon model verification and validation and designing the reactor, we simulated the proposed reactor for a plant with an inlet methane flowrate of 50 tons/day to optimize operating conditions and reactor design parameters. The simulation results indicated that at a bulk temperature of 800°C, the optimized design of the proposed reactor can (i) achieve nearly complete ($\geq$0.98) methane conversion by only

four reactors and (ii) ensure a uniform distribution of electromagnetic waves with more than 97% of microwave absorption by loaded oxygen carrier beds.

Keywords: Reactor design; Microwave heating; Cyclic simulated moving bed reactor; Dry reforming of methane; Chemical looping; Syngas.

6.1 Introduction

Syngas (synthesis gas), i.e., a mixture made of carbon monoxide (CO) and hydrogen (H_2), is an essential feedstock for producing valuable chemicals, like synthetic fuels [1-3]. In addition, the global demand for H_2 is mainly (over 50%) supported by its separation from syngas. Different sectors, including chemical production industries, heavily rely on H_2. Moreover, H_2 is highly valued as a clean and/or sustainable energy carrier and is anticipated to aid in supplying the future energy demand [4-7]. Syngas is predominantly generated by catalytic steam (vapor phase of water (H_2O)) reforming of methane (CH_4), referred to as C-SRM here [2, 8]. However, the C-SRM suffers from its high rate of carbon dioxide (CO_2) emissions, exceeding nine kg of CO_2 emission for producing one kg of H_2 [2, 3, 8, 9]. Therefore, we need to develop viable and environmentally friendly technologies for generating syngas.

In Figure 6.1a, we schematically illustrated dry reforming of CH_4 (DRM) through a chemical looping (CL) process. As implied from this figure, CL-DRM leverages from: (i) reduction of M_xO_y (an oxygen carrier in solid phase) to M_xO_{y-1} by CH_4 to generate syngas in a fuel (reducer) reactor, and (ii) oxidation of M_xO_{y-1} to M_xO_y by CO_2 to generate CO in an oxidizer reactor. CO_2 and CH_4 account for more than 90% of the greenhouse gas (GHG) emissions [6, 10, 11]. The advancement of the CL-DRM, enabling simultaneous syngas generation and GHG utilization, is of global interest [12-16]. Nevertheless, the high operating temperature (usually exceeding 900°C [12-16]) of the fuel reactor and the presence of unfavorable reactions, in particular, CH_4 decomposition to coke in the gas phase of the fuel reactor, are major challenges that make the CL-DRM a nonideal syngas-generating technology [12, 16-19].

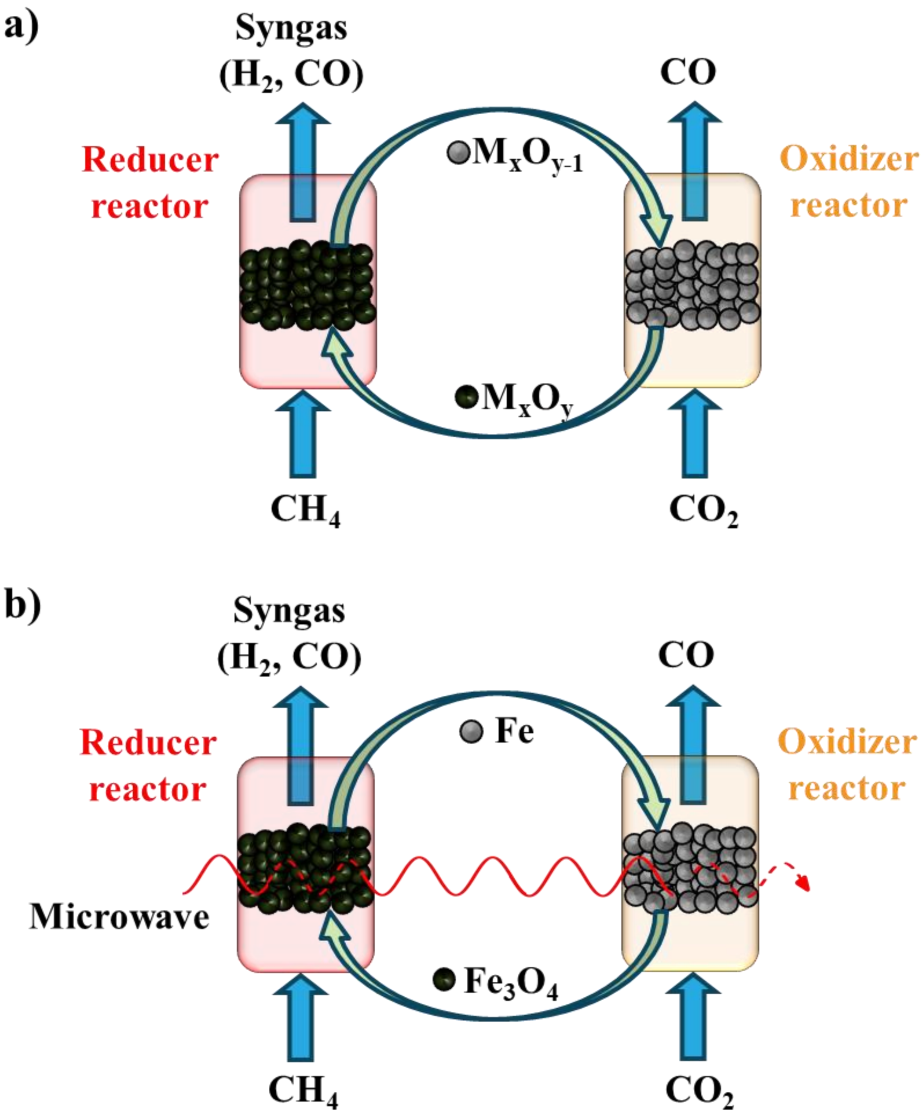

Figure 6.1. Schematic illustration of a) CHCL-DRM and b) MWHCL-DRM. We adopted magnetite (Fe_3O_4) as the oxygen carrier ($M_xO_{y(s)}$). $M_xO_{y-1(s)}$ stands for the reduced state of $M_xO_{y(s)}$. Fe is iron here.

In the realm of chemical engineering [20-33], microwave heating (MWH) involves generating electromagnetic waves (EMWs) at frequencies of 915 MHz or 2.45 GHz to supply process heat. The electricity needed to generate microwaves (MWs) can be powered from renewable sources [20, 21, 27]. Accordingly, applying MWH to electrify processes can decrease GHG emissions resulting from fossil fuel-based heat generation. One can classify different materials into three classes based on their interactions with MWs as [20, 21, 27]: MW-transparent, MW-absorbing, and

MW-reflective. Materials in the first class, i.e., MW-transparent, like gaseous argon (Ar), do not deflect (absorb or reflect) MWs. In contrast, a material being MW-absorbing, like water at 25°C, absorbs MWs and heats up. MW-reflective materials, like non-magnetic stainless-steel plates, reflect MWs. Hence, through a careful screening and synthesis of materials with the desired electromagnetic (EM) properties, in particular, relative permittivity ε_r, relative permeability μ_r, and electrical conductivity σ (see Refs. [20, 21, 27] for definitions of these parameters), MWs can help selectively heat the target material(s) instead of the whole media. Different researchers [22, 23, 25, 26, 28-33] adopted this interesting feature of MWs, i.e., selective heating (SH), and explored its impacts on advancing various reactions. For instance, to advance a reaction that is endothermic (like catalytic DRM) in a gas-solid reactor containing MW-absorbing solid catalysts, irradiating MWs can lead to a higher temperature of the catalysts compared to gas [20, 21, 27]. This can enhance the rate of preferred catalytic reactions, while minimizing/suppressing unfavorable secondary reactions inside the gas [20, 21, 27]. Accordingly, the MW's SH feature can enhance process productivity. In addition to the SH, MWs rely on volumetric heating (VH), i.e., direct transfer of energy to the material. This feature can yield a (nearly) uniform distribution of temperature throughout the MW-absorbing materials [20, 21, 27]. Therefore, as presented in Figure 6.1b, to leverage from the SH and VH characteristics of MWs in resolving the aforementioned hurdles of the CL-DRM, we introduced MWH-assisted CL-DRM, termed MWHCL-DRM, and demonstrated it at laboratory-scale [34].

Owing to the EM properties of Fe_3O_4, we selected it as the oxygen carrier in this study similar to our earlier study [34]. Since CH_4 and CO_2 (present in the gaseous phase in the targeted reactions here) are transparent to MWs, the Fe_3O_4 particles can selectively be heated by MWs. Conventional heating (CH) can lead to a local temperature balance/equilibrium of the same gas and particle/solid temperatures, T_g and T_s, respectively, to the temperature of the bulk T_b. Different from the CH, MWH can create a non-local temperature balance/equilibrium, i.e., $T_s > T_g$, while preserving the bed at thermal equilibrium [20, 21, 27].

We confirmed [34] that the mentioned non-local temperature balance/equilibrium, i.e., SH of MWs, could augment the performance of the MWHCL-DRM relative to CH-assisted DRM (CHCL-DRM). Results of our previous experiments underlined that relative to the CHCL-DRM, the MWHCL-DRM: (i) accelerated the rate of favorable reactions, i.e., reduction and oxidation (redox), (ii) inhibited unfavorable reaction, i.e., thermal decomposition of CH_4 leading to the coke generation, and (iii) stimulated complete conversion of Fe_3O_4 to iron (Fe) [34].

To deploy MWHCL-DRM at commercial scale, it is imperative to resolve its technical and economic hurdles allied with the commercial scale. The main technical challenge that decelerates scale-up of MWH-assisted units, including the MWHCL-DRM, is the availability of a maximum effective MW power of 65 kW (100 kW paired with associated electricity to power generation efficiency) in each commercial magnetron-based MW generator. This leads to the application of many MWH-assisted reactors in parallel, which may pose some operational and financial challenges on a large scale. To address this critical technical challenge, in this study, we introduced and simulated a novel reactor, i.e., MWH-assisted cyclic simulated moving bed reactor (MWH-CSMBR).

In this study, we proposed, designed, and optimized the novel MWH-CSMBR for producing syngas at large scale. We first presented the concept of MWH-CSMBR and its design background in Section 6.2.1. We then developed a model to simulate the MWH-CSMBR (Section 6.2.2). In Section 6.3, we presented experimental and model parameters for model verification and validation. We presented basic design parameters of the MWH-CSMBR in Section 6.4.1. We then performed a grid independency analysis in Section 6.4.2. We subsequently verified and validated the developed model in Section 6.4.3. Lastly, in Section 6.4.4, by employing the verified and validated model, we conducted a set of parametric studies by simulating the MWH-CSMBR for various scenarios to optimize the reactor design.

6.2 Model development

6.2.1 Problem description, modeling assumptions, and boundary conditions

Similar to our earlier study [34], in the current study, we adopted Fe_3O_4 to behave as the MW-absorbing oxygen carrier. For the laboratory-scale MWHCL-DRM, we observed a uniform distribution of temperature throughout the packed/fixed bed [34]. In addition, in the same study [34], we observed that CH_4 conversion x_{CH_4} (also representative of Fe_3O_4 reactivity) was consistent after three redox cycles when completing twenty redox cycles. Consequently, for a shallow loaded bed made of Fe_3O_4 or a mixture of Fe_3O_4-Fe, we confirmed that a fixed/packed bed reactor can efficiently be applied for the MWHCL-DRM. However, one needs to optimize the design and number of MWHCL-DRM reactors when applying this technology at commercial scale as (i) syngas-generating reactors at commercial scale (typically above 10 tons/day of syngas production) have high energy consumptions (in the order of tens to hundreds of megawatts) [35, 36] and (ii) a maximum effective P_{MW} of 65 kW is currently available for the commercial magnetron-based MW generators [20, 21, 25]. P_{MW} represents the power of the MW. The high energy consumption and limited P_{MW} correspondingly lead to the application of a large number (typically over a hundred) MW-heated reactors in parallel. This causes technical and economic hurdles for the design, construction, and operation of a high number of MW-heated reactors in parallel at commercial scale. To resolve this challenge, we were inspired by distillation columns and simulated moving bed (SMB) technology and proposed a novel MWH-CSMBR, as depicted in Figure 6.2.

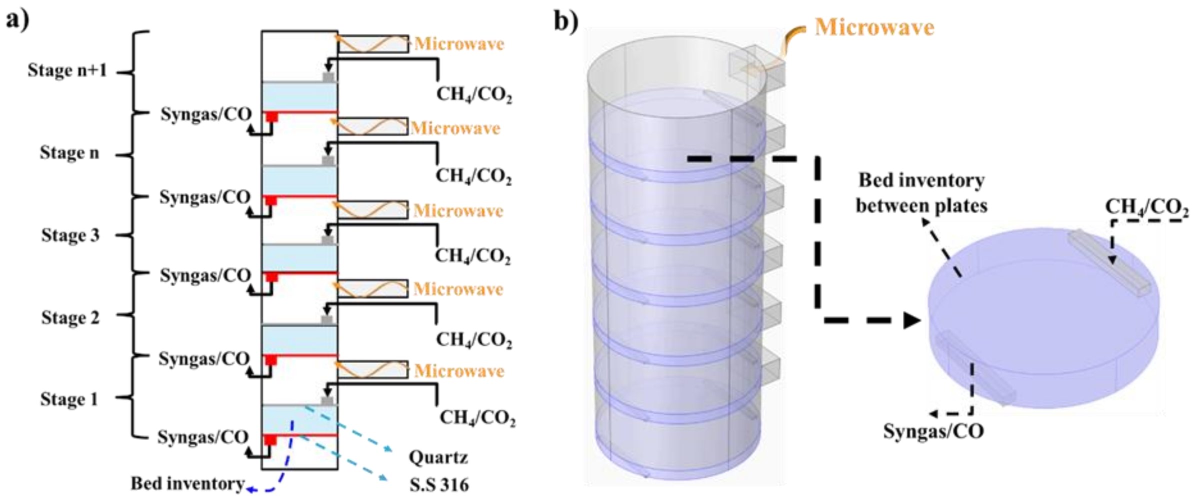

Figure 6.2. Schematic representation of proposed MWH-CSMBR: a) 2D, and b) 3D diagrams.

Different researchers focused on application and testing of moving bed reactors (MBRs) for CL processes at pilot scale owing to their promising advantages [37, 38]. For the technology targeted here, a low axial mixing and multi-stage reaction pattern in the MBRs could facilitate oxygen carrier's full reduction, i.e., the full reduction of Fe_3O_4 ($Fe_3O_4 \rightarrow FeO \rightarrow Fe$) here [39-41]. Simple control and design of separate reactors/zones for redox reactions, which decreases the total (capital and operating) costs and minimizes the operational complexities of the process, is another benefit of the MBRs. In addition, heating a moving bed with MWs to increase the rate of catalytic conversion and gasification has already been demonstrated [42, 43]. Compared to a moving bed heated by MWs, in the MWH-CSMBR, as depicted in Figure 6.2, each reactor stage contains a fixed bed medium through which the gaseous feed (CH_4 or CO_2) passes to progress either of the redox reactions. Accordingly, unlike a moving bed with counter-current, co-current, or cross-current flow streams of solids inventory and the passing fluid [37-41], in simulated moving bed reactors (SMBRs), the loaded bed remains stationary and the flow streams of solids inventory and the fluid can occur by implementing switching valves, i.e., changing the gaseous feed from CH_4 to CO_2 and vice versa. Therefore, by employing fixed bed medium and applying switching valves, the proposed MWH-CSMBR can achieve the performance of a moving bed heated by MW. As shown in Figure 6.2, waveguides connect the MW generator to each reactor stage, transferring the created MWs to each reactor stage. We employed a stainless-steel 316 plate (S.S 316 plate) and a quartz plate, depicted by red and grey lines in Figure 6.2a, respectively, to apply a fixed bed in each reactor stage. The S.S 316 plate behaves as an MW-reflective, preventing MW leakage between the reactor stages. Quartz, being MW-transparent, ensures that the introduced MWs into each reactor stage reach the loaded bed. In addition, by installing a quarter-wavelength choke, the MW leakage from inlet and outlet nozzles of the gas streams can be decreased below the standard limit (10 mW/cm^2).

As alluded to earlier, we adopted a Multiphysics modeling approach to optimize the design of the proposed reactor design and evaluate its performance under the reactive conditions of interest to this study. The general assumptions of the current study for model development are:

i. For superficial gas velocity $\mathrm{U_g}$ below 10 cm/s in the laboratory-scale MWHCL-DRM [34], we confirmed a uniform $\mathrm{T_b}$ throughout the loaded bed for a bed height $\mathrm{H_{bed}}$ of around 2 cm with $\mathrm{H_{bed}/D_r} \approx 0.7$. $\mathrm{D_r}$ represents the reactor's inner diameter. Consequently, taking into account the comparatively high $\mathrm{U_g}$ (over 70 cm/s) in the designed MWH-CSMBR in this study and a shallow bed ($\mathrm{H_{bed}}$ of 4 cm; referring to Section 6.4.1) with a $\mathrm{H_{bed}/D_r}$ of around 0.1 (referring to Section 6.4.1), we assumed a uniform temperature distribution throughout the loaded bed.

ii. For $\mathrm{T_b}$ of around 800°C (±25°C) and selected $\mathrm{Q_{CH_4}/m_{Fe_3O_4}}$ and $\mathrm{Q_{CO_2}/m_{Fe}}$, we assumed that the gas-solid temperature difference measured in the laboratory-scale setup ($\mathrm{T_s}$-$\mathrm{T_b}$= 165°C) is also applicable to the designed fuel and oxidizer reactors in this study. $\mathrm{Q_{CO_2}}$ and

Q_{CH_4} represent the volumetric flowrates of CO_2 and CH_4, respectively. $m_{Fe_3O_4}$ and m_{Fe} are the masses of Fe_3O_4 and Fe loaded in the bed.

iii. Based on our previous study [34], for $\alpha_r \leq 0.27$, where α_r is the reduction extent of the solid sample, we measured a negligible (<3%) T_b fluctuation during the redox reactions in the laboratory-scale. Similarly, in this study, for $\alpha_r \leq 0.27$, we assumed constant EM properties of the loaded beds when proceeding the redox reactions.

iv. For the proposed reactor in this study, bed hydrodynamics do not influence the EMW distribution. This assumption is discussed further in the relevant section (Section 6.2.2.4).

In addition, we considered the following boundary conditions to simulate the MWH-CSMBR:

i. Impedance boundary conditions for reactor and waveguide walls.
ii. ε_r and μ_r of 1 for quartz.
iii. No slip boundary condition for reactor and waveguide walls.
iv. By properly insulating the reactor walls, we can prevent heat transfer between the reactor and the environment, i.e., zero heat flux between the reactor wall and the environment.
v. A total of inlet mass flowrate of CH_4 $\dot{m}_{CH_4}$ at 50 tons/day to compare the designed reactor with that of conventional gaseous syngas-generating plants for large-scale applications [44].
vi. A zero-gauge pressure for the outlet gaseous stream of the reactor stages.
vii. An inlet gaseous temperature of 25°C.

To ensure a steady syngas production by the proposed MWH-CSMBR at large scale, we also proposed a cycle period of 180 s. According to this, at odd stages, we initially inject CH_4 for 95 s to achieve the reduction extent α_r of 0.27. We then switch the gas to CO_2 to proceed with the oxidation reaction. After 85 s of CO_2 injection and reaching the oxidation extent α_o of 1, i.e., we achieve a bed with 100 wt.% Fe_3O_4, we stop CO_2 injection. The cycle for the reactor stage continues (CH_4 must be injected again). An inverse gas switching with associated injection times are considered for even reactor stages.

6.2.2 Multiphysics coupling

In the developed Multiphysics model, we explained fluid dynamics, kinetic and mass balance, and temperature distribution in Sections 6.2.2.1, 6.2.2.2, and 6.2.2.3, respectively, which are investigated by “Stationary” and “Time Dependent” studies of COMSOL Multiphysics. We also predicted the EM field distribution by “Frequency Domain” study, which is explained in Section 6.2.2.4.

6.2.2.1 Hydrodynamic model

The continuity equation is presented in Eq. (6.1). To determine gas velocity field distribution, we applied the “Free and Porous Media Flow” module of the COMSOL Multiphysics. For a fixed/packed bed medium, we described the fluid dynamics between the solid particles, i.e., in the bulk of fluid, by Navier Stocks (Eq. (6.2)) equation. We also applied the Brinkman equation (Eq. (6.3)) to describe the fluid dynamics in the porous medium.

$$\nabla.\left(\rho_g\vec{u}_g\right) = 0 \tag{6.1}$$

$$\rho_g\left(\frac{\partial\vec{u}_g}{\partial t} + \left(\vec{u}_g.\nabla\right)\vec{u}_g\right) = \nabla.\left(-P\vec{I} + \vec{K}\right) + \vec{F} \tag{6.2}$$

$$\frac{\rho_g}{\varepsilon_g}\left(\frac{\partial\vec{u}_g}{\partial t} + \frac{1}{\varepsilon_g}\left(\vec{u}_g.\nabla\right)\vec{u}_g\right) = \nabla.\left(-PI + \vec{K'}\right) - \left(\frac{\mu_g}{k} + \beta\rho_g\left|\vec{u}_g\right|\right)\vec{u}_g + \vec{F} \tag{6.3}$$

where ρ_g is the gas density and μ_g is the dynamic viscosity of the gas. ε_g is the bed voidage and $\vec{u}_g$ represents the local gas velocity. $\frac{\partial\vec{u}_g}{\partial t}$ and $\left(\vec{u}_g.\nabla\right)\vec{u}_g$ appeared in Eqs. (6.2) and (6.3) represent the accumulation of momentum with time and the advection momentum flux, respectively. Pressure gradient, viscous forces, and volume force are taken into consideration by $\nabla.\left(-P\vec{I}\right)$, $\vec{K}/\vec{K'}$, and $\vec{F}$, respectively. In addition, to describe the drag force for particles with the particle size of d_p, we adapted the term $\left(\frac{\mu_g}{k} + \beta\rho_g\left|\vec{u}_g\right|\right)\vec{u}_g$. $\vec{K}$, $\vec{K'}$, k, and β employed in Eqs. (6.2) and (6.3) are described in Eqs. (6.4) to (6.7), respectively.

$$\vec{K} = \mu_g\left(\nabla\vec{u}_g + \left(\nabla\vec{u}_g\right)^T\right) \tag{6.4}$$

$$\overrightarrow{K'} = \frac{\mu_g}{\varepsilon_g}\left(\nabla\vec{u}_g + \left(\nabla\vec{u}_g\right)^T\right) - \frac{2}{3}\frac{\mu_g}{\varepsilon_g}\left(\nabla.\vec{u}_g\right)\vec{I} \tag{6.5}$$

$$k = \frac{\varepsilon_g^3 d_p^2}{150\left(1-\varepsilon_g\right)^2} \tag{6.6}$$

$$\beta = \frac{1.75(1-\varepsilon_g)}{d_p\varepsilon_g^2} \tag{6.7}$$

6.2.2.2 Kinetic model and mass balance

We developed the governing mass balance equation (Eq. (6.8)) for determining ocal composition of species i.

$$\rho_g\frac{\partial\omega_i}{\partial t} + \nabla.\vec{j}_i + \rho_g\left(\vec{u}_g.\nabla\right)\omega_i = r_i \tag{6.8}$$

where $\vec{j}_i$ is the diffusive mass transfer flux of species i. ω_i and r_i represent the mass fraction and rate of reaction (consumption) of species i, respectively.

In our laboratory-scale study [34], we achieved syngas production with an H_2 to CO ratio of nearly 2:1 in the fuel reactor (R-6.1 occurs in the fuel reactor). Accordingly, one can assume $\alpha_r = \frac{n_{io}-n_i}{4n_{io}}$, where n_i and n_{io} are final and initial moles of component i, respectively, considering CH_4 as the component i here. Similar to the reduction reaction, based on our previous experimental study [34], we can neglect the formation of intermediate iron oxide phases, like wüstite ($Fe_{0.91}O$), during the Fe oxidation by CO_2. Consequently, we can assume a complete oxidation of Fe to Fe_3O_4 in the oxidizer reactor (R-6.2 occurs in the oxidizer reactor) and $\alpha_o = \frac{3(n_{io}-n_i)}{4n_{io}}$, while considering CO_2 as the component i. Similar to our laboratory-scale study [34], due to a low T_g (below 650°C), we neglected the unfavorable CH_4 decomposition in the gas phase. Hence, we employed intrinsic kinetics of redox reactions as presented in Table 6.1 for the MWHCL-DRM. We comprehensively studied kinetics of redox reactions under MW heating in a separate study by the group "International Journal of Hydrogen Energy, submitted for publication".

$$Fe_3O_{4\,(s)} + 4CH_{4\,(g)} \rightarrow 4CO_{(g)} + 8H_{2\,(g)} + 3Fe_{(s)} \tag{R-6.1}$$

$$3Fe_{(s)} + 4CO_{2\,(g)} \rightarrow 4CO_{(g)} + Fe_3O_{4\,(s)} \quad \text{(R-6.2)}$$

Table 6.1. Intrinsic reaction rates.

Reaction	***Kinetic expression***
Reduction of Fe_3O_4 using CH_4 under MWH	$\frac{d\alpha_r}{dt} = 11.01 \exp\left(-\frac{10.3 \times 10^3}{T_s}\right).(1\text{-}\alpha_r)^{2/3}$
Oxidation of Fe using CO_2 under MWH	$\frac{d\alpha_o}{dt} = 0.09 \exp\left(-\frac{2.6 \times 10^3}{T_s}\right).(1\text{-}\alpha_o)^{2/3}$

6.2.2.3 Temperature distribution model

Based on assumptions (i) and (ii) in Section 6.2.1, we integrated MWH into the energy balance of the packed/fixed medium to determine the temperature distribution model, presented in Eq. (6.9).

$$\rho_b C_{p,b} \frac{\partial T_b}{\partial t} + \rho_b C_{p,b} \vec{u}_g . \nabla T_g - k_b \nabla T_b + q_{MW} - r_{r/o} \Delta H_{r/o} = 0 \quad (6.9)$$

where ρ_p and ρ_b are the particle/solid and bulk densities, respectively. $C_{p,b}$ (defined in Eq. (6.10)) and k_b (defined by Eq. (6.11)) are the specific heat capacity and thermal conductivity coefficient of the bulk, respectively. q_{MW} is the absorbed MW by the bed. We employed Eq. (6.12) to estimate q_{MW}, as the heat source. As shown in Section 6.4.4, by an appropriate integration of the waveguide around the MW-heated reactor, one can achieve a MW absorption efficiency η_{MW} of above 97%. We defined η_{MW} as the efficiency of MW dissipation within the loaded bed, i.e., the percentage of the irradiated MWs that is dissipated throughout the bed. The last term in Eq. (6.9) represents the effect of redox reactions on heat generation/consumption throughout the bed.

$$C_{p,b} = \varepsilon_g C_{p,g} + (1 - \varepsilon_g) C_{p,p} \quad (6.10)$$

$$k_b = \varepsilon_g k_g + (1 - \varepsilon_g) k_p \quad (6.11)$$

$$q_{MW} = 0.25 P_{MW} \eta_{MW} \pi D_r^2 H_{bed} \quad (6.12)$$

where $\mathrm{k_g}$ and $\mathrm{k_p}$ are the thermal conductivity of the gas and particle/solid, respectively. $\mathrm{C_{p,g}}$ and $\mathrm{C_{p,p}}$ are also the specific heat capacity of gas and particle/solid, respectively.

6.2.2.4 Electromagnetic field

We predicted EMW distribution throughout the system by solving the Maxwell's equation (Eq. (6.13)). To solve Maxwell's equation, we applied the "Electromagnetic Waves, Frequency Domain" module of COMSOL Multiphysics.

$$\nabla \times \left(\mu_{r,b}^{-1} \nabla \times \vec{E}\right) - k_o^2 \left(\varepsilon_{r,b} - \frac{j\sigma_b}{\omega \varepsilon_g}\right)\vec{E} = 0 \tag{6.13}$$

where $\vec{E}$, $\mathrm{k_o}$, and ω are respectively the electric field, free space wave number, and angular frequency. $\varepsilon_{r,b}$ is the relative permittivity of the bulk, $\mu_{r,b}$ is the relative permeability of the bulk, and σ_b is the electrical conductivity of the bulk. $\mathrm{k_o}$, $\varepsilon_{r,b}$, $\mu_{r,b}$, and σ_b can be described as:

$$k_o = \frac{\omega}{c_o} \tag{6.14}$$

$$\varepsilon_{r,b} = \varepsilon_g \varepsilon_{r,g} + \left(1 - \varepsilon_g\right)\varepsilon_{r,p} \tag{6.15}$$

$$\mu_{r,b} = \varepsilon_g \mu_{r,g} + \left(1 - \varepsilon_g\right)\mu_{r,p} \tag{6.16}$$

$$\sigma_b = \varepsilon_g \sigma_g + \left(1 - \varepsilon_g\right)\sigma_p \tag{6.17}$$

where $\varepsilon_{r,p}$ and $\mu_{r,p}$ are the relative permittivity and relative permeability of the particle/solid, respectively. σ_g and σ_p are also the electrical conductivity of gas phase and particle/solid, respectively. Considering the assumption (iii), presented in Section 6.2.1, we assumed that the advancement of the redox reactions does not influence EM properties of the bed. In addition, as shown in Eq. (6.13), for a fixed medium, bed hydrodynamics, in particular $\mathrm{U_g}$, influences the temperature distribution throughout the bed, rather than the EMW distribution. Therefore, the bed hydrodynamics does not influence the EMW distribution. Hence, we can separately employ the "Frequency Domain" study of COMSOL Multiphysics to simulate the EMW distribution throughout the system.

6.3 Experimental and model parameters for model verification and validation

To verify the developed model and ensure that it appropriately predicts the EMW distribution, we simulated the EMW distribution within a WR-340 waveguide by the developed model and compared it with the simulation results obtained by Yan et al. [45]. The length and width of the WR-340 waveguide, which was employed by Yan et al. [45], are 86.4 and 43.2 mm, respectively (referring to Figure 6.6). In addition, identical to the simulations performed by Yan et al. [45], we applied impedance boundary condition for the waveguide walls. Moreover, we set P_{MW} and operating frequency of the MWs at 100 W and 2.45 GHz, respectively.

We validated the model by comparing our simulation results with the experimental data. Relying on the best of authors' knowledge, no research has yet developed a pilot or industrial-scale setup for MW-heated reactors in CL applications. We thus deployed the laboratory-scale setup powered by the MWH (Figure 6.3) to obtain the needed experimental data for model validation. In the elucidated setup, we connected a magnetron capable of creating MWs between 110 and 1100 W at a frequency of 2.45 GHz to a MW cavity. We irradiated the adopted quartz reactor, i.e., a MW-transparent material, with MWs and operated it under a fixed bed regime. Details of the setup are described elsewhere [34].

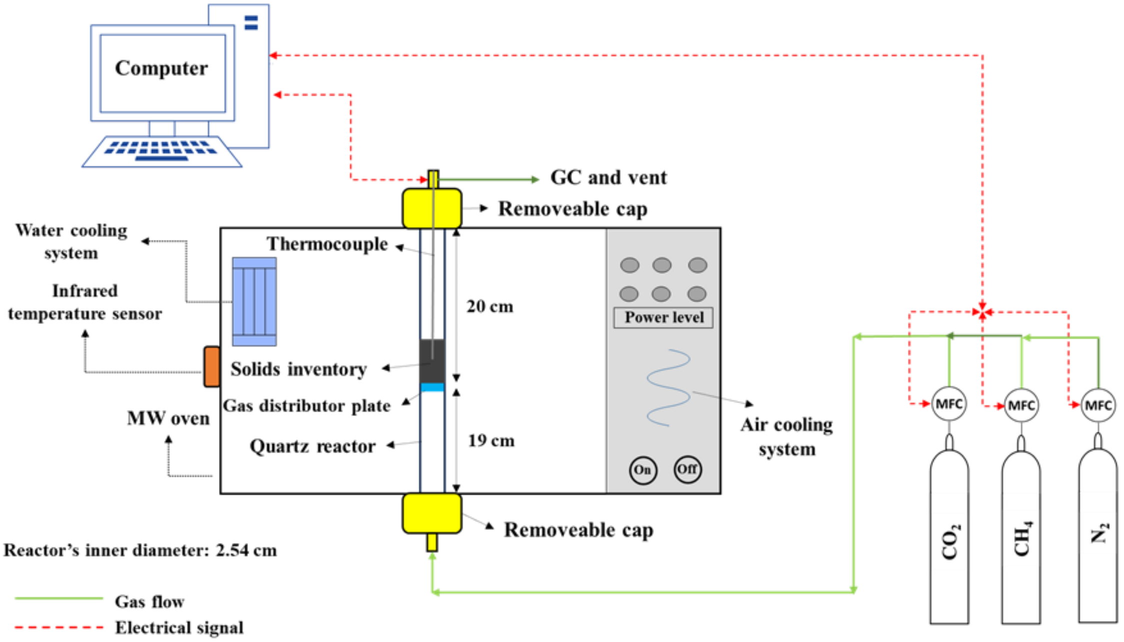

Figure 6.3. A schematic representation of the adopted MWH-assisted laboratory-scale setup.

We conducted laboratory-scale experiments to (i) reduce Fe_3O_4 (with the EM properties shown in Table 6.2) using CH_4 and (ii) oxidize Fe to Fe_3O_4 using CO_2. This was attained by preparing beds of 5 gm and 20 gm, each made of Fe_3O_4. To reduce and re-oxidize the bed, we employed mixtures of CH_4-N_2 and CO_2-N_2. The experimental procedure is summarized as follows:

- Load the solid sample (Fe_3O_4; d_p of 10 µm, and product of ThermoFisher Scientific) to the reactor.
- Feed the reactor with N_2 at 2.7 lit/min for five minutes to fully remove air from the system.
- Increase the reactor temperature to reach T_b = 800°C while feeding N_2 to the reactor at 2.7 lit/min under MWH.
- Switch the feed composition to CH_4-N_2 with 5 and 20 vol.% CH_4, while keeping the gas flowrate at 2.7 lit/min, to reduce 5 and 20 gm of Fe_3O_4, respectively, for 95 seconds.
- After 95 seconds of reduction, change the feed to pure N_2 at 2.7 lit/min of flow, while continuing the MWH to guarantee T_b = 800°C.
- Change the feed gas composition to CO_2-N_2 with 5 and 20 vol.% CO_2 to oxidize 5 and 20 gm of Fe, respectively, for 85 seconds, while keeping the gas flowrate at 2.7 lit/min.
- Switch the feed gas composition to pure N_2, while keeping the gas flowrate at 2.7 lit/min.
- Stop the MWH.
- Preserve an inlet gas flow of 2.7 lit/min of pure N_2 to reach $T_b \leq 40$°C.

Table 6.2. EM characteristics of Fe_3O_4 particles.

Parameter	***Value***	***Reference***
$\varepsilon_{r,p}$ (−)	8 – 2.5j	Measured[a]
$\mu_{r,p}$ (−)	1.5 – 0.3j	Measured
σ_p (S/ m)	0	Measured

[a] By a vector network analyzer.

6.4 Results and discussion

6.4.1 Reactor design: basic parameters

We schematically elucidated the proposed MWH-CSMBR in Figure 6.4.

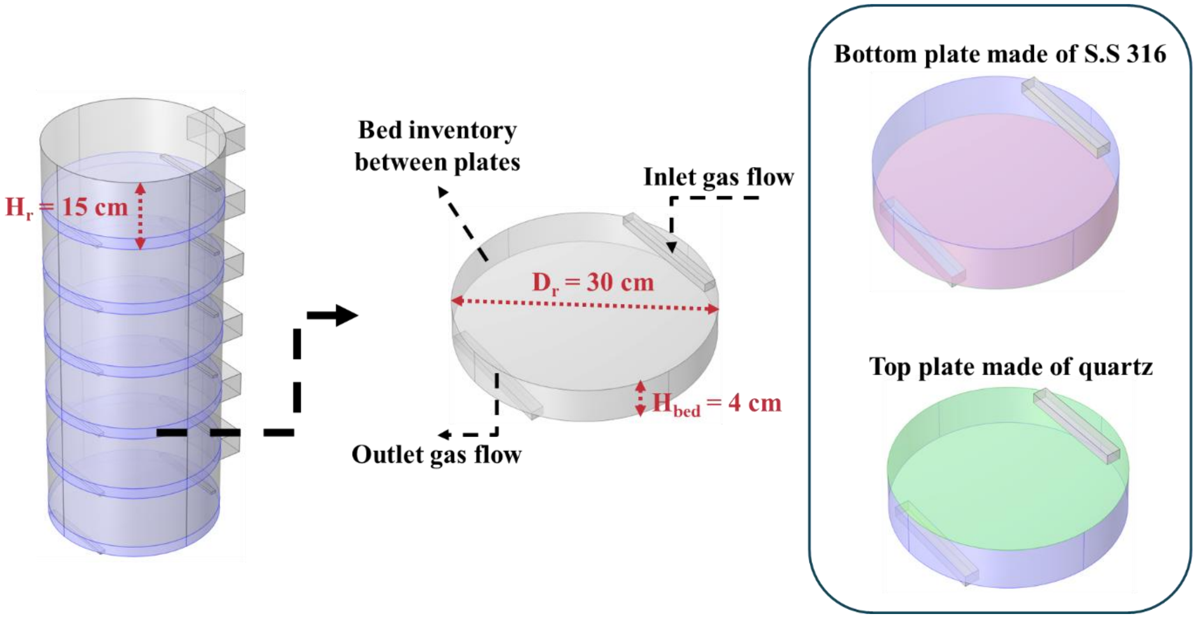

Figure 6.4. Schematic representation of the proposed MWH-CSMBR and the loaded bed of each reactor stage.

To determine the design parameters of the proposed MWH-CSMBR, we initially selected a H_{bed} of 4 cm. This ensured (i) selecting a H_{bed} that is not too tall, allowing the EMWs to reach all the particles within the loaded bed, and (ii) achieving a uniform MWH throughout the loaded bed. In addition, considering (i) the availability of a maximum P_{MW} of 65 kW for the current MW generators, (ii) the endothermic reaction of reducing Fe_3O_4 in the fuel reactor employing CH_4, (iii) total $\dot{m}_{CH_4}$ = 50 tons/day), and (iv) ρ_b of 2125 kg/m^3 for the bed made of 100 wt.% Fe_3O_4, we selected D_r of 30 cm. This decision can also help minimize the effect of standing wave formation throughout each reactor stage. Moreover, to minimize the effect of standing wave formation, we selected 15 cm as the height of each reactor stage H_r. Furthermore, considering the shallow height of the loaded bed (H_{bed} of 4 cm), to maximize the residence time between the gaseous feed and the loaded bed, we applied a network of nozzles evenly distributed over the surface of the bed inventory, shown in Figure 6.4. As shown in this figure, to avoid MW leakage between the reactor stages, we employed a MW-reflective plate made of S.S 316. For the upper plate of the loaded bed, we employed a MW-transparent quartz plate. The MW-reflective plates prevent leakage between reactor stages, while the MW-transparent plates ensure that the MWs introduced into each reactor stage reach the loaded bed. To direct the generated MWs toward the loaded beds, we positioned the waveguide's input port of each reactor stage 3 cm away from the upper wall (plate). We made this decision to minimize the possibility of sparking and arc formation resulting from the interaction of the MWs with sharp edges. Accordingly, the design parameters of the proposed MWH-CSMBR are summarized in Table 6.3. By employing four of the proposed MWH-CSMBR with the design parameters presented in Table 6.3, one can produce syngas with H_2/CO of 2:1 for a total $\dot{m}_{CH_4}$ of 50 tons/day.

Table 6.3. The design parameters of the proposed MWH-CSMBR.

D_r (cm)	30
H_r (cm)	15
H_{bed} (cm)	4
$\dot{m}_{CH_4}$ of each stage (kg/hr)	12
Number of stages (-)	44
Total height of the reactor (m)	7
Waveguide type	WR-340
Waveguide dimensions	3.4 in × 6.8 in

We selected d_p of 250 μm to mitigate the internal mass transfer from controlling the reaction mechanisms, while minimizing the influence of sintering and agglomeration on achieving a stable x_{CH_4}. Further information regarding the effect of d_p on solving the potential issues due to the particle's sintering and agglomeration under the MWH can be found in our previous study [34].

Upon determining the basic design parameters of the proposed MWH-CSMBR, we need to accomplish further simulations to optimize the proposed design. To carry out the simulations, we first determined the optimum mesh resolution in Section 6.4.2. Subsequently, we conducted a set of simulations in Section 6.4.3 to verify and validate the developed model. Lastly, in Section 6.4.4, we conducted a parametric study to investigate the effect of (i) operating conditions (feed flowrate and temperature), (ii) $\mathrm{H_{bed}}$, (iii) material selection, in particular the plates dividing the reactor stages, and (iv) MW introduction to each reactor stage on reactor performance. It should be noted that we considered (i) achieving a maximum $\mathrm{x_{CH_4}}$, while minimizing the total energy consumption, (ii) maximizing the energy transfer ($\mathrm{\eta_{MW}}$), and (iii) achieving a uniform MW dissipation throughout the loaded beds as key reference parameters to analyze the reactor performance.

6.4.2 Grid independency analysis

In this section, we conducted the mesh resolution study to minimize computational costs, while ensuring accurate results with the selected mesh size. To achieve this, we compared the effect of mesh resolution on $\mathrm{\eta_{MW}}$ for a single reactor stage of the MWH-CSMBR illustrated in Figure 6.2. To generate different mesh/cell sizes (summarized in Table 6.4) and investigate their impacts on the simulation's accuracy (Figure 6.5), we considered (i) a bed inventory made of Fe_3O_4 with $\mathrm{d_p}$ = 250 µm and EM properties summarized in Table 6.2, (ii) 30, 15, and 4 cm for $\mathrm{D_r}$, $\mathrm{H_r}$, and $\mathrm{H_{bed}}$, respectively, and (iii) $\mathrm{P_{MW}}$ of 65 kW at a frequency of 2.45 GHz.

Table 6.4. Grid independency analysis of a single reactor stage of the MWH-CSMBR.

Mesh resolution	***Number of meshes***	***Maximum mesh size***
Extra fine	540,280	λ/15
Fine	105,081	λ/12
Normal	28,649	λ/6

Due to the comparable η_{MW} obtained by normal and the extra fine meshes (see Figure 6.5) and the lower cell numbers of the normal mesh resolution (referring to Table 6.4), we selected the normal mesh resolution to simulate the MWH-CSMBR.

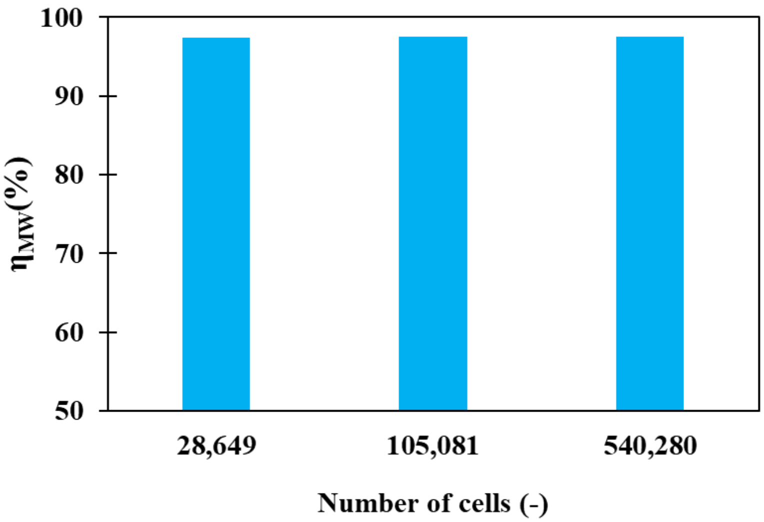

Figure 6.5. Effect of number of cells on η_{MW} for a single reactor stage of the MWH-CSMBR.

6.4.3 Model verification and validation

For model verification, the prediction of electric field intensity $|\vec{E}|$ within a WR-340 waveguide was compared with the results obtained in the study by Yan et al. [45], presented in Figure 6.6b. As shown in this figure, the sinusoidal electric field is well distributed within the waveguide, consistent with the simulation results presented by Yan et al. [45] (Figure 6.6b). Consequently, the developed Multiphysics model was verified.

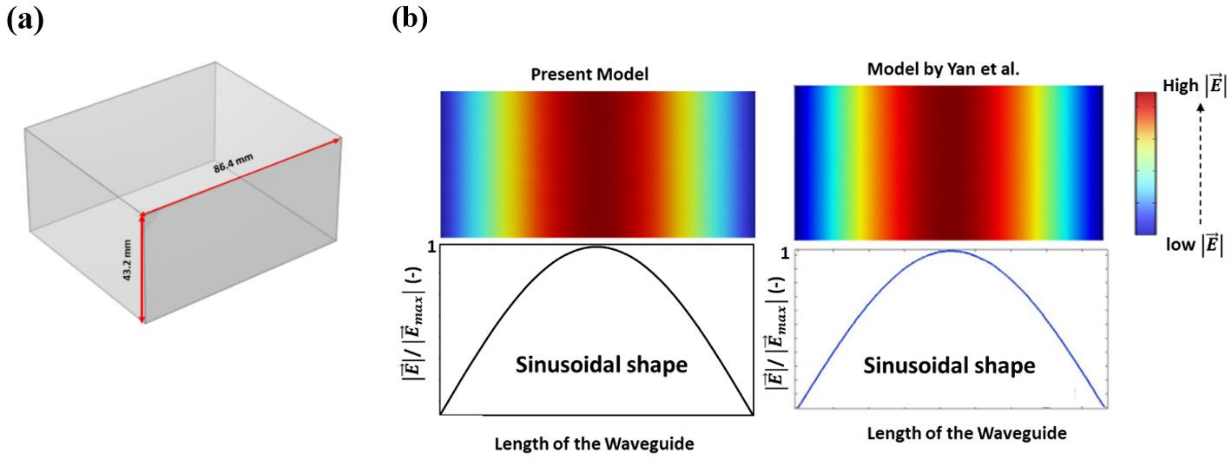

Figure 6.6. Verification of the developed model in this study by comparing its predictions with the corresponding simulation results reported in the study by Yan et al. [45]: a) dimensions and geometry of the WR-340 rectangular waveguide employed for model verification, b) $|\vec{E}|$ distribution simulation results of the present model and those reported in the study by Yan et al. [45] at the cross section of the WR-340 waveguide. $|\vec{E}_{max}|$ represents the maximum $|\vec{E}|$ observed at the cross section of the waveguide.

For model validation, the accuracy of the developed model to predict x_{CH_4} and x_{CO_2} was compared with the corresponding experimental values obtained in the current study. As shown in Figure 6.7, the simulation results match the experimental data, confirming the accuracy of the developed model. It is worth mentioning that, based on the XRD and GC analysis in our previous study [34], at T_b of 800°C, Fe_3O_4 reduction with CH_4 and Fe oxidation with CO_2, respectively, occur via R-6.1 and R-6.2. Consequently, in this study, at T_b of 800°C and under MW irradiation, the model validation based on the rate of Fe_3O_4 reduction and Fe oxidation is equivalent to the model validation for CH_4 and CO_2 conversions, respectively.

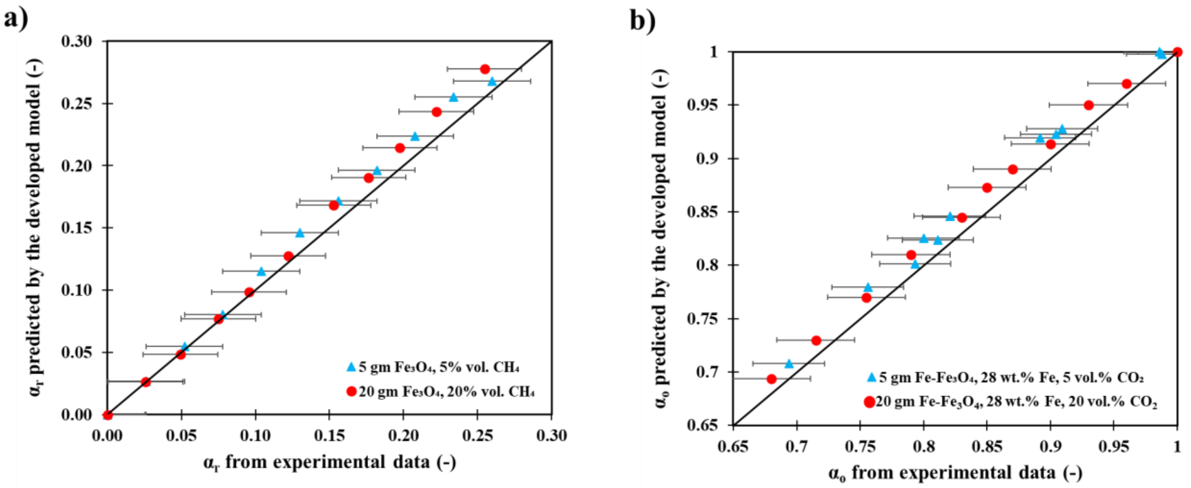

Figure 6.7. Comparison of the developed model and the experimental data for α_r and α_o. Similar to the experimental investigation, d_p was fixed at 10 µm and we assumed an ambient temperature of 25°C to run the simulation. Thermodynamic properties of the gas phase, quartz tube, and Fe_3O_4 were applied using the database of the COMSOL Multiphysics.

6.4.4 Parametric studies

For the parametric studies, we considered the following factors to optimize the design of the proposed MWH-CSMBR: (i) the effect of T_s, $\dot{m}_{CH_4}$, and H_{bed} on x_{CH_4}, (ii) energy efficiency of each reactor stage, i.e., η_{MW} in each reactor stage, (iii) overall energy efficiency of the reactor, i.e., the overall η_{MW}, (iv) uniform distribution of η_{MW} among different reactor stages, and (v) uniform $|\vec{E}|$ throughout the loaded beds.

Unlike the catalytic reforming of CH_4, in non-catalytic Fe_3O_4 reduction by CH_4, consuming Fe_3O_4 (i.e., conversion of Fe_3O_4 to Fe) influences x_{CH_4}. Accordingly, by conducting a dynamic simulation (time dependent), we studied the effect of reaction time on x_{CH_4}, presented in Figure 6.8. As shown in this figure, during the reduction of Fe_3O_4 by CH_4, x_{CH_4} decreases, which can be attributed to the conversion of Fe_3O_4 to Fe, leading in decreased availability of Fe_3O_4 for the conversion of CH_4. However, for the selected reduction time of 95 s in one cycle, we achieved nearly complete and consistent x_{CH_4} (average x_{CH_4} of 0.99). Hence, we assumed a stable condition, i.e., steady CH_4 conversion, to further investigate the effect of operating conditions and design parameters on the performance of the reactor.

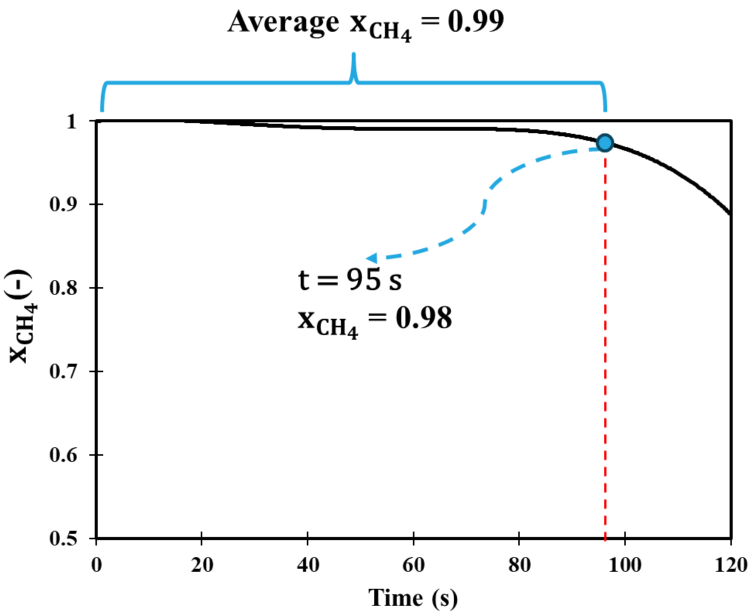

Figure 6.8. The effect reaction time on x_{CH_4} for each reactor stage of the MWH-CSMBR. H_{bed}, T_s, D_r, $\dot{m}_{CH_4}$ of each reactor stage, d_p, and ρ_b were fixed at 4 cm, 950°C, 30 cm, 12 kg/hr, 250 µm, and 2125 kg/m^3, respectively.

6.4.4.1 Effect of temperature on reactor performance

In the first stage of the optimization, we studied the effect of T_s on x_{CH_4}, which is presented in Figure 6.9. As shown in this figure, regarding the endothermic reaction of CH_4 with Fe_3O_4 (R-6.1), by enhancing T_s, x_{CH_4} was increased. However, to minimize the process's energy consumption, while maximizing x_{CH_4}, we selected T_s = 950°C as the optimum temperature.

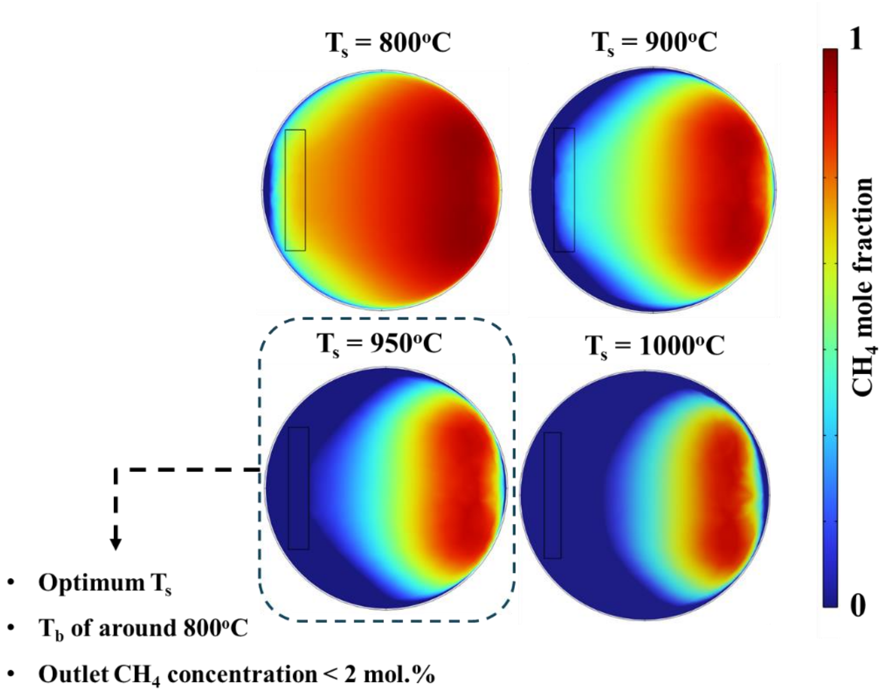

- Optimum T_s
- T_b of around 800°C
- Outlet CH_4 concentration < 2 mol.%

Figure 6.9. The effect of T_s on CH_4 mole fraction distribution throughout the bed inventory. D_r, H_{bed}, $\dot{m}_{CH_4}$ of each reactor stage, d_p, and ρ_b were fixed at 30 cm, 4 cm, 12 kg/hr, 250 µm, and 2125 kg/m^3, respectively.

6.4.4.2 Effect of bed height on reactor performance

In the next step of the optimization, we investigated the effect of H_{bed} on x_{CH_4}, presented in Figure 6.10, to determine the optimum value for H_{bed}. Analyzing Figure 6.10, an increase in H_{bed} leads to an increase in x_{CH_4}, which can be attributed to the longer residence time of the gaseous stream and the higher availability of Fe_3O_4 (bed inventory) to progress the reduction reaction. Consequently, regarding the information presented in Figure 6.10, to achieve a nearly complete x_{CH_4} ($\geq$ 0.98), while minimizing the bed inventory, we selected H_{bed} of 4 cm.

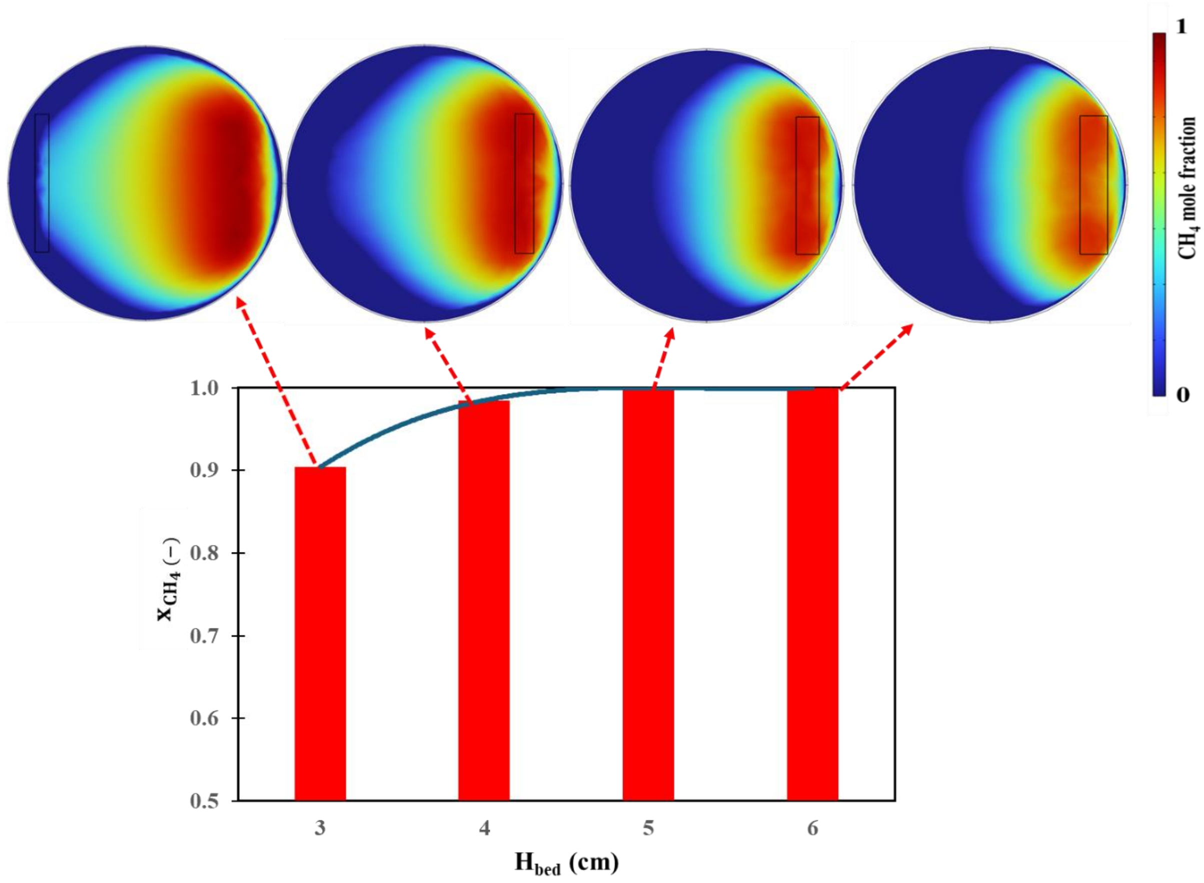

Figure 6.10. The effect H_{bed} on x_{CH_4} for each reactor stage of the MWH-CSMBR. T_s, D_r, $\dot{m}_{CH_4}$ of each reactor stage, d_p, and ρ_b were fixed at 950°C, 30 cm, 12 kg/hr, 250 μm, and 2125 kg/m^3, respectively.

6.4.4.3 Effect of feed flowrate on reactor performance

In this section, we studied the effect of the plant's capacity, i.e., $\dot{m}_{CH_4}$, on x_{CH_4}, presented in Figure 6.11. As shown in this figure, by increasing $\dot{m}_{CH_4}$, x_{CH_4}decreases, which can be attributed to the lower residence time of the gaseous stream. Consequently, regarding the information presented in Figure 6.11, to achieve a nearly complete CH_4 conversion ($x_{CH_4} \geq 0.98$), while maximizing the reactor's capacity, we selected a total $\dot{m}_{CH_4}$ of 50 tons/day. This also meets the required capacity of the industrial-scale syngas production plants.

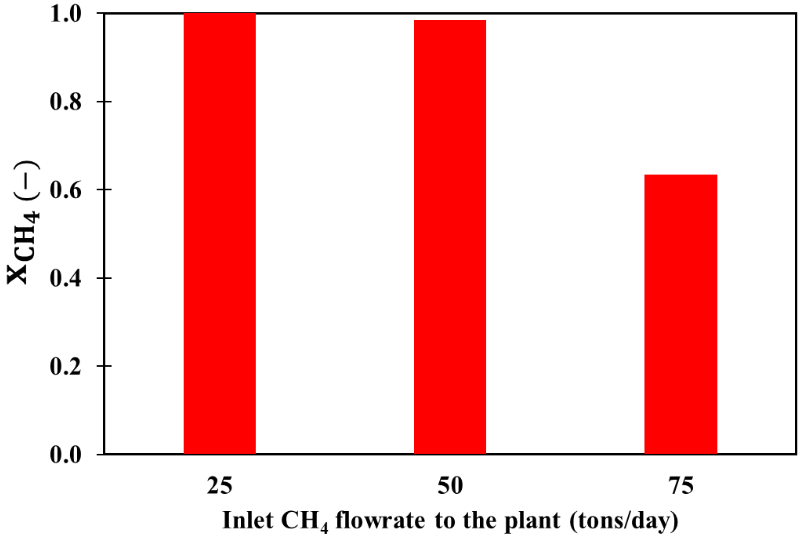

Figure 6.11. The effect of $\dot{m}_{CH_4}$ on x_{CH_4}. T_s, D_r, H_{bed}, d_p, and ρ_b were fixed at 950°C, 30 cm, 4 cm, 250 µm, and 2125 kg/m^3, respectively.

6.4.4.4 Effect of internal design on reactor performance

To ensure an optimum design for the MWH-CSMBR, we also need to optimize the energy efficiency. Accordingly, as shown in Figure 6.12a, we applied two different scenarios for the internal design of the MWH-CSMBR:

- First scenario (referring to Figure 6.12a): Similar to the basic design presented in Section 6.4.1, in this scenario, to mitigate MW leakage between the reactor stages, we employed MW-reflective plates made of S.S 316 to separate the stages (employing S.S 316 for the bottom plates of the loaded bed). For the upper plate of the loaded bed, we employed a MW-transparent quartz plate. The MW-reflective plates prevent leakage between reactor stages, while the MW-transparent plates ensure that the MWs introduced into each reactor stage reach the loaded bed.
- Second scenario (referring to Figure 6.12b): Unlike the first scenario, in this scenario, we replaced the S.S 316 plates with quartz. Therefore, in this configuration, the possible MW leakage from one reactor stage to another is permitted. We proposed this configuration to study its capability to enhance the total MW absorption.

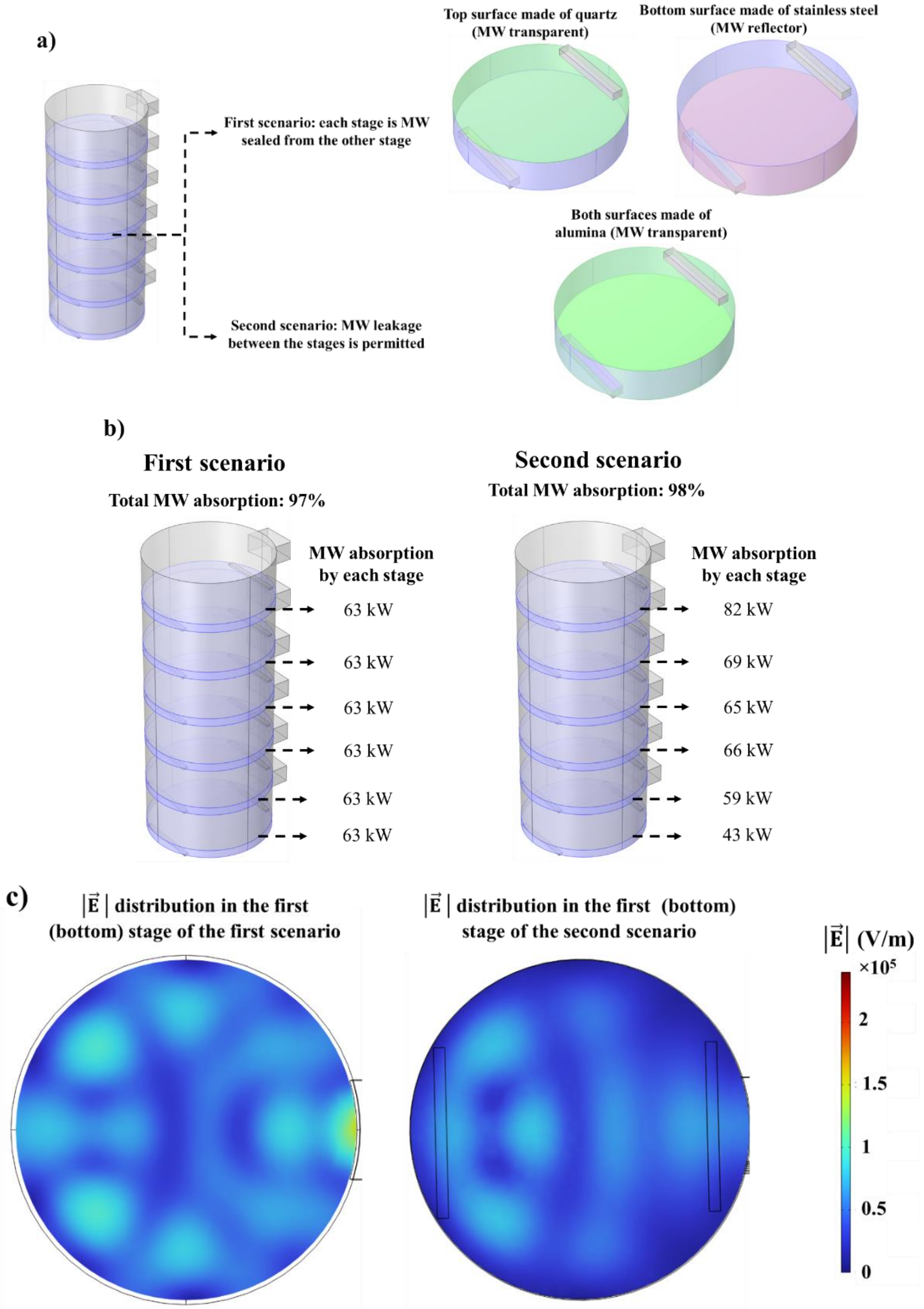

Figure 6.12. a) Bed design of the MWH-CSMBR for two different scenarios, b) MW absorption by the bed inventories for two different scenarios, and c) $|\vec{E}|$ distributions of the first reactor stage (top view) for two different scenarios. D_r, H_r, H_{bed}, d_p, and ρ_b were fixed at 30 cm, 15 cm, 4 cm, 250 µm, and 2125 kg/m^3, respectively. P_{MW} for each reactor stage was fixed at 65 kW with a frequency of 2.45 GHz.

As shown in Figure 6.12, the second scenario had a higher η_{MW}. However, both scenarios guaranteed a total η_{MW} of above 97%. In addition, compared to the first scenario, we observed non-uniform MW dissipation throughout the loaded beds of the second scenario. This non-uniform MW dissipation can be attributed to the placement of the waveguide input port and the interaction of the introduced MW to reactor stage n with stages n-1 and n+1. Although changing the placement of the waveguide input ports to the reactor can yield a uniform MW dissipation throughout the loaded beds of the second scenario, we selected the first scenario (Figure 6.12a) as the optimum design. We decided on this scenario to facilitate the MW tuning and implementation and improve the process flexibility and reliability when employing beds with different EM properties. It is worth mentioning that we selected six reactor stages to compare the proposed scenarios concerning energy efficiency. However, we obtained similar results by altering the number of reactor stages.

6.4.4.5 Effect of microwave introduction on reactor performance

For the last step of the optimization, as shown in Figure 6.13, we studied the impact of waveguide location on η_{MW} and $|\vec{E}|$ distribution. As shown in Figure 6.13, for Position 1 in Figure 6.13, we located the waveguide's input port at 3 cm away from the upper wall (plate). We made this decision to (i) mitigate the possibility of sparking and arc formation resulting from the interaction of the MWs with sharp edges and (ii) avoid standing wave formation in each reactor stage. Simulation results (Figure 6.13) indicate that the maximum η_{MW} is achieved when the waveguide's input port is located in Positions 1 and 3. Therefore, as shown in Figure 6.13, avoiding $|\vec{E}|$ accumulation near the input port of the waveguide in Position 1 outperformed Position 3. It should be noted that $|\vec{E}|$ accumulation near the input port of the waveguide for the Position 3 can be attributed to the proximity of the waveguide to the dense bed. In addition, compared to Position 1 and Position 3, locating the waveguide port at the central height of the solids inventory (Position 2) increases the MW reflection toward the MW source, which decreases η_{MW}.

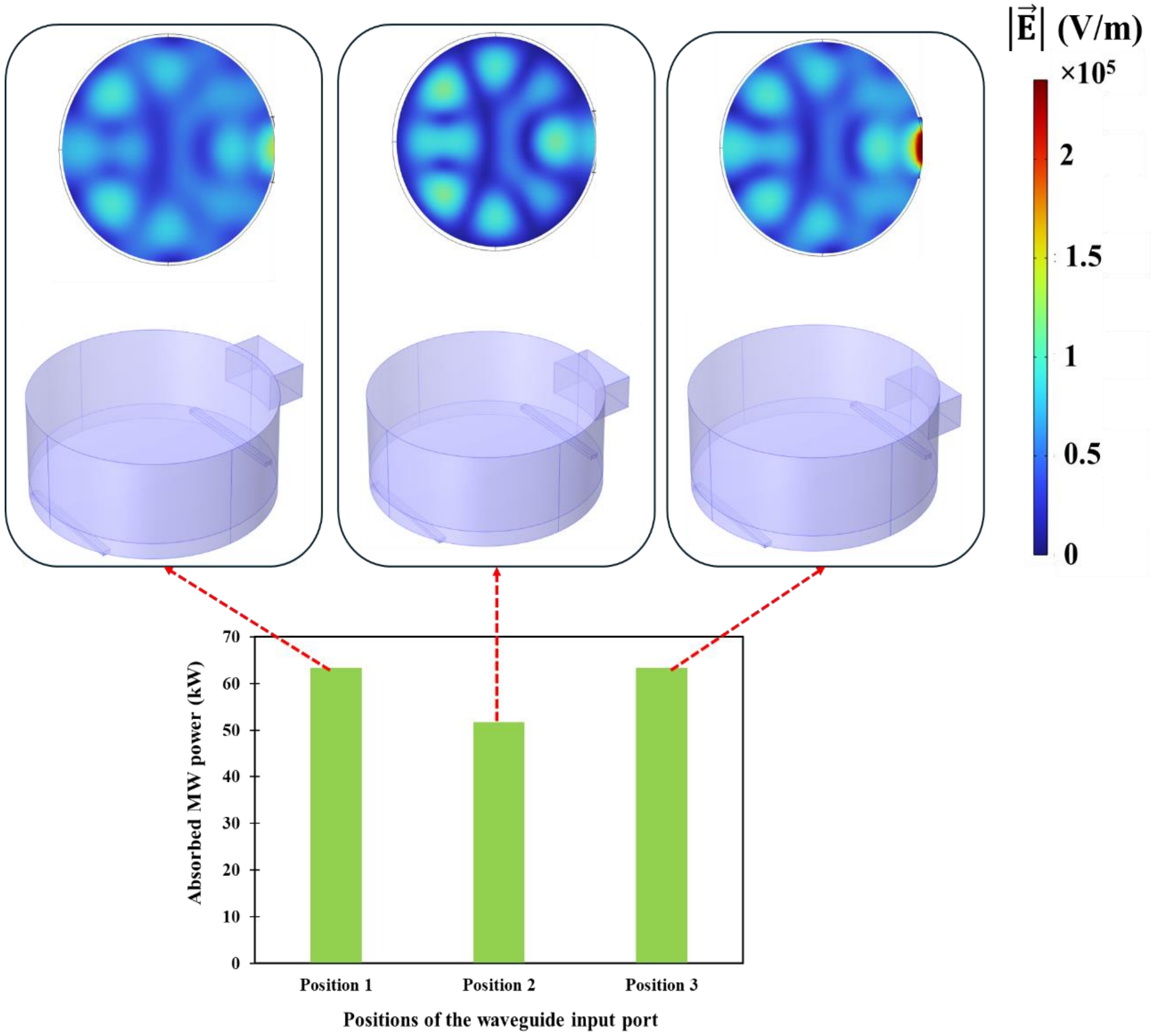

Position 1: Waveguide's input port, 3 cm away from the upper wall

Position 2: Waveguide's input port in the middle of the stage

Position 3: Waveguide's input port right above the loaded bed

Figure 6.13. Effect of waveguide location of a reactor stage for the first scenario presented in Figure 6.12. D_r, H_r, H_{bed}, d_p, and ρ_b were fixed at 30 cm, 15 cm, 4 cm, 250 µm, and 2125 kg/m^3, respectively. P_{MW} was fixed at 65 kW with a frequency of 2.45 GHz.

Based on the simulation results presented in Section 6.4.4, we have summarized the optimal design parameters of the proposed MWH-CSMBR in Table 6.5.

Table 6.5. The optimal design parameters of the proposed MWH-CSMBR.

D_r (cm)	30
H_r (cm)	15
Number of reactor stages (-)	44
Total height of the reactor (m)	7
H_{bed} (cm)	4
T_s (°C)	950
$\dot{m}_{CH_4}$ of each reactor stage (kg/hr)	12
Waveguide type	WR-340
Waveguide dimension	3.4 in × 6.8 in
Location of the waveguide's input port in each reactor stage	3 cm away from the upper wall (plate)
Internal Material selection	(i) S.S 316 to separate the reactor stages. (ii) Quartz for the upper plate of the loaded beds in each reactor stage.

6.5 Conclusion

Installing a large number (typically over a hundred) of MW-heated reactors in parallel is a significant technical challenge that hinders the scaling up of MWH-assisted syngas-generating plants, including MWHCL-DRM, for large-scale applications. Hence, in this study, we introduced a novel MW-heated reactor, i.e., MWH-CSMBR, which addressed this technical challenge. We developed a model that incorporates bed hydrodynamics, reaction kinetics, and mass transfer, coupled with temperature distribution in the loaded bed, to simulate the reactivity of the loaded bed with CH_4 and CO_2. We also applied Maxwell's equation to develop a model for predicting the distribution of EMWs throughout the system.

Upon model verification and validation and designing the reactor, to optimize the operating conditions and design parameters, we simulated a MWH-CSMBR for a plant with a total $\dot{m}_{CH_4}$ of 50 tons/day. We considered the following factors to optimize the design of the proposed MWH-CSMBR: (i) the effect of T_s, plant's capacity, and H_{bed} on x_{CH_4}, (ii) energy efficiency of each reactor stage, i.e., η_{MW} in each reactor stage, (iii) overall energy efficiency of the reactor, i.e., the overall η_{MW}, (iv) uniform distribution of η_{MW} among different reactor stages, and (v) uniform $|\vec{E}|$ throughout the loaded beds. For the optimized design of the proposed MWH-CSMBR, with D_r of 30 cm, H_r of 15 cm, and total height of 7 m, at H_{bed} = 4 cm and T_s = 950°C, we achieved $x_{CH_4} \geq 0.98$ by only four reactors. In addition, we predicted that proper location of a waveguide's input port could yield $\eta_{MW} \geq 97\%$, while minimizing the formation of standing waves throughout the system. Moreover, for the optimized design, the simulation results confirmed a uniform (less than 1% of the relative difference) EMW dissipation within the loaded beds of different reactor stages. Therefore, the MWH-CSMBR mitigated the main technical challenge – application of many reactors in parallel – that impedes the scaling up of the syngas and H_2 production plants heated by MW.

In this study, we developed an innovative MWH-assisted reactor, i.e., MWH-CSMBR. However, to highlight the remaining technical and economic hurdles during the large-scale implementation of the MWHCL-DRM, one needs to execute a comprehensive techno-economic assessment. In addition, to complete a holistic conclusion of this syngas-generating technology, we also recommend conducting a life cycle assessment.

CRediT authorship contribution statement

Mohammad Khodabandehloo: Conceptualization, Formal analysis, Writing - Original draft, Software, Validation, Visualization, Methodology, Investigation, Data curation.

Jaber Shabanian: Project administration, Methodology, Co-supervision, Writing - review & editing.

Jean-Phillipe Harvey: Project administration, Co-supervision, Writing - review & editing, Methodology.

Jamal Chaouki: Conceptualization, Supervision, Resources, Writing - review & editing, Funding acquisition.

Nomenclature

Acronym

CH	Conventional heating
CL-DRM	Chemical looping dry reforming of methane
CHCL-DRM	Conventional heating-assisted chemical looping dry reforming of methane
CL	Chemical looping
CLR	Chemical looping reforming
C-SRM	Catalytic steam reforming of methane
DRM	Dry reforming of methane
EMW	Electromagnetic wave
GHG	Greenhouse gas
MBR	Moving bed reactor
MW	Microwave
MWH	Microwave heating
MWHCL-DRM	Microwave heating-assisted chemical looping dry reforming of methane
MWH-CSMBR	Microwave heating-assisted cyclic simulated moving bed reactor
Redox	Reduction and oxidation
SH	Selective heating
SMB	Simulated moving bed
SMBR	Simulated moving bed reactor
SRM	Steam reforming of methane
VH	Volumetric heating

Symbols

$\vec{j}_i$	Diffusive mass transfer flux of species i (kg/(m^2.s))
$\vec{u}_g$	Local gas velocity (m/s)

C_i	Molar concentration of component i (mol/m^3)
$C_{p,b}$	Specific heat capacity of bulk (J/(kg.°C))
C_{io}	Initial molar concentration of component i (mol/m^3)
$C_{p,g}$	Specific heat capacity of gas phase (J/(kg.°C))
D_{ik}	Diffusion mass transfer coefficient of species i in species k (m/s)
D_i^m	diffusion mass transfer coefficient of species i in the mixture (m^2/s)
D_i^m	Diffusion mass transfer coefficient of species i in the mixture (m/s)
D_r	Inner diameter of the reactor (m)
d_p	Particle size (m)
$\bar{E}$	Electric field (V/m)
$\lvert\vec{E}\rvert$	Electric field intensity (V/m)
H_{bed}	Height of the loaded bed (m)
H_r	Height of each reactor stage (m)
k_b	Thermal conductivity coefficient of bulk (W/(m·K))
k_p	Thermal conductivity coefficient of particle (W/(m·K))
k_g	Thermal conductivity coefficient of gas (W/(m·K))
k_o	Free space wave number (-)
$m_{Fe_3O_4}$	Mass of Fe_3O_4 throughout the bed inventory (gm)
m_{Fe}	Mass of Fe throughout the bed inventory (gm)
$\dot{m}_{CH_4}$	Inlet CH_4 flowrate (kg/s)
n_i	Final mole of component i (mol)
n_{io}	Initial mole of component i (mol)
P_{MW}	Power of irradiate microwaves (J/s)
Q_{CH_4}	Inlet CH_4 flow (l/min)
Q_{CO_2}	Inlet CO_2 flow (l/min)
Q_{N_2}	Inlet N_2 flow (l/min)
q_{MW}	Microwave irradiation that is absorbed by bed inventory (J/s)
q_{we}	convection heat transfer between the reactor wall and the environment (J/s)
r_i	Rate of reaction (consumption) of species i (kg/(m^3.s))
$r_{r/o}$	Rate of redox reactions (1/s)
T_b	Bulk temperature (°C)
T_g	Gas temperature (°C)
T_s	Solid temperature (°C)
x_{CH_4}	CH_4 conversion

x_{CO_2}	CO_2 conversion
x_k	Mole fraction of species k (-)

Greek letters

α	Extent of solid conversion (-)
$\varepsilon_{r,b}$	Relative permittivity of bulk (-)
$\varepsilon_{r,p}$	Relative permittivity of particle (-)
$\varepsilon_{r,g}$	Relative permittivity of gas (-)
$\mu_{r,b}$	Relative permeability of bulk (-)
$\mu_{r,p}$	Relative permeability of particle (-)
$\mu_{r,g}$	Relative permeability of gas (-)
σ_g	Electrical conductivity of gas (S/m)
σ_b	Electrical conductivity of bulk (S/m)
σ_p	Electrical conductivity of particle (S/m)
$\Delta H_{r/o}$	Enthalpy of redox reactions (J/kg)
α_o	Oxidation extent of the solid sample (-)
α_r	Reduction extent of the solid sample (-)
ε_g	Bed voidage (-)
η_{MW}	Microwave absorption efficiency (-)
μ_g	Dynamic viscosity of gas (Pa.s)
ρ_b	Bulk density (kg/m^3)
ρ_g	Gas density (kg/m^3)
ρ_p	Particle density (kg/m^3)
ω_i	Mass fraction of species i (-)
ω	Angular frequency (1/s)
α	Extent of solid conversion (-)

Acknowledgments

It is with sincere gratitude that Mr. Khodabandehloo acknowledges the Fonds de Recherche du Québec - Nature et Technologies (FRQNT) for their scholarship encouragement and support. An additional financial resource for this study was supported by the Natural Sciences and Engineering Research Council of Canada (NSERC), in particular through the Alliance Missions grants (Grant no. ALLPR 570793-2021), as well as the OCP Group of Morocco. To both groups, the authors offer their deepest appreciation. Mr. Khodabandehloo would like to express his sincere gratitude to Mr. Siavash Beigiparast for his invaluable insights and brainstorming sessions during this work.

6.6 References

1. Abdul Mujeebu, M., Hydrogen and syngas production by superadiabatic combustion – A review. Applied Energy, 2016. 173: pp. 210-224, https://doi.org/10.1016/j.apenergy.2016.04.018.
2. de Dios García, I., A. Stankiewicz and H. Nigar, Syngas production via microwave-assisted dry reforming of methane. Catalysis Today, 2021. 362: pp. 72-80, https://doi.org/10.1016/j.cattod.2020.04.045.
3. Hamzehlouia, S., S.A. Jaffer and J. Chaouki, Microwave heating-assisted catalytic dry reforming of methane to syngas. Scientific reports, 2018. 8(1): pp. 1-7, https://doi.org/10.1038/s41598-018-27381-6.
4. Zhang, Q., L. Wang, W. Chen and C. Zhang, Assessing the impact of hydrogen trade towards low-carbon energy transition. Applied Energy, 2024. 376: pp. 124233, https://doi.org/10.1016/j.apenergy.2024.124233.
5. Park, J., S. Kang, S. Kim, H. Kim, S.-K. Kim and J.H. Lee, Optimizing green hydrogen systems: Balancing economic viability and reliability in the face of supply-demand volatility. Applied Energy, 2024. 368: pp. 123492, https://doi.org/10.1016/j.apenergy.2024.123492.
6. Rissman, J., C. Bataille, E. Masanet, N. Aden, W.R. Morrow, N. Zhou, N. Elliott, R. Dell, N. Heeren, B. Huckestein, J. Cresko, S.A. Miller, J. Roy, P. Fennell, B. Cremmins, T. Koch Blank, D. Hone, E.D. Williams, S. de la Rue du Can, B. Sisson, M. Williams, J. Katzenberger, D. Burtraw, G. Sethi, H. Ping, D. Danielson, H. Lu, T. Lorber, J. Dinkel and J. Helseth, Technologies and policies to decarbonize global industry: Review and assessment of mitigation drivers through 2070. Applied Energy, 2020. 266: pp. 114848, https://doi.org/10.1016/j.apenergy.2020.114848.
7. Gradisher, L., B. Dutcher and M. Fan, Catalytic hydrogen production from fossil fuels via the water gas shift reaction. Applied Energy, 2015. 139: pp. 335-349, https://doi.org/10.1016/j.apenergy.2014.10.080.
8. Kalamaras, C.M. and A.M. Efstathiou. Hydrogen production technologies: current state and future developments. in Conference papers in science. 2013. Hindawi https://doi.org/10.1155/2013/690627.
9. Mondal, K., S. Sasmal, S. Badgandi, D.R. Chowdhury, V.J.E.S. Nair and P. Research, Dry reforming of methane to syngas: a potential alternative process for value added chemicals—a techno-economic perspective. 2016. 23(22): pp. 22267-22273, https://doi.org/10.1007/s11356-016-6310-4.

10. Beccarello, M. and G. Di Foggia, Review and perspectives of key decarbonization drivers to 2030. Energies, 2023. 16(3): pp. 1345, https://doi.org/10.3390/en16031345.

11. Bouaboula, H., J. Chaouki, Y. Belmabkhout and A. Zaabout, Comparative review of Direct air capture technologies: From technical, commercial, economic, and environmental aspects. Chemical Engineering Journal, 2024. 484: pp. 149411, https://doi.org/10.1016/j.cej.2024.149411.

12. Tang, M., L. Xu and M. Fan, Progress in oxygen carrier development of methane-based chemical-looping reforming: A review. Applied Energy, 2015. 151: pp. 143-156, https://doi.org/10.1016/j.apenergy.2015.04.017.

13. Zhu, Y., N. Jin, R. Liu, X. Sun, L. Bai, H. Tian, X. Ma and X. Wang, Bimetallic BaFe2MAl9O19 (M = Mn, Ni, and Co) hexaaluminates as oxygen carriers for chemical looping dry reforming of methane. Applied Energy, 2020. 258: pp. 114070, https://doi.org/10.1016/j.apenergy.2019.114070.

14. Shah, V., Z. Cheng, D.S. Baser, J.A. Fan and L.-S. Fan, Highly Selective Production of Syngas from Chemical Looping Reforming of Methane with CO2 Utilization on MgO-supported Calcium Ferrite Redox Materials. Applied Energy, 2021. 282: pp. 116111, https://doi.org/10.1016/j.apenergy.2020.116111.

15. Kang, D., H.S. Lim, M. Lee and J.W. Lee, Syngas production on a Ni-enhanced Fe2O3/Al2O3 oxygen carrier via chemical looping partial oxidation with dry reforming of methane. Applied Energy, 2018. 211: pp. 174-186, https://doi.org/10.1016/j.apenergy.2017.11.018.

16. Lu, C., K. Li, H. Wang, X. Zhu, Y. Wei, M. Zheng and C. Zeng, Chemical looping reforming of methane using magnetite as oxygen carrier: Structure evolution and reduction kinetics. Applied Energy, 2018. 211: pp. 1-14, https://doi.org/10.1016/j.apenergy.2017.11.049.

17. Li, D., R. Xu, Z. Gu, X. Zhu, S. Qing and K. Li, Chemical-looping conversion of methane: a review. Energy Technology, 2020. 8(8): pp. 1900925, https://doi.org/10.1002/ente.201900925.

18. Ramezani, R., L. Di Felice and F. Gallucci, A review of chemical looping reforming technologies for hydrogen production: recent advances and future challenges. Journal of Physics: Energy, 2023 https://doi.org/10.1088/2515-7655/acc4e8.

19. Chein, R.-Y. and W.-H. Hsu, Thermodynamic analysis of syngas production via chemical looping dry reforming of methane. Energy, 2019. 180: pp. 535-547, https://doi.org/10.1016/j.energy.2019.05.083.

20. Chaouki, J., P. Leclerc, A. Solouki, M. Monzavi, A. Hussain, Z. Chen and A. Amini, Non-uniform Microwave Heating of Heterogeneous Systems: How to Turn Problems into Opportunities. 2023 https://doi.org/10.1039/BK9781837670277-00347.

21. Chaouki, J., S. Farag, M. Attia and J. Doucet, The development of industrial (thermal) processes in the context of sustainability: The case for microwave heating. The Canadian Journal of Chemical Engineering, 2020. 98(4): pp. 832-847, https://doi.org/10.1002/cjce.23710.

22. Adavi, K., J. Shabanian and J. Chaouki, Temperature Distribution Assessment in Gas–Solid Reactive and Nonreactive Systems Heated by Microwaves. Industrial & Engineering Chemistry Research, 2023 https://doi.org/10.1021/acs.iecr.3c00575.

23. Monzavi, M. and J. Chaouki, Microwave catalytic pyrolysis of heavy oil: A lump kinetic study approach. Journal of Analytical and Applied Pyrolysis, 2024. 179: pp. 106472, https://doi.org/10.1016/j.jaap.2024.106472.

24. Adavi, K., A. Amini, M. Latifi, J. Shabanian and J. Chaouki, Kinetic study of multiphase reactions under microwave irradiation: a mini-review. Frontiers in Chemical Engineering: pp. 102, https://doi.org/10.3389/fceng.2022.1059160.

25. Solouki, A., S.A. Jaffer and J. Chaouki, Process development and techno-economic analysis of microwave-assisted demetallization and desulfurization of crude petroleum oil. Energy Reports, 2022. 8: pp. 4373-4385, https://doi.org/10.1016/j.egyr.2022.03.122.

26. Hamzehlouia, S., M. Latifi and J. Chaouki, Development of a novel silica-based microwave receptor for high temperature processes. Powder technology, 2022. 399: pp. 117180, https://doi.org/10.1016/j.powtec.2022.117180.

27. Amini, A., M. Latifi and J. Chaouki, Electrification of materials processing via microwave irradiation: A review of mechanism and applications. Applied Thermal Engineering, 2021. 193: pp. 117003, https://doi.org/10.1016/j.applthermaleng.2021.117003.

28. Hamzehlouia, S., J. Shabanian, M. Latifi and J. Chaouki, Effect of microwave heating on the performance of catalytic oxidation of n-butane in a gas-solid fluidized bed reactor. Chemical Engineering Science, 2018. 192: pp. 1177-1188, https://doi.org/10.1016/j.ces.2018.08.054.

29. Hamzehlouia, S., S.A. Jaffer and J. Chaouki, Microwave heating-assisted catalytic dry reforming of methane to syngas. Scientific reports, 2018. 8(1): pp. 8940, https://doi.org/10.1038/s41598-018-27381-6.

30. Wang, J., M. Wen, X. La, J. Ren, J. Jiang and D.C.W. Tsang, Resonance-driven microwave heating for improved methane conversion to hydrogen. Applied Energy, 2024. 375: pp. 124100, https://doi.org/10.1016/j.apenergy.2024.124100.

31. Cui, Y., Y. Zhang, L. Cui, Q. Xiong and E. Mostafa, Microwave-assisted fluidized bed reactor pyrolysis of polypropylene plastic for pyrolysis gas production towards a sustainable development. Applied Energy, 2023. 342: pp. 121099, https://doi.org/10.1016/j.apenergy.2023.121099.

32. Li, J., J. Tao, B. Yan, K. Cheng, G. Chen and J. Hu, Microwave reforming with char-supported Nickel-Cerium catalysts: A potential approach for thorough conversion of biomass tar model compound. Applied Energy, 2020. 261: pp. 114375, https://doi.org/10.1016/j.apenergy.2019.114375.

33. Appleton, T.J., R.I. Colder, S.W. Kingman, I.S. Lowndes and A.G. Read, Microwave technology for energy-efficient processing of waste. Applied Energy, 2005. 81(1): pp. 85-113, https://doi.org/10.1016/j.apenergy.2004.07.002.

34. Khodabandehloo, M., J. Shabanian, J.-P. Harvey and J. Chaouki, Microwave heating-assisted chemical looping dry reforming of methane. International Journal of Hydrogen Energy, 2024. 71: pp. 1380-1391, https://doi.org/10.1016/j.ijhydene.2024.05.295.

35. Szima, S. and C.-C. Cormos, CO2 utilization technologies: A techno-economic analysis for synthetic natural gas production. Energies, 2021. 14(5): pp. 1258.

36. Lee, K., P. Sun, A. Elgowainy, K.H. Baek and P. Bobba, Techno-economic and life cycle analysis of synthetic natural gas production from low-carbon H2 and point-source or atmospheric CO2 in the United States. Journal of CO2 utilization, 2024. 83: pp. 102791, https://doi.org/10.1016/j.jcou.2024.102791.

37. Chen, C., H.-H. Lee, W. Chen, Y.-C. Chang, E. Wang, C.-H. Shen and K.-E. Huang, Study of an Iron-Based Oxygen Carrier on the Moving Bed Chemical Looping System. Energy & fuels, 2018. 32(3): pp. 3660-3667, https://doi.org/10.1021/acs.energyfuels.7b03721.

38. Xu, D., Y. Zhang, T.-L. Hsieh, M. Guo, L. Qin, C. Chung, L.-S. Fan and A. Tong, A novel chemical looping partial oxidation process for thermochemical conversion of biomass to syngas. Applied Energy, 2018. 222: pp. 119-131, https://doi.org/10.1016/j.apenergy.2018.03.130.

39. Kong, F., C. Li, Y. Zhang, Y. Gu, M. Kathe, L.-S. Fan and A. Tong, Hydrogen Production from Natural Gas Using an Iron-Based Chemical Looping Technology: Process Modeling, Heat Integration, and Exergy Analysis. Energy Technology, 2020. 8(8): pp. 1900377, https://doi.org/10.1002/ente.201900377.

40. Chiu, P.-C., Y. Ku, H.-C. Wu, Y.-L. Kuo and Y.-H. Tseng, Spent isopropanol solution as possible liquid fuel for moving bed reactor in chemical looping combustion. Energy & fuels, 2014. 28(1): pp. 657-665, https://doi.org/10.1021/ef4012438.

41. Tong, A., L. Zeng, M.V. Kathe, D. Sridhar and L.-S. Fan, Application of the Moving-Bed Chemical Looping Process for High Methane Conversion. Energy & fuels, 2013. 27(8): pp. 4119-4128, https://doi.org/10.1021/ef3020475.

42. Hedong, Z., G. Zuopeng, A. Wenya, F. Jie, R. Chunmei, M. Xiao, K. Qinhao, L. Yang, L. Guangqing and C. Xiaochun, Characterization and analysis of textile sludge char from moving bed pyrolyser under microwave irradiation. CIESC Journal, 2017. 68(6): pp. 2510.

43. Bai, X. and P. Muley, Microwave-assisted Moving-bed Gasifier Design for Solid Fuel Conversion. 2023, National Energy Technology Laboratory (NETL), Pittsburgh, PA, Morgantown, WV ….

44. Ogden, J.M., Review of small stationary reformers for hydrogen production. Report to the international energy agency, 2001. 609.

45. Yan, P., A.I. Stankiewicz, F.E. Sarabi and H. Nigar, Microwave heating in heterogeneous catalysis: Modelling and design of rectangular traveling-wave microwave reactor. Chemical Engineering Science, 2021. 232: pp. 116383, https://doi.org/10.1016/j.ces.2020.116383.

CHAPTER 7 INDUSTRIAL-SCALE HYDROGEN PRODUCTION VIA MICROWAVE HEATING-ASSISTED CHEMICAL LOOPING DRY REFORMING OF METHANE: TECHNO-ECONOMIC EVALUATION AND LIFE CYCLE ASSESSMENT WITH INTEGRATED CARBON CAPTURE AND UTILIZATION

7.1 Introduction

As articulated earlier in CHAPTER 6, the inventive solution of microwave heating-assisted cyclic simulated moving bed reactor (MWH-CSMBR) could resolve the technical bottleneck of operating numerous MW-heated reactors together in syngas and hydrogen (H_2) manufacturing plants, e.g., MWH-assisted chemical looping dry reforming of methane (MWH-CLDRM). Hence, to stress on the remaining technical bottlenecks and economic setbacks during the large-scale execution of the MWHCL-DRM for H_2 manufacturing, we undertook TEA, where TEA stands for techno-economic analysis. To execute the TEA for large-scale MWHCL-DRM targeting at H_2 manufacturing through separation of H_2 from syngas, we used an industrial process simulator (IPS; Aspen Plus software) merged with the results of the Multiphysics simulation tool (COMSOL Multiphysics software in CHAPTER 6). To deliver an extensive conclusion of this H_2 manufacturing solution, we also measured its environmental footprints via the executed life cycle assessment (LCA).

In this chapter, we first built the process flow diagram of the MWHCL-DRM for H_2 manufacturing (Section 7.2.1). Additionally, the requisite steps to execute the detailed economic analysis was articulated in Section 7.2.3. Moreover, to study the environmental footprints of this H_2 manufacturing solution, we applied the cradle to gate method for executing the LCA, articulated in Section 7.2.4.

To execute the plant's mass and energy (ME) balances, we relied on the constructed model in CHAPTER 6 for simulating CH_4 conversion x_{CH_4} and CO_2 conversion x_{CO_2} in the MWH-CSMBR (Section 7.2.2). The simulated x_{CH_4} and x_{CO_2}were then entered to the process simulation to execute the plant's ME balances (Section 7.3.1). The requisite design parameters for succeeding equipment cost evaluation were also delivered (Section 7.3.1). Hence, by executing the plant's mass balance, along with its energy balance, as well as calculating the design parameters of the unit operations, total costs/expenses of production (TCOP) was estimated (Section 7.3.2.1). We also executed an extensive sensitivity analysis to identify the influence of independent parameters on TCOP (Section 7.3.2.2). In addition, we estimated CO_2 equivalent (eq) and energy consumption of the MWHCL-DRM for H_2 manufacturing (Section 7.3.3).

7.2 Method

To design the plant's process sequence and execute the TEA and LCA, we applied the steps outlined below:

1. We fixed the plant's feed at 50 tons-CH_4/day to compare the designed plant's TCOP with that of conventional gaseous H_2 manufacturing plants [1].
2. We created a process flow diagram to identify the process sequence and the unit operations.
3. We relied on the constructed model in CHAPTER 6 for simulating $x_{\mathrm{CH_4}}$ and $x_{\mathrm{CO_2}}$.
4. Upon simulating $x_{\mathrm{CH_4}}$ and $x_{\mathrm{CO_2}}$, we executed the plant's ME balances employing Aspen Plus software. Gas and solid phases properties were respectively calculated using the Peng-Robinson equation of state and ideal solid.
5. We determined the essential design parameters for evaluating capital expenditures (CAPEX) and operating expenditures (OPEX).
6. We estimated CAPEX, OPEX, and TCOP.
7. We executed a sensitivity analysis to underline the factors affecting TCOP.
8. We executed a cradle to gate LCA to estimate the CO_2 eq and energy consumption of the plant.

7.2.1 Process design

The constructed process for a plant with an inlet flowrate of 50 tons-CH_4/day is outlined in Figure 7.1. As shown in this figure, we divided the process into 5 sections. In Section 1, the redox reactions progress to manufacture syngas via R-01 (the reducer reactor) and CO via R-02 (the oxidizer reactor). Although pressure swing adsorption (PSA) is industrially validated to separate H_2 from a gaseous stream, H_2 separation from syngas is not recommended for syngas streams with moderate to high molar concentration (above 5 mol.%) of CO. Instead, the industrial-scale plants suggest converting CO to H_2 applying the reaction of water gas shift to: (i) increase the rate of H_2 manufacturing, and (ii) facilitate the separation of H_2 from CO_2 in comparison with the mixture of H_2 and CO. Therefore, by employing a shift reactor at high temperature (R-03; inlet temperature of 340°C) and a shift reactor at low temperature (R-04; inlet temperature of 180°C), the CO content of the manufactured syngas (exhaust gaseous stream of the R-01) was mainly (more than 97% of CO conversion) converted to H_2 via R-03 and R-04. Followed by converting the CO content of syngas to CO_2 via Section 2 of Figure 7.1, we designed Section 3 to remove the water content of the gaseous stream via a condenser (Sep-01). Sep-01 was capable of decreasing the H_2O content of the gaseous stream to around 3 mol.%. We then employed a packed bed column made of silica gel (Sep-02) to decrease the H_2O content of the gaseous stream to below 0.1 mol.% before entering the stream to the H_2 and CO_2 separation section (Section 4 of Figure 7.1). It should be also noted that to modify the generated H_2/CO ratio, the oxidizer reactor's gaseous inlet flowrate can be modified by co-injection of H_2O and CO_2 or by injection of pure H_2O. For instance, feeding the oxidizer reactor via H_2O enables inherent pure H_2 production, which accordingly enhances the total H_2/CO ratio to 3, meeting the H_2/CO ratio of steam reforming of natural gases.

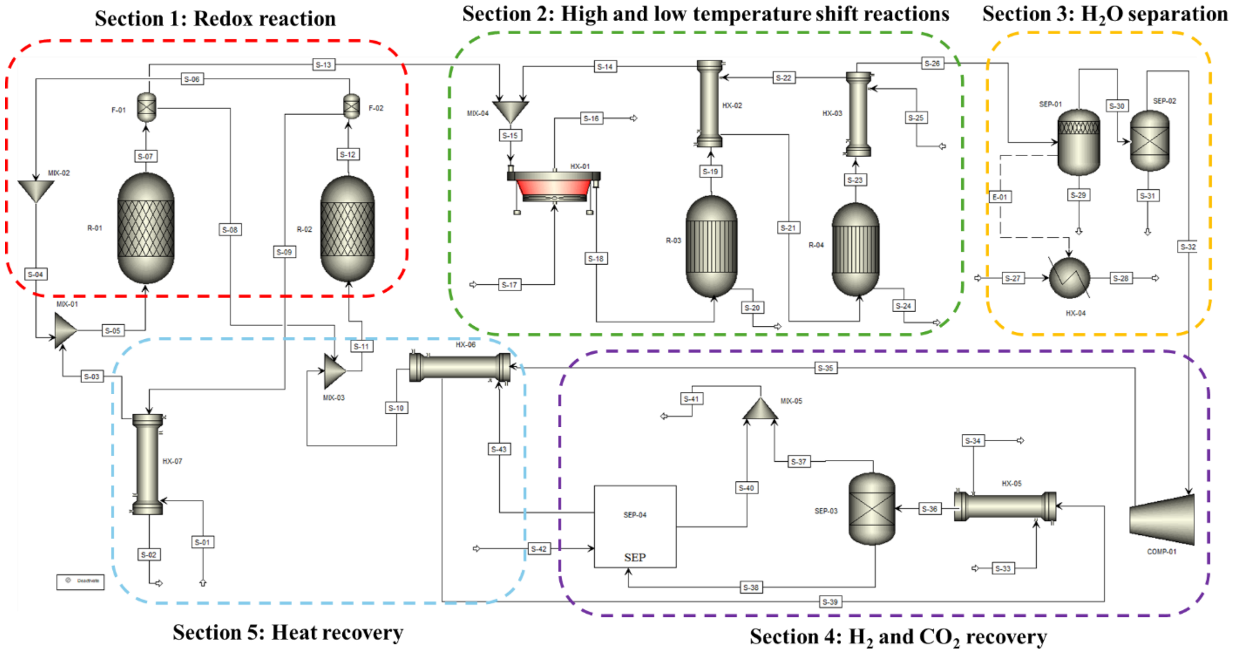

Figure 7.1. The constructed process for the MWHCL-DRM plant.

Aspen Plus software solves unit operations and processes sequentially, meaning that a recycle stream in Aspen Plus is resolved iteratively. To achieve convergence, Aspen Plus adapts the tearing method, starting with the tear stream (the recycled stream). Consequently, when a stream is recycled, it creates an iteration procedure from the tear stream. If an initial value is provided for the tear stream, Aspen Plus software begins the iteration from that value; otherwise, it starts from zero. In our study, we have two streams recycled back into the process, both handled as tear streams. To ensure appropriate initial values for these iterations, we utilized the "Calculator" subroutine in Aspen Plus software. The design specification's key role is to determine and input the appropriate initial guess. To ensure our initial guesses are accurate, we employed the following method:

- For the CO_2 stream recycled back into the system, we employed the outlet CO flow from the oxidizer reactor as the initial guess.
- For the Fe_3O_4 recycled back, we employed the stoichiometric ratio of CH_4 to Fe_3O_4, considering a 0.27 conversion of Fe_3O_4, as shown in reaction R-6.1 of CHAPTER 6.

We need to ensure steady operation of the plant, i.e., steady syngas manufacturing. As detailed in CHAPTER 6, the constructed MWH-CSMBRs in this study can deliver a steady syngas manufacturing. However, to progress the process simulation via the IPS, we operated two reactors (R-01 and R-02 presented in Figure 7.1) together, as outlined in Figure 7.1. As displayed in this figure, Fe_3O_4 is reduced by CH_4 within the first reactor (R-01 in Figure 7.1) to manufacture syngas. Simultaneously, in the second reactor (R-02 in Figure 7.1), by employing CO_2, iron (Fe) is re-oxidized to Fe_3O_4 to manufacture CO. Based on our previous experimental studies in a lab-scale reactor [2], for reduction molar conversion α_r of up to 0.27, we detected a negligible (<3%) temperature fluctuation within the medium. Correspondingly, we continued the reduction reaction in R-01 till attaining α_r of 0.27. Considering the kinetic data represented in Section 6.2.2.2 of CHAPTER 6 and based on the inlet CH_4 to the reducer reactor (R-01), for T_b of 800°C, we achieved α_r of 0.27 after 95 s. After attaining to α_r of 0.27, to fully oxidize Fe to Fe_3O_4 (oxidation molar conversion α_o of 1), based on the kinetic data represented in Section 6.2.2.2 of CHAPTER 6 and the inlet flow of CO_2 to the oxidizer reactor (R-02), one needs to progress the oxidation for 85 s. Therefore, we selected a cyclic period of 180 s for the constructed process. To ensure steady syngas manufacturing, we took the following factors into account for the operation of the reactors:

- We assumed that beds of R-01 and R-02 initially contained 100 wt.% Fe_3O_4 and Fe-Fe_3O_4 mixture (27 wt.% Fe), respectively.
- R-01 operation: we at first fed CH_4 for 95 s to get $\alpha_r = 0.27$. We then halted CH_4 injection and R-01 acted as an oxidizer reactor, i.e., we injected CO_2. After 85 s of feeding CO_2, we succeeded $\alpha_o = 1$, i.e., bed with 100 wt.% Fe_3O_4. We ceased CO_2 injection, and the cycle continued (CH_4 was injected again).
- R-02 operation: we at first fed CO_2 for 85 s to get $\alpha_o = 1$. We then ceased CO_2 injection and R-02 behaved as a reducer reactor, i.e., we fed CH_4. After 95 s of CH_4 injection, we succeeded $\alpha_r = 0.27$. Subsequently, we ceased CH_4 injection, and the cycle continued (feeding CO_2 again).

As showed in Figure 7.1, to decrease the total energy consumption of the plant, instead of a conventional PSA, we chose an elevated temperature PSA (ET-PSA; Sep-03 Figure 7.1) for separating H_2. PSA, a proven H_2 separation technique, usually operates at temperature and pressure in the ranges of 25 to 75^oC and 15-25 bar, respectively. Instead of the PSA, one can adopt an ET-PSA for separating H_2 at a temperature up to 200^oC. This separation unit can separate H_2 from the gas with 80-95% of H_2 recovery and achieving an ultra-pure H_2 stream, i.e., a gaseous stream with more than 99.99 mol.% of H_2 purity. Hence, to separate H_2, we first pressurized the produced syngas to an elevated pressure (20 bar, which was selected regarding the similar H_2 separation units) by the compressor (COMP-01 in Figure 7.1). Afterwards, to cool down the pressurized stream to 200^oC, we applied a heat exchanger (HX-05 in Figure 7.1). The CO_2-enriched stream (S-38 in Figure 7.1), which contained 85 mol.% of CO_2, was then sent to the CO_2 capturing unit (SEP-04) to provide the required CO_2 of the oxidizer reactor (R-02 in Figure 7.1). This separation helped supply the requisite CO_2 feed for the plant. Stream S-42 in Figure 7.1 was also utilized to supply the remaining CO_2 needed for the R-02 in Figure 7.1. Stream S-42 in Figure 7.1 contributed to less than 3 mol.% of the required CO_2 of the plant and CO_2 capturing was capable of providing more than 97 mol.% of the required CO_2 for R-02 in Figure 7.1. Stream S-40 in Figure 7.1, which is the H_2 reached (more than 84 mol.% of H_2 content) outlet stream of CO_2 capturing unit, was mixed with the recover H_2 via the ET-PSA (Sep-03 in Figure 7.1) to finally achieve a high purity H_2 stream (more than 99 mol.% H_2 in stream S-41 in Figure 7.1) as the final H_2 manufacturing of the plant.

Electricity consumption is a critical factor in decreasing the TCOP for H_2 manufacturing plants powered by electricity. Accordingly, as implied in Figure 7.1, before entering CH_4 and CO_2 streams to R-01 and R-02 in Figure 7.1, by employing heat exchangers (HX-06 and HX-07 in Section 5 of Figure 7.1; shell and tube types), we leveraged the heat content of the exhaust gaseous streams to decrease the total energy consumption of the reactors. In addition, as featured in Figure 7.1, by taking advantage of the heat content of the exhaust gaseous stream from R-01, i.e., syngas, we preheated the fed streams to the shift reactors (R-03 and R-04 in Figure 7.1).

7.2.2 Reactor simulation

Aspen Plus software, as an IPS, offers a user-friendly environment with an extensive thermodynamic package for gas, liquid, and solid phases, while providing ideal chemical unit operations, such as plug flow and completely mixed reactors. Nevertheless, the complex dynamic of gas-solid mediums renders the ideal chemical units provided by IPSs inadequate to accurately simulate the behavior of the fixed and fluidized bed reactors. Contrary to Aspen Plus software, the COMSOL Multiphysics software can examine the performance of the MWH-assisted fixed/packed bed reactors by coupling the hydrodynamic behavior of the medium with the kinetic and temperature distribution models. Therefore, we employed the model constructed in CHAPTER 6 to simulate the MWH-CSMBR. Subsequently, as implied in Figure 7.2, we adopted the calculated x_{CH_4} and x_{CO_2} by the simulation to carry out the “RStoic” reactor module of the Aspen Plus software. As explained in CHAPTER 6, the developed MWHCL-DRM avoided carbon formation. One needs to consider that formation of coke is detrimental for both non-catalytic and catalytic reactions, like the reduction of Fe_3O_4 using CH_4. However, there are processes like thermal pyrolysis of CH_4 for pure H_2 and solid carbon generation. Accordingly, in addition to generating pure H_2 as the gaseous product, the generated solid carbon can be a graphitic material, which is a highly valuable product. In addition, as previously mentioned in CHAPTER 5, considering relatively high U_g in the industrial-scale compared to the laboratory-scale, the obtained reaction kinetics are intrinsic

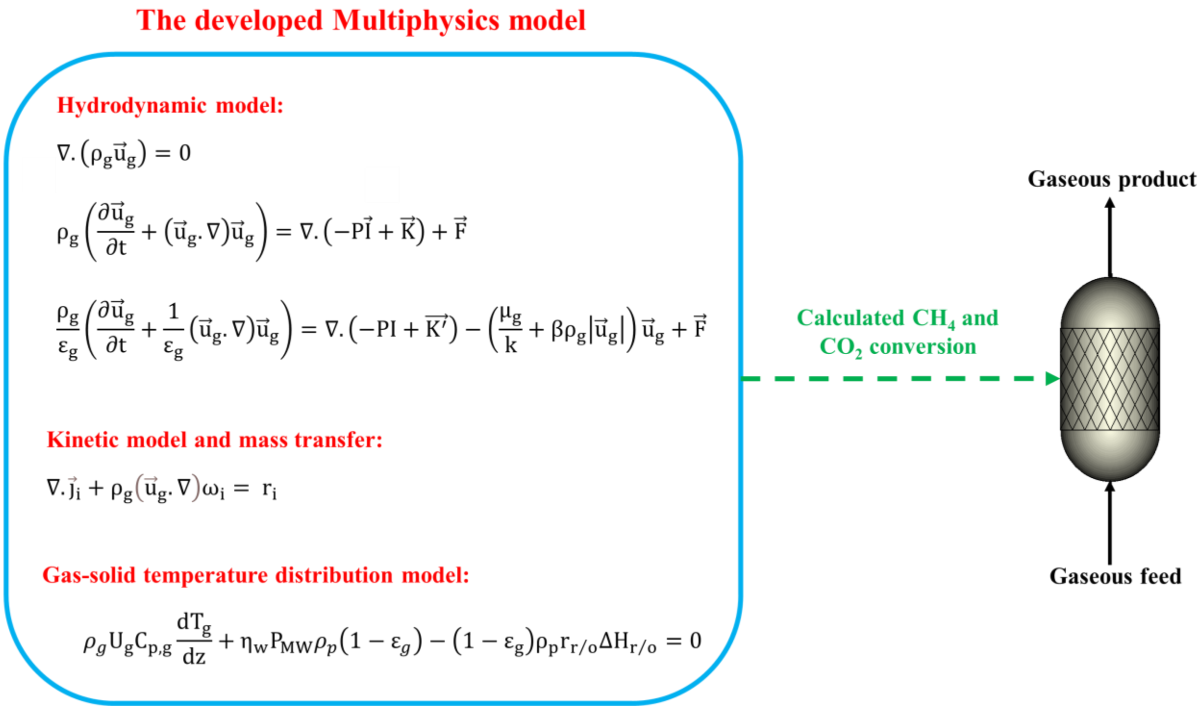

Figure 7.2. Coupling the constructed model with the RStoic reactor module of Aspen Plus software.

7.2.3 Economic analysis

Our primary phase in accomplishing the economic analysis involves determining the detailed costs, including unit operations and all elements that contribute to CAPEX and OPEX. Based on the process flow diagrams elucidated in Figure 7.1, a detailed breakdown of CAPEX and OPEX is presented in Table 7.1.

Table 7.1. Detailed costs contributed to CAPEX and OPEX.

CAPEX

- MWH-assisted reactors ($)
- MW generators ($)
- Compressors ($)
- Shift reactors ($)
- ET-PSA ($)
- Heat exchangers ($)
- H_2O separation (packed bed made of silica gel) ($)
- OSBL ($)

Table 7.1 (Continued). Detailed costs contributed to CAPEX and OPEX.

- Contingency ($)
- Engineering ($)
- Land ($)

OPEX

Variable OPEX

- CH_4 consumption ($/year)
- Cooling water (CW) consumption ($/year)
- Electricity consumption ($/year)
- CO_2 separation unit ($/year)

Fixed OPEX

- Operating labor/workforce ($/year)
- Direct salary overhead ($/year)
- Supervision of the plant ($/year)
- Maintenance of the plant ($/year)
- Property tax and insurance costs ($/year)

Once the components contributing to CAPEX and OPEX are identified, we can calculate TCOP. Subsequently, a thorough sensitivity analysis is imperative to underline the factors affecting TCOP. The TCOP must also be compared with existing industrial plants of H_2 manufacturing, namely SRM. We employed the commonly adopted [3, 4] method (Eq. (7.1)) to calculate TCOP.

$$\mathrm{TCOP} = \mathrm{OPEX} + \mathrm{ACC} \tag{7.1}$$

ACC stands for annual capital charge. By considering the effect of plant life n and interest rate i as the capital recover factor CRF, we annualized CAPEX to ACC (referring to Eq. (7.2)). Consequently, to ensure the annualized effect of CAPEX is regarded on TCOP, one needs to initially estimate ACC.

$$\mathrm{ACC} = \mathrm{CAPEX} \times \mathrm{CRF} \tag{7.2}$$

$$\mathrm{CRF} = \mathrm{i} \times \frac{(1+\mathrm{i})^{\mathrm{n}}}{(1+\mathrm{i})^{\mathrm{n}}-1} \tag{7.3}$$

To estimate TCOP, the following assumptions were considered:

1. One year is regarded as the construction time of the plant.
2. n in Eq. (7.3) is 25 years.
3. i in Eq. (7.3) is 5%.
4. Working capital investment, abbreviated as WCI, equals 0.15 × CAPEX.
5. Inside battery limit, abbreviated as ISBL, investment represents the total equipment cost.
6. Outside battery limit (OSBL) investment includes the costs allied with the site infrastructure and equals 0.05 × ISBL.
7. Engineering cost, which includes the costs for engineering services and plant design, equals 0.05 × ISBL.
8. Contingency charge includes expenses that might be neglected, which equals 0.1 × ISBL.
9. Maintenance cost = 0.05 × ISBL.
10. Costs for renting/buying the land = 0.02 × ISBL.
11. Operating labor/workforce is estimated based on the widely employed method for large-scale chemical plants [5]. Therefore, based on the number of operators in an 8-hour shift and 50 tons-CH_4/day of the feed flowrate, we estimated 750,000 $/year as the operating labor/workforce cost.
12. The effect of installation of the purchased equipment on TCOP is considered within the engineering and operating labor cost.
13. Supervision cost = 0.25 × (the operating labor/workforce cost).
14. Direct Salary overhead = 0.25 × (the operating labor/workforce cost).
15. Property tax and insurance costs = 0.02 × ISBL.

The assumed prices for cost evaluation are shown in Table 7.2.

Table 7.2. The assumed prices based on the literature [3, 4, 6].

CW ($/ton)	0.1
Electricity (¢/kWh)	0.078
Working hours per year (hr)	8000
CH_4 price ($/m^3)	0.1
Tax rate (%)	30
CO_2 separation/capture cost ($/ton)	100
Oxygen carrier and catalyst ($/kg)	20
Oxygen carrier’s and catalyst lifetime (year)	1

To estimate the equipment purchased cost C_{eq}, we employed Eq. (7.4).

$$C_{eq} = f_m . f_{ci}(a + b(S/S_o)^m) \quad (7.4)$$

In Eq. (7.4), a, b, and m represent cost constants (referring to Table 7.3). S is also the size parameter (Table 7.3). In addition, to include the effect of material selection on C_{eq}, we employed material factor f_m. The effect of cost index f_{ci}, i.e., equipment costs associated with year 2024, is also considered to estimate C_{eq}. S_o represents the unit size parameter, which has the value of 1 with the identical unit as S in Table 7.3.

Table 7.3. The employed parameters to estimate C_{eq} [3, 4].

Equipment	***S***	***a ($)***	***b ($)***	***m (-)***
Reactor	Mass of the reactor (kg)	17,400	79	0.85
Heat exchanger	Heat transfer area (m^2)	10,000	88	1
Compressor	Consumed power (kW)	260,000	2,700	0.75
ET-PSA	Mass of the vessel (kg)	17,400	79	0.85

One must choose a MW source for heating the MWH-assisted reactors. The main MW sources can be categorized into magnetron and solid-state generators. Klystrons and gyrotrons are also available MW sources, even though they are mainly designed and employed for high-frequency MWs (> 2.45 GHz). Moreover, for MW frequency of 2.45 GHz, in comparison with the solid-state MW sources with electricity to MW conversion efficiency of around 50%, the magnetrons have higher (up to 65%) electricity to MW conversion efficiency. Accordingly, we selected magnetrons as MW sources to supply the requisite heat of the reactors [7, 8]. Considering the available commercial magnetrons, we selected MWH-assisted reactors with the maximum electricity consumption of 100 kW at 2.45 GHz, corresponding to 65 kW as the maximum MW power generation. Moreover, by employing the available commercial data, we calculated the purchased cost of the magnetrons, assuming $2 per watt of MW power produced [7, 8]. It should be mentioned that the detailed design and operation of MW sources is beyond the scope of this research.

7.2.4 Environmental and energy impacts

To achieve a holistic conclusion over the MWHCL-DRM for large-scale H_2 manufacturing, one needs to measure environmental and energy impacts by executing an LCA study. LCA can delve the global environmental impact of a process and/or product from raw material to the end use to compare it with other processes and/or products in terms of the real environmental footprints [9-15]. We employed openLCA 2.1 software. We also applied the Ecoinvent default database v3.1 to execute the LCA analysis. In addition, to undertake the LCA, we need to define the system's boundary. Accordingly, to compare the results of this study with other H_2 manufacturing methods [9-15], we employed the cradle to gate (well to tank) system's boundary, as shown in Figure 7.3. In this method, the H_2 manufacturing system is considered from the extraction of raw materials (natural gas in this study) to final product (plant’s gate), which is the produced H_2. Therefore, we considered the effect of upstream processes to provide natural gas as the feed stock of the plant, while the transportation and utilization of the produced H_2 was not included in the executed LCA.

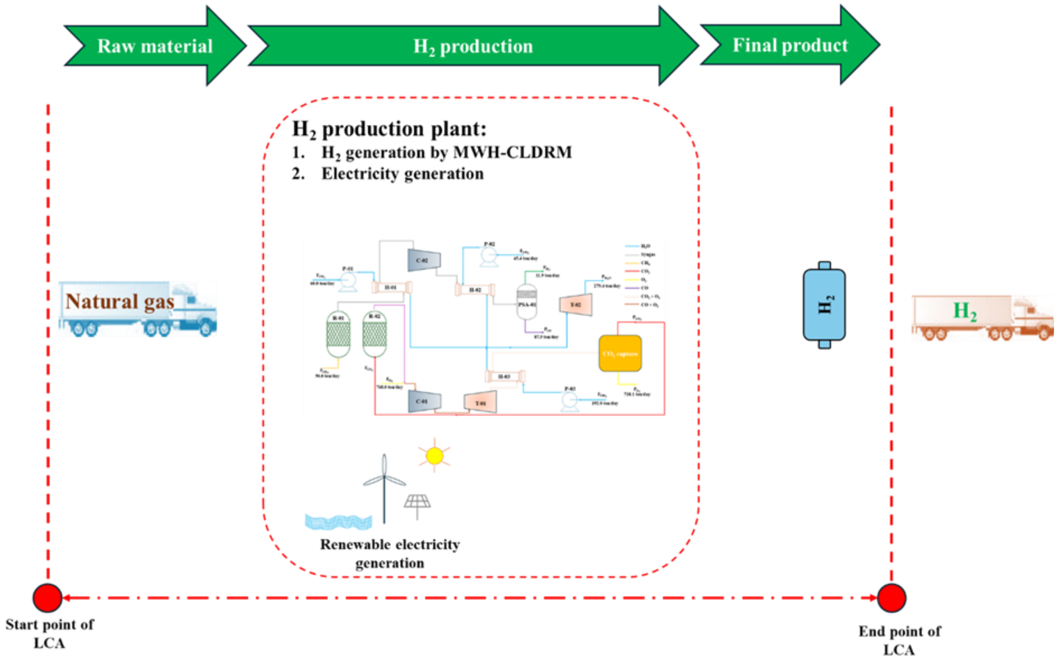

Figure 7.3. System’s boundary of the performed LCA.

In addition to the boundary of the system, the manufacturing of 1 kg of H_2 was considered as the functional unit to undertake the LCA. North America was also considered to be the geographical scope of our study. Moreover, due to the low daily consumption of Fe_3O_4 (below 50 kg/day) compared to natural gas consumption (50 tons/day of CH_4), we neglected the effect of Fe_3O_4 preparation on the environmental impacts. CO_2 eq and energy consumption were selected as the main parameters to compare the environmental and energy impacts of the MWHCL-DRM.

7.3 Results and discussion

7.3.1 Mass and energy balances and equipment design

The constructed process flow diagram of the MWHCL-DRM for a plant with an inlet flowrate of 50 tons-CH_4/day is shown in Figure 7.1. The corresponding properties of inlet and outlet streams are presented in Table 7.4 and Table **7.5**. The redox reactions were evolved at T_b of around 800°C. For the feed rate of 50 tons-CH_4/day, to achieve $x_{CH_4} \approx 1$ with H_2/CO of 2, we fixed a reduction time of 95 s. Additionally, the produced Fe was completely re-oxidized in 85 s. Therefore, we considered 180 s as the redox period for the plant.

Table 7.4**.** Properties of the inlet material streams of the plant shown in Figure 7.1**.**

	S-01	***S-17***	***S-25***	***S-27***	***S-33***	***S-42***
Temperature (°C)	25	25	25	25	25	25
Pressure (bar)	1	1	1	1	1	1
Mass Flows (ton/day)						
CH_4	50.0	0.0	0.0	0.0	0.0	0.0
CO_2	0.0	0.0	0.0	0.0	0.0	4.0
CO	0.0	0.0	0.0	0.0	0.0	0.0
H_2	0.0	0.0	0.0	0.0	0.0	0.0
H_2O	0.0	0.0	115.1	1680.0	360.0	0.0
Air	0.0	692.4	0.0	0.0	0.0	0.0
Mole Flows (kmol/hr)						
CH_4	129.9	0.0	0.0	0.0	0.0	0.0
CO_2	0.0	0.0	0.0	0.0	0.0	3.7
CO	0.0	0.0	0.0	0.0	0.0	0.0
H_2	0.0	0.0	0.0	0.0	0.0	0.0
H_2O	0.0	0.0	266.2	3885.6	832.6	0.0
Air	0.0	1000	0.0	0.0	0.0	0.0

Table 7.5. Properties of the outlet material streams of the plant shown in Figure 7.1. Stream S-20 and S-24 have zero flowrate.

	S-02	***S-16***	***S-28***	***S-29***	***S-31***	***S-34***	***S-41***
Temperature (°C)	30	29.1	46.2	25	25	58.0	199.8
Pressure (bar)	1	1	1	1	1	1	1
Mass Flows (ton/day)							
CH_4	0.0	0.0	0.0	0.0	0.0	0.0	0.0
CO_2	0.0	0.0	0.0	0.5	0.0	0.0	0.0
CO	87.3	0.0	0.0	0.0	0.0	0.0	2.2
H_2	0.0	0.0	0.0	0.0	0.0	0.0	18.7
H_2O	0.0	0.0	1680.0	53.1	7.3	360.0	0.0
Air	0.0	692.4	0.0	0.0	0.0	0.0	0.0
Mole Flows (kmol/hr)							
CH_4	0.0	0.0	0.0	0.0	0.0	0.0	0.0
CO_2	0.0	0.0	0.0	0.5	0.0	0.0	0.0
CO	129.9	0.0	0.0	0.0	0.0	0.0	3.3
H_2	0.0	0.0	0.0	0.0	0.0	0.0	386.3
H_2O	0.0	0.0	3885.6	122.8	16.8	832.6	0.0
Air	0.0	1000.0	0.0	0.0	0.0	0.0	0.0

As detailed earlier in Section 7.2.1, we employed an ET-PSA (SEP-03) to separate H_2. To achieve a high purity (>99.99%) H_2 stream (S-37 in Figure 7.1) with 95% of H_2 recovery, the employed ET-PSA worked at operating temperature of 200^{o}C and pressure of 20 bar. In addition, we leveraged the energy content of the exhaust stream of the high shift (R-03 in Figure 7.1 that was simulated by a “REquil” module of the Aspen Plus software) and low shift (R-04 in Figure 7.1 that was simulated by a “REquil” module of the Aspen Plus software) reactors via two heat exchangers (HX-02 and HX-03 in Figure 7.1) to preheat the stream fed to the high temperature shift reactor. The air cooler (HX-01 in Figure 7.1) was employed as the overdesign to guarantee reaching the target inlet temperature of the shift reactor. Sep-01 and HX-04 in Figure 7.1 together represent a condenser working at operating temperature of 25°C for condensing H_2O content of the stream.

The packed bed column of silica gel (SEP-02 in Figure 7.1) removed the remaining humidity of the gaseous stream. The inlet gaseous stream to the ET-PSA (SEP-03 in Figure 7.1) was initially pressurized to 20 bar by a multi-stage compressor (COMP-01 in Figure 7.1). HX-05 in Figure 7.1 was employed to ensure cooling the inlet gaseous stream to ET-PSA to 200°C. We also employed HX-06 and HX-07 (shown in Figure 7.1) to preheat the inlet gaseous streams to the MWH-assisted reactors. Considering the operating temperature and pressure of unit operations and material streams as well as employing the Peng-Robinson thermodynamic package, we executed the energy balance diagram of the plant, detailed in Figure 7.4.

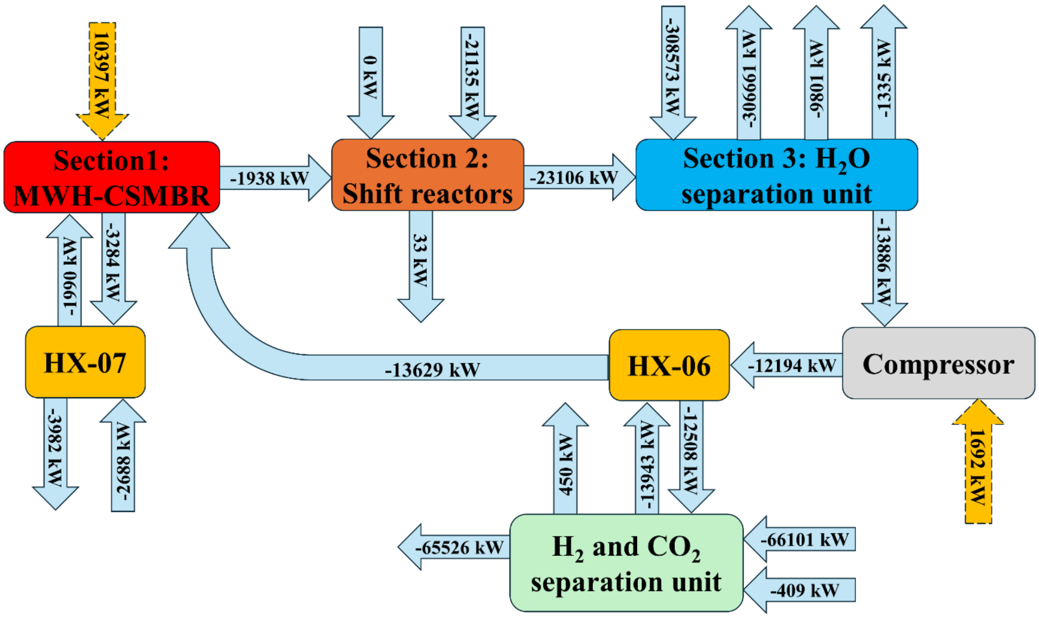

Figure 7.4. Energy flow diagram of the constructed plant (energy balance). Air at 25°C and 1 bar with the energy content of 0 kW is considered as the reference energy stream.

In addition to executing the plant's ME balances, the requisite design parameters for cost evaluation of the employed unit operations are summarized in Table 7.6.

Table 7.6. Unit operations design parameters for cost evaluation.

Unit operations in Figure 7.1	*Remarks*
R-01 and R-02	Reactor type: MWH-CSMBR Inner diameter: 30 cm Reactor's total height: 7 m Dense bed height of each stage: 4 cm Stage spacing: 15 cm

Table 7.6 (Continued). Unit operations design parameters for cost evaluation.

Unit operations in Figure 7.1	***Remarks***
	Material: S.S 316 and quartz Operating temperature < 1100°C Operating pressure < 10 bar Design pressure: 20 bar Total bed inventory of each reactor ~ 300 kg
R-03	Reactor type: adiabatic fixed/packed bed Inner diameter: 2.5 m Reactor's total height: 10 m Catalyst type: Fe_2O_3/Cr_2O_3 Material: S.S 316 Inlet temperature: 340°C Outlet temperature: 500°C Design pressure: 20 bar
R-04	Reactor type: adiabatic fixed/packed bed Inner diameter: 2.5 m Reactor's total height: 10 m Catalyst type: $Cu/ZnO/Al_2O_3$ Material: S.S 316 Inlet temperature: 180°C Outlet temperature: 240°C Design pressure: 20 bar
SEP-02	Column type: fixed/packed bed adsorber Inner diameter: 2.5 m Column's height: 6 m Adsorber type: silica gel Column's material: S.S 316 Operating temperature: 25°C
COMP-01	Multi-stage Number of stages: 4 Inlet pressure: 1 bar Discharge pressure: 20 bar Operating temperature < 700°C Isentropic efficiency: 95% Mechanical efficiency: 95%
SEP-03 (ET-PSA)	Adsorbent: Molecular sieve Operating temperature < 200°C Operating Pressure < 40 bar H_2 purity: 99.9% H_2 recovery: 95%
HX-01	Heat exchanger type: Air cooler Heat transfer area: 5 m^2 Maximum temperature approach: 5°C Material: S.S 316 Over design for fouling factor: 5%

Table 7.6 (Continued). Unit operations design parameters for cost evaluation

Unit operations in Figure 7.1	***Remarks***
HX-02	Heat exchanger type: Shell and tube Heat transfer area: 15 m^2 Maximum temperature approach: 5°C Material: S.S 316 Over design for fouling factor: 15%
HX-03	Heat exchanger type: shell and tube Heat transfer area: 30 m^2 Maximum temperature approach: 5°C Material: S.S 316 Over design for fouling factor: 15%
HX-05	Heat exchanger type: shell and tube Heat transfer area: 4 m^2 Maximum temperature approach: 5°C Material: S.S 316 Over design for fouling factor: 15%
HX-06	Heat exchanger type: shell and tube Heat transfer area: 15 m^2 Maximum temperature approach: 5°C Material: S.S 316 Over design for fouling factor: 15%
HX-07	Heat exchanger type: shell and tube Heat transfer area: 17 m^2 Maximum temperature approach: 5°C Material: S.S 316 Over design for fouling factor: 15%

7.3.2 Economic analysis

7.3.2.1 Detailed cost analysis

To determine TCOP, we first calculated CAPEX. For calculating CAPEX, based on the design parameters (Table 7.6) and Eq. (7.4), we initially determined the equipment cost, as shown in Table 7.7. Subsequently, by considering the cost evaluation assumptions presented in Section 7.2.3, OSBL, engineering, contingency, and land costs were calculated. Therefore, as articulated in Section 7.2.3, by assuming n = 25 years, and 5% for interest rate (i in Eq. (7.3)), we estimated a CAPEX of around 25.1 M$, i.e., ACC of around 1.8 M$/year (Table 7.7). By considering the plant’s ME balances and the assumed prices presented in Table 7.2, we estimated the variable OPEX (Table 7.7). Similar to CAPEX, by considering the cost evaluation assumptions presented in Section 7.2.3, fixed OPEX were calculated. Therefore, we estimated an OPEX of around 20.5

M$/year (Table 7.7). It should be mentioned that compared to the MWH-CSMBR with equipment cost of $350K, employing numerous MWH-assisted reactors together results in a reactor equipment cost of around $10M. Therefore, in addition to addressing the technical bottlenecks of employing numerous reactors together on an industrial-scale, the proposed MWH-CSMBR significantly decreased the CAPEX of the plant.

Table 7.7**.** The detailed costs of H_2 manufacturing by the constructed plant in this study (Figure 7.1), for the plant with feed flowrate of 50 tons-CH_4/day.

CAPEX	
• MWH-CSMBRs (K$)	350
• MW generators (K$)	19,000
• Compressors (K$)	1,643
• High and low temperature shift reactors (K$)	521
• ET-PSA (K$)	112
• Heat exchangers (K$)	220
• H_2O separation (packed bed made of silica gel) (K$)	211
• Costs of engineering (K$)	1,103
• OSBL (K$)	551
• Land (K$)	331
• Contingency costs (K$)	1,103
Plant's life (year)	25
Interest rate (%)	5%
CRF (-)	0.071
CAPEX (M$)	25.1
Annualized CAPEX (M$/year)	1.8
OPEX	
• Variable OPEX	
CH_4 (K$/year)	2,728
CW (K$/year)	60
Electricity (K$/year)	11,158
CO_2 separated by carbon capture unit (K$/year)	4,572
• Fixed OPEX	
Workforce/operating labor (K$/year)	750
Plant's supervision (K$/year)	188
Overhead's direct salary (K$/year)	375
Plant's maintenance (K$/year)	441
Property tax and insurance costs (K$/year)	221
OPEX (M$/year)	20.5
TCOP (M$/year)	22.3
TCOP ($/kg-$H_2$)	3.58

7.3.2.2 Sensitivity analysis

To underline the independent factors affecting TCOP and plant's profitability, one must undertake the sensitivity analysis. Accordingly, we executed a sensitivity analysis for ±50% variation of independent factors and elucidated their effects on TCOP, as displayed in Figure 7.5a. As presented in this figure, electricity consumption and CO_2 capturing stand out as the critical factors influencing TCOP. Accordingly, we underlined the effect of electricity consumption and CO_2 capturing, as the most influential items on TCOP, detailed in Figure 7.5b. In addition, among different factors that influence CAPEX, MW generator is the critical item.

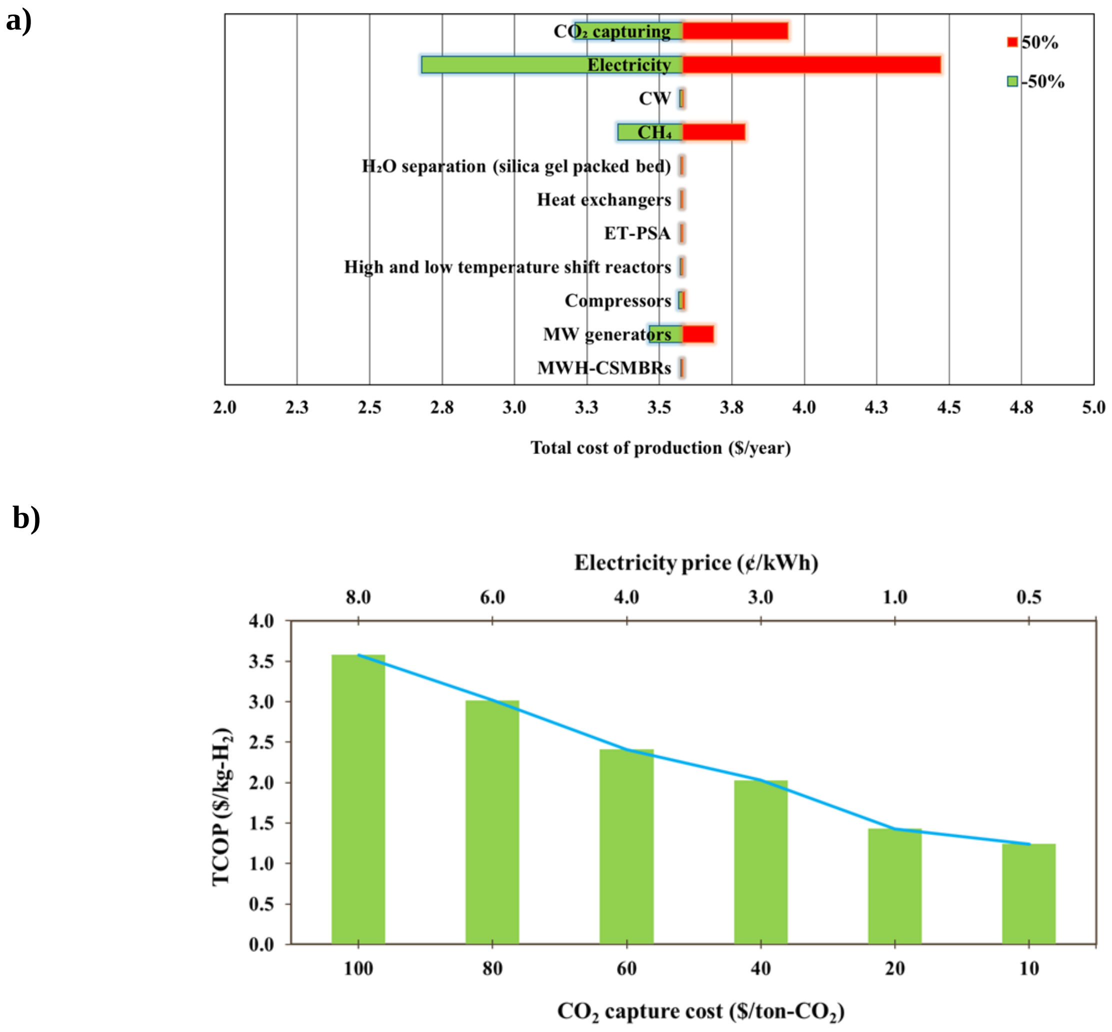

Figure 7.5. a) sensitivity analysis and b) effect of electricity consumption and CO_2 capturing/separation on TCOP of the plant displayed in Figure 7.1.

We compared the estimated TCOP of the current plant with the conventional methods of H_2 manufacturing, represented in Figure 7.6. As shown in this figure, by: (i) decreasing the costs linked to CO_2 capturing and electricity price, (ii) the advancement of the MW generators resulting in decreasing the MW source cost, and (iii) potential increases in costs due to carbon taxes (taxes on CO_2 emissions), a notably lower TCOP can be anticipated for clean H_2 manufacturing processes, like the MWHCL-DRM, in the future.

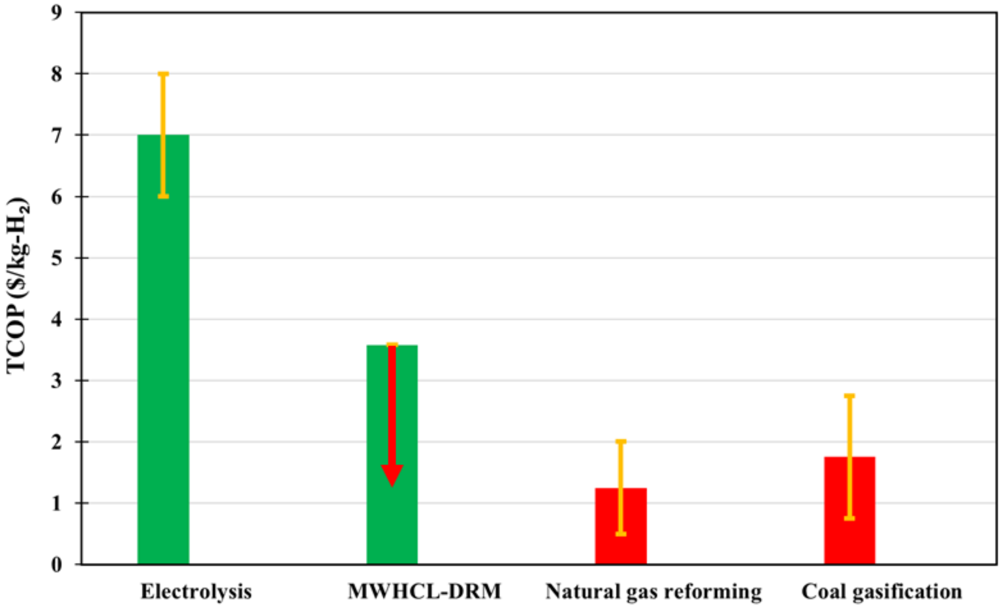

Figure 7.6. Comparison of the TCOP of the constructed plant by the available industrial-scale methods of H_2 manufacturing. Error bar indicates the variation of TCOP for each plant based on the variation of parameters contributed to CAPEX and OPEX.

7.3.3 Life cycle assessment

Due to the global energy crisis and the detrimental effect of GHG emissions on climate change and the increasing concern of global warming, we selected CO_2 eq emission and energy consumption as two critical factors to compare the environmental impact of the MWHCL-DRM for H_2 manufacturing with SRM (the most dominant pathway of H_2 manufacturing) and electrolysis (an industrialized clean H_2 manufacturing pathway).

Prior to studying the CO_2 eq emission of the MWHCL-DRM with SRM and electrolysis, we compared their energy consumption, referring to Figure 7.7a. The higher consumption of energy of the SRM compared to the MWHCL-DRM can be related to the high operating temperature (normally in the range of 800-950°C) of SRM and the requisite energy to supply superheated steam as the feed of the reactor. In addition, the higher energy consumption of the commercial electrolysis can be related to their low electricity to H_2 conversion efficiency (up to 73%) due to several factors including: (i) electrolyte quality, i.e., the presence of impurities such as magnesium and chloride, (ii) the influence of temperature on decreasing the materials' stability, and (iii) physicochemical effect of electrodes on efficiency of the process. Moreover, as represented in Figure 7.1, to decrease the total energy consumption of the plant, we employed a heat exchanger network to maximize the heat recovery from the gaseous streams leaving the unit operations. Consequently, as shown in Figure 7.7a, the constructed process sequence for the MWHCL-DRM (Figure 7.7) significantly decreased the energy requirement of the plant compared to SRM and electrolysis.

The CO_2 eq emission of the MWHCL-DRM, SRM, and electrolysis for H_2 manufacturing are elucidated in Figure 7.7b. Note that supplying the necessary heat of SRM's reaction and generating superheated steam as the reactor feed are the reasons why SRM emits more CO_2 eq than MWHCL-DRM. In addition, as shown in Figure 7.7b, the high energy demand of electrolysis, compared to MWHCL-DRM and SRM, leads to CO_2 eq emissions exceeding 30 kg CO_2 eq when fossil fuel-based sources are employed to generate the required electricity. Even with renewable electricity sources, due to the higher energy consumption of the electrolysis compared to the MWHCL-DRM, an average value of around 2.5 kg CO_2 eq emission was reported in literature for the H_2 manufacturing by electrolysis. It should be also mentioned that in addition to the direct parameter, i.e., CO_2 eq emission caused by supplying the raw materials (natural gas) for the MWHCL-DRM, indirect parameters, i.e., renewable electricity generation, can influence the global warming potential of the MWHCL-DRM. Based on the LCA, around 97% of the total CO_2 eq emission (2.05 kg CO_2 eq) of the constructed plant is due to supplying the natural gas as the raw material (direct CO_2 eq emission) and renewable electricity manufacturing contributed to 0.06 kg CO_2 eq emission. Hence, by decreasing the impact of supplying natural gas, e.g., employing biogas to generate CH_4, one can decrease the CO_2 eq emission of the MWHCL-DRM to below 0.1 kg CO_2 eq. Therefore, while the developed process (Figure 7.1) does not generate net CO_2, from an LCA perspective, the process still has a global warming potential due to CO_2 emissions associated with the supply of the required CH_4 for the plant and the electricity needed for the MWH-assisted reactors.

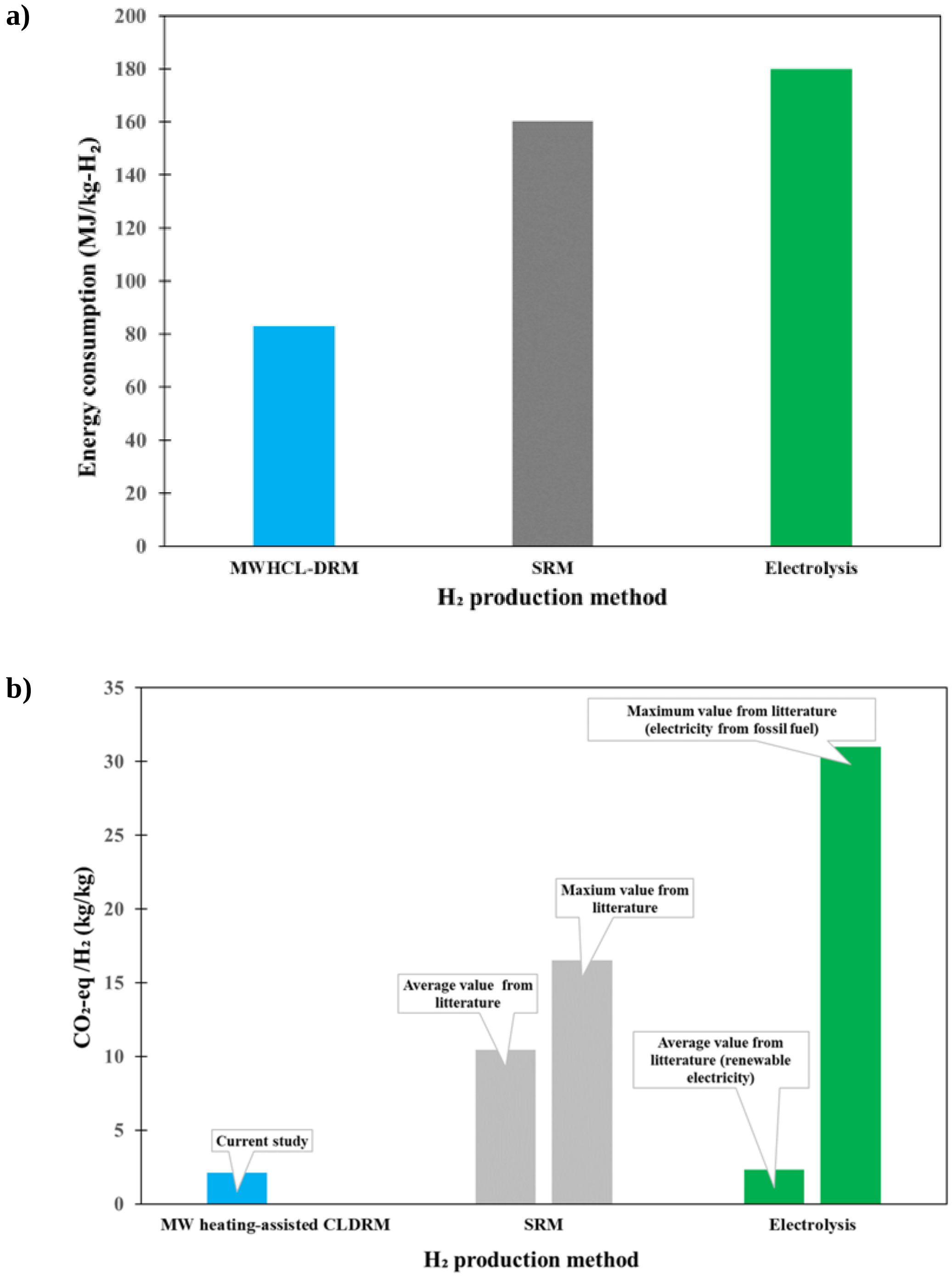

Figure 7.7. Comparison of a) total energy consumption and b) CO_2-eq emission of MWHCL-DRM, SRM, and electrolysis for H_2 manufacturing.

7.4 Conclusion

In addition to proposing the MWH-CSMBR in CHAPTER 6 to solve the critical technical bottleneck of deploying numerous MW heated reactors together, in this chapter, we executed a thorough TEA to ascertain the remained technical and economic factors affecting the commercialization of large-scale H_2 manufacturing via the MWHCL-DRM for a plant with an inlet flowrate of 50 tons-CH_4/day. Moreover, we executed a LCA based on the cradle to gate system's boundary to estimate the environmental footprints, CO_2 eq and energy consumption in this study, of the MWHCL-DRM for large-scale manufacturing of H_2. We executed the LCA for North America, the selected geographical scope in this research.

To carry out the TEA and LCA, one needs to create a process flow diagram with corresponding design parameters of the unit operations. Consequently, we first created the process flow diagram of a plant for H_2 manufacturing via the MWHCL-DRM and with integrated CO_2 capturing and utilization. We then integrated the result of the simulation from CHAPTER 6, particularly the obtained x_{CH_4} and x_{CO_2}, with Aspen Plus software to execute the plant's ME balances. In addition to the ME balances, we calculated the required design parameters for further economic analysis. Since electricity consumption is a critical factor in decreasing TCOP for large-scale H_2 manufacturing plants, by employing heat exchangers, we leveraged the energy content of the exhaust gaseous streams to preheat the gaseous streams fed to the reactors.

Assuming interest rate, plant life, methane (CH_4) price, electricity price, and carbon dioxide (CO_2) capturing/separation cost of 5%, 25 years, 3.5 \$/GJ, 0.078 \$/kWh, and 100 \$/ton-CO_2, respectively, we estimated TCOP of 3.6 \$/kg-H_2. CAPEX with 25.1 M\$ (annualized of 1.8 M\$/year) and OPEX with 20.5 M\$/year contributed to 10% and 90% of the TCOP, respectively. Among the factors influencing OPEX, electricity consumption, CO_2 separation for supplying the required CO_2 in the oxidizer reactor, and the CH_4 price for reduction reactions contributed to 54%, 21%, and 13% of the OPEX, respectively. In addition, the cost associated with the MW generator, which accounts for 76% of CAPEX, was the primary factor affecting CAPEX. We also demonstrated that by decreasing electricity price, CO_2 capturing/separation cost, and MW generator cost, the proposed plant could compete with the conventional methods of H_2 manufacturing.

In addition to the detailed TEA, by executing a cradle to gate LCA, we demonstrated that the MWHCL-DRM causes 2.11 kg CO_2 eq as the total global warming potential. We also estimated that natural gas supply with 2.05 kg CO_2 eq contributed to more than 97% of the global warming potential of the MWHCL-DRM. Accordingly, we accomplished a sensitivity analysis to scrutinize the effect of natural gas extraction footprint on CO_2 eq emission. We illustrated that by decreasing the effect of natural gas extraction (supply), e.g., employing biogas, one can decrease the CO_2 eq emission of the MWHCL-DRM to below 0.1 kg CO_2 eq. In addition to the global warming potential, compared to the SRM with around 160 MJ/kg-H_2 as the total energy demand, the constructed MWHCL-DRM required less than 80.3 MJ/kg-H_2. Hence, based on the executed TEA and considering high global warming potential of SRM (>9 kg CO_2 eq) and electrolysis (>30 kg CO_2 eq when fossil fuel sources are employed to produce electricity) compared to the MWHCL-DRM, we recommend the development of the MWHCL-DRM for large-scale H_2 manufacturing in North America.

Nomenclature

Acronym

ACC	Annual capital charge
CAPEX	Capital expenditures
CDCF	Cumulative discounted cashflow
CH	Conventional heating
CL-DRM	Chemical looping dry reforming of methane
CLR	Chemical looping reforming
CRF	Capital recovery factor
C-SRM	Catalytic steam reforming of methane
CW	Cooling water
DRM	Dry reforming of methane
eq	Equivalent
ET-PSA	Elevated temperature pressure swing adsorption
GHG	Greenhouse gas
IPS	Industrial process simulator
ISBL	Inside battery limit
LCA	Life cycle assessment
MBR	Moving bed reactor
ME	Mass and energy
MW	Microwave
MWH	Microwave heating

MWHCL-DRM	Microwave heating-assisted chemical looping dry reforming of methane
MWH-CSMBR	Microwave heating-assisted cyclic simulated moving bed reactor
OPEX	Operating expenditures
OSBL	Outside battery limit
PSA	Pressure swing adsorption
Redox	Reduction and oxidation
SMBR	Simulated moving bed reactor
SRM	Steam reforming of methane
TCOP	Total cost of production
TEA	Techno-economic analysis
WCI	Working capital investment

Symbols

d_p	Particle size (m)
f_{ci}	Cost index (-)
f_m	Material factor (-)
$m_{Fe_3O_4}$	Mass of Fe_3O_4 within the bed inventory (gm)
m_{Fe}	Mass of Fe within the bed inventory (gm)
Q_{CH_4}	Inlet CH_4 flow (l/min)
Q_{CO_2}	Inlet CO_2 flow (l/min)
T_b	Bulk temperature (°C)
T_g	Gas temperature (°C)
T_s	Solid temperature (°C)
x_{CH_4}	CH_4 conversion
x_{CO_2}	CO_2 conversion

Greek letters

α_o	Oxidation extent of the solid sample (-)
α_r	Reduction extent of the solid sample (-)
α	Extent of solid conversion (-)

CHAPTER 8 GENERAL DISCUSSION

Developing inventive GHG utilization technologies for producing syngas is a serious global target. C-SRM, the widely commercialized process of syngas and H_2 manufacturing, suffers from significant (> 9 kg) CO_2 emissions for each kg of H_2 generated. Unlike the C-SRM, the exothermic C-POM can decrease the process's energy consumption, which can decrease the rate of CO_2 emission. However, the safety issues of pure O_2 injection to the reactor and deposition of coke are the core challenges delaying the scale up of the C-POM. Compared to the C-SRM and C-POM, C-DRM is a CO_2 utilization pathway. The C-DRM also produces a synthesis gas with equimolar CO and H_2 (H_2/CO of 1), which makes it suitable for synthesizing liquid hydrocarbons through the FT process. However, the unresolved downside of deposition of coke stops the scale up of the CDRM. Although the rate of coke generation can be diminished by merging MWH with the C-DRM, the thermodynamic favorability of deposition of coke still delays commercialization of the MWH-assisted C-DRM at large scale. The concept of CHCL-DRM can tackle the thermodynamic constraint of deposition of coke caused by the concurrent feeding of CO_2 and CH_4 into the reactor. However, this process cannot avoid the deposition of coke raised by the gas phase thermal decomposition of CH_4.

The first part of this research thus proposed and examined the inventive concept of MWHCL-DRM to fully resolve the problem of deposition of coke and increase the productivity of the process. After concluding the proof of concept (first stage), this research's second part focused on understanding the reaction kinetics. By adapting the results of the first and second phases, this research's third part was dedicated to accomplishing the design, simulation, and optimization of a novel reactor, MWH-CSMBR, for industrial-scale syngas manufacturing. Separating H_2 from the synthesis gas is the leading H_2 production pathway. Subsequently, the fourth objective of this research focused on constructing the process simulation, evaluate the techno-economic aspects, and lastly conduct a LCA applying the cradle to gate method for large-scale production of H_2 in North America and via the MWHCL-DRM.

In the first part of this research, firstly, a detailed comparison of heating capacity of Fe_3O_4 (the selected oxygen carrier) with SiC was conducted. Simultaneous interaction of Fe_3O_4 with E-field and M-field of MW resulted in a greater heating capacity relative to SiC. Steady syngas manufacturing was ensured by progressing twenty periodic redox cycles. Carbon deposition and the rates of redox reactions in the laboratory-scale MWHCL-DRM were compared with the CHCL-DRM. The major outcomes of the first part of this research thus can be summarized as:

- Proof of concept for the MWHCL-DRM was attained.
- Compared to CHCL-DRM, CH_4 conversion, i.e., Fe_3O_4 reduction, was approximately 2.5 times greater in the MWHCL-DRM.
- A synthesis gas with a H_2/CO ratio of almost 2 was generated in the reducer (fuel) reactor of the MWHCL-DRM.
- Compared to the CHCL-DRM, CO_2 conversion, i.e., Fe oxidation, was approximately 1.5 times greater in the MWHCL-DRM.
- Contrasting the CHCL-DRM, the MWHCL-DRM prevented the deposition of coke.

The second part of this research was dedicated to investigating the rate of reactions for the MWHCL-DRM. This stage aimed at achieving intrinsic kinetic models (controlled by chemical reactions) for the redox reactions to obtain a reliable result. Accordingly, by optimizing the values of U_g around 9 cm/s and d_p down to 10 μm, the influence of mass transfers (both external and internal) on controlling the kinetic models was minimized. Additionally, the intrinsic kinetic models were formulated using two T_{rx}, i.e., $T_{rx} = T_b$ and $T_{rx} = T_s$. Using CH_4, the calculated activation energies for the reduction step under MWH were compared to those for the reduction step under CH. This comparison showed that for the MWHCL-DRM using Fe_3O_4 as the oxygen carrier, the MW's influence on the intrinsic kinetic models can be disregarded, meaning that in the current study, MW accelerated the reaction rate constants instead of impacting the activation energies. Hence, the second part of this research recommends using $T_{rx} = T_s$ for acquiring a reliable kinetic model for the solid-fluid(gas) reactions heated by MW. Accordingly, the major outcomes of the second part of this research are:

- The redox reactions' intrinsic kinetic models for the MWHCL-DRM using Fe_3O_4 was formulated for $T_{rx} = T_b$ and $T_{rx} = T_s$.
- This research recommends using $T_{rx} = T_s$ for acquiring a reliable kinetic model for the solid-fluid(gas) reactions heated by MW.

The third part of this research aimed at design, simulation, and optimization of MWH-CSMBR – a novel reactor – to tackle the technical bottleneck of applying multiple parallel MWH-assisted reactors for large-scale syngas manufacturing plants. The simulation findings confirmed the potential of the MWH-CSMBR in resolving this bottleneck. This simulation was accomplished using the experimental findings and the reaction kinetics as the outcomes of the first and second stages of this research. The major outcome of the third part of this research is:

- The new concept of MWH-CSMBR can overcome the technical limitation of applying multiple rectors in parallel for large-scale syngas manufacturing plants.

The fourth part of this research performed a TEA and a LCA for generating H_2 in industrial-scale via the MWHCL-DRM. The simulation findings from the third objective, notably x_{CH_4} and x_{CO_2}, were used as the input of the plant's process simulation, which was performed using Aspen Plus software. During the plant's ME balances in the fourth objective of this research, by creating a heat network utilization, the process simulation was optimized. Followed by the process simulation, the fourth stage performed the TEA and LCA. The key results of the fourth part of this research thus are:

- Decreasing CO_2 and electricity costs can decrease the total cost of producing H_2 by the MWHCL-DRM, which could enable the MWHCL-DRM in competing with the C-SRM.
- Producing H_2 via the MWHCL-DRM has a lower CO_2 eq than the C-SRM and fossil fuel-based electrolysis, assuming that electrolysis utilizes electricity supplied from fossil fuel sources.
- Eliminating the CO_2 emissions footprint of supplying CH_4 for the MWHCL-DRM can lead to a CO_2 eq emission similar to clean electrolysis, assuming that electrolysis utilizes renewable electricity.
- Utilizing the energy content of the hot gaseous streams decreased the plant's overall energy consumption.

CHAPTER 9 CONCLUSION AND RECOMMANDATIONS

9.1 Concluding remarks and original contributions

The MWHCL-DRM, a novel GHG utilization method for producing syngas, was proposed and studied in this research. In addition to the proof of concept of the MWHCL-DRM (the first part of this research), the MWHCL-DRM's intrinsic redox kinetics using Fe_3O_4 was studied as the second part of the research. The third stage of the research proposed, designed, and optimized the MWH-CSMBR for syngas manufacturing plants. Lastly, the fourth stage of the research sought to identify the economic and technical factors affecting the proposed technology's scale-up and analyze its environmental footprints.

The findings of this study offer critical insights and knowledge regarding the development of the MWHCL-DRM, which is a technology for GHG utilization to produce syngas. GHG emissions are the most influential factors affecting global warming and climate change. The development of sustainable GHGs utilization technologies to produce syngas is thus a transformative solution for syngas and H_2 manufacturing. The main innovations of this research can be compactly summarized as:

i. A novel greenhouse gas utilization method for syngas production was developed.
ii. A selective-heating technique (microwave heating) was applied for the first time for the chemical looping dry reforming of methane that prevented deposition of carbon.
iii. A selective-heating technique (microwave heating) was applied for the first time for the chemical looping dry reforming of methane that accelerated the rate of favorable reactions, i.e., reduction and oxidation.
iv. Vast experimental investigations were conducted to achieve stable syngas production.
v. A study was conducted to investigate the intrinsic kinetics of magnetite reduction and reoxidation using methane and carbon dioxide, respectively, based on the solid and bulk temperatures.
vi. The conducted kinetic study revealed that microwave heating primarily exerted a thermal influence, as opposed to a non-thermal influence, on the reaction kinetics.
vii. A novel reactor – microwave heating-assisted cyclic simulated moving bed reactor – was proposed, designed, and optimized.

viii. A comprehensive techno-economic and life cycle assessment was conducted to holistically highlight the key parameters impacting the scalability of the proposed process.

9.2 Recommendations for future studies

Since MWHCL-DRM was proposed as a novel syngas production method in this research, the following research directions are recommended for future works:

i. **Detailed CFD-DEM simulation of the microwave heating-assisted cyclic simulated moving bed reactor:** Coupling the electromagnetic field with a CFD-DEM simulation should be conducted to achieve a micro-meso scale study of the reactor's behavior. This study can help analyze uniform heating, the possibility of sparking and arc formation, and thermal and non-thermal influences of electromagnetic waves on the reactions.

ii. **Synthesizing oxygen carriers**: Synthesizing microwave receptor (absorber) oxygen carriers that can be employed inside the fluidized bed reactors heated by microwave. Significant mass and density changes are critical barriers to successfully adapting the microwave absorber oxygen carriers inside in a fluidized bed medium.

iii. **Particle agglomeration and sintering**: Particle agglomeration and sintering is a major issue when applying the microwave heating method. Accordingly, fabricating microwave receptor particles that are resistant to sintering and agglomeration while accomplishing reduction and oxidation is critical.

iv. **Aging effect**: While the stable reduction and re-oxidation of magnetite were investigated, the effects of long-run operations on the reactivity and microwave absorption capacity of the oxygen carrier are mandatory before scaling up.

REFERENCES

CHAPTER 1

1. Kalamaras, C.M. and A.M. Efstathiou. Hydrogen production technologies: current state and future developments. in Conference papers in science. 2013. Hindawi https://doi.org/10.1155/2013/690627.

2. The Center for Climate and Energy Solutions. Available from: https://www.c2es.org/.

3. Yang, Z.-X., X.-G. Li, Q.-L. Yao, Z.-H. Lu, N. Zhang, J. Xia, K. Yang, Y.-Q. Wang, K. Zhang and H.-Z. Liu, 2022 roadmap on hydrogen energy from production to utilizations. Rare Metals, 2022: pp. 1-17, https://doi.org/10.1007/s12598-022-02029-7.

4. EPA, U. Sources of Greenhouse Gas Emissions. 2019; Available from: https://www.epa.gov/ghgemissions/sources-greenhouse-gas-emissions.

5. Martino, M., C. Ruocco, E. Meloni, P. Pullumbi and V.J.C. Palma, Main Hydrogen Production Processes: An Overview. 2021. 11(5): pp. 547, https://doi.org/10.3390/catal11050547.

6. Chen, L., Z. Qi, S. Zhang, J. Su and G.A.J.C. Somorjai, Catalytic hydrogen production from methane: A review on recent progress and prospect. 2020. 10(8): pp. 858, http://dx.doi.org/10.3390/catal10080858.

7. Falciglia, P.P., P. Roccaro, L. Bonanno, G. De Guidi, F.G. Vagliasindi and S. Romano, A review on the microwave heating as a sustainable technique for environmental remediation/detoxification applications. Renewable and sustainable energy reviews, 2018. 95: pp. 147-170, https://doi.org/10.1016/j.rser.2018.07.031.

8. Chaouki, J., S. Farag, M. Attia and J. Doucet, The development of industrial (thermal) processes in the context of sustainability: The case for microwave heating. The Canadian Journal of Chemical Engineering, 2020. 98(4): pp. 832-847, https://doi.org/10.1002/cjce.23710.

9. Amini, A., M. Latifi and J. Chaouki, Electrification of materials processing via microwave irradiation: A review of mechanism and applications. Applied Thermal Engineering, 2021: pp. 117003, https://doi.org/10.1016/j.applthermaleng.2021.117003.

10. Sun, J., W. Wang and Q. Yue, Review on microwave-matter interaction fundamentals and efficient microwave-associated heating strategies. Materials transactions, 2016. 9(4): pp. 231, https://doi.org/10.3390/ma9040231.

11. Hamzehlouia, S., Development of microwave heating-assisted catalytic reaction process: Application for dry reforming of methane optimization. 2017, Ecole Polytechnique, Montreal (Canada).

12. Goyal, H., T.-Y. Chen, W. Chen and D.G. Vlachos, A review of microwave-assisted process intensified multiphase reactors. Chemical Engineering Journal, 2022. 430: pp. 133183, https://doi.org/10.1016/j.cej.2021.133183.

13. Nguyen, H.M., J. Sunarso, C. Li, G.H. Pham, C. Phan and S. Liu, Microwave-assisted catalytic methane reforming: a review. Applied Catalysis A: General, 2020. 599: pp. 117620, https://doi.org/10.1016/j.apcata.2020.117620.

14. Bayham, S.C., A. Tong, M. Kathe and L.S. Fan, Chemical looping technology for energy and chemical production. Wiley Interdisciplinary Reviews: Energy and Environment, 2016. 5(2): pp. 216-241, https://doi.org/10.1002/wene.173.

15. Li, D., R. Xu, Z. Gu, X. Zhu, S. Qing and K. Li, Chemical-looping conversion of methane: a review. Energy Technology, 2020. 8(8): pp. 1900925, https://doi.org/10.1002/ente.201900925.

16. Ramezani, R., L. Di Felice and F. Gallucci, A review of chemical looping reforming technologies for hydrogen production: recent advances and future challenges. Journal of Physics: Energy, 2023 https://doi.org/10.1088/2515-7655/acc4e8.

17. Chein, R.-Y. and W.-H. Hsu, Thermodynamic analysis of syngas production via chemical looping dry reforming of methane. Energy, 2019. 180: pp. 535-547, https://doi.org/10.1016/j.energy.2019.05.083.

18. Mantripragada, H.C. and G. Veser, Hydrogen production via chemical looping dry reforming of methane: Process modeling and systems analysis. AIChE Journal, 2022. 68(5): pp. e17612, https://doi.org/10.1002/aic.17612.

19. García-García, F. and I.S. Metcalfe, Chemical looping dry reforming of methane using mixed oxides of iron and cerium: Operation window. Catalysis Communications, 2021. 160: pp. 106356, https://doi.org/10.1016/j.catcom.2021.106356.

20. Mondal, K., S. Sasmal, S. Badgandi, D.R. Chowdhury, V.J.E.S. Nair and P. Research, Dry reforming of methane to syngas: a potential alternative process for value added chemicals—a techno-economic perspective. 2016. 23(22): pp. 22267-22273, https://doi.org/10.1007/s11356-016-6310-4.

21. Di, Z., Y. Cao, F. Yang, K. Zhang and F. Cheng, Thermodynamic analysis on the parametric optimization of a novel chemical looping methane reforming in the separated productions of H2 and CO. Energy Conversion and Management, 2019. 192: pp. 171-179, https://doi.org/10.1016/j.enconman.2019.04.046.

22. Zare, A.A.D., M. Yari, H. Nami and F. Mohammadkhani, Low-carbon hydrogen, power and heat production based on steam methane reforming and chemical looping combustion. Energy Conversion and Management, 2023. 279: pp. 116752, https://doi.org/10.1016/j.enconman.2023.116752.

23. Jiang, Q., H. Zhang, Y. Cao, H. Hong and H. Jin, Solar hydrogen production via perovskite-based chemical-looping steam methane reforming. Energy Conversion and Management, 2019. 187: pp. 523-536, https://doi.org/10.1016/j.enconman.2019.01.112.

24. Khodabandehloo, M., J. Shabanian, J.-P. Harvey and J. Chaouki, Microwave heating-assisted chemical looping dry reforming of methane. International Journal of Hydrogen Energy, 2024. 71: pp. 1380-1391, https://doi.org/10.1016/j.ijhydene.2024.05.295.

CHAPTER 2

1. Kalamaras, C.M. and A.M. Efstathiou. Hydrogen production technologies: current state and future developments. in Conference papers in science. 2013. Hindawi https://doi.org/10.1155/2013/690627.

2. Bernardi, A., J.E. Graciano and B. Chachuat, Production of chemicals from syngas: An enviro-economic model-based investigation, in Computer Aided Chemical Engineering. 2019, Elsevier. pp., 367-372, https://doi.org/10.1016/B978-0-12-818634-3.50062-X.

3. Chaouki, J., S. Farag, M. Attia and J. Doucet, The development of industrial (thermal) processes in the context of sustainability: The case for microwave heating. The Canadian Journal of Chemical Engineering, 2020. 98(4): pp. 832-847, https://doi.org/10.1002/cjce.23710.

4. George, C., Carbon monoxide. Kirk-Othmer Encyclopedia of Chemical Technology, 2000.

5. Abdalla, A.M., S. Hossain, O.B. Nisfindy, A.T. Azad, M. Dawood and A.K. Azad, Hydrogen production, storage, transportation and key challenges with applications: A review. Energy Conversion and Management, 2018. 165: pp. 602-627, https://doi.org/10.1016/j.enconman.2018.03.088.

6. Chen, L., Z. Qi, S. Zhang, J. Su and G.A.J.C. Somorjai, Catalytic hydrogen production from methane: A review on recent progress and prospect. 2020. 10(8): pp. 858, http://dx.doi.org/10.3390/catal10080858.

7. Yu, Y.-X., J. Yang, K.-K. Zhu, Z.-J. Sui, D. Chen, Y.-A. Zhu and X.-G.J.A.C. Zhou, High-throughput screening of alloy catalysts for dry methane reforming. 2021. 11(14): pp. 8881-8894, https://doi.org/10.1021/acscatal.0c04911.

8. Aramouni, N.A.K., J.G. Touma, B.A. Tarboush, J. Zeaiter, M.N.J.R. Ahmad and S.E. Reviews, Catalyst design for dry reforming of methane: Analysis review. 2018. 82: pp. 2570-2585, https://doi.org/10.1016/j.rser.2017.09.076.

9. de Dios García, I., A. Stankiewicz and H. Nigar, Syngas production via microwave-assisted dry reforming of methane. Catalysis Today, 2021. 362: pp. 72-80, https://doi.org/10.1016/j.cattod.2020.04.045.

10. Hamzehlouia, S., S.A. Jaffer and J. Chaouki, Microwave heating-assisted catalytic dry reforming of methane to syngas. Scientific reports, 2018. 8(1): pp. 1-7, https://doi.org/10.1038/s41598-018-27381-6.

11. Pham, T., K.S. Ro, L. Chen, D. Mahajan, T.J. Siang, U. Ashik, J.-i. Hayashi, D. Pham Minh and D.-V.N. Vo, Microwave-assisted dry reforming of methane for syngas production: a review. Environmental Chemistry Letters, 2020. 18(6): pp. 1987-2019, https://doi.org/10.1007/s10311-020-01055-0.

12. Mondal, K., S. Sasmal, S. Badgandi, D.R. Chowdhury, V.J.E.S. Nair and P. Research, Dry reforming of methane to syngas: a potential alternative process for value added chemicals—a

techno-economic perspective. 2016. 23(22): pp. 22267-22273, https://doi.org/10.1007/s11356-016-6310-4.

13. Papadopoulou, C., H. Matralis and X.J.C.f.a.e.g. Verykios, Utilization of biogas as a renewable carbon source: dry reforming of methane. 2012: pp. 57-127, https://doi.org/10.1007/978-1-4614-0344-9_3.

14. Amini, A., M. Latifi and J. Chaouki, Electrification of materials processing via microwave irradiation: A review of mechanism and applications. Applied Thermal Engineering, 2021: pp. 117003, https://doi.org/10.1016/j.applthermaleng.2021.117003.

15. Sun, J., W. Wang and Q. Yue, Review on microwave-matter interaction fundamentals and efficient microwave-associated heating strategies. Materials transactions, 2016. 9(4): pp. 231, https://doi.org/10.3390/ma9040231.

16. Hamzehlouia, S., Development of microwave heating-assisted catalytic reaction process: Application for dry reforming of methane optimization. 2017, Ecole Polytechnique, Montreal (Canada).

17. Goyal, H., T.-Y. Chen, W. Chen and D.G. Vlachos, A review of microwave-assisted process intensified multiphase reactors. Chemical Engineering Journal, 2022. 430: pp. 133183, https://doi.org/10.1016/j.cej.2021.133183.

18. Nguyen, H.M., J. Sunarso, C. Li, G.H. Pham, C. Phan and S. Liu, Microwave-assisted catalytic methane reforming: a review. Applied Catalysis A: General, 2020. 599: pp. 117620, https://doi.org/10.1016/j.apcata.2020.117620.

19. Radoiu, M., Industrial Microwave Reactors: Components and set-up, in Microwave Chemistry. 2017. pp., 65-90, https://doi.org/10.1515/9783110479935-005.

20. Metaxas, A.a. and R.J. Meredith, Industrial microwave heating. 1983: IET.

21. Siddique, I.J., A.A. Salema, E. Antunes and R. Vinu, Technical challenges in scaling up the microwave technology for biomass processing. Renewable and sustainable energy reviews, 2022. 153: pp. 111767, https://doi.org/10.1016/j.rser.2021.111767.

22. Julian, I., C. Pedersen, A. Jensen, A. Baden, J. Hueso, A. Friderichsen, H. Birkedal, R. Mallada and J. Santamaria, From bench scale to pilot plant: A 150x scaled-up configuration of a

microwave-driven structured reactor for methane dehydroaromatization. Catalysis Today, 2022. 383: pp. 21-30, https://doi.org/10.1016/j.cattod.2021.04.013.

23. Radoiu, M., Microwave drying process scale-up. Chemical Engineering and Processing-Process Intensification, 2020. 155: pp. 108088, https://doi.org/10.1016/j.cep.2020.108088.

24. Fidalgo, B., A. Domínguez, J.J. Pis and J.A. Menéndez, Microwave-assisted dry reforming of methane. International Journal of Hydrogen Energy, 2008. 33(16): pp. 4337-4344, https://doi.org/10.1016/j.ijhydene.2008.05.056.

25. Shi, Y., L. Wang, M. Wu and F. Wang, Order-of-magnitude increase in rate of methane dry reforming over Ni/CeO2-SiC catalysts by microwave catalysis. Applied Catalysis B: Environmental, 2023. 337: pp. 122927, https://doi.org/10.1016/j.apcatb.2023.122927.

26. Olowoyo, J.O., S. Sharifvaghefi and Y. Zheng, Syngas production via microwave-assisted Dry Reforming of Methane over NiFe/MgAl2O4 alloy catalyst. Chemical Engineering and Processing - Process Intensification, 2024. 203: pp. 109899, https://doi.org/10.1016/j.cep.2024.109899.

27. Bayham, S.C., A. Tong, M. Kathe and L.S. Fan, Chemical looping technology for energy and chemical production. Wiley Interdisciplinary Reviews: Energy and Environment, 2016. 5(2): pp. 216-241, https://doi.org/10.1002/wene.173.

28. Li, D., R. Xu, Z. Gu, X. Zhu, S. Qing and K. Li, Chemical-looping conversion of methane: a review. Energy Technology, 2020. 8(8): pp. 1900925, https://doi.org/10.1002/ente.201900925.

29. Ramezani, R., L. Di Felice and F. Gallucci, A review of chemical looping reforming technologies for hydrogen production: recent advances and future challenges. Journal of Physics: Energy, 2023 https://doi.org/10.1088/2515-7655/acc4e8.

30. Chein, R.-Y. and W.-H. Hsu, Thermodynamic analysis of syngas production via chemical looping dry reforming of methane. Energy, 2019. 180: pp. 535-547, https://doi.org/10.1016/j.energy.2019.05.083.

31. Mantripragada, H.C. and G. Veser, Hydrogen production via chemical looping dry reforming of methane: Process modeling and systems analysis. AIChE Journal, 2022. 68(5): pp. e17612, https://doi.org/10.1002/aic.17612.

32. García-García, F. and I.S. Metcalfe, Chemical looping dry reforming of methane using mixed oxides of iron and cerium: Operation window. Catalysis Communications, 2021. 160: pp. 106356, https://doi.org/10.1016/j.catcom.2021.106356.

CHAPTER 4

1. Wang, C., Y. Wang, M. Chen, D. Liang, Z. Yang, W. Cheng, Z. Tang, J. Wang and H. Zhang, Recent advances during CH4 dry reforming for syngas production: A mini review. International Journal of Hydrogen Energy, 2021. 46(7): pp. 5852-5874, https://doi.org/10.1016/j.ijhydene.2020.10.240.

2. Kalamaras, C.M. and A.M. Efstathiou. Hydrogen production technologies: current state and future developments. in Conference papers in science. 2013. Hindawi https://doi.org/10.1155/2013/690627.

3. George, C., Carbon monoxide. Kirk-Othmer Encyclopedia of Chemical Technology, 2000.

4. Ighalo, J.O. and P.B. Amama, Recent advances in the catalysis of steam reforming of methane (SRM). International Journal of Hydrogen Energy, 2024. 51: pp. 688-700, https://doi.org/10.1016/j.ijhydene.2023.10.177.

5. Dincer, I. and C. Acar, Review and evaluation of hydrogen production methods for better sustainability. International Journal of Hydrogen Energy, 2015. 40(34): pp. 11094-11111, https://doi.org/10.1016/j.ijhydene.2014.12.035.

6. Ishaq, H., I. Dincer and C. Crawford, A review on hydrogen production and utilization: Challenges and opportunities. International Journal of Hydrogen Energy, 2022. 47(62): pp. 26238-26264, https://doi.org/10.1016/j.ijhydene.2021.11.149.

7. Dincer, I. and C. Acar, Innovation in hydrogen production. International Journal of Hydrogen Energy, 2017. 42(22): pp. 14843-14864, https://doi.org/10.1016/j.ijhydene.2017.04.107.

8. Das, S., A. Biswas, J. Bhattacharya, C.S. Tiwary and M. Paliwal, Utilization of laterite ore as an oxygen carrier in chemical looping reforming of methane for syngas production. International

Journal of Hydrogen Energy, 2023. 48(51): pp. 19411-19421, https://doi.org/10.1016/j.ijhydene.2023.02.054.

9. Wang, X., S. Abanades, S. Chuayboon, J. Zhang and J. Wei, Solar-driven chemical looping reforming of methane over SrFeO3-δ-Ca0.5Mn0.5O nanocomposite foam. International Journal of Hydrogen Energy, 2022. 47(79): pp. 33664-33676, https://doi.org/10.1016/j.ijhydene.2022.07.241.

10. Hu, Z., Z. Miao, J. Wu and E. Jiang, Nickel-iron modified natural ore oxygen carriers for chemical looping steam methane reforming to produce hydrogen. International Journal of Hydrogen Energy, 2021. 46(80): pp. 39700-39718, https://doi.org/10.1016/j.ijhydene.2021.09.242.

11. Nazari, M., M. Soltanieh, A. Heydarinasab and B. Maddah, Synthesis of a new self-supported Mgy(CuxNi0.6-xMn0.4)1-yFe2O4 oxygen carrier for chemical looping steam methane reforming process. International Journal of Hydrogen Energy, 2021. 46(37): pp. 19397-19420, https://doi.org/10.1016/j.ijhydene.2021.03.081.

12. Bhosale, R., F. AlMomani and G. Takalkar, Thermodynamic analysis of solar-driven chemical looping steam methane reforming over Cr2O3/Cr redox pair. International Journal of Hydrogen Energy, 2020. 45(17): pp. 10370-10380, https://doi.org/10.1016/j.ijhydene.2019.08.205.

13. Quan, J., Y. Chen, H. Mai, Q. Zeng, J. Lv, E. Jiang and Z. Hu, Uniformly dispersed NiFeAlO4 as oxygen carrier for chemical looping steam methane reforming to produce syngas. International Journal of Hydrogen Energy, 2024. 61: pp. 901-913, https://doi.org/10.1016/j.ijhydene.2024.02.355.

14. Bayham, S.C., A. Tong, M. Kathe and L.S. Fan, Chemical looping technology for energy and chemical production. Wiley Interdisciplinary Reviews: Energy and Environment, 2016. 5(2): pp. 216-241, https://doi.org/10.1002/wene.173.

15. Li, D., R. Xu, Z. Gu, X. Zhu, S. Qing and K. Li, Chemical-looping conversion of methane: a review. Energy Technology, 2020. 8(8): pp. 1900925, https://doi.org/10.1002/ente.201900925.

16. Ramezani, R., L. Di Felice and F. Gallucci, A review of chemical looping reforming technologies for hydrogen production: recent advances and future challenges. Journal of Physics: Energy, 2023 https://doi.org/10.1088/2515-7655/acc4e8.

17. Chein, R.-Y. and W.-H. Hsu, Thermodynamic analysis of syngas production via chemical looping dry reforming of methane. Energy, 2019. 180: pp. 535-547, https://doi.org/10.1016/j.energy.2019.05.083.

18. Mantripragada, H.C. and G. Veser, Hydrogen production via chemical looping dry reforming of methane: Process modeling and systems analysis. AIChE Journal, 2022. 68(5): pp. e17612, https://doi.org/10.1002/aic.17612.

19. García-García, F. and I.S. Metcalfe, Chemical looping dry reforming of methane using mixed oxides of iron and cerium: Operation window. Catalysis Communications, 2021. 160: pp. 106356, https://doi.org/10.1016/j.catcom.2021.106356.

20. Chen, L., Z. Qi, S. Zhang, J. Su and G.A.J.C. Somorjai, Catalytic hydrogen production from methane: A review on recent progress and prospect. 2020. 10(8): pp. 858, http://dx.doi.org/10.3390/catal10080858.

21. Zhang, X., A.C.K. Yip and S. Pang, Advances in the application of active metal-based sorbents and oxygen carriers in chemical looping biomass steam gasification for H2 production. International Journal of Hydrogen Energy, 2023. 48(28): pp. 10394-10422, https://doi.org/10.1016/j.ijhydene.2022.11.317.

22. Siriwardane, R., H. Tian and J. Fisher, Production of pure hydrogen and synthesis gas with Cu–Fe oxygen carriers using combined processes of chemical looping combustion and methane decomposition/reforming. International Journal of Hydrogen Energy, 2015. 40(4): pp. 1698-1708, https://doi.org/10.1016/j.ijhydene.2014.11.090.

23. Das, S., A. Biswas, C.S. Tiwary and M. Paliwal, Hydrogen production using chemical looping technology: A review with emphasis on H2 yield of various oxygen carriers. International Journal of Hydrogen Energy, 2022. 47(66): pp. 28322-28352, https://doi.org/10.1016/j.ijhydene.2022.06.170.

24. Siddique, I.J., A.A. Salema, E. Antunes and R. Vinu, Technical challenges in scaling up the microwave technology for biomass processing. Renewable and sustainable energy reviews, 2022. 153: pp. 111767, https://doi.org/10.1016/j.rser.2021.111767.

25. Goyal, H., T.-Y. Chen, W. Chen and D.G. Vlachos, A review of microwave-assisted process intensified multiphase reactors. Chemical Engineering Journal, 2022. 430: pp. 133183, https://doi.org/10.1016/j.cej.2021.133183.

26. Amini, A., M. Latifi and J. Chaouki, Electrification of materials processing via microwave irradiation: A review of mechanism and applications. Applied Thermal Engineering, 2021: pp. 117003, https://doi.org/10.1016/j.applthermaleng.2021.117003.

27. Chaouki, J., S. Farag, M. Attia and J. Doucet, The development of industrial (thermal) processes in the context of sustainability: The case for microwave heating. The Canadian Journal of Chemical Engineering, 2020. 98(4): pp. 832-847, https://doi.org/10.1002/cjce.23710.

28. Li, K., H. Wang and Y. Wei, Syngas generation from methane using a chemical-looping concept: a review of oxygen carriers. Journal of Chemistry, 2013. 2013 https://doi.org/10.1155/2013/294817.

29. Tian, M., C. Wang, Y. Han and X. Wang, Recent advances of oxygen carriers for chemical looping reforming of methane. ChemCatChem, 2021. 13(7): pp. 1615-1637, https://doi.org/10.1002/cctc.202001481.

30. Cheng, Z., L. Qin, J.A. Fan and L.-S. Fan, New insight into the development of oxygen carrier materials for chemical looping systems. Engineering, 2018. 4(3): pp. 343-351, https://doi.org/10.1016/j.eng.2018.05.002.

31. Luo, S., L. Zeng and L.-S. Fan, Chemical looping technology: oxygen carrier characteristics. Annual review of chemical and biomolecular engineering, 2015. 6: pp. 53-75, https://doi.org/10.1146/annurev-chembioeng-060713-040334.

32. Zhu, X., Y. Wei, H. Wang and K. Li, Ce–Fe oxygen carriers for chemical-looping steam methane reforming. International Journal of Hydrogen Energy, 2013. 38(11): pp. 4492-4501, https://doi.org/10.1016/j.ijhydene.2013.01.115.

33. Sun, J., W. Wang and Q. Yue, Review on microwave-matter interaction fundamentals and efficient microwave-associated heating strategies. Materials transactions, 2016. 9(4): pp. 231, https://doi.org/10.3390/ma9040231.

34. Lu, C., K. Li, H. Wang, X. Zhu, Y. Wei, M. Zheng and C. Zeng, Chemical looping reforming of methane using magnetite as oxygen carrier: Structure evolution and reduction kinetics. Applied Energy, 2018. 211: pp. 1-14, https://doi.org/10.1016/j.apenergy.2017.11.049.

35. Kim, Y.T., J.-J. Lee and J. Lee, Electricity-driven reactors that promote thermochemical catalytic reactions via joule and induction heating: A review. Chemical Engineering Journal, 2023: pp. 144333, https://doi.org/10.1016/j.cej.2023.144333.

36. Wang, W., G. Tuci, C. Duong-Viet, Y. Liu, A. Rossin, L. Luconi, J.-M. Nhut, L. Nguyen-Dinh, C. Pham-Huu and G. Giambastiani, Induction heating: An enabling technology for the heat management in catalytic processes. ACS Catalysis, 2019. 9(9): pp. 7921-7935, https://doi.org/10.1021/acscatal.9b02471.

37. Ke, C., T. Liu, Y. Zhang and Q. Xiong, Energy absorption performances of silicon carbide particles during microwave heating process. Chemical Engineering and Processing-Process Intensification, 2022. 172: pp. 108796, https://doi.org/10.1016/j.cep.2022.108796.

38. Hamzehlouia, S., S.A. Jaffer and J. Chaouki, Microwave heating-assisted catalytic dry reforming of methane to syngas. Scientific reports, 2018. 8(1): pp. 1-7, https://doi.org/10.1038/s41598-018-27381-6.

39. de Dios García, I., A. Stankiewicz and H. Nigar, Syngas production via microwave-assisted dry reforming of methane. Catalysis Today, 2021. 362: pp. 72-80, https://doi.org/10.1016/j.cattod.2020.04.045.

40. Zhang, M., Y. Gao, Y. Mao, W. Wang, J. Sun, Z. Song, J. Sun and X. Zhao, Enhanced dry reforming of methane by microwave-mediated confined catalysis over Ni-La/AC catalyst. Chemical Engineering Journal, 2023. 451: pp. 138616, https://doi.org/10.1016/j.cej.2022.138616.

41. Harvey, J.-P., F. Lebreux-Desilets, J. Marchand, K. Oishi, A.-F. Bouarab, C. Robelin, A.E. Gheribi and A.D. Pelton, On the application of the Factsage thermochemical software and databases in materials science and pyrometallurgy. Processes, 2020. 8(9): pp. 1156, https://doi.org/10.3390/pr8091156.

42. Nasr, S. and K.P. Plucknett, Kinetics of iron ore reduction by methane for chemical looping combustion. Energy & fuels, 2014. 28(2): pp. 1387-1395, https://doi.org/10.1021/ef402142q.

43. Su, M., J. Ma, X. Tian and H. Zhao, Reduction kinetics of hematite as oxygen carrier in chemical looping combustion. Fuel Processing Technology, 2017. 155: pp. 160-167.

44. Adavi, K., J. Shabanian and J. Chaouki, Temperature Distribution Assessment in Gas–Solid Reactive and Nonreactive Systems Heated by Microwaves. Industrial & Engineering Chemistry Research, 2023 https://doi.org/10.1021/acs.iecr.3c00575.

45. Amini, A., K.-i. Ohno, T. Maeda and K. Kunitomo, Effect of the ratio of magnetite particle size to microwave penetration depth on reduction reaction behaviour by H2. Scientific reports, 2018. 8(1): pp. 15023, https://doi.org/10.1038/s41598-018-33460-5.

46. Lide, D.R. and H. Frederikse, CRC Handbook of Chemistry and Physics 76th Eddition. New York, 1994: pp. 1195-1996.

47. Fedunik-Hofman, L., A. Bayon and S.W. Donne, Kinetics of solid-gas reactions and their application to carbonate looping systems. Energies, 2019. 12(15): pp. 2981, https://doi.org/10.3390/en12152981.

48. Go, K.S., S.R. Son and S.D. Kim, Reaction kinetics of reduction and oxidation of metal oxides for hydrogen production. International Journal of Hydrogen Energy, 2008. 33(21): pp. 5986-5995, https://doi.org/10.1016/j.ijhydene.2008.05.039.

49. Zhong, Y., Z. Wang, Z. Guo and Q. Tang, Defluidization behavior of iron powders at elevated temperature: Influence of fluidizing gas and particle adhesion. Powder technology, 2012. 230: pp. 225-231, https://doi.org/10.1016/j.powtec.2012.07.036.

CHAPTER 5

1. Niu, J., F. Guo, J. Ran, W. Qi and Z. Yang, Methane dry (CO2) reforming to syngas (H2/CO) in catalytic process: From experimental study and DFT calculations. International Journal of Hydrogen Energy, 2020. 45(55): pp. 30267-30287, https://doi.org/10.1016/j.ijhydene.2020.08.067.

2. Wang, C., Y. Wang, M. Chen, D. Liang, Z. Yang, W. Cheng, Z. Tang, J. Wang and H. Zhang, Recent advances during CH4 dry reforming for syngas production: A mini review. International Journal of Hydrogen Energy, 2021. 46(7): pp. 5852-5874, https://doi.org/10.1016/j.ijhydene.2020.10.240.

3. Kalamaras, C.M. and A.M. Efstathiou. Hydrogen production technologies: current state and future developments. in Conference papers in science. 2013. Hindawi https://doi.org/10.1155/2013/690627.

4. Sharifianjazi, F., A. Esmaeilkhanian, L. Bazli, S. Eskandarinezhad, S. Khaksar, P. Shafiee, M. Yusuf, B. Abdullah, P. Salahshour and F. Sadeghi, A review on recent advances in dry reforming of methane over Ni- and Co-based nanocatalysts. International Journal of Hydrogen Energy, 2022. 47(100): pp. 42213-42233, https://doi.org/10.1016/j.ijhydene.2021.11.172.

5. Awad, M.M., I. Hussain, U. Mustapha, O. Ahmed Taialla, A. Musa Alhassan, E. Kotob, A. Shafiu Abdullahi, S.A. Ganiyu and K. Alhooshani, A critical review of recent advancements in catalytic dry reforming of methane: Physicochemical properties, current challenges, and informetric insights. International Journal of Hydrogen Energy, 2024. 76: pp. 202-233, https://doi.org/10.1016/j.ijhydene.2024.03.319.

6. Hamzehlouia, S., S.A. Jaffer and J. Chaouki, Microwave heating-assisted catalytic dry reforming of methane to syngas. Scientific reports, 2018. 8(1): pp. 1-7, https://doi.org/10.1038/s41598-018-27381-6.

7. Pham, T., K.S. Ro, L. Chen, D. Mahajan, T.J. Siang, U. Ashik, J.-i. Hayashi, D. Pham Minh and D.-V.N. Vo, Microwave-assisted dry reforming of methane for syngas production: a review. Environmental Chemistry Letters, 2020. 18(6): pp. 1987-2019, https://doi.org/10.1007/s10311-020-01055-0.

8. Mondal, K., S. Sasmal, S. Badgandi, D.R. Chowdhury, V.J.E.S. Nair and P. Research, Dry reforming of methane to syngas: a potential alternative process for value added chemicals—a techno-economic perspective. 2016. 23(22): pp. 22267-22273, https://doi.org/10.1007/s11356-016-6310-4.

9. Li, D., R. Xu, Z. Gu, X. Zhu, S. Qing and K. Li, Chemical-looping conversion of methane: a review. Energy Technology, 2020. 8(8): pp. 1900925, https://doi.org/10.1002/ente.201900925.

10. Ramezani, R., L. Di Felice and F. Gallucci, A review of chemical looping reforming technologies for hydrogen production: recent advances and future challenges. Journal of Physics: Energy, 2023 https://doi.org/10.1088/2515-7655/acc4e8.

11. Zhu, X., Y. Wei, H. Wang and K. Li, Ce–Fe oxygen carriers for chemical-looping steam methane reforming. International Journal of Hydrogen Energy, 2013. 38(11): pp. 4492-4501, https://doi.org/10.1016/j.ijhydene.2013.01.115.

12. Das, S., A. Biswas, J. Bhattacharya, C.S. Tiwary and M. Paliwal, Utilization of laterite ore as an oxygen carrier in chemical looping reforming of methane for syngas production. International Journal of Hydrogen Energy, 2023. 48(51): pp. 19411-19421, https://doi.org/10.1016/j.ijhydene.2023.02.054.

13. Wang, X., S. Abanades, S. Chuayboon, J. Zhang and J. Wei, Solar-driven chemical looping reforming of methane over SrFeO3-δ-Ca0.5Mn0.5O nanocomposite foam. International Journal of Hydrogen Energy, 2022. 47(79): pp. 33664-33676, https://doi.org/10.1016/j.ijhydene.2022.07.241.

14. Hu, Z., Z. Miao, J. Wu and E. Jiang, Nickel-iron modified natural ore oxygen carriers for chemical looping steam methane reforming to produce hydrogen. International Journal of Hydrogen Energy, 2021. 46(80): pp. 39700-39718, https://doi.org/10.1016/j.ijhydene.2021.09.242.

15. Nazari, M., M. Soltanieh, A. Heydarinasab and B. Maddah, Synthesis of a new self-supported Mgy(CuxNi0.6-xMn0.4)1-yFe2O4 oxygen carrier for chemical looping steam methane reforming process. International Journal of Hydrogen Energy, 2021. 46(37): pp. 19397-19420, https://doi.org/10.1016/j.ijhydene.2021.03.081.

16. Bhosale, R., F. AlMomani and G. Takalkar, Thermodynamic analysis of solar-driven chemical looping steam methane reforming over Cr2O3/Cr redox pair. International Journal of Hydrogen Energy, 2020. 45(17): pp. 10370-10380, https://doi.org/10.1016/j.ijhydene.2019.08.205.

17. Quan, J., Y. Chen, H. Mai, Q. Zeng, J. Lv, E. Jiang and Z. Hu, Uniformly dispersed NiFeAlO4 as oxygen carrier for chemical looping steam methane reforming to produce syngas.

International Journal of Hydrogen Energy, 2024. 61: pp. 901-913, https://doi.org/10.1016/j.ijhydene.2024.02.355.

18. Amini, A., M. Latifi and J. Chaouki, Electrification of materials processing via microwave irradiation: A review of mechanism and applications. Applied Thermal Engineering, 2021: pp. 117003, https://doi.org/10.1016/j.applthermaleng.2021.117003.

19. Chaouki, J., S. Farag, M. Attia and J. Doucet, The development of industrial (thermal) processes in the context of sustainability: The case for microwave heating. The Canadian Journal of Chemical Engineering, 2020. 98(4): pp. 832-847, https://doi.org/10.1002/cjce.23710.

20. Goyal, H., T.-Y. Chen, W. Chen and D.G. Vlachos, A review of microwave-assisted process intensified multiphase reactors. Chemical Engineering Journal, 2022. 430: pp. 133183, https://doi.org/10.1016/j.cej.2021.133183.

21. Adavi, K., J. Shabanian and J. Chaouki, Temperature Distribution Assessment in Gas–Solid Reactive and Nonreactive Systems Heated by Microwaves. Industrial & Engineering Chemistry Research, 2023 https://doi.org/10.1021/acs.iecr.3c00575.

22. Khodabandehloo, M., J. Shabanian, J.-P. Harvey and J. Chaouki, Microwave heating-assisted chemical looping dry reforming of methane. International Journal of Hydrogen Energy, 2024. 71: pp. 1380-1391, https://doi.org/10.1016/j.ijhydene.2024.05.295.

23. Shirchi, S., B. Khoshandam and F. Hormozi, Reduction kinetics of cobalt oxide powder by methane in a fluidized bed reactor. Journal of the Taiwan Institute of Chemical Engineers, 2015. 51: pp. 171-176.

24. Su, M., J. Ma, X. Tian and H. Zhao, Reduction kinetics of hematite as oxygen carrier in chemical looping combustion. Fuel Processing Technology, 2017. 155: pp. 160-167.

25. Yang, L., Z. Zhao, J. Hao, J. Wei and J. Zhang, Oxygen release and reduction kinetics of La0. 35Sr0. 35Ba0. 3Fe1-xCoxO3 as oxygen carriers for chemical looping dry reforming of methane. Applications in Energy and Combustion Science, 2023. 15: pp. 100173.

26. Nasr, S. and K.P. Plucknett, Kinetics of iron ore reduction by methane for chemical looping combustion. Energy & fuels, 2014. 28(2): pp. 1387-1395, https://doi.org/10.1021/ef402142q.

27. He, K., Z. Zheng and Z. Chen, Multistep reduction kinetics of Fe3O4 to Fe with CO in a micro fluidized bed reaction analyzer. Powder technology, 2020. 360: pp. 1227-1236, https://doi.org/10.1016/j.powtec.2019.10.094.

28. Monazam, E.R., R.W. Breault, R. Siriwardane, G. Richards and S. Carpenter, Kinetics of the reduction of hematite (Fe2O3) by methane (CH4) during chemical looping combustion: A global mechanism. Chemical Engineering Journal, 2013. 232: pp. 478-487, https://doi.org/10.1016/j.cej.2013.07.091.

29. Go, K.S., S.R. Son and S.D. Kim, Reaction kinetics of reduction and oxidation of metal oxides for hydrogen production. International Journal of Hydrogen Energy, 2008. 33(21): pp. 5986-5995, https://doi.org/10.1016/j.ijhydene.2008.05.039.

30. Longbottom, R.J. and L. Kolbeinsen, Iron ore reduction with CO and H2 gas mixtures–Thermodynamic and kinetic modelling. 2008.

31. Domşa, A., L. Szabó, Z. Spîrchez and A. Pálfalvi, The kinetics of direct reduction of iron oxides with methane, in Modern Developments in Powder Metallurgy: Volume 1 Fundamentals and Methods. 1966, Springer. pp., 3-14, https://doi.org/10.1007/978-1-4684-7706-1_1.

32. Fedunik-Hofman, L., A. Bayon and S.W. Donne, Kinetics of solid-gas reactions and their application to carbonate looping systems. Energies, 2019. 12(15): pp. 2981, https://doi.org/10.3390/en12152981.

33. Hancock, J. and J. Sharp, Method of comparing solid-state kinetic data and its application to the decomposition of kaolinite, brucite, and BaCO3. Journal of the American Ceramic Society, 1972. 55(2): pp. 74-77, https://doi.org/10.1111/j.1151-2916.1972.tb11213.x.

34. Dai, X., J. Cheng, Z. Li, M. Liu, Y. Ma and X. Zhang, Reduction kinetics of lanthanum ferrite perovskite for the production of synthesis gas by chemical-looping methane reforming. Chemical Engineering Science, 2016. 153: pp. 236-245, https://doi.org/10.1016/j.ces.2016.07.011.

35. Shabanian, J. and J. Chaouki, Fluidized Beds for Gas–Solid Reactions☆. Essentials of Fluidization Technology, 2020: pp. 363-404.

36. Khawam, A. and D.R. Flanagan, Solid-state kinetic models: basics and mathematical fundamentals. The journal of physical chemistry B, 2006. 110(35): pp. 17315-17328.

37. Cetinkaya, S. and S. Eroglu, A Single-Step Process for Direct Reduction of Iron Oxide to Sponge Iron by Undiluted Methane. JOM, 2017. 69: pp. 993-998, https://doi.org/10.1007/s11837-017-2323-9.

38. Alizadeh, R., E. Jamshidi and H. Ale Ebrahim, Kinetic study of nickel oxide reduction by methane. Chemical Engineering & Technology: Industrial Chemistry-Plant Equipment-Process Engineering-Biotechnology, 2007. 30(8): pp. 1123-1128, https://doi.org/10.1002/ceat.200700067.

39. Tang, Q., Y. Ma and K. Huang, Fe3O4/ZrO2 composite as a robust chemical looping oxygen carrier: a kinetics study on the reduction process. ACS Applied Energy Materials, 2021. 4(7): pp. 7091-7100, https://doi.org/10.1021/acsaem.1c01152.

40. Yang, L., Z. Zhao, J. Hao, J. Wei and J. Zhang, Oxygen release and reduction kinetics of La0.35Sr0.35Ba0.3Fe1-xCoxO3 as oxygen carriers for chemical looping dry reforming of methane. Applications in Energy and Combustion Science, 2023. 15: pp. 100173, https://doi.org/10.1016/j.jaecs.2023.100173.

41. Hosseini, S.Y., M.R. Khosravi-Nikou and A. Shariati, Kinetic Study of the Reduction Step for Chemical Looping Steam Methane Reforming by CeO2-Fe2O3 Oxygen Carriers. Chemical Engineering & Technology, 2020. 43(3): pp. 540-552, https://doi.org/10.1002/ceat.201900290.

42. Liu, W., J.Y. Lim, M.A. Saucedo, A.N. Hayhurst, S.A. Scott and J.S. Dennis, Kinetics of the reduction of wüstite by hydrogen and carbon monoxide for the chemical looping production of hydrogen. Chemical Engineering Science, 2014. 120: pp. 149-166, https://doi.org/10.1016/j.ces.2014.08.010.

43. Lu, C., K. Li, H. Wang, X. Zhu, Y. Wei, M. Zheng and C. Zeng, Chemical looping reforming of methane using magnetite as oxygen carrier: Structure evolution and reduction kinetics. Applied Energy, 2018. 211: pp. 1-14, https://doi.org/10.1016/j.apenergy.2017.11.049.

44. Adavi, K., A. Amini, M. Latifi, J. Shabanian and J. Chaouki, Kinetic study of multiphase reactions under microwave irradiation: a mini-review. Frontiers in Chemical Engineering: pp. 102, https://doi.org/10.3389/fceng.2022.1059160.

CHAPTER 5 – SUPPLEMENTARY MATERIAL

1. Das, S., M. Shah, R.K. Gupta and A.J.J.o.C.U. Bordoloi, Enhanced dry methane reforming over Ru decorated mesoporous silica and its kinetic study. 2019. 29: pp. 240-253, https://doi.org/10.1016/j.jcou.2018.12.016.

2. Zhou, L., L.R. Enakonda, Y. Saih, S. Loptain, D. Gary, P. Del-Gallo and J.M.J.C. Basset, Catalytic methane decomposition over Fe-Al2O3. 2016. 9(11): pp. 1243-1248, https://doi.org/10.1002/cssc.201600310.

3. Santacesaria, E. and R.J.C.S.I.P.A.d. Tesser, The Chemical Reactor from Laboratory to Industrial Plant. 2018. 10: pp. 978-3, https://doi.org/10.1007/978-3-319-97439-2.

4. Fogler, H.S. and S.H. Fogler, Elements of chemical reaction engineering. 1999: Pearson Educación.

5. Weisz, P. and C. Prater, Interpretation of measurements in experimental catalysis, in Advances in catalysis. 1954, Elsevier. pp., 143-196, https://doi.org/10.1016/S0360-0564(08)60390-9.

6. Tesser, R. and E.J.P. Santacesaria, Revisiting the Role of Mass and Heat Transfer in Gas–Solid Catalytic Reactions. 2020. 8(12): pp. 1599, https://doi.org/10.3390/pr8121599.

7. Pino, L., C. Italiano, M. Laganà, A. Vita, V.J.C.S. Recupero and Technology, Kinetic study of the methane dry (CO 2) reforming reaction over the Ce 0.70 La 0.20 Ni 0.10 O 2− δ catalyst. 2020. 10(8): pp. 2652-2662, https://doi.org/10.1039/C9CY02192B.

CHAPTER 6

1. Abdul Mujeebu, M., Hydrogen and syngas production by superadiabatic combustion – A review. Applied Energy, 2016. 173: pp. 210-224, https://doi.org/10.1016/j.apenergy.2016.04.018.

2. de Dios García, I., A. Stankiewicz and H. Nigar, Syngas production via microwave-assisted dry reforming of methane. Catalysis Today, 2021. 362: pp. 72-80, https://doi.org/10.1016/j.cattod.2020.04.045.

3. Hamzehlouia, S., S.A. Jaffer and J. Chaouki, Microwave heating-assisted catalytic dry reforming of methane to syngas. Scientific reports, 2018. 8(1): pp. 1-7, https://doi.org/10.1038/s41598-018-27381-6.

4. Zhang, Q., L. Wang, W. Chen and C. Zhang, Assessing the impact of hydrogen trade towards low-carbon energy transition. Applied Energy, 2024. 376: pp. 124233, https://doi.org/10.1016/j.apenergy.2024.124233.

5. Park, J., S. Kang, S. Kim, H. Kim, S.-K. Kim and J.H. Lee, Optimizing green hydrogen systems: Balancing economic viability and reliability in the face of supply-demand volatility. Applied Energy, 2024. 368: pp. 123492, https://doi.org/10.1016/j.apenergy.2024.123492.

6. Rissman, J., C. Bataille, E. Masanet, N. Aden, W.R. Morrow, N. Zhou, N. Elliott, R. Dell, N. Heeren, B. Huckestein, J. Cresko, S.A. Miller, J. Roy, P. Fennell, B. Cremmins, T. Koch Blank, D. Hone, E.D. Williams, S. de la Rue du Can, B. Sisson, M. Williams, J. Katzenberger, D. Burtraw, G. Sethi, H. Ping, D. Danielson, H. Lu, T. Lorber, J. Dinkel and J. Helseth, Technologies and policies to decarbonize global industry: Review and assessment of mitigation drivers through 2070. Applied Energy, 2020. 266: pp. 114848, https://doi.org/10.1016/j.apenergy.2020.114848.

7. Gradisher, L., B. Dutcher and M. Fan, Catalytic hydrogen production from fossil fuels via the water gas shift reaction. Applied Energy, 2015. 139: pp. 335-349, https://doi.org/10.1016/j.apenergy.2014.10.080.

8. Kalamaras, C.M. and A.M. Efstathiou. Hydrogen production technologies: current state and future developments. in Conference papers in science. 2013. Hindawi https://doi.org/10.1155/2013/690627.

9. Mondal, K., S. Sasmal, S. Badgandi, D.R. Chowdhury, V.J.E.S. Nair and P. Research, Dry reforming of methane to syngas: a potential alternative process for value added chemicals—a techno-economic perspective. 2016. 23(22): pp. 22267-22273, https://doi.org/10.1007/s11356-016-6310-4.

10. Beccarello, M. and G. Di Foggia, Review and perspectives of key decarbonization drivers to 2030. Energies, 2023. 16(3): pp. 1345, https://doi.org/10.3390/en16031345.

11. Bouaboula, H., J. Chaouki, Y. Belmabkhout and A. Zaabout, Comparative review of Direct air capture technologies: From technical, commercial, economic, and environmental aspects. Chemical Engineering Journal, 2024. 484: pp. 149411, https://doi.org/10.1016/j.cej.2024.149411.

12. Tang, M., L. Xu and M. Fan, Progress in oxygen carrier development of methane-based chemical-looping reforming: A review. Applied Energy, 2015. 151: pp. 143-156, https://doi.org/10.1016/j.apenergy.2015.04.017.

13. Zhu, Y., N. Jin, R. Liu, X. Sun, L. Bai, H. Tian, X. Ma and X. Wang, Bimetallic BaFe2MAl9O19 (M = Mn, Ni, and Co) hexaaluminates as oxygen carriers for chemical looping dry reforming of methane. Applied Energy, 2020. 258: pp. 114070, https://doi.org/10.1016/j.apenergy.2019.114070.

14. Shah, V., Z. Cheng, D.S. Baser, J.A. Fan and L.-S. Fan, Highly Selective Production of Syngas from Chemical Looping Reforming of Methane with CO2 Utilization on MgO-supported Calcium Ferrite Redox Materials. Applied Energy, 2021. 282: pp. 116111, https://doi.org/10.1016/j.apenergy.2020.116111.

15. Kang, D., H.S. Lim, M. Lee and J.W. Lee, Syngas production on a Ni-enhanced Fe2O3/Al2O3 oxygen carrier via chemical looping partial oxidation with dry reforming of methane. Applied Energy, 2018. 211: pp. 174-186, https://doi.org/10.1016/j.apenergy.2017.11.018.

16. Lu, C., K. Li, H. Wang, X. Zhu, Y. Wei, M. Zheng and C. Zeng, Chemical looping reforming of methane using magnetite as oxygen carrier: Structure evolution and reduction kinetics. Applied Energy, 2018. 211: pp. 1-14, https://doi.org/10.1016/j.apenergy.2017.11.049.

17. Li, D., R. Xu, Z. Gu, X. Zhu, S. Qing and K. Li, Chemical-looping conversion of methane: a review. Energy Technology, 2020. 8(8): pp. 1900925, https://doi.org/10.1002/ente.201900925.

18. Ramezani, R., L. Di Felice and F. Gallucci, A review of chemical looping reforming technologies for hydrogen production: recent advances and future challenges. Journal of Physics: Energy, 2023 https://doi.org/10.1088/2515-7655/acc4e8.

19. Chein, R.-Y. and W.-H. Hsu, Thermodynamic analysis of syngas production via chemical looping dry reforming of methane. Energy, 2019. 180: pp. 535-547, https://doi.org/10.1016/j.energy.2019.05.083.

20. Chaouki, J., P. Leclerc, A. Solouki, M. Monzavi, A. Hussain, Z. Chen and A. Amini, Non-uniform Microwave Heating of Heterogeneous Systems: How to Turn Problems into Opportunities. 2023 https://doi.org/10.1039/BK9781837670277-00347.

21. Chaouki, J., S. Farag, M. Attia and J. Doucet, The development of industrial (thermal) processes in the context of sustainability: The case for microwave heating. The Canadian Journal of Chemical Engineering, 2020. 98(4): pp. 832-847, https://doi.org/10.1002/cjce.23710.

22. Adavi, K., J. Shabanian and J. Chaouki, Temperature Distribution Assessment in Gas–Solid Reactive and Nonreactive Systems Heated by Microwaves. Industrial & Engineering Chemistry Research, 2023 https://doi.org/10.1021/acs.iecr.3c00575.

23. Monzavi, M. and J. Chaouki, Microwave catalytic pyrolysis of heavy oil: A lump kinetic study approach. Journal of Analytical and Applied Pyrolysis, 2024. 179: pp. 106472, https://doi.org/10.1016/j.jaap.2024.106472.

24. Adavi, K., A. Amini, M. Latifi, J. Shabanian and J. Chaouki, Kinetic study of multiphase reactions under microwave irradiation: a mini-review. Frontiers in Chemical Engineering: pp. 102, https://doi.org/10.3389/fceng.2022.1059160.

25. Solouki, A., S.A. Jaffer and J. Chaouki, Process development and techno-economic analysis of microwave-assisted demetallization and desulfurization of crude petroleum oil. Energy Reports, 2022. 8: pp. 4373-4385, https://doi.org/10.1016/j.egyr.2022.03.122.

26. Hamzehlouia, S., M. Latifi and J. Chaouki, Development of a novel silica-based microwave receptor for high temperature processes. Powder technology, 2022. 399: pp. 117180, https://doi.org/10.1016/j.powtec.2022.117180.

27. Amini, A., M. Latifi and J. Chaouki, Electrification of materials processing via microwave irradiation: A review of mechanism and applications. Applied Thermal Engineering, 2021. 193: pp. 117003, https://doi.org/10.1016/j.applthermaleng.2021.117003.

28. Hamzehlouia, S., J. Shabanian, M. Latifi and J. Chaouki, Effect of microwave heating on the performance of catalytic oxidation of n-butane in a gas-solid fluidized bed reactor. Chemical Engineering Science, 2018. 192: pp. 1177-1188, https://doi.org/10.1016/j.ces.2018.08.054.

29. Hamzehlouia, S., S.A. Jaffer and J. Chaouki, Microwave heating-assisted catalytic dry reforming of methane to syngas. Scientific reports, 2018. 8(1): pp. 8940, https://doi.org/10.1038/s41598-018-27381-6.

30. Wang, J., M. Wen, X. La, J. Ren, J. Jiang and D.C.W. Tsang, Resonance-driven microwave heating for improved methane conversion to hydrogen. Applied Energy, 2024. 375: pp. 124100, https://doi.org/10.1016/j.apenergy.2024.124100.

31. Cui, Y., Y. Zhang, L. Cui, Q. Xiong and E. Mostafa, Microwave-assisted fluidized bed reactor pyrolysis of polypropylene plastic for pyrolysis gas production towards a sustainable development. Applied Energy, 2023. 342: pp. 121099, https://doi.org/10.1016/j.apenergy.2023.121099.

32. Li, J., J. Tao, B. Yan, K. Cheng, G. Chen and J. Hu, Microwave reforming with char-supported Nickel-Cerium catalysts: A potential approach for thorough conversion of biomass tar model compound. Applied Energy, 2020. 261: pp. 114375, https://doi.org/10.1016/j.apenergy.2019.114375.

33. Appleton, T.J., R.I. Colder, S.W. Kingman, I.S. Lowndes and A.G. Read, Microwave technology for energy-efficient processing of waste. Applied Energy, 2005. 81(1): pp. 85-113, https://doi.org/10.1016/j.apenergy.2004.07.002.

34. Khodabandehloo, M., J. Shabanian, J.-P. Harvey and J. Chaouki, Microwave heating-assisted chemical looping dry reforming of methane. International Journal of Hydrogen Energy, 2024. 71: pp. 1380-1391, https://doi.org/10.1016/j.ijhydene.2024.05.295.

35. Szima, S. and C.-C. Cormos, CO2 utilization technologies: A techno-economic analysis for synthetic natural gas production. Energies, 2021. 14(5): pp. 1258.

36. Lee, K., P. Sun, A. Elgowainy, K.H. Baek and P. Bobba, Techno-economic and life cycle analysis of synthetic natural gas production from low-carbon H2 and point-source or atmospheric CO2 in the United States. Journal of CO2 utilization, 2024. 83: pp. 102791, https://doi.org/10.1016/j.jcou.2024.102791.

37. Chen, C., H.-H. Lee, W. Chen, Y.-C. Chang, E. Wang, C.-H. Shen and K.-E. Huang, Study of an Iron-Based Oxygen Carrier on the Moving Bed Chemical Looping System. Energy & fuels, 2018. 32(3): pp. 3660-3667, https://doi.org/10.1021/acs.energyfuels.7b03721.

38. Xu, D., Y. Zhang, T.-L. Hsieh, M. Guo, L. Qin, C. Chung, L.-S. Fan and A. Tong, A novel chemical looping partial oxidation process for thermochemical conversion of biomass to syngas. Applied Energy, 2018. 222: pp. 119-131, https://doi.org/10.1016/j.apenergy.2018.03.130.

39. Kong, F., C. Li, Y. Zhang, Y. Gu, M. Kathe, L.-S. Fan and A. Tong, Hydrogen Production from Natural Gas Using an Iron-Based Chemical Looping Technology: Process Modeling, Heat Integration, and Exergy Analysis. Energy Technology, 2020. 8(8): pp. 1900377, https://doi.org/10.1002/ente.201900377.

40. Chiu, P.-C., Y. Ku, H.-C. Wu, Y.-L. Kuo and Y.-H. Tseng, Spent isopropanol solution as possible liquid fuel for moving bed reactor in chemical looping combustion. Energy & fuels, 2014. 28(1): pp. 657-665, https://doi.org/10.1021/ef4012438.

41. Tong, A., L. Zeng, M.V. Kathe, D. Sridhar and L.-S. Fan, Application of the Moving-Bed Chemical Looping Process for High Methane Conversion. Energy & fuels, 2013. 27(8): pp. 4119-4128, https://doi.org/10.1021/ef3020475.

42. Hedong, Z., G. Zuopeng, A. Wenya, F. Jie, R. Chunmei, M. Xiao, K. Qinhao, L. Yang, L. Guangqing and C. Xiaochun, Characterization and analysis of textile sludge char from moving bed pyrolyser under microwave irradiation. CIESC Journal, 2017. 68(6): pp. 2510.

43. Bai, X. and P. Muley, Microwave-assisted Moving-bed Gasifier Design for Solid Fuel Conversion. 2023, National Energy Technology Laboratory (NETL), Pittsburgh, PA, Morgantown, WV ….

44. Ogden, J.M., Review of small stationary reformers for hydrogen production. Report to the international energy agency, 2001. 609.

45. Yan, P., A.I. Stankiewicz, F.E. Sarabi and H. Nigar, Microwave heating in heterogeneous catalysis: Modelling and design of rectangular traveling-wave microwave reactor. Chemical Engineering Science, 2021. 232: pp. 116383, https://doi.org/10.1016/j.ces.2020.116383.

CHAPTER 7

1. Ogden, J.M., Review of small stationary reformers for hydrogen production. Report to the international energy agency, 2001. 609.

2. Khodabandehloo, M., J. Shabanian, J.-P. Harvey and J. Chaouki, Microwave heating-assisted chemical looping dry reforming of methane. International Journal of Hydrogen Energy, 2024. 71: pp. 1380-1391, https://doi.org/10.1016/j.ijhydene.2024.05.295.

3. Sinnott, R. and G.P. Towler, Chemical Engineering Design: Principles, Practice, and Economics of Plant and Process Design. 2012: Butterworth-Heinemann.

4. Khodabandehloo, M., A. Larimi and F. Khorasheh, Comparative process modeling and techno-economic evaluation of renewable hydrogen production by glycerol reforming in aqueous and gaseous phases. Energy Conversion and Management, 2020. 225: pp. 113483.

5. Alkhayat, W. and A. Gerrard, Estimating manning levels for process plants. AACE Transactions, 1984. 1: pp. 2.1-2.4.

6. eia, T.U.S.E.I.A. United States Natural Gas Prices. [cited 2024; Available from: https://www.eia.gov/.

7. Radoiu, M., Industrial Microwave Reactors: Components and set-up, in Microwave Chemistry. 2017. pp., 65-90, https://doi.org/10.1515/9783110479935-005.

8. Brown, E.F., The next-generation consumer microwave oven: a review. Journal of Microwave Power and Electromagnetic Energy, 2022. 56(2): pp. 82-86, https://doi.org/10.1080/08327823.2022.2066772.

9. Postels, S., A. Abánades, N. von der Assen, R.K. Rathnam, S. Stückrad and A. Bardow, Life cycle assessment of hydrogen production by thermal cracking of methane based on liquid-metal technology. International Journal of Hydrogen Energy, 2016. 41(48): pp. 23204-23212, https://doi.org/10.1016/j.ijhydene.2016.09.167.

10. Patel, G.H., J. Havukainen, M. Horttanainen, R. Soukka and M. Tuomaala, Climate change performance of hydrogen production based on life cycle assessment. Green Chemistry, 2024. 26(2): pp. 992-1006.

11. Dufour, J., J.L. Gálvez, D.P. Serrano, J. Moreno and G. Martínez, Life cycle assessment of hydrogen production by methane decomposition using carbonaceous catalysts. International Journal of Hydrogen Energy, 2010. 35(3): pp. 1205-1212, https://doi.org/10.1016/j.ijhydene.2009.11.093.

12. Li, G., S. Wang, J. Zhao, H. Qi, Z. Ma, P. Cui, Z. Zhu, J. Gao and Y. Wang, Life cycle assessment and techno-economic analysis of biomass-to-hydrogen production with methane tri-reforming. Energy, 2020. 199: pp. 117488, https://doi.org/10.1016/j.energy.2020.117488.

13. Hajjaji, N., S. Martinez, E. Trably, J.-P. Steyer and A. Helias, Life cycle assessment of hydrogen production from biogas reforming. International Journal of Hydrogen Energy, 2016. 41(14): pp. 6064-6075, https://doi.org/10.1016/j.ijhydene.2016.03.006.

14. Zang, G., E.J. Graham and D. Mallapragada, H2 production through natural gas reforming and carbon capture: A techno-economic and life cycle analysis comparison. International Journal of Hydrogen Energy, 2024. 49: pp. 1288-1303, https://doi.org/10.1016/j.ijhydene.2023.09.230.

15. G. Camacho, F., R.M. Afzal, P.A.L. de Souza and N. Mahinpey, Life cycle assessment of different hydrogen production setups from chemical looping reforming system using carburization reactions. International Journal of Hydrogen Energy, 2024. 73: pp. 63-72, https://doi.org/10.1016/j.ijhydene.2024.06.016.

APPENDIX A

1. Sources of Greenhouse Gas Emissions, U.S. Environmental Protection Agency. 2020.

2. Carbon Dioxide Information Analysis Center, Oak Ridge National Laboratory. 2017.

3. World Energy Outlook, International Energy Agency. 2020.

4. Amini, A., M. Latifi and J. Chaouki, Electrification of materials processing via microwave irradiation: A review of mechanism and applications. Applied Thermal Engineering, 2021: pp. 117003, https://doi.org/10.1016/j.applthermaleng.2021.117003.

5. Siddique, I.J., A.A. Salema, E. Antunes and R. Vinu, Technical challenges in scaling up the microwave technology for biomass processing. Renewable and sustainable energy reviews, 2022. 153: pp. 111767, https://doi.org/10.1016/j.rser.2021.111767.

6. Goyal, H., T.-Y. Chen, W. Chen and D.G. Vlachos, A review of microwave-assisted process intensified multiphase reactors. Chemical Engineering Journal, 2022. 430: pp. 133183, https://doi.org/10.1016/j.cej.2021.133183.

7. Falciglia, P.P., P. Roccaro, L. Bonanno, G. De Guidi, F.G. Vagliasindi and S. Romano, A review on the microwave heating as a sustainable technique for environmental remediation/detoxification applications. Renewable and sustainable energy reviews, 2018. 95: pp. 147-170, https://doi.org/10.1016/j.rser.2018.07.031.

8. Chaouki, J., S. Farag, M. Attia and J. Doucet, The development of industrial (thermal) processes in the context of sustainability: The case for microwave heating. The Canadian Journal of Chemical Engineering, 2020. 98(4): pp. 832-847, https://doi.org/10.1002/cjce.23710.

9. Chen, Z., M. Monzavi, M. Latifi, S. Samih and J. Chaouki, Microwave-responsive SiC foam@ zeolite core-shell structured catalyst for catalytic pyrolysis of plastics. Environmental Pollution, 2022: pp. 119573.

10. Ambrosetti, M., A perspective on power-to-heat in catalytic processes for decarbonization. Chemical Engineering and Processing-Process Intensification, 2022. 182: pp. 109187.

11. Wismann, S.T., J.S. Engbæk, S.B. Vendelbo, F.B. Bendixen, W.L. Eriksen, K. Aasberg-Petersen, C. Frandsen, I. Chorkendorff and P.M. Mortensen, Electrified methane reforming: A compact approach to greener industrial hydrogen production. Science, 2019. 364(6442): pp. 756-759.

12. Sun, J., W. Wang and Q. Yue, Review on microwave-matter interaction fundamentals and efficient microwave-associated heating strategies. Materials transactions, 2016. 9(4): pp. 231, https://doi.org/10.3390/ma9040231.

13. Wei, M. and C.A. McMillan, Electrification of industry: potential, challenges and outlook. Current Sustainable/Renewable Energy Reports, 2019. 6(4): pp. 140-148.

14. Palma, V., D. Barba, M. Cortese, M. Martino, S. Renda and E. Meloni, Microwaves and Heterogeneous Catalysis: A Review on Selected Catalytic Processes. Catalysts, 2020. 10(2): pp. 246.

15. Haque, K.E., Microwave energy for mineral treatment processes—a brief review. International Journal of Mineral Processing, 1999. 57(1): pp. 1-24, https://doi.org/10.1016/S0301-7516(99)00009-5.

16. Loharkar, P.K., A. Ingle and S. Jhavar, Parametric review of microwave-based materials processing and its applications. Journal of Materials Research and Technology, 2019. 8(3): pp. 3306-3326.

17. Huang, W., Y. Zhang, H. Qiu, J. Huang, J. Chen, L. Gao, M. Omran and G. Chen, Drying characteristics of ammonium polyvanadate under microwave heating based on a thin-layer drying kinetics fitting model. Journal of Materials Research and Technology, 2022. 19: pp. 1497-1509.

18. Regier, M., K. Knoerzer and H. Schubert, The microwave processing of foods. 2016: Woodhead publishing.

19. Chandrasekaran, S., S. Ramanathan and T. Basak, Microwave food processing—A review. Food research international, 2013. 52(1): pp. 243-261, https://doi.org/10.1016/j.foodres.2013.02.033.

20. Solanki, H.K., V.D. Prajapati and G.K. Jani, Microwave technology—a potential tool in pharmaceutical science. ChemInform, 2011. 42(24): pp. no.

21. Bennamoun, L., Z. Chen and M.T. Afzal, Microwave drying of wastewater sludge: experimental and modeling study. Drying Technology, 2016. 34(2): pp. 235-243.

22. Chen, Z., M.T. Afzal and A.A. Salema, Microwave drying of wastewater sewage sludge. Journal of Clean Energy Technologies, 2014. 2(3): pp. 282-286.

23. Binner, E., E. Lester, S. Kingman, C. Dodds, J. Robinson, T. Wu, P. Wardle and J.P. Mathews, A review of microwave coal processing. Journal of Microwave Power and Electromagnetic Energy, 2014. 48(1): pp. 35-60.

24. Parvez, A.M., M.T. Afzal, P. Jiang and T. Wu, Microwave-assisted biomass pyrolysis polygeneration process using a scaled-up reactor: Product characterization, thermodynamic assessment and bio-hydrogen production. Biomass and Bioenergy, 2020. 139: pp. 105651.

25. Nizamuddin, S., H.A. Baloch, M. Siddiqui, N. Mubarak, M. Tunio, A. Bhutto, A.S. Jatoi, G. Griffin and M. Srinivasan, An overview of microwave hydrothermal carbonization and

microwave pyrolysis of biomass. Reviews in Environmental Science and Bio/Technology, 2018. 17(4): pp. 813-837.

26. Motasemi, F. and M.T. Afzal, A review on the microwave-assisted pyrolysis technique. Renewable and sustainable energy reviews, 2013. 28: pp. 317-330.

27. Li, K., Q. Jiang, G. Chen, L. Gao, J. Peng, Q. Chen, S. Koppala, M. Omran and J. Chen, Kinetics characteristics and microwave reduction behavior of walnut shell-pyrolusite blends. Bioresource technology, 2021. 319: pp. 124172.

28. Mishra, R.R. and A.K. Sharma, Microwave–material interaction phenomena: Heating mechanisms, challenges and opportunities in material processing. Composites Part A: Applied Science and Manufacturing, 2016. 81: pp. 78-97.

29. Li, K., J. Chen, J. Peng, R. Ruan, M. Omran and G. Chen, Dielectric properties and thermal behavior of electrolytic manganese anode mud in microwave field. Journal of hazardous materials, 2020. 384: pp. 121227.

30. Stefanidis, G.D., A.N. Munoz, G.S. Sturm and A. Stankiewicz, A helicopter view of microwave application to chemical processes: reactions, separations, and equipment concepts. Reviews in Chemical Engineering, 2014. 30(3): pp. 233-259.

31. Priecel, P. and J.A. Lopez-Sanchez, Advantages and limitations of microwave reactors: from chemical synthesis to the catalytic valorization of biobased chemicals. ACS Sustainable Chemistry & Engineering, 2018. 7(1): pp. 3-21.

32. Horikoshi, S. and N. Serpone, Role of microwaves in heterogeneous catalytic systems. Catalysis Science & Technology, 2014. 4(5): pp. 1197-1210.

33. Kalinke, I., P. Kubbutat, S. Taghian Dinani, S. Ambros, M. Ozcelik and U. Kulozik, Critical assessment of methods for measurement of temperature profiles and heat load history in microwave heating processes—A review. Comprehensive reviews in food science and food safety, 2022 https://doi.org/10.1111/1541-4337.12940.

34. Nguyen, H.M., J. Sunarso, C. Li, G.H. Pham, C. Phan and S. Liu, Microwave-assisted catalytic methane reforming: a review. Applied Catalysis A: General, 2020. 599: pp. 117620, https://doi.org/10.1016/j.apcata.2020.117620.

35. Radoiu, M., Microwave drying process scale-up. Chemical Engineering and Processing-Process Intensification, 2020. 155: pp. 108088, https://doi.org/10.1016/j.cep.2020.108088.

36. Radoiu, M., Industrial Microwave Reactors: Components and set-up, in Microwave Chemistry. 2017. pp., 65-90, https://doi.org/10.1515/9783110479935-005.

37. Brown, E.F., The next-generation consumer microwave oven: a review. Journal of Microwave Power and Electromagnetic Energy, 2022. 56(2): pp. 82-86, https://doi.org/10.1080/08327823.2022.2066772.

38. Andreev, D., A. Kuskov and E. Schamiloglu, Review of the relativistic magnetron. Matter and Radiation at Extremes, 2019. 4(6): pp. 067201, 10.1063/1.5100028.

39. Brown, W.C., The microwave magnetron and its derivatives. IEEE Transactions on Electron Devices, 1984. 31(11): pp. 1595-1605, 10.1109/T-ED.1984.21757.

40. Osepchuk, J.M. The magnetron and the microwave oven: A unique and lasting relationship. in 2010 International Conference on the Origins and Evolution of the Cavity Magnetron. 2010. 10.1109/CAVMAG.2010.5565567.

41. Fuks, M.I. and E. Schamiloglu, 70% Efficient Relativistic Magnetron With Axial Extraction of Radiation Through a Horn Antenna. IEEE Transactions on Plasma Science, 2010. 38(6): pp. 1302-1312, 10.1109/TPS.2010.2042823.

42. Fuks, M.I., S. Prasad and E. Schamiloglu, Efficient Magnetron With a Virtual Cathode. IEEE Transactions on Plasma Science, 2016. 44(8): pp. 1298-1302, 10.1109/TPS.2016.2525921.

43. Vyas, S.K., S. Maurya and V.P. Singh, Efficiency Enhancement of CW Magnetron by Ferrite Material Filling. IEEE Transactions on Plasma Science, 2016. 44(12): pp. 3262-3267, 10.1109/TPS.2016.2625339.

44. Thostenson, E.T. and T.W. Chou, Microwave processing: fundamentals and applications. Composites Part A: Applied Science and Manufacturing, 1999. 30(9): pp. 1055-1071, 10.1016/S1359-835X(99)00020-2.

45. Peng, Z. and J.-Y. Hwang, Microwave-assisted metallurgy. International Materials Reviews, 2015. 60(1): pp. 30-63, 10.1179/1743280414Y.0000000042.

46. Strite, S. and H. Morkoç, GaN, AlN, and InN: A review. Journal of Vacuum Science & Technology B: Microelectronics and Nanometer Structures Processing, Measurement, and Phenomena, 1992. 10(4): pp. 1237-1266, 10.1116/1.585897.

47. Husna Hamza, K. and D. Nirmal, A review of GaN HEMT broadband power amplifiers. AEU - International Journal of Electronics and Communications, 2020. 116: pp. 153040, https://doi.org/10.1016/j.aeue.2019.153040.

48. Pengelly, R.S., S.M. Wood, J.W. Milligan, S.T. Sheppard and W.L. Pribble, A Review of GaN on SiC High Electron-Mobility Power Transistors and MMICs. IEEE Transactions on Microwave Theory and Techniques, 2012. 60(6): pp. 1764-1783, 10.1109/TMTT.2012.2187535.

49. Flack, T.J., B.N. Pushpakaran and S.B. Bayne, GaN Technology for Power Electronic Applications: A Review. Journal of Electronic Materials, 2016. 45(6): pp. 2673-2682, 10.1007/s11664-016-4435-3.

50. Burk, A.A., M.J. O'Loughlin, R.R. Siergiej, A.K. Agarwal, S. Sriram, R.C. Clarke, M.F. MacMillan, V. Balakrishna and C.D. Brandt, SiC and GaN wide bandgap semiconductor materials and devices. Solid-State Electronics, 1999. 43(8): pp. 1459-1464, https://doi.org/10.1016/S0038-1101(99)00089-1.

51. THERMEX-THERMATRON. 2022; Available from: https://thermex-thermatron.com/.

52. SAIREM. 2022; Available from: https://www.sairem.com/.

53. Richardson Electronics. 2022; Available from: https://www.rellpower.com/.

54. everythingRF. 2022; Available from: https://www.everythingrf.com/.

55. Atuonwu, J.C. and S.A. Tassou, Energy issues in microwave food processing: A review of developments and the enabling potentials of solid-state power delivery. Critical Reviews in Food Science and Nutrition, 2019. 59(9): pp. 1392-1407, 10.1080/10408398.2017.1408564.

56. Julian, I., C. Pedersen, A. Jensen, A. Baden, J. Hueso, A. Friderichsen, H. Birkedal, R. Mallada and J. Santamaria, From bench scale to pilot plant: A 150x scaled-up configuration of a microwave-driven structured reactor for methane dehydroaromatization. Catalysis Today, 2022. 383: pp. 21-30, https://doi.org/10.1016/j.cattod.2021.04.013.

57. Bowman, M.D., J.L. Holcomb, C.M. Kormos, N.E. Leadbeater and V.A. Williams, Approaches for scale-up of microwave-promoted reactions. Organic Process Research and Development, 2008. 12(1): pp. 41-57, https://doi.org/10.1021/op700187w.

58. Radoiu, M., Microwave drying process scale-up. Chemical Engineering Processing-Process Intensification, 2020. 155: pp. 108088, https://doi.org/10.1016/j.cep.2020.108088.

59. Metaxas, A.a. and R.J. Meredith, Industrial microwave heating. 1983: IET.

60. Fuks, M.I. and E. Schamiloglu, Application of a magnetic mirror to increase total efficiency in relativistic magnetrons. Physical Review Letters, 2019. 122(22): pp. 224801, https://doi.org/10.1103/PhysRevLett.122.224801.

61. Mega Industries. 2022; Available from: https://www.megaind.com/wp-content/uploads/2020/12/Rigid-Waveguide-Technical-Data.pdf.

62. Sudhakar, M. and V. Khare, Microwave Engineering, ed. F. edition. 2016, India: S. Chand Publishing.

63. Lin, F., X.-T. Feng, C. Yang, S. Li, J. Zhang, X. Su and T. Tong, Microwave response characteristics and influencing factors of ores based on dielectric properties of synthetic samples. Journal of Rock Mechanics and Geotechnical Engineering, 2022. 14(2): pp. 315-328.

64. Kudryavtsev, I.V., O.B. Gotselyuk, E.S. Novikov and V.G. Demin, Specific features of waveguide heating due to transmission of high-power microwave signals. Technical Physics, 2017. 62(1): pp. 101-106, 10.1134/S1063784217010133.

65. Ulbrich, Inconel® 625 (Alloy 625) UNS N06625. 2022; Available from: https://www.ulbrich.com/.

66. Cheng, C., Y. Xiao, M.J. Haché, Z. Liu, J.M. Wheeler and Y. Zou, Probing the small-scale plasticity and phase stability of an icosahedral quasicrystal i-Al-Pd-Mn at elevated temperatures. Physical Review Materials, 2021. 5(5): pp. 053602.

67. Marinel, S., N. Renaut, E. Savary, R. Macaigne, G. Riquet, C. Coureau, T. Gadeyne and D. Guillet, Tuning, impedance matching, and temperature regulation during high-temperature microwave sintering of ceramics. Advances in Materials Science and Engineering, 2018. 2018.

68. Rakhmankulov, D., S.Y. Shavshukova, F. Latypova and V. Zorin, Laboratory and industrial applications of microwave techniques. Russian Journal of Applied Chemistry, 2002. 75(9): pp. 1377-1383.

69. Eghbal Sarabi, F., M. Ghorbani, A. Stankiewicz and H. Nigar, Coaxial traveling-wave microwave reactors: Design challenges and solutions. Chemical Engineering Research and Design, 2020. 153: pp. 677-683, https://doi.org/10.1016/j.cherd.2019.11.022.

70. Albuquerque, C.D., S. Curet and L. Boillereaux. Microwave processing of food samples: Influence of cavity design and dielectric properties. in 17th International Conference on Microwave and High Frequency Heating, AMPERE 2019, September 9, 2019 - September 12, 2019. 2019. Valencia, Spain: American Society for Precision Engineering, ASPE 10.4995/Ampere2019.2019.9911.

71. Hara, K., M. Hayashi, M. Sato and K. Nagata, Continuous pig iron making by microwave heating with 12.5 kW at 2.45 GHz. Journal of Microwave Power and Electromagnetic Energy, 2011. 45(3): pp. 137-147, https://doi.org/10.1080/08327823.2011.11689808.

72. Hara, K., M. Hayashi, M. Sato and K. Nagata, Pig iron making by focused microwave beams with 20 kW at 2.45 GHz. ISIJ international, 2012. 52(12): pp. 2149-2157, https://doi.org/10.2355/isijinternational.52.2149.

73. Dąbrowska, S., T. Chudoba, J. Wojnarowicz and W. Łojkowski, Current Trends in the Development of Microwave Reactors for the Synthesis of Nanomaterials in Laboratories and Industries: A Review. Crystals, 2018. 8(10) 10.3390/cryst8100379.

74. Kashimura, K., K. Nagata and M. Sato, Concept of Furnace for Metal Refining by Microwave Heating —A Design of Microwave Smelting Furnace with Low CO₂ Emission&mdash. MATERIALS TRANSACTIONS, 2010. 51(10): pp. 1847-1853, 10.2320/matertrans.M2010026.

75. Nagata, K., K. Hara and M. Sato, Continuous Process of Pig Ironmaking using Focused Microwave Beams at 2.45 GHz. ISIJ International, 2019. 59(6): pp. 1033-1040, 10.2355/isijinternational.ISIJINT-2018-766.

76. Shang, X., D. Zhai, F. Zhang, C. Wei, J. Chen, M. Liu and J. Peng, Electromagnetic waves transmission performance of alumina refractory ceramics in 2.45 GHz microwave heating.

Ceramics International, 2019. 45(17, Part B): pp. 23493-23500, https://doi.org/10.1016/j.ceramint.2019.08.055.

77. Weidner, A., Y. Ranglack-Klemm, T. Zienert, C.G. Aneziris and H. Biermann, Mechanical High-Temperature Properties and Damage Behavior of Coarse-Grained Alumina Refractory Metal Composites. Materials, 2019. 12(23) 10.3390/ma12233927.

78. Xiaobiao, S., C. Junruo and P. Jinhui, Dynamic Transmission Performances of Alumina and Mullite Refractory Ceramics in Microwave High-Temperature Heating. High Temperature Materials and Processes, 2016. 35(1): pp. 113-119, https://doi.org/10.1515/htmp-2014-0167.

79. Anggono, J., Mullite Ceramics: Its Properties, Structure, and Synthesis. Jurnal Teknik Mesin, 2005. 7.

80. Schneider, H. and E. Eberhard, Thermal Expansion of Mullite. Journal of the American Ceramic Society, 1990. 73(7): pp. 2073-2076, 10.1111/j.1151-2916.1990.tb05270.x.

81. Kriven, W.M., J.W. Palko, S. Sinogeikin, J.D. Bass, A. Sayir, G. Brunauer, H. Boysen, F. Frey and J. Schneider, High temperature single crystal properties of mullite. Journal of the European Ceramic Society, 1999. 19(13): pp. 2529-2541, https://doi.org/10.1016/S0955-2219(99)00124-7.

82. Amini, A., K. Ohno, T. Maeda and K. Kunitomo, Effect of particle size and apparent density on the initial stages of temperature increase during the microwave heating of Fe3O4. Powder Technology, 2018. 338: pp. 101-109, https://doi.org/10.1016/j.powtec.2018.06.047.

83. Sturm, G.S.J., A.Q. Van Braam Houckgeest, M.D. Verweij, T. Van Gerven, A.I. Stankiewicz and G.D. Stefanidis, Exploration of rectangular waveguides as a basis for microwave enhanced continuous flow chemistries. Chemical Engineering Science, 2013. 89: pp. 196-205, https://doi.org/10.1016/j.ces.2012.11.039.

84. Kybartas, D., E. Ibenskis and R. Surna, Single Mode Circular Waveguide Applicator for Microwave Heating of Oblong Objects in Food Research. Elektronika ir Elektrotechnika, 2011. 114(8) 10.5755/j01.eee.114.8.701.

85. Yadav, H.N.S., M. Kumar, A. Kumar and M. Das, COMSOL simulation of microwave plasma polishing on different surfaces. Materials Today: Proceedings, 2021. 45: pp. 4803-4809.

86. Salvi, D., D. Boldor, G. Aita and C. Sabliov, COMSOL Multiphysics model for continuous flow microwave heating of liquids. Journal of food engineering, 2011. 104(3): pp. 422-429.

87. Salvi, D., D. Boldor, J. Ortego, G. Aita and C. Sabliov, Numerical modeling of continuous flow microwave heating: a critical comparison of COMSOL and ANSYS. Journal of Microwave Power and Electromagnetic Energy, 2010. 44(4): pp. 187-197.

88. Yan, P., A.I. Stankiewicz, F.E. Sarabi and H. Nigar, Microwave heating in heterogeneous catalysis: Modelling and design of rectangular traveling-wave microwave reactor. Chemical Engineering Science, 2021. 232: pp. 116383, https://doi.org/10.1016/j.ces.2020.116383.

89. Lapshinov, B., Temperature measurement methods in microwave heating technologies. Measurement Techniques, 2021. 64(6): pp. 453-462, https://doi.org/10.1007/s11018-021-01954-w.

90. Bartoli, M., M. Frediani, C. Briens, F. Berruti and L. Rosi, An overview of temperature issues in microwave-assisted pyrolysis. Processes, 2019. 7(10): pp. 658.

91. García-Baños, B., J. Reinosa, F.L. Penaranda-Foix, J.F. Fernandez and J.M. Catalá-Civera, Temperature assessment of microwave-enhanced heating processes. Scientific reports, 2019. 9(1): pp. 1-10, https://doi.org/10.1038/s41598-019-47296-0.

92. Kappe, C.O., How to measure reaction temperature in microwave-heated transformations. Chemical Society Reviews, 2013. 42(12): pp. 4977-4990.

93. Luo, Y., T. Liao, X. Yu, J. Li, L. Zhang and Y. Xi, Dielectric properties and microwave heating behavior of neutral leaching residues from zinc metallurgy in the microwave field. Green Processing and Synthesis, 2020. 9(1): pp. 97-106.

94. Bradshaw, S., Van Wyk, EJ. and J. De Swardt, Microwave heating principles and the application to the regeneration of granular activated carbon. Journal of the Southern African Institute of Mining and Metallurgy, 1998. 98(4): pp. 201-210.

95. Bradshaw, S., S. Delport and E.v. Wyk, Qualitative measurement of heating uniformity in a multimode microwave cavity. Journal of Microwave Power and Electromagnetic Energy, 1997. 32(2): pp. 87-95.

96. Johnson, A., R. Espinosa and W. Lewis, Use of a variable frequency microwave furnace for large-area, uniform processing. Ceramic Transaction, 1993. 36: pp. 563-570.

97. Ju, H.-J. and Q. Zhao, Simulation and experimental method for microwave oven. Journal of Electronic Science and Technology, 2009. 7(2): pp. 188-191.

98. Gold, S., A. Fliflet, D. Lewis III, R. Bruce, N. Zharova and V. Semenov, Method of determining the wall conductivity of a multimode microwave applicator. Review of scientific instruments, 2004. 75(8): pp. 2678-2685.

99. Luan, D., J. Tang, P.D. Pedrow, F. Liu and Z. Tang, Performance of mobile metallic temperature sensors in high power microwave heating systems. Journal of food engineering, 2015. 149: pp. 114-122.

100. Cuccurullo, G., L. Giordano, D. Albanese, L. Cinquanta and M. Di Matteo, Infrared thermography assisted control for apples microwave drying. Journal of food engineering, 2012. 112(4): pp. 319-325.

101. Bond, G., R. Moyes, S. Pollington and D. Whan, Measurement of temperature during microwave heating (chemical reactions enhancement). Measurement Science and Technology, 1991. 2(6): pp. 571.

102. Farag, S. and J. Chaouki, A modified microwave thermo-gravimetric-analyzer for kinetic purposes. Applied Thermal Engineering, 2015. 75: pp. 65-72.

103. Luan, D., J. Tang, P.D. Pedrow, F. Liu and Z. Tang, Using mobile metallic temperature sensors in continuous microwave assisted sterilization (MATS) systems. Journal of food engineering, 2013. 119(3): pp. 552-560.

104. Tang, J., Unlocking potentials of microwaves for food safety and quality. Journal of food science, 2015. 80(8): pp. E1776-E1793.

105. Cuccurullo, G., P. Berardi, R. Carfagna and V. Pierro, IR temperature measurements in microwave heating. Infrared physics and technology, 2002. 43(3-5): pp. 145-150.

106. Belotserkovsky, E., O. Shenfeld and A. Katzir, Infrared fiberoptic temperature control of the heating process in a microwave oven. IEEE transactions on microwave theory and techniques, 1994. 42(5): pp. 901-903.

107. Yin, S., P.B. Ruffin and T. Francis, Fiber optic sensors. 2017: CRC press.

108. Ramopoulos, V., G. Link, S. Soldatov and J. Jelonnek, Industrial scale microwave applicator for high temperature alkaline hydrolysis of PET. International Journal of Microwave and Wireless Technologies, 2018. 10(5-6): pp. 709-716, https://doi.org/10.23919/EuMC.2017.8230998.

109. Ano, T., F. Kishimoto, R. Sasaki, S. Tsubaki, M.M. Maitani, E. Suzuki and Y. Wada, In situ temperature measurements of reaction spaces under microwave irradiation using photoluminescent probes. Physical Chemistry Chemical Physics, 2016. 18(19): pp. 13173-13179.

110. Guan, D., P. Gray, D.H. Kang, J. Tang, B. Shafer, K. Ito, F. Younce and T. Yang, Microbiological validation of microwave-circulated water combination heating technology by inoculated pack studies. Journal of food science, 2003. 68(4): pp. 1428-1432.

111. Moraru, C.I., Heating: Fiber-Optic Measurement: Microwave and Radio Frequency (RF), in Encyclopedia of Agricultural, Food, and Biological Engineering-2 Volume Set (Print Version). 2010, CRC Press. pp., 862-866.

112. Leroy, Y., B. Bocquet and A. Mamouni, Non-invasive microwave radiometry thermometry. Physiological measurement, 1998. 19(2): pp. 127.

113. Hand, J., G. Van Leeuwen, S. Mizushina, J. Van de Kamer, K. Maruyama, T. Sugiura, D. Azzopardi and A. Edwards, Monitoring of deep brain temperature in infants using multi-frequency microwave radiometry and thermal modelling. Physics in Medicine and Biology, 2001. 46(7): pp. 1885.

114. Ravi, V.M. and K. Arunachalam, A low noise stable radiometer front-end for passive microwave tissue thermometry. Journal of Electromagnetic Waves and Applications, 2019. 33(6): pp. 743-758.

115. Bacsa, B., K. Horvati, S. Bosze, F. Andreae and C.O. Kappe, Solid-phase synthesis of difficult peptide sequences at elevated temperatures: a critical comparison of microwave and conventional heating technologies. The Journal of organic chemistry, 2008. 73(19): pp. 7532-7542.

116. Cresson, P.-Y., C. Ricard, L. Dubois, S. Vaucher, T. Lasri and J. Pribetich. Temperature measurement by microwave radiometry. in 2008 IEEE Instrumentation and Measurement Technology Conference. 2008. IEEE.

117. Daw, J., J. Rempe and S. Wilkins, Ultrasonic thermometry for in-pile temperature detection. 2002, Idaho National Lab.(INL), Idaho Falls, ID (United States).

118. Mutton, M.J., J. Lloyd and D. Yuhas. Temperature and Heat Flux Measurement Methods Using Ultrasound. in Fall Conference 2010. 2010.

119. Hwang, O., M.C. Lee, W. Weng, Y. Zhang and Z. Li, Development of novel ultrasonic temperature measurement technology for combustion gas as a potential indicator of combustion instability diagnostics. Applied Thermal Engineering, 2019. 159: pp. 113905.

120. Industrial Measurement Systems, Inc. 2022; Available from: https://imsysinc.com/Knowledgebase/ultratherm.htm.

121. Horikoshi, S., M. Kamata, T. Mitani and N. Serpone, Control of microwave-generated hot spots. 6. Generation of hot spots in dispersed catalyst particulates and factors that affect catalyzed organic syntheses in heterogeneous media. Industrial and Engineering Chemistry Research, 2014. 53(39): pp. 14941-14947.

122. Julian, I., H. Ramirez, J.L. Hueso, R. Mallada and J. Santamaria, Non-oxidative methane conversion in microwave-assisted structured reactors. Chemical Engineering Journal, 2019. 377: pp. 119764.

123. Haneishi, N., S. Tsubaki, E. Abe, M.M. Maitani, E.-i. Suzuki, S. Fujii, J. Fukushima, H. Takizawa and Y. Wada, Enhancement of fixed-bed flow reactions under microwave irradiation by local heating at the vicinal contact points of catalyst particles. Scientific reports, 2019. 9(1):

124. Hamzehlouia, S., S.A. Jaffer and J. Chaouki, Microwave heating-assisted catalytic dry reforming of methane to syngas. Scientific reports, 2018. 8(1): pp. 1-7, https://doi.org/10.1038/s41598-018-27381-6.

125. de Dios García, I., A. Stankiewicz and H. Nigar, Syngas production via microwave-assisted dry reforming of methane. Catalysis Today, 2021. 362: pp. 72-80, https://doi.org/10.1016/j.cattod.2020.04.045.

126. Menéndez, J., A. Arenillas, B. Fidalgo, Y. Fernández, L. Zubizarreta, E.G. Calvo and J.M. Bermúdez, Microwave heating processes involving carbon materials. Fuel Processing Technology, 2010. 91(1): pp. 1-8.

127. Neha, S., K.P.K. Ramesh and N. Remya, Techno-economic analysis and life cycle assessment of microwave co-pyrolysis of food waste and low-density polyethylene. Sustainable Energy Technologies and Assessments, 2022. 52: pp. 102356.

128. Ishizaki, K., K. Nagata and T. Hayashi, Production of pig iron from magnetite ore-coal composite pellets by microwave heating. ISIJ International, 2006. 46: pp. 1403-1409, 10.2355/isijinternational.46.1403.

129. Nagata, K., M. Sato, K. Hara, T. Hotta, Y. Kitamura, M. Hayashi, K. Kashimura, T. Mitani and J. Fukushima, Microwave Blast Furnace and Its Refractories. Journal of the Technical Association of Refractories Japan, 2014. 34(2): pp. 8.

130. Zein, S.H. and A. Antony, Techno-Economic Analysis and Feasibility of Industrial-Scale Activated Carbon Production from Agricultural Pea Waste Using Microwave-Assisted Pyrolysis: A Circular Economy Approach. Processes, 2022. 10(9): pp. 1702.

131. Lam, S.S., W.A.W. Mahari, Y.S. Ok, W. Peng, C.T. Chong, N.L. Ma, H.A. Chase, Z. Liew, S. Yusup and E.E. Kwon, Microwave vacuum pyrolysis of waste plastic and used cooking oil for simultaneous waste reduction and sustainable energy conversion: Recovery of cleaner liquid fuel and techno-economic analysis. Renewable and sustainable energy reviews, 2019. 115: pp. 109359.

132. Chaouki, J. and R. Sotudeh-Gharebagh, Scale-Up Processes: Iterative Methods for the Chemical, Mineral and Biological Industries. 2021: Walter de Gruyter GmbH & Co KG.

APPENDIX A SCALE-UP OF MICROWAVE HEATING-ASSISTED PROCESSES: A REVIEW

A.1 Introduction

Transportation, electricity production, industry (mainly burning fossil fuels to drive chemical reactions), businesses and residential operation, and agriculture, respectively, contributed to 27%, 25%, 24%, 13%, and 11% of greenhouse gas (GHG) emissions in the U.S. in 2020 [1]. Carbon dioxide (CO_2)– causing 76% of GHGs – emissions from industrial sectors are divided into direct (in facility) and indirect (off site) emissions [2, 3]. Burning fossil fuel to meet the energy demand is the leading source of direct and indirect emissions of CO_2 in the industry [1]. Hence, to continue the operation of existing industrial processes and upgrade them in a sustainable manner, i.e., economically viable, environmentally friendly, and socially acceptable, it is indispensable to create and/or deploy clean heating methods [4-6]. Process electrification, which could be coupled with renewable electricity sources, e.g., hydro power and wind turbines, is a viable strategy to develop sustainable processes, as it aids suppress or minimize GHG emissions [4, 7, 8] and boosts the process productivity [9]. Process electrification, which plays a central role in the process intensification, is also transforming reactor and process designs drastically [10]. Resistive [11], ultrasound, Joule [4], microwave (MW) [4], induction [12], and plasma heating [12], as well as electrochemistry [13] are some forms of process electrification methods. With MW heating's (MWH) high potential, it has drawn significant attentions among researchers and in industry in various areas, such as: (i) chemical reactions [6, 14], (ii) mineral processing [15-17], (iii) food drying [18, 19], (iv) pharmaceutical industry [20], (v) wastewater treatment [21, 22], (vi) coal drying [23], and (vii) pyrolysis [24-27].

Based on the electromagnetic (EM) properties of materials, they are classified as follows: (i) insulators, which are transparent to the MW irradiations, (ii) conductors, which reflect MWs, and (iii) dielectric materials, which absorb the irradiated MWs. By a proper material selection, i.e., selection of the magnetic and/or non-magnetic MW absorbers based on their relative permittivity ε_r and relative permeability μ_r, as well as their penetration depth D_p and material size, one can utilize the selective heating (SH) and volumetric heating (VH) of the MW. ε_r, μ_r, D_p, as well as loss tangent $\tan(\delta)$ and magnetic loss tangent $\tan(\delta_\mu)$ are detailed in Section 2.3 of CHAPTER 2.

The SH features of MW prevent heating-up all the material in the MW cavity (applicator), i.e., an enclosed non-magnetic and metallic chamber in which MWs are emitted to the sample and EM waves (EMWs) are confined, for a specific application, yet only heating the targeted phase in an engineered manner. VH and SH of MW are discussed in detail in CHAPTERs 2 to 7. In addition, interested readers are advised to review [4, 6, 28, 29] for information about several materials' MW absorption ability.

In addition to the VH and SH of MWs, by increasing the contribution of the renewable electricity sources to the energy demand of the industry, the MWH linked with renewable electricity has a great capacity to substitute the existing conventional methods of heat generation in the industry [4, 6]. When the above-mentioned benefits of the MWH have been considered, many research endeavors centered on using the MWH to power the processes, as elucidated in Figure A. 1. Compared to laboratory-scale investigations (Figure A. 1.a), a few studies focused on pilot- and/or industrial-scale MW heating assisted processes (Figure A. 1.b).

a)

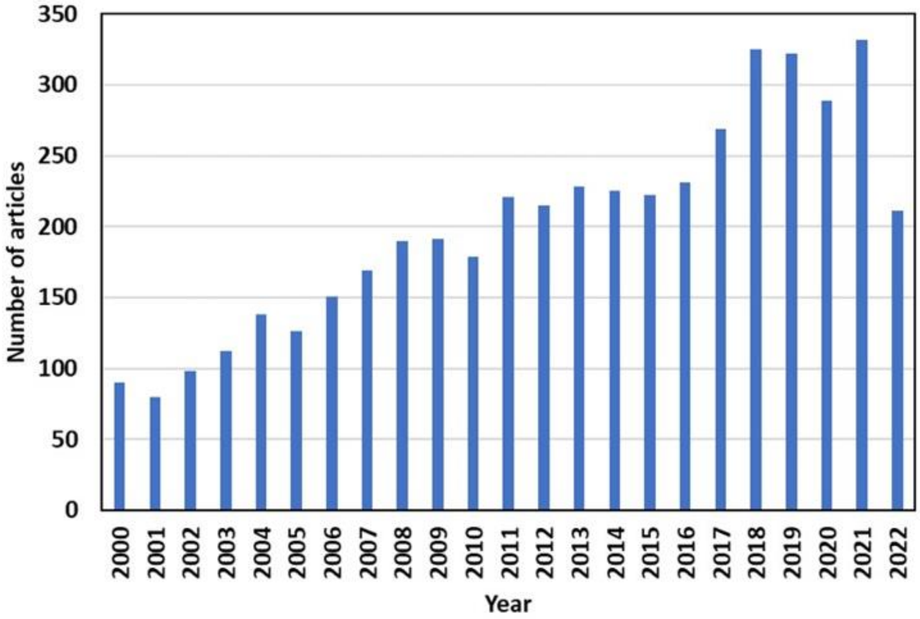

b)

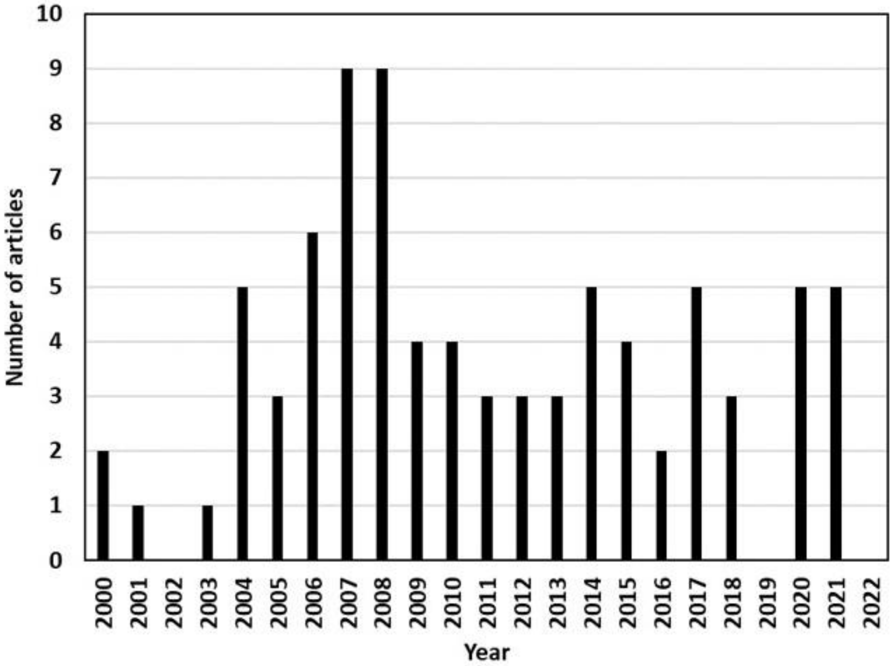

Figure A. 1. Publications with the following names appeared in their titles: a) “Microwave” and “heating”, and b) “Microwave” and “scale up/scale-up/large scale/industrial scale” s. Based on the information presented in “www.webofscience.com” in 2022-11-01.

Several review articles and book chapters focused on the fundamentals of MWH, and benefits and applications of this heating method to electrify chemical processes [4, 6, 7, 12, 19, 23, 30-35]. Although the large-scale use of MWH is not a novel notion, one can observe its relatively slow progress. In addition, the available review papers and book chapters mostly focused on: (i) specific implementations and benefits of MWH for food drying, fluid-solid catalytic reactions, and coal industries [6, 7, 19, 23, 30-32, 34], (ii) screening and/or fabrication of materials based on their EM properties [4, 12], (iii) MW drying and different components of MW systems for pilot-scales [30, 35, 36], and (iv) environmental impacts of electrifying processes via MWH [4, 6, 7, 12, 34, 35]. Hence, there are still rarely explored areas in literature for successful and accelerated large-scale deployment of this heating method for different industries. They can be listed as: (i) selection of the most appropriate components for large-scale deployment the MWH, (ii) effect of design parameters and components on maximizing the MW dissipation and uniform heating within the sample, (iii) safety challenges, (iv) selection of an appropriate scale-up approach, and (v) the application of numerical modeling for large-scale deployment of MWH to reduce scale-up costs and time, while promoting its accuracy. Hence, this review aimed at covering these rarely studied/reported topics in this review.

To investigate the aforementioned issues in depth, we initially presented an overview of the MW components, which encompass the MW generator (source), waveguide, MW cavity, and conveyors, as well as temperature measurement techniques in Section A.2. The linked obstacles and potential answers for the large-scale operation of these components are also overviewed in Section A.2. Uniform heating and selection and fabrication of MW receptors (absorbers) are other scale-up challenges reviewed in Section A.2. This review further presented an overview of the techno-economic studies related to the pilot- and large-scale systems (Section A.3). The iterative approach, as a novel approach for process scale-up, is also presented (Section A.3). Future directions to move toward commercialization of MWH for large-scales are introduced in Section A.4. Finally, a brief summary of the problems and the potential solutions as well as opportunities for large-scale deployment of MWH is presented in Section A.4.

A.2 Microwave heating for large-scale applications: components and challenges

A.2.1 Microwave components for large-scale

Key components to consider during the design and construction of the MW heating-assisted processes for large-scale applications include: (i) the MW generator, which converts electricity to EMWs, (ii) the waveguide system, which transmits the created MWs from the MW generator toward the cavity, (iii) the MW cavity, and (iv) temperature measurement. In this section, the key concerns of these components for large-scale applications and proposed the potential solutions and/or research directions to address them were reviewed.

A.2.1.1 Microwave generator

Magnetron, solid-state generators, klystron, and gyrotron are the main MW generators employed for industrial applications. Although klystrons and gyrotrons are high-power MW generators, capable of producing tens to hundreds of kilowatts of MW power with stable operating frequencies, they are designed for elevated frequencies (above 2.45 GHz). In addition, magnetrons and solid-state are more cost-effective than other types of MW generators. Accordingly, magnetrons and solid-state MW generators are more suitable to power processes with MW [36, 37]. Magnetron's structure has been developed to enhance the efficiency of electricity to MW conversion [37-43]. It is made of a vacuum tube containing an external cylindrical-shaped anode conductor, e.g., made of copper, and an axial cathode. In a magnetron, by heating up the cathode to an elevated temperature, e.g., 1750^{o}C, and creating a strong electric potential difference between anode and cathode, the thermionic emission of electrons, i.e., the electron liberation from the cathode, occurs. The mentioned thermionic emission of electrons in a cycloidal path from the cathode generates MWs [44, 45]. Considering the simple structure of the magnetrons, they have a fixed operating frequency and operating power level, which are proportional to the anode size.

Solid-state MW generators employ semiconductor devices, such as field-effect and bipolar junction transistors, to adjust the electron flow within the crystal lattice structure of the semiconductor materials, e.g. gallium nitride (GaN), to subsequently generate and amplify electromagnetic waves. The adapted semiconductor materials have high electron mobility, a high breakdown field (i.e., the highest voltage that the compound can be exposed to it), and wide band gap energy (i.e., a measure of the compound stability) [37, 46-50]. Hence, by adapting the semiconductor devices, the solid-state MW generators conveniently operate within a flexible range of frequencies and power levels instantaneously. Since the detailed design and operation of the MW generators is beyond the current study's scope, the challenges and opportunities of the large-scale deployment of magnetrons and solid-state MW generators rather than their detailed structure and design were reviewed (Table A. 1).

Table A. 1. Main specifications of the most common commercially available MW generators for large-scale applications [36, 51-54].

Parameter	***Magnetron***		***Solid-state MW generator***	
	915 MHz[a]	2.45 GHz[b]	915 MHz[a]	2.45 GHz[b]
Electricity to MW efficiency (%)	80	65	60	50
Lifetime (h)	6000	7000	≥ 10000	≥ 10000
Maximum power (kW)	≤100	≤30	≤100	≤20
Relative equipment cost	Moderate		High	
Cooling system	Water and/or air cooling		Water and/or air cooling	
MW reflection control system	Internal circulator		Internal and adaptive circulator	
Operating power control	Fixed and manual		Instantaneous and autonomous	
Operating frequency control	Fixed and manual		Instantaneous and autonomous	
Reliability (power and frequency control)	Moderate		High	
Power Supply	High voltage		Moderate to low voltage	
Startup and/or shut down time	Up to 10 min		Instantaneous	

a: for the solid-state MW generators, the frequency can conveniently vary between 902 to 928 MHz.

b: for the solid-state MW generators, the frequency can conveniently vary between 2.4 to 2.5 GHz.

Lower electricity to MW efficiency of magnetrons at higher frequencies (see Table A. 1) can be attributed to the relatively higher overheating that occurs at these frequencies. Compared to solid state MW generators, magnetrons have been developed and studied by scientists and engineers over several decades. Accordingly, they exhibit higher electricity to MW efficiency [24, 36, 55-59]. For instance, the literature reports promising results regarding the increased efficiency of magnetrons [38]. In 2019, it was reported [38, 60] that the magnetic mirror effect was used to enhance the electron to MW and overall efficiencies of magnetrons up to 92%.

Despite the higher electricity to MW efficiency of magnetrons, since solid-state MW generators do not have moving components, they have a higher lifespan (see Table A. 1). Therefore, due to the ease of operation, significantly higher lifetime, flexibility (convenient changes of frequency, power level, and phase), and compact design, the solid-state MW generators are being introduced by several researchers as future MW generators [24, 56-59]. However, high equipment costs and low electricity to MW efficiency are currently the primary barriers of employing the solid-state MW generators for large-scale applications. Therefore, further research is required to improve the performance of both magnetrons and solid-state MW generators, in particular their limited maximum power and electricity to MW efficiency, for large-scale applications.

A.2.1.2 Waveguide system

The created MWs by the MW generator are directed towards the cavity via the waveguide system. Waveguide selection and design mostly depends on the frequency and power of the created MWs as well as the electromagnetic properties of the waveguide. Rectangular, coaxial, circular, elliptical, and ridged shapes are the main configurations that are employed for waveguides. Due to the high bandwidth of rectangular waveguides in comparison with other configurations, it is the most adapted type, and one can find commercial rectangular waveguides with different dimensions. The cross section of a rectangular waveguide is illustrated in Figure A. 2. this review also summarized some of the commercially available rectangular waveguides based on their operating frequency, maximum power, and size in Table A. 2. A detailed list can be found elsewhere [61].

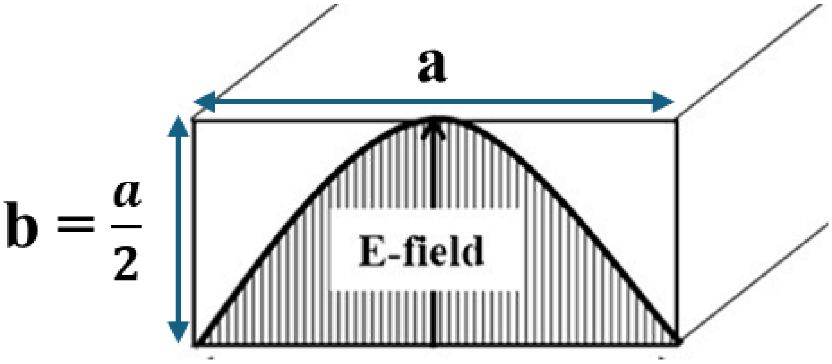

Figure A. 2. Cross section of a rectangular waveguide. Source: Adapted from Radoiu [36].

Table A. 2. Characteristics of some of the common commercial rectangular waveguides [36].

frequency (MHz)	***Waveguide standards***			***a (mm)****	***b (mm)****	***Guided Wavelength (mm)***	***Maximum power (kW)***
	US	***UK***	***IEC***[†]				
2450	WR284	WG10	R32	72.14	34.04	230.89	12
	WR340	WG9A	R26	86.36	43.18	173.23	20
	WR430	WG8	R22	109.22	54.61	147.57	35
915	WR975	WG4	R9	247.65	123.82	495.81	100

[†] International Electrotechnical Commission

*Dimensions illustrated in Figure A. 2.

The created MWs must be transmitted above the cutoff frequency f_c of the waveguide, i.e., the minimum frequency that MW irradiations are transmitted within the waveguide without power loss, and below f_c of the other modes, where their f_c is not the minimum. Accordingly, the applicable frequency is determined by f_c. For a rectangular waveguide, f_c is calculated according to Eq.(A. 1) [24, 43, 56-59].

$$f_c = \frac{c_o}{2\sqrt{\mu_{r,g}\varepsilon_{r,g}}}\sqrt{\left(\frac{m}{a}\right)^2 + \left(\frac{n}{b}\right)^2} \tag{A. 1}$$

where c_o, $\mu_{r,g}$, and $\varepsilon_{r,g}$ respectively represent light's velocity in a vacuum, relative permeability of gas phase, and relative permittivity of gas phase. m and n also represent the variations of the electromagnetic waves in x and y directions, respectively. In addition, this review represented the waveguide's width and height by a and b, respectively. An increase in the waveguide dimension, i.e., "a", reduces the applicable frequency range. For example, waveguide WR2300 with an "a" of 584.2 mm is applicable in the frequency range of 320 to 450 MHz only [62]. Therefore, depending on the operating frequency, limitations on the waveguide dimensions must be considered for designing and scale-up.

In addition to waveguide's geometry, material selection is a critical aspect to design waveguides. MW absorption by waveguide walls decreases the system's energy efficiency and likely overheats the MW source. Hence, in addition to the geometry of the waveguide, to maximize transferring the energy of the created MW towards the cavity, i.e., to avoid MW dissipation within the waveguide, non-magnetic metals with low D_p are designed/selected as waveguide walls. Due to the low D_p of non-magnetic metals (typically bellow 0.5 mm [12, 63], at 9.15 MHz and 2.45 GHz as the operating frequencies), one can adapt the term skin depth δ instead of D_p. Accordingly, by neglecting the polarization loss factor for non-magnetic metals [12], δ can be described by Eq.(A. 2) [12, 35].

$$\delta = \sqrt{\frac{2\rho_w}{2\pi f \mu_{r,w}\mu_o}} \tag{A. 2}$$

As presented in Eq.(A. 2), to minimize δ of the waveguide material, one needs to select a non-magnetic metal with high electrical conductivity, such as copper and aluminum [35, 56, 59], or coat the inside of the waveguide walls with proper materials, such as gold or silver [64]. At low and medium operating temperatures (<400°C), one could select copper and aluminum as the waveguide materials. For high temperature processes (>400°C), like MWH assisted methane (CH_4) reforming, and/or for pharmaceutical and food industries, it is advised to employ non-magnetic metals, such as SUS 316L and Inconel 625, as the waveguide material [36, 65].

A schematic representation of a typical MW system with the traveling MW cavity is presented in Figure A. 3. To prevent overheating of the MW source, one needs to avoid the reflection of MWs back towards the MW generator. To achieve this, as shown in Figure A. 3, a circulator/directional coupler with a dummy load and absorbing terminators can be employed as additional components of the waveguides to act as one-port MW absorbers. While a circulator permits the emitted MWs to be transmitted from the MW generator toward the cavity, the dummy load, as a MW absorber, absorbs the reflected MWs back towards the MW generator. The dummy load is an oscillator protection circuit, classified mainly into water- and air-cooled types. The water-cooled type is applicable in processes with an output MW power of over 1.5 kW, which is the primary situation for large-scale applications, whereas, the air-cooled type, which employs ferrite or SiC as the MW absorber, is applied for MW heating assisted processes with MW power of less than 1.5 kW [35, 36, 56, 59, 66].

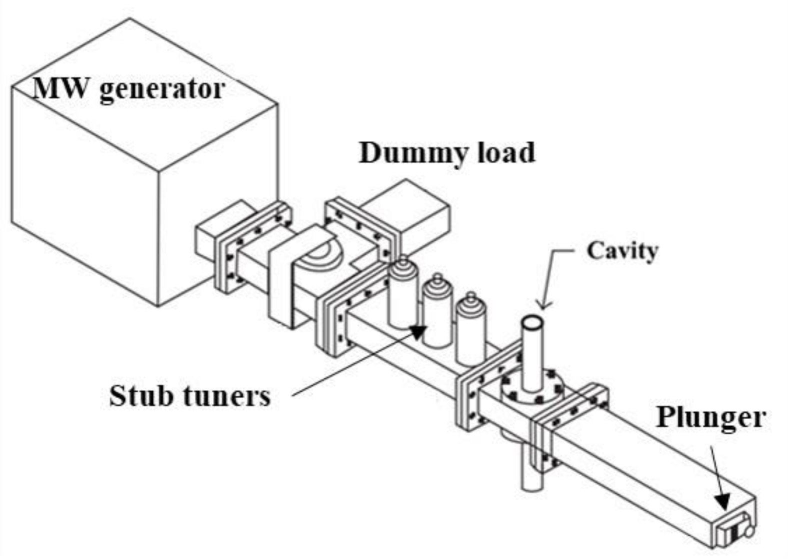

Figure A. 3. Schematic representation of different components of a MW system with the traveling MW cavity (TMC). Source: Adapted from Marinel et al. [67].

To preventing the overheating of MW generator, minimizing the MW reflection back towards the MW generator, i.e., increasing the sample's MW absorption, is a necessary design parameter to raise the overall efficiency of the processes powered by MWH. Accordingly, impedance matching, i.e., resistance matching of the loaded sample and the MW generator, is a critical design parameter to scale up the processes powered by MWH for maximum MW dissipation within the sample [35, 59, 67]. If the loaded sample's resistance is higher than the MW generator's resistance, the excess dissipated power in the MW generator could break it. When the MW generator's resistance is higher than that of the loaded sample, the power dissipation in the loaded sample will decrease. Hence, to maximize the energy transfer from the MW generator toward the loaded sample, i.e., to reduce power loss, one should design a MW heating assisted process with ideally identical resistance for the loaded sample and the MW generator [59]. Primary design parameters to achieve impedance matching in a MW heating-assisted process are sample position and size, EM properties of the sample, cavity dimension, waveguide design, and waveguide components, which are mainly short circuits and stub tuners [5, 35, 59]. In Table A. 3, this review summarized the main remarks of the common components available for rectangular waveguides, as the most adapted type of waveguides for MW heating-assisted processes, to achieve impedance matching.

Table A. 3. Main remarks of the common components available for rectangular waveguides to achieve impedance matching.

Component	***Main remarks***
Stub tuners	• It should be installed on the waveguide wall before the input port of the waveguide to the cavity. • It is designed to minimize MW reflection towards the MW generator. • It achieves impedance matching by adjusting one or more screws. • It can be employed for single- and multi-modes cavities. • It can help achieve precise impedance matching for a wide range of MW powers. • It requires modification for each application. • It is principally employed for systems with MW power up to a few kilowatts. • For high MW power applications, proper justifications are required to prevent safety concerns, in particular electrical current to the waveguide wall. • Higher cost in comparison with short circuits. • It is adjustable for different MW powers and frequencies (need to be tuned).

Table A. 3 (Continued). Main remarks of the common components available for rectangular waveguides to achieve impedance matching.

Short Circuits	• It terminates the waveguide systems. • By reflecting an inverted phase, this component avoids MW reflection from the cavity towards the waveguide input port to the cavity. • Simple design and construction. • It can be employed for single- and multi-modes cavities. • This component is not ideal for achieving precise impedance matching. • It can be employed where MW reflection back towards the MW generator is a critical concern than achieving maximum MW absorption by the loaded sample. • It is mainly employed for systems with low MW power (up to a few kilowatts). • For fixed MW power and frequencies (not adjustable).
Circulators/directional couplers	• It is installed before the input port of the waveguide to the cavity. • Higher cost in comparison with stub tuners and short circuits. • Simple design yet needs careful installation. • It can be employed where MW reflection back towards the MW generator is a critical concern than achieving maximum MW absorption by the loaded sample. • It should be coupled with dummy (matched) load to achieve impedance matching. • For fixed MW power and frequencies (not adjustable).

Stub tuners, which consist of one or more adjustable screws, are inserted in the waveguide from the top of its width dimension along the vertical axis. The insertion extent of the screws to the waveguide and the diameter of the screws are two parameters of the waveguide stub tuners that adjust impedance machining between the loaded sample and the MW generator. Although multi-screw tuners are cheap impedance matching equipment, current flow to the top of the waveguide's width dimension along the vertical axis and the possibility of arcing are the primary challenges of this impedance matching equipment for MW power above 2 kW and 10 kW for operating frequencies of 2.45 GHz and 915 MHz, respectively. In addition to achieving impedance matching in the MW heating-assisted processes, the waveguide tuners (stub tuners) protect the MW generator from the reflected MWs from the cavity back towards the MW generator [5, 35, 36, 56, 59, 67, 68].

A.2.1.3 MW cavity

MWH efficiency is a function of dielectric loss in the object (loaded sample), ohmic loss in the cavity walls, and coupling loss within MW ports and openings of the systems [5, 6, 59, 68-70]. For a higher MWH efficiency, the object loss should be maximized, while the losses in the cavity walls and MW ports and openings of the systems should be minimized. Accordingly, primary design and construction parameters of the MW cavity, which affect the MWH efficiency are [5, 6, 59, 68-70]: (i) shape and dimensions of the cavity, (ii) appropriate material selection for the cavity and insulators, (iii) MW leakage from the system, and (iv) waveguide design around the cavity.

To minimize MW absorption by the cavity wall, a non-magnetic metal, like SUS 316L, with low electrical resistivity ($<7\times10^{-7}$ Ω.m at 20°C), should be selected to reduce δ [71, 72]. In addition, an ideal insulator employed inside the MW cavity to minimize the heat loss is transparent to MWs, has sufficient heat and corrosion resistance, and provides adequate mechanical strength [8, 71-75]. Alumina, mullite, and quartz are the most common insulators for MW treatment. As shown in Table A. 4, alumina can be employed up to 1900°C and shows good thermal shock resistance with a low $\tan(\delta)$, which represents the material's capability for converting the incident electric field to heat, at room temperature. However, $\tan(\delta)$ increases with temperature, and alumina absorbs MWs at elevated temperatures. Mullite is a better choice than alumina owing to better performance as an insulator and a lower $\tan(\delta)$ compared to alumina. However, the preparation of mullite is relatively difficult and limits its application to laboratory-scales. Quartz shows the best performance regarding thermal shock resistance, MW transparency, and thermal conductivity, however a relatively low mechanical strength and low working temperature limit its utilization for reactions below 1100 °C [45].

Table A. 4. Thermal and dielectric properties of alumina and mullite insulators.

Properties	***Thermal expansion coefficient (K^{-1})***	ε'			ε''		
Temperature (°C)	1000–2000	25	1050	1379	25	1050	1379
Alumina [76, 77]	$25–35\times10^{-6}$	8.9	10.8	11.8	0.004	0.16	0.48
Mullite [78-81]	$5.5–8\times10^{-6}$	6.1	8.1	9.7	0.035	0.97	-

In addition to minimizing the MW absorption by the cavity wall, preventing MW leakage from cavities, which can occur due to the coupling loss within MW ports and openings, increases the MW heating efficiency. Besides enhancing the energy consumption of the process, MW leakage from cavities poses a significant safety challenge in the large-scale development of MW heating assisted processes. Primary sources of MW leakage from cavities in batch, like MW vacuum drying in pharmaceutical applications, and continuous, like MW heating-assisted pyrolysis, processes are inlet and/or outlet openings/doors [5, 6, 18-20, 23, 35, 36, 56, 57, 59, 68].

For MW heating-assisted batch processes, quarter-wavelength choke systems are well-established to ensure MW leakage remains under the acceptable standard limits, i.e., less than 10 mW/cm^2 at a distance of 5.08 cm from the unit. Compared to the batch processes, the continuous processes require a more complex MW leakage monitoring due to the continuous inflow and outflow of materials from openings of the cavities. To minimize MW leakage from the openings of the continuous processes, the following considerations can be taken into account [5, 35, 36, 59, 67, 68]: (i) employing openings with dimensions that are less than half of the operating wavelength and waveguide dimensions, i.e., bellow f_c (e.g., $f_c = 1.69$ for WR340), (ii) designing a reactive choking system for the quarter-wave structure with a high reflection coefficient, and (iii) employing a MW absorbent system to decrease MW leakage from the openings. The detailed information related to designing the choke systems are discussed elsewhere [5, 35, 36, 59].

In another classification, two types of cavities are employed for MWH systems: (i) single-mode and (ii) multi-mode. A moveable plunger is employed for the single-mode cavity to adjust the electric and magnetic fields for exposing the loaded sample [82]. Despite a predictable and controllable field pattern, the formation of standing waves within the single-mode cavity causes the non-uniform heating of an object [59]. In addition, the single-mode cavity has a restricted size in the range of one wavelength to support one resonant mode [44]. Consequently, scaling up is a limitation challenge for the single-mode cavity.

Compared to the single-mode cavity, a multi-mode cavity is a large non-magnetic metal chamber in which the sample is exposed to MW. Therefore, in comparison with the single-mode cavities, the multi-mode cavities are preferred choices for large-scale applications. However, the large size of the multi-mode cavity and multiple reflections of MWs from the walls generate many modal patterns, which can pose technical limitations, in particular yielding a non-uniform process condition and MW reflection back towards the MW generator [83, 84]. As a general rule of thumb, for multiple waveguides connected to a single cavity, to minimize MW reflection back towards the MW source, the size of the multi-mode cavity is suggested to be at least five times larger than the wavelength of the created MWs [71, 72]. In addition, to achieve a uniform distribution of EMWs within the cavity, a smaller cavity with a higher frequency (shorter wavelength) can be applied [44]. However, to increase the D_p of MWs for heating large samples more homogeneously, MW with frequency of 915 MHz can be applied, instead of 2.45 GHz. Therefore, by determining the EMWs distribution inside the cavity, one can determine the optimum cavity design and sample loading for the multi-mode cavities [5, 35, 59]. To achieve this, Multiphysics modeling of the MWH-assisted units should be conducted. COMSOL Multiphysics software, as a commercial process simulator software, can help simulate a MWH system by coupling chemical reactions, fluid dynamics, and heat and mass transfers in solids and fluids with the EMWs [85-88]. Hence, prior to the construction and detailed design of the pilot- and large-scale MW heated units, this commercial software could help researchers to predict the conditions for impedance matching, where the maximum MW absorption by the loaded sample occurs. This review also summarized the key concerns and the potential solutions for large-scale design and construction of MW cavities (Table A. 5).

Table A. 5. Main challenges and the potential solutions for large-scale design and construction of MW cavities.

Challenge	***Potential solution***
Limited capacity of MW generators	• New design and configurations to integrate multiple MW generators, instead of multiple reactors. • Increasing the capacity of MW generators.
Impedance matching	• Multiphysics simulation of the system to optimize cavity design, sample loading, and waveguide arrangement around the cavity. • Coupling the real-time feedback control systems with the impedance matching devices, such as stub tuners, circulators, and short circuits for continuous control of impedance matching. • Homogeneous EM properties of the loaded sample. • Proper sample size selection and loading by numerical and experimental investigations.
Undesired hot and/or cold spots formation	• Employing multi-mode cavities for more homogenous distribution of electromagnetic waves compared to single mode cavities. • Proper distribution and/or mixing of MW absorbers inside the cavity, e.g., employing fluidized beds. • Real-time temperature measurement to continuously monitor hot and/or cold spots formation. • Multipoint temperature measurement inside the loaded bed. • Homogeneous EM properties of the loaded sample.
MW leakage	• Employing quarter-wavelength choke systems for batch systems. • MW leakage monitoring in the environment. • Employing openings well below the f_c of the operating MWs for continuous systems. • Designing a reactive choking section for continuous systems. • Designing a MW absorbent system in the openings.
Sparks and arcs	• Employing opto-electric devices for real-time arc detection. • Real-time and multipoint temperature measurement for monitoring abrupt temperature increase. • Shielding the contact temperature measurement devices, like shielded thermocouples with aluminum. • Grounding the MW cavity properly. • Optimize cavity design by Multiphysics simulation to avoid electromagnetic concentration and achieve uniform MW distribution.

A.2.1.4 Temperature measurement

Developing a reliable temperature measurement technique for the processes powered by the MWH is a major difficulty for their large-scale construction and operation. Thermocouples, thermal indicators, mobile temperature sensors, and constant gas volume/air thermometers are the main contact temperature measurement techniques [5, 33, 89, 90]. Thermocouples are broadly used for temperature measurement of the processes powered by the MWH. However, due to the metallic structure of the thermocouples and their interaction with the EMWs, this temperature measurement technique suffers from key challenges, which are [33, 89, 91]: (i) inaccurate temperature measurement, MW source breakdown, and safety issues due to the possible arc formation and (ii) inaccurate temperature measurement owing to the metal's high thermal conductivity. To overcome these difficulties, some researchers investigated the capability of shielded thermocouples for the processes powered by the MWH. Over the last two decades, different researchers [91-94] have reported that by employing a thin layer of MW reflector material, like aluminum, the modified shielded thermocouples can measure temperature up to 800 ^{o}C, while achieving 2 ^{o}C of error under MW irradiations. The complex design and implementation of shielded thermocouples and the disparity of thermal and electromagnetic characteristics of the shield with temperature are the principal challenges of employing this temperature measurement technique for the processes powered by the MWH [91-94].

Thermal indicators are materials that experience color, luminescence brightness, and/or shape changes upon a change in temperature. Principal thermal indicators employed for the processes powered by the MWH are: (i) liquid crystals, (ii) thermal indicator paint, and (iii) thermal melting indicators. While liquid crystals experience structural changes with a temperature increase, thermal indicator paint and thermal melting indicators illustrate color change with a temperature increase [33, 89-91]. In addition to temperature measurement, as shown in Figure A. 4.a, one could employ a MW absorber thermal indicator, like thermal papers, to assess the electromagnetic field distribution inside the cavity [95-98]. Results collected from thermal indicators can help validate the results of numerical models describing the interaction of the EMWs with the sample [97]. Thermal indicators were successfully employed for a wide range of operating temperatures (30 ^{o}C - 1280 ^{o}C) with a low measurement error (around 2 ^{o}C) [33, 95-98]. However, the incapability of determining temperature gradient inside the sample, single step and irreversible temperature measurement, the difficulty in validating the technique with other temperature measurement techniques, the complexity of online temperature measurement, and the necessity of coating some thermal indicators with a MW absorber are the principal challenges of employing thermal indicators in large-scale applications [33, 95-98].

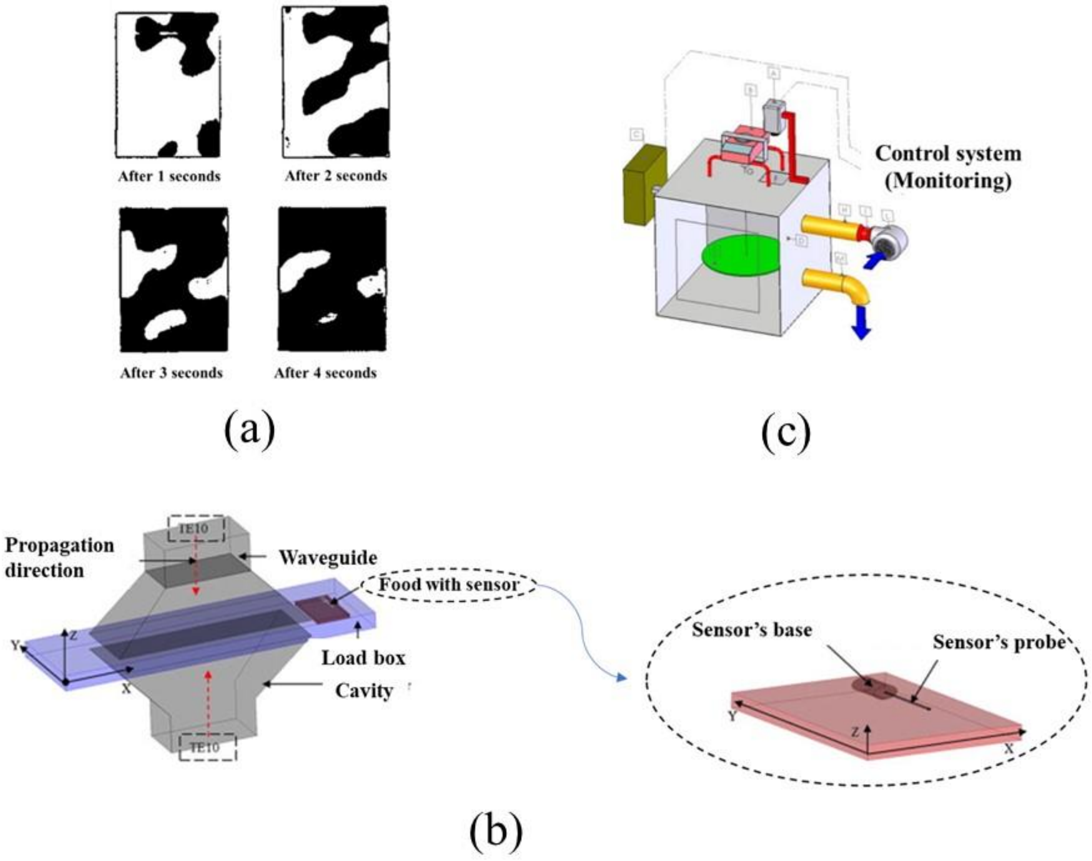

Figure A. 4. Schematic representation of: a) color change of thermal papers under the MW irradiations (source: adopted from Bradshaw et al. [95]), b) a mobile temperature measurement device (source: adopted from Luan et al. [99]), and c) automatic integration of thermal imaging technique with a batch MW heating assisted process (source: adopted from Cuccurullo et al. [100]).

Constant gas volume/air thermometers operate based on Gay-Lussac's law, where changes in the temperature of the confined air in the probe results in pressure change. The external pressure transducer connected to the miniature probe helps monitor the temperature change. To measure the operating temperature while avoiding the interaction of the probes with the EMWs, MW transparent probes, like quartz, are employed. The fragile probes are unsuitable for harsh environments with moving solids, like a gas-solid fluidized bed reactor (FBR). Therefore, low spatial resolution and the necessity of using fragile MW transparent probes are challenging issues to implement this temperature measurement technique in large-scale processes powered by the MWH [101, 102].

As shown in Figure A. 4.b, mobile temperature sensors consist of a base, normally a cylindrical type, and a sensor probe, which store and sense temperature, respectively. Mobile temperature sensors are commercially available. To protect the sensor and the probe from high temperature environment, while mitigating interference of the device with the electromagnetic field, the mobile temperature sensors are typically shielded similar to the shielded thermocouples explained earlier in this section. It is reported that these devices deliver useful information to measure temperature inside packaged foods [99]. The mobile temperature sensors have also been successfully implemented in the pilot-scale MWH-assisted thermal sterilization system [103]. The combination of this technique with the numerical simulations could also help investigate the thermal behaviour of a process heated by the MW [33, 99, 103, 104]. However, similar to thermocouples, due to the metallic components employed in the mobile metallic temperature sensors, they could interfere with the electromagnetic field distribution inside the cavity.

Considering the abovementioned problems related to the application of contact temperature measurement techniques under the MW irradiation, more researchers are investigating the possibility of employing contactless temperature measurement techniques for the processes powered by the MWH [5, 33, 36, 59, 68, 89, 90]. Contactless temperature measurement techniques could be categorized into [5, 33, 36, 59, 68, 89, 90]: (i) thermal imaging technique, (ii) pyrometer, (iii) optical fiber sensors, (iv) MW radiometry, and v) ultrasonic thermometer.

The thermal imaging technique detects the emitted infrared radiation (IR) from the heated sample. In this technique, IR-sensitive cameras are employed to illustrate the temperature distribution on the sample’s surface. The distance from the loaded sample and the optical density of the camera are two parameters that could enhance the temperature distribution resolution of the sample’s surface. Since the accuracy of this technique depends on emissivity of the loaded sample, materials with non-uniform emissivity could decrease the accuracy of the temperature measurement, like employing the MWH to vaporize the water content of the sample. For online implementation of this temperature measurement technique, the electrical components of the device exposed to MW irradiation should be shielded. In addition, construction of an optical window for installing an IR device must be taken into consideration [33, 100, 105, 106]. As shown in Figure A. 4.c, it is reported [100] that this temperature measurement technique could be automatically integrated within the processes powered by the MWH to develop an automated temperature-regulated process. However, measuring the inner temperature of large samples on a pilot- and/or industrial-scale is still a barrier for this temperature measurement technique.

A pyrometer works based on the IR detection emitted from the hot sample. However, despite a thermal imaging technique that detects the temperature on a large surface of the material, the pyrometer covers a small area of the hot surface (due to the low D_p of the IR), which mitigates the inner temperature measurement of the loaded sample in pilot- and/or industrial-scale applications. Compared to the thermal imaging technique, the pyrometer does not require costly optical and scanning devices, which introduced it as a widely employed technique for the processes powered by the MWH in laboratory-scale investigations. In addition, for pilot- and large-scale applications, in cases of handling material with uniform chemical and EMW properties without hot and/or cold spot formations, a combination of pyrometers installed in different positions could help extrapolate a continuous temperature distribution on the surface of the hot samples. Moreover, the pyrometer requires a small optical window, which facilitates MW leakage control in this technique [33, 89]. However, if the cavity is not transparent and/or does not have an optical window, one may not/cannot adopt the pyrometer.

Temperature change of the sample influences the properties of the emitted lights. Accordingly, by comparing the emitted and reflected lights, which results in the interference pattern, the optical fiber sensor measures the temperature of the sample [33, 89, 91]. The principal advantages of the optical fiber sensors are [89, 91, 107-111]: (i) they do not interfere with the EMWs, (ii) it is reported that this temperature measurement technique is able to have measurement accuracy of 0.1 ^{o}C, (iii) they could have a fast response time as low as 0.05 seconds, and (iv) they deliver continuous online temperature measurement. Hence, considering the operating temperature of food drying and cooking, this technique can be successfully employed for MWH-assisted food processing [18, 110, 111]. In addition to the limited temperature range of this measurement technique, there are still key challenges for industrial-scale applications of optical fiber sensors in the processes powered by the MWH. Since fiber optic sensors are mechanically sensitive and the direct contact of the loaded sample and the sensor increase the accuracy of the internal temperature measurement, implementation of this temperature measurement technique is challenging for harsh environments, like fluid-solid fluidized beds [89, 91, 107-111]. However, employing protective coating can enhance their durability within the harsh environment.

The working principal of a MW radiometry temperature measurement technique is similar to the thermal imaging technique. However, MW radiometry employs a radiometer instead of an IR to detect the emitted MWs from the sample [112-115]. To mitigate the possibility of the interaction of the electromagnetic field created via the processes powered by the MWH and the MW radiometry, one could employ a multifrequency MW radiometry to measure the temperature of the loaded sample. This measurement technique is also capable of measuring the inner temperature of the loaded sample in the range of centimeters. Hence, this temperature measurement technique has the potential to be adapted for fluid-solid medias, where detecting the hot and cold spots in the loaded sample are of the critical importance. In addition, compared to the other contactless temperature measurement techniques, MW radiometers are economically viable devices. The main drawbacks of this temperature measurement technique are [112-116]: (i) the long response time compared to thermocouple, which limits its application for the continuous temperature control of processes heated by the MWH, (ii) low spatial resolution (in the range of cm^2) in comparison with the thermal imaging and pyrometer (in the range of mm^2), and (iii) complex implementation. Researchers [114, 116] have reported the successful implementation of this technique for accurate temperature measurement for human tissue and the internal body. However, comprehensive studies are required to assess the practical application of this temperature measurement technique for large-scale processes powered by the MWH.

Ultrasonic thermometers, as a precise temperature measurement technique (measurement precision $< 1\ ^{o}C$), work based on the effect of the media on the acoustic velocity, i.e., speed of sound in the media. In the pulse echo technique, which is the most common technique employed in ultrasonic thermometers, one first sends an ultrasonic pulse towards the media. Subsequently, by measuring the required time between the initial and reflected pulses, the acoustic velocity is estimated. As shown in Eq. (A. 3), since the elastic modulus and density of the media depend on the temperature, a change in temperature affects the acoustic velocity. Hence, the sound traveling throughout the material contains the relevant information about the temperature. Ultrasonic thermometers, as remote temperature measurement devices, do not interfere with MW irradiation. In addition, while the ultrasonic thermometers have a fast response time, they are not limited to the operating temperature (over 2000 ^{o}C). Moreover, this temperature measurement technique has been successfully employed for several solid materials, such as metals and ceramics. Although one could apply the inversion techniques to estimate the local temperature, ultrasonic thermometers are typically employed to measure the average temperature of the sound's propagation path. Comparably high equipment cost and the dependency of the measurement accuracy on ablation and/or erosion of the solid inventory are other drawbacks of this temperature measurement technique [117-120].

$$\mathrm{v(T)} = \sqrt{\frac{\mathrm{E(T)}}{\rho\mathrm{(T)}}} \tag{A. 3}$$

The suitability of commonly adapted contact and contactless temperature measurement techniques for large-scale MW heating assisted processes were summarized (Table A. 6).

Table A. 6. Comparison of different temperature measurement techniques for large-scale MW heating assisted processes. (✓): Viable, (×): Not Viable, (△): Conditional, (+) Moderate.

Technique	*Spatial resolution*	*Typical measurement range (°C)*	*Typical response time (s)*	*Accuracy*	*Cost*	*Automation (online power control) compatibility*	*Operation and maintenance*	*Ability to work in harsh condition*	*Safety (avoid arc*
Contact									
Thermocouples	+	-200 to 2500	0.02 to 3	△	✓	✓	✓	✓	×
Thermal indicators	×	-30 to 150	Offline	+	✓	×	△	△	✓
Mobile temperature sensors	△	-40 to 125	< 1	△	✓	✓	✓	✓	×
Constant gas volume/air thermometers	×	25 to 700	< 1	✓	✓	✓	△	×	✓
Contactless									
Thermal imaging	+	-50 to 2500	< 0.01	△	✓	✓	✓	✓	✓
Pyrometer	+	-50 to 2200	< 0.002	△	✓	✓	✓	✓	✓
Optical sensors	✓	-200 to 450	0.05-2	△	△	✓	△	△	✓
Microwave radiometry	△	-50 to 1600	< 1	✓	△	✓	✓	✓	✓
Ultrasonic thermometers	×	-50 to 8000	< 0.001	✓	×	✓	×	✓	✓

A.2.2 Uniform heating

Hot spots with temperatures much elevated than their surroundings in the sample could cause a sharp temperature gradient within the sample, as illustrated in Figure A. 5 [6, 7]. While hot spot formation in the processes powered by the MWH can behave as an undesired phenomena, like causing the agglomeration of solid particles in catalytic reactions, one can take advantage of this phenomena to enhance the reaction progress and decrease the required energy, for instance to increase methane (CH_4) conversion in the catalytic dry and/or steam CH_4 reforming [6, 7, 12]. Therefore, considering the complex behavior of hot spots formation, prior to large-scale development of the processes powered by the MWH, laboratory and/or virtual experiments of each case study is necessary.

In fluid-solid multiphase systems, such as gas-solid fluidized or slurry beds, where the fluid applies a large enough drag force on the particles, the heat transfer among the fluid and solid phase increases that results in achieving a uniform temperature distribution throughout the loaded sample. In addition, the movement and/or circulation of solid particles help them to experience different magnitudes of the electromagnetic field. Hence, solid particle movement and recirculation could eliminate or reduce hot and cold spots formation in MWH-assisted fluid-solid multiphase systems [6, 7, 12, 121]. As shown in Figure A. 6, by increasing the stirring rate of the slurry from 0 to 1500 rpm, the hot spot formations are reduced significantly [121]. Similarly, fixed bed reactors suffer from hot spot formations, which restrict large-scale development of these reactors heated by microwave. Compared to the fixed bed reactors, structured reactors reduce the contact points of the sphere particles, and increase the heat transfer via conduction thorough the media [6, 122].

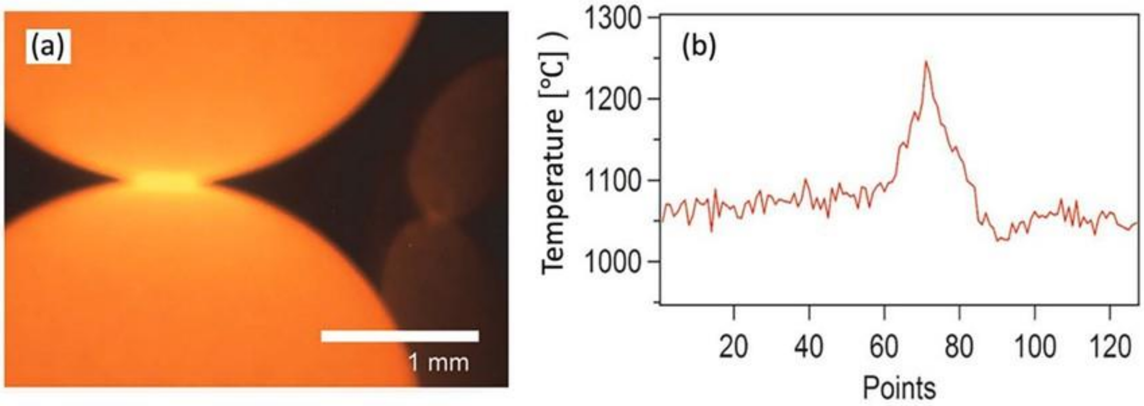

Figure A. 5. MW heating effect on a) hot spot formation and b) the corresponding temperature distribution for two SiC sphere particles with a diameter of 2.38 mm that are in contact in a fixed-bed reactor. Source: Adopted from Haneishi et al. [123].

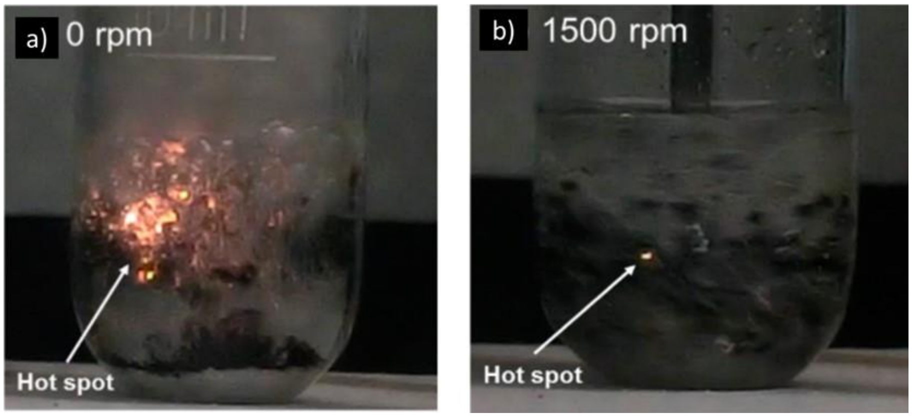

Figure A. 6. Effect of stirring rate on hot spot formation in Pd/activated carbon catalysts during MW heating at 550 W inside a 25 mm wide tube reactor. Source: Adopted from Horikoshi et al. *[121]*.

A.2.3 MW absorber screening and fabrication

The MW absorption ability of the target solid particle is another challenge of the large-scale application of the processes powered by the MWH, specifically in heterogenous catalytic reactions or in reactions where the feedstock is composed of solid particles such as biomass [5, 6, 14, 34]. Different researchers [124, 125] employed a catalyst mixed with a MW absorber, like SiC and/or carbon coated silicon dioxide (C-SiO_2), to advance the catalytic dry reforming of methane (DRM) heated under MW irradiation on a laboratory-scale. However, to avoid difficulties of employing two separate solid phases in MWH-assisted FBRs for catalytic reactions, fabrication of MW absorber catalyst(s) is necessary [9, 124]. In addition, in the case of MW-heated biomass processing, biomass materials are typically poor MW absorbers, unless they are converted to biochar. Hence, developing a good MW absorber to be mixed with the biomass feed that does not deviate the reaction from the desired products, while it can be practically separated from the final products is a critical scale-up challenge for MW heated biomass processing [6, 126]. It should be noted that the effect of particle size on selecting/synthesizing MW receptors was discussed in CHAPTER 2.

A.3 MW scale-up practices and the iterative scale up approach

Neha et al. [127] accomplished a techno-economic analysis and a life cycle assessment for the MWH-assisted co-pyrolysis of food waste and low-density polyethylene. While the landfill and open dumping of food waste were responsible for 200 and 420 kg CO_2 equivalent (eq), respectively, the MWH-assisted co-pyrolysis of food waste reduced the emission to 38.8 kg CO_2 eq only. In addition, it was also illustrated that the MWH-assisted co-pyrolysis of food waste is economically viable. In iron and steelmaking industries, a large CO_2 emission and lack of high-grade raw materials (iron ore and coal) prompted research into environmentally-friendly technologies with a higher energy efficiency to respond to the large demand for high-quality steel production. Nagata et al. [71, 72, 75, 128, 129] studied ironmaking from a mixture of low-grade iron ore and graphite (containing impurities of phosphorus, silicon, and sulfur) via MWH to 1400 ℃ for halving the CO_2 emission. Currently, they can produce 10 tons of pure pig iron/m^2 in a MWH-assisted blast furnace, employing inferior ore with low strength. Their MWH-assisted blast furnace can provide 120 kW power [129] using four 30 kW-klystron as MW generators (Figure A. 7). Since pig iron reflects MWs, they heat the produced pig iron conventionally to avoid clogging the outlet.

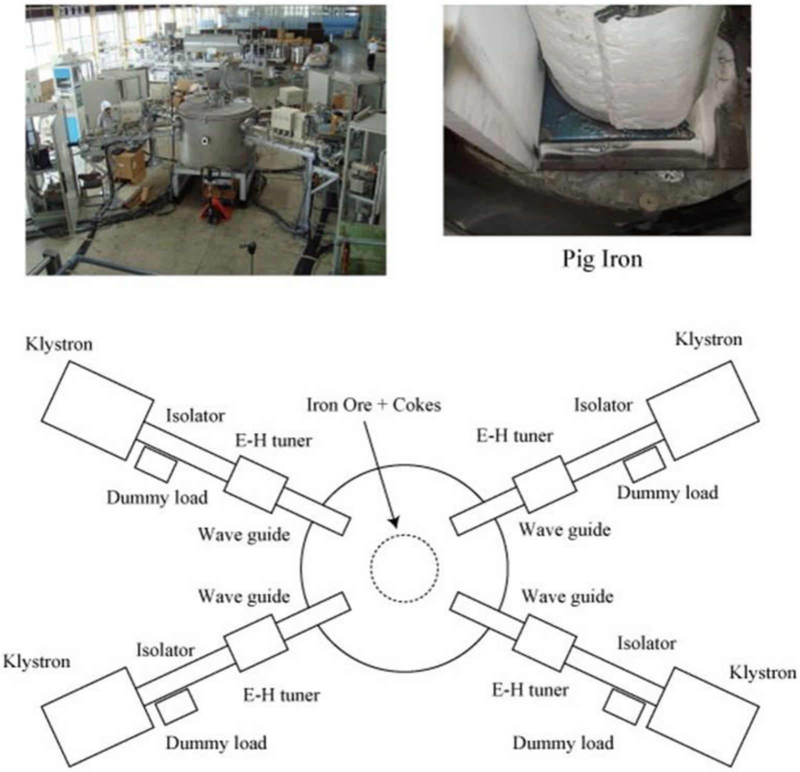

Figure A. 7. Schematic illustration of 120 kW (4×30 kW) microwave blast furnace for producing 10 tons of pure pig iron/m^2 in a MW assisted blast furnace. Source: Adopted from Nagata et al. *[129]*.

Operating expenditures and the corresponding total cost is likely reduced, while the efficiency of the process increases, by connecting the processes powered by the MWH with renewable electricity, and taking advantage of the SH. MWH-assisted activated carbon production from agricultural Pea waste was studied by Sharif H. Zein et al. [130] for a plant with a capacity of 3468 ton/year of activated carbon. Based on their evaluations, 3 years was estimated as the payback period of the plant. In addition, with GBP 100,953,125 as the required total investment of the plant, internal rate of return, net present value (NPV), and return on investment were estimated to be 55%, GBP 4,476,137,298, and 52%, respectively. A study of the MWH-assisted vacuum pyrolysis for simultaneous waste plastic and used cooking oil processing for fuel manufacturing in a plant capacity of 100 kg/h was done [131]. In addition to a higher heating rate and lower processing time owing to the MWH, the synergic effect of the MWH and activated carbon reaction increased the liquid oil yield up to 84 wt.%. Compared to the market price of diesel fuel in Malaysia (0.523 $/L), the techno-economic investigation showed a lower cost of production of 0.25 $/L of the produced liquid fuel, which introduced this waste reduction and energy conversion technology as a encouraging suggestion to the conventional methods of diesel fuel production [131].

To measure the scaling up feasibility of a proposed technology from technical, environmental, and economic perspective, one may apply conventional scale-up approach. The conventional scale-up approach, depicted in Figure A. 8a, classically involves the sequential (stage-by-stage) passage of a chemical process from lab to industry. The core concerns with this well-established approach are:

- Its time-intensive nature.
- Substantial financial investment that is required to accomplish the sequential transition.
- Potential design and operational challenges causing from the sequential transition.

Unlike the conventional scale-up, applying the iterative scale-up and leveraging the available CFD simulation tools and process simulators, as shown in Figure A. 8b, one can focus the technical and economic problems and concerns for scaling up rather than building the intermediate steps of pilot and demonstration plants [132]. This review then recommend leveraging the inventive approach of iterative scale-up to find and resolve the possible issues before scaling up the processes powered by the MWH. For more information related to implementation of this scale-up approach, interested readers could refer to Ref [132].

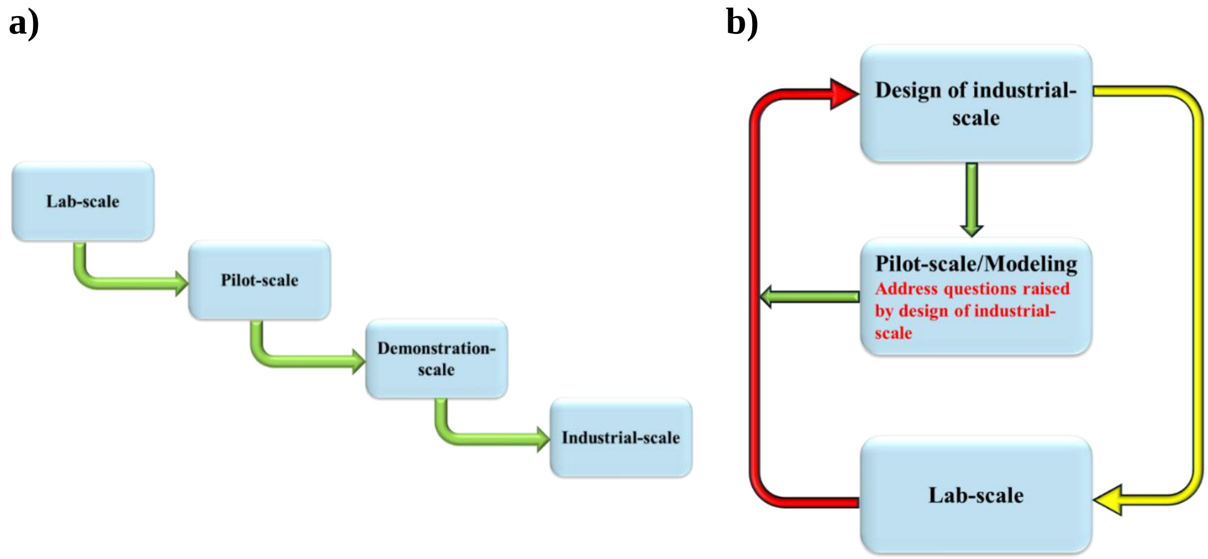

Figure A. 8. Schematic representations of (a) conventional and (b) iterative process scale-up approaches.

A.4 Future direction

Among the various factors articulated in this study, two major difficulties that are delaying the scale-up of the processes powered by the MWH are the accurate and safe temperature measurement and the limited capacity (below 100 kW) of the MW generators that are currently available. By simultaneous implementation of contact and contactless temperature measurement techniques, one may reach to a reliable temperament measurement in the unit operations heated by MW. However, the limited capacity of the MW generators that are currently available inevitably yields the employment of several reactors. This limitation increases the cost of manufacturing and creates technical problems during the scale-up. Hence, this review recommend further experimental and simulations studies.

A.4.1 Experimental studies

While Multiphysics simulations can be applied to explore alternative cavity and reactor designs to overcome the limitations of MW generators (their limited capacity) and to improve system energy efficiency, experimental studies are necessary for the development of temperature measurement techniques that do not interfere with EMWs yet provide high spatial resolution of the temperature distribution within the sample. In this context, to improve the reliability of the contactless temperature measurement devices and techniques for large-scale unit operations heated by the MW, further research is unavoidable to answer the bottleneck of surface temperature measurement and the low spatial resolution of these temperature measurement techniques.

A.4.2 Simulation studies

While experimental studies are expensive and time-consuming, progress in numerical simulations is promising for a more effective scale-up of Multiphase systems. COMSOL Multiphysics software can integrate EMWs by solving Maxwell’s equations in the frequency domain, along with fluid dynamics and heat and mass transfer, which are solved in the time-dependent domain, to conduct a frequency-transient study. Hence, this modeling/simulation tool could create valuable guidelines for the design and construction of large-scale processes powered by the MWH. Recommended studies for the numerical modeling of the MW heating-assisted processes, aiming to facilitate their large-scale deployment are summarized in Table A. 7.

Table A. 7. Recommended studies for the numerical modeling of the MWH-assisted processes, aiming to facilitate their large-scale deployment.

Simulation	***Description***
Implementation	Coupling EMW with energy, momentum, and mass balances: 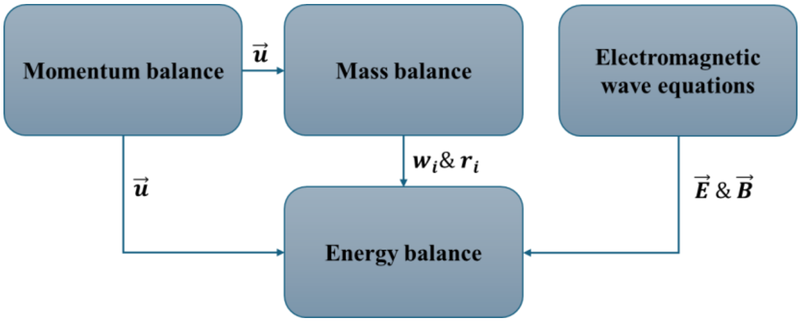
Expected Outcomes	• Predict EMWs distribution. • Predict temperature distribution. • Optimize the geometry of the MW cavity. • Waveguide arrangement and installation. • Effect of the sample’s EM properties. • Effect of process parameters, e.g., MW power and frequency. • Effect of sample size and shape.

A.5 Conclusion

Among various factors studied in this review, the topmost challenges and/or areas that must be concerned for successful scale-up of the processes powered by the MWH are: (i) exploring alternative cavity and reactor designs to overcome the limitations of MW generators (their limited capacity), (ii) maximizing MW dissipation and uniform heating, (iii) accurate, safe, and reliable temperature measurement, and (iv) safety challenges raised by MW leakage, sparking, and arc formation.

MW generators, as core of the MW system, are classified into solid-state MW generators and magnetrons. Compared to magnetrons, solid-state MW generators conveniently operate within a flexible range of frequencies and MW power levels instantaneously, which reduce energy loss resulted from impedance mismatching. However, a lower electricity to EMW efficiency (≤65%) and high equipment cost restrict the application of solid-state MW generators to laboratory-scales. Compared to solid-state MW generators, by adapting the magnetic mirror effect in magnetrons, it is possible to increase the electricity to EMW efficiency up to 92%. However, for industrial-scale magnetrons, the electricity to EMW efficiencies are typically around 80% and 65% for the operating frequencies of 2.45 GHz and 915 MHz, respectively. The available MW sources/generators maximum capacity/power is also restricted to 30 kW and 100 kW for operating frequencies of 2.45 GHz and 915 MHz, respectively. Hence, improving the MW generators' capacity, electricity to MW efficiency, and lifetime is necessary to scale-up the processes powered by the MWH.

Design of waveguides and MW cavities influence MW dissipation and uniform heating. Short circuits and stub tuners are the main components of waveguide to enhance energy efficiency (maximizing energy transfer to the sample and to achieve impedance matching) of a process powered by the MWH. However, current flow to the top of the waveguide's width dimension along the vertical axis and the possibility of arcing are the primary challenges of using stub tuners for MWs with a power over 2 kW at a frequency of 2.45 GHz and 10 kW at a frequency of 915 MHz. Similar to the stub tuners, due to the limited MW power handling capability of short circuits, they are primarily recommended for TMCs. Thus, in addition to adapting and developing waveguide's components, such as short circuits and stub tuners, this review recommend new reactor design and waveguide arrangement to enhance the performance of the process and resolve the concern resulting from the limited MW generator's capacities. To achieve this, this review recommend numerical modeling and simulation by using a Multiphysics software (like COMSOL Multiphysics) to integrate EMWs along with fluid dynamics and heat and mass transfer to conduct a frequency-transient study.

Developing a reliable temperature measurement technique, which can be used accurately under EM radiation, is another challenge of deploying processes powered by the MWH. Thermocouples, thermal indicators, mobile temperature sensors, and constant gas volume/air thermometers are the main contact temperature measurement techniques. The thermal imaging method, pyrometer, optical method, MW radiometry, and ultrasonic thermometers are the main contactless temperature measurement techniques. Although thermocouples are the most widely used temperature measurement technique for laboratory-scale setups powered by the MWH, they may interfere with the EMWs, which can result in inaccurate temperature measurement and the possibility of arc formation and sparking. Hence, to employ contactless temperature measurement techniques in large-scales units powered by the MWH without interfering with the MWs, more research endeavors are needed to address surface temperature measurement and low spatial resolution, as the principal limitations of contactless temperature measurement techniques.

Nomenclature

Acronym

CAPEX	Capital expenditures
DRM	Dry reforming of methane
EM	Electromagnetic
EMW	Electromagnetic wave
eq	Equivalent
FBR	Fluidized bed reactor
GHG	Greenhouse gas
IR	Infrared radiation
MW	Microwave
MWH	Microwave heating
NPV	Net present value
OPEX	Operating expenditures
RIS	Real industrial-scale
TCOP	Total cost of production
TMC	Traveling microwave cavity
VIS	Virtual industrial-scale

Symbols

a	Waveguide width (m)
b	Waveguide height (m)
c_o	Speed of light in vacuum (m/s), i.e., 2.9×10^8 m/s
D_p	Penetration depth (m)
E(T)	Elastic modulus (Pa)
f_c	Cutoff frequency of a rectangular waveguide (Hz)
f_{cc}	Cutoff frequency of a coaxial waveguide (Hz)
g	Gravitational acceleration $\left(\frac{m}{s^2}\right)$

k_o	Free space wave number (-)
m	Variations of the electromagnetic waves in x direction (-)
n	Variations of the electromagnetic waves in y direction (-)
r_i	Radius of the inner conductor (m)
r_o	Radius of the outer conductor (m)
T	Temperature (K)
$\tan(\delta)$	Loss tangent (-)
$\tan(\delta_\mu)$	Magnetic loss tangent (-)
$v(T)$	Acoustic velocity (m/s)
Z_o	Characteristic impedance (Ω)

Greek letters

ε'	Relative dielectric constant (-)
ε''	Relative loss factor (-)
ε_r	Relative permittivity (-)
$\varepsilon_{r,g}$	Relative permittivity of gas phase (-)
μ'	Relative magnetic constant (-)
μ''	Relative magnetic loss factor (-)
μ_r	Relative permeability (-)
$\mu_{r,o}$	Relative permeability of the free space (-)
$\mu_{r,g}$	Relative permeability of gas phase (-)
$\mu_{r,W}$	Relative permeability of the waveguide (-)
$\rho(T)$	Density of the media (kg/m^3)
ρ_W	Electrical resistivity of the waveguide (Ω·m)
δ	Skin depth (m)
ω	Angular frequency (1/s)